11 April 2008 | $10

Science

AAAS

COVER

A lined day gecko (*Phelsuma lineata*) from Andasibe, eastern Madagascar. This gecko is one of the 2315 species analyzed to identify optimal expansion sites for protected areas within Madagascar, as described on page 222.

Photo: Miroslav Honzák

DEPARTMENTS

EDITORIAL

NEWS OF THE WEEK

NEWS FOCUS

LETTERS

BOOKS *ET AL.*

POLICY FORUM

PERSPECTIVES

CONTENTS continued >>

SCIENCE EXPRESS

www.sciencexpress.org

MOLECULAR BIOLOGY

Endogenous siRNAs Derived from Transposons and mRNAs in *Drosophila* Somatic Cells

M. Ghildiyal et al.

Endogenous small interfering RNAs transcribed from both transposons and messenger RNAs are found in somatic cells of flies and may act to silence "selfish" genetic elements.

10.1126/science.1157396

IMMUNOLOGY

Innate Immune Activation Through Nalp3 Inflammasome Sensing of Asbestos and Silica

C. Dostert et al.

A large multiprotein complex detects particulate airborne pollutants that have been taken up by immune cells in the lung and initiates a potent inflammatory response.

10.1126/science.1156995

APPLIED PHYSICS

Subnanometer Motion of Cargoes Driven by Thermal Gradients Along Carbon Nanotubes

A. Barreiro et al.

A segment of the outer shell of a multiwall carbon nanotube can move back and forth in response to a thermal gradient created by electrical current passing through the nanotube.

10.1126/science.1155559

NEUROSCIENCE

Temperature Sensing by an Olfactory Neuron in a Circuit Controlling Behavior of *C. elegans*

A. Kuhara et al.

An olfactory neuron in *Caenorhabditis elegans* also senses the ambient temperature and is necessary for worms' propensity to seek out the temperature at which they were raised.

10.1126/science.1148922

REVIEW

BREVIA

RESEARCH ARTICLES

REPORTS

CONTENTS continued >>

REPORTS *CONTINUED...*

ADVANCING SCIENCE, SERVING SOCIETY

SCIENCE (ISSN 0036-8075) **is published weekly on Friday, except the last week in December, by the American Association for the Advancement of Science, 1200 New York Avenue, NW, Washington, DC 20005.** Periodicals Mail postage (publication No. 484460) paid at Washington, DC, and additional mailing offices. Copyright © 2008 by the American Association for the Advancement of Science. The title SCIENCE is a registered trademark of the AAAS. Domestic individual membership and subscription (51 issues): $144 ($74 allocated to subscription). Domestic institutional subscription (51 issues): $772; Foreign postage extra: Mexico, Caribbean (surface mail) $55; other countries (air assist delivery) $85. First class, airmail, student, and emeritus rates on request. Canadian rates with GST available upon request, GST #125439822. Publications Mail Agreement Number 1069624. **Printed in the U.S.A.**

Change of address: Allow 4 weeks, giving old and new addresses and 8-digit account number. **Postmaster:** Send change of address to AAAS, P.O. Box 96178, Washington, DC 20090-6178. **Single-copy sales:** $10.00 current issue, $15.00 back issue prepaid includes surface postage; bulk rates on request. **Authorization to photocopy** material for internal or personal use under circumstances not falling within the fair use provisions of the Copyright Act is granted by AAAS to libraries and other users registered with the Copyright Clearance Center (CCC) Transactional Reporting Service, provided that $20.00 per article is paid directly to CCC, 222 Rosewood Drive, Danvers, MA 01923. The identification code for Science is 0036-8075. Science is indexed in the *Reader's Guide to Periodical Literature* and in several specialized indexes.

CONTENTS continued >>

Birdseed. Friend or foe?

SCIENCENOW

www.sciencenow.org DAILY NEWS COVERAGE

Birds on the Dole
Does the backyard bird feeder help or hurt your feathered friends?

The Long and Short of It
Dozens of genes and DNA regions linked to height.

Converted Cells Show Promise for Parkinson's
Induced pluripotent stem cells mitigate movement disorder in rats.

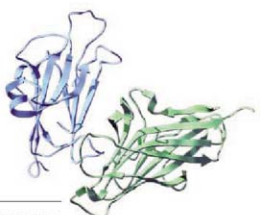

Eph-ephrin interactions.

SCIENCE SIGNALING

www.sciencesignaling.org
THE SIGNAL TRANSDUCTION KNOWLEDGE ENVIRONMENT

REVIEW: Eph, a Protein Family Coming of Age—More Confusion, Insight, or Complexity?
M. Lackmann and A. W. Boyd
Eph receptors and their ephrin ligands coordinate cell-positioning programs during development and oncogenesis.

JOURNAL CLUB: GABA Effects on Neurogenesis—An Arsenal of Regulation
Y.-F. Yuan
γ-aminobutyric acid (GABA) regulates neurogenesis in various circumstances.

Today's undergrads, tomorrow's scientists.

SCIENCE CAREERS

www.sciencecareers.org/career_development
CAREER RESOURCES FOR SCIENTISTS

Special Feature: Undergraduates
J. Austin
Today's college kids are the scientists of the future—and in some cases, the present.

The Truth About Gen Y
E. Pain
Experts consider "millennials" one of the greatest generations ever to hit the workplace.

Does Grad School Make Financial Sense?
S. Webb
Although a Ph.D. in science may work out financially over an entire career, money woes can be considerable in the short term.

Community Colleges Fuel the Science Workforce
S. Carpenter
With minority scientists in short supply, officials turn to 2-year colleges as a source of talent.

SCIENCE PODCAST

Download the 11 April *Science* Podcast to hear about possible radioprotective drugs, modeling the Cretaceous supergreenhouse, new treatments for alcoholism, and more.
www.sciencemag.org/about/podcast.dtl

CREDITS: (SCIENCENOW) GILLIAN FOAN; (SCIENCE CAREERS) ATLANTA CENTER FOR BEHAVIORAL NEUROSCIENCE/NATIONAL SCIENCE FOUNDATION; (SCIENCE SIGNALING) C. BICKEL

Separate individual or institutional subscriptions to these products may be required for full-text access.

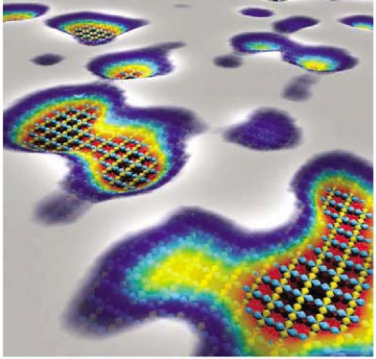

CREDITS (TOP TO BOTTOM): A. YAZDANI/PRINCETON UNIVERSITY; SHEPPARD ET AL.

<< No Glue for Cuprate Superconductors?

More than 20 years after their appearance, it is still unclear how the charge carriers in the high-temperature superconducting cuprates pair up and condense into the superconducting state. Some scenarios argue for a boson-mediated "glue" to bring them together, as in conventional superconductors, whereas in other scenarios, the glue is unnecessary and electronic correlation provides the necessary pairing energy. **Pasupathy *et al.*** (p. 196) now present temperature-dependent scanning tunneling spectroscopy data above and below the superconducting transition temperature that they believe to be strong evidence for the latter "no glue" picture.

Magnetic Domain-Wall Memory

Present memory storage is generally based on two architectures: random access memories, which are fast but expensive, and hard disk drives, which are cheap but slow. Other memory architectures are being developed, but they are also inherently two-dimensional and based on a one-bit, one-memory design. Thus, the expected improvement in memory density and speed is somewhat incremental. In an overview, **Parkin *et al.*** (p. 190) lay out the basic concept of "race-track memory," in which information is stored as a sequence of domain walls (interfaces between regions of different magnetization direction) on a magnetic strip. As many domain walls can be written on the wire and can be shifted along the strip by current-induced domain-wall motion, one-bit, many-memory designs are possible that could lead to orders of magnitude improvement in performance. A realization of the basic working principles of racetrack memory is presented by **Hayashi *et al.*** (p. 209), who show that it is possible to shift multiple domain walls to and fro along a magnetic nanowire repeatedly at high speed using nanosecond current pulses without any external magnetic fields.

Reservoir Logs

Although the contributions of melting glaciers and ice sheets to sea-level rise garner the most attention, global warming also increases sea level through the increased volume of warmer ocean water. When the thermal effects of ocean heating are calculated and the net observed rate of sea-level rise are subtracted, the remainder is commonly equated with ice-melt contributions. However, **Chao *et al.*** (p. 212; published online 13 March) have reconstructed the history of water impoundment in reservoirs filled during the last century and show that filling the reservoirs of the world depressed sea-level rise substantially. Thus, the amount of water contributed by ice melting was correspondingly higher than had been assumed.

Hematite Currents

A wide range of abundant minerals, such as hematite (Fe_2O_3), are semiconductors, but this electrical property has rarely been considered in analyses of these materials' natural geochemistry. **Yanina and Rosso** (p. 218, published online 6 March; see the Perspective by **Eggleston**) show through a series of carefully controlled experiments that when two crystallographically distinct faces of hematite are exposed to an acidic aqueous solution, a potential gradient is induced across the crystal by their differing ion adsorption properties. This potential drives redox chemistry at each surface by coupled current flow through the bulk mineral. Specifically, island growth is observed at one surface with compensatory etching at another. The authors argue that the finding should be broadly generalizable.

Bacterial Speciation Uncovered

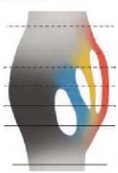

The mating behavior, life history, and ecology of individual bacteria cannot be tracked, and our knowledge of the ecology of natural bacterial populations is rudimentary. By genotyping a large, broadly sampled collection of two important human zoonotic pathogens, *Campylobacter jejuni* and *Campylobacter coli*, **Sheppard *et al.*** (p. 237) have observed speciation going into reverse, probably as a consequence of intensive agricultural practice. These results offer a direct insight into mechanisms of bacterial speciation.

Fast Receptors in Every Respect

Lateral diffusion of receptors has been characterized as an important process for receptor trafficking in and out of synapses. The demonstration of this role has been limited to relatively slow events (in the range of minutes) that occur during development or turnover of receptors, during basal transmission, or during certain forms of neuronal plasticity. **Heine *et al.*** (p. 201; see the Perspective by **Silver and Kanichay**) now report that receptor lateral movements are also involved in fast (tens of milliseconds) regulation of synaptic transmission. Recovery from synaptic depression involves exchange of desensitized receptors with functional ones through lateral movements within or from nearby the postsynaptic density.

Radioprotection: Taking the Toll Road

Radiation therapy is a well-established and highly effective treatment for certain types of cancer, but it can destroy healthy cells in the body, especially bone-marrow cells and cells in the gastrointestinal tract. **Burdelya *et al.*** (p. 226; see news story by **Bhattacharjee**) have developed a drug that may prevent or reduce

Continued on page 153

Continued from page 151

these side effects. The drug (a peptide called CBLB502) binds to Toll-like receptor 5 (TLR5) and activates the nuclear factor–κB signaling pathway, a pathway that cancer cells often activate to avoid cell death. When mice and rhesus monkeys were treated with CBLB502 shortly before exposure to lethal doses of total body irradiation, the animals exhibited less damage to healthy bone marrow and gastrointestinal cells and survived significantly longer than controls. In tumor-bearing mice, CBLB502 did not compromise the antitumor efficacy of radiation therapy.

Mounting Mutations

Of the numerous intracellular factors that help cells protect themselves from invading viruses, some of the most prominent belong to the APOBEC family of cytidine deaminases. These act against retroviruses such as HIV by peppering the single-stranded DNA generated during reverse transcription with deleterious C→U mutations. Now **Vartanian *et al.*** (p. 230) show that APOBEC editing also works on the human papillomavirus (HPV), a DNA virus. Equivalent mutations were observed in cells from plantar warts and precancerous cervical biopsies and in experiments in which plasmid DNA was cotransfected with different APOBEC family members. APOBEC enzymes seem to be able to mutate nuclear DNA, which raises the question whether elevated APOBEC activity, such as seen in HPV-infected cells, might have any causal link with the development of cancer.

Keeping Axons on Track

Like cars on a highway, neuronal signaling routes merge and diverge between origin and destination. By identifying developing motor and sensory neurons in the mouse embryo with distinguishable labels, **Gallarda *et al.*** (p. 233; see the Perspective by **Murai and Pasquale**) have visualized how the growing axons keep entanglement at bay. The axons grew into parallel but separated bundles. Signaling through the ephrin A receptors and ligands present on the growing axons served to keep like axons bundled with like.

Leiomodin in Muscle Actin Assembly

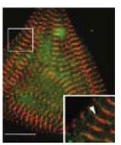

The dynamic assembly of the actin cytoskeleton plays a central role in many cellular functions, but actin polymerization does not occur spontaneously in cells. Filament nucleation factors mediate this process in a highly regulated and localized fashion. **Chereau *et al.*** (p. 239) describe an actin-filament nucleator from muscle cells, which they name leiomodin. Leiomodin nucleates actin filaments in muscle cell sarcomeres, with very high efficiency and without the need for other factors. The nucleation activity of leiomodin is enhanced by direct interaction with tropomyosin, which also mediates its localization to actin filament pointed ends in muscle sarcomeres. Thus, leiomodin appears to be adapted specifically to nucleate the de novo assembly of tropomyosin-decorated filaments in muscle cells.

Promoting Polyketide Production

Many useful natural products are produced in bacteria by modular polyketide synthases (PKS) in which each domain of a multidomain protein is used once in an "assembly-line" process. Eukaryotes also make polyketides, but reuse PKS domains in a poorly understood iterative process. Now **Crawford *et al.*** (p. 243; see the Perspective by **Weissman**) describe the functional dissection of a fungal PKS involved in aflatoxin biosynthesis that reveals the synthetic roles of each catalytic domain. The mechanistic features are likely to be general for the catalyzed production of aromatic polyketides and could guide rational engineering of these biosynthetic proteins.

Synaptic Transmission in Living Color

Actually observing microscopic events in real time can generate a richness of insight unattainable with static approaches. **Westphal *et al.*** (p. 246, published online 21 February; see the Perspective by **Pinaud and Dahan**) present a movie of synaptic vesicles in live neurons, using fluorescent markers to label the vesicles and then collecting video-rate optical images at subdiffraction resolution. As might have been anticipated, vesicles either moved short distances within a single synaptic bouton or made longer journeys into and out of multiple boutons. However, the ability to see nanoscale motion as it happens should promote ever deeper insight into synaptic transmission.

CREDIT: CHEREAU ET AL.

Bruce Alberts is Editor-in-Chief of *Science*.

Hybrid Vigor in Science

When I was president of the U.S. National Academy of Sciences, I came to believe that the future success of humanity may depend on learning to use the tools of science—including the collection of objective evidence on what works and why—at all levels of decision-making. Thus, the National Academies have repeatedly addressed questions such as "How can we make a science out of education?" or "How can we make a science out of sustainable development?" Developing a sound platform of knowledge to address such critical issues will require harnessing research of the highest quality, both in the natural and social sciences. And for this research to be effective, scientists will need to develop much deeper connections with the rest of society.

A formative experience in my first few months as president of the National Academy of Sciences was participating in a workshop for a study on violence in urban America, for which a mixture of social and behavioral scientists, law enforcement agents, mayors, and others came together to formulate recommendations. The wide range of perspectives created an electric, highly creative, and collaborative atmosphere at the workshop that informed and enriched the results. Many of the scientists made new connections that seemed certain to improve their future research, as well as to make their findings more useful for society. Since then, I have repeatedly witnessed the innovation that arises from recruiting scientists and outstanding practitioners to work together, using scientific approaches to tackle important problems.

A recent experience began when the National Academies confronted the question of why research has supported innovation and continuous improvement in medicine, agriculture, and transportation, but not in education. The two successive committees that struggled with this problem were composed of a mixture of national leaders in business, research, policy, and educational practice. The result is the Strategic Education Research Partnership (SERP, a nonprofit organization whose board I chair). SERP is a 3-year-old experiment in which school districts are established as research "field sites," the first two being Boston and San Francisco.

In a field site, a cooperative team of distinguished researchers works hand in hand with local school district personnel to address a select set of challenges that have been identified by the school district. The research is carried out in real classrooms to explore the effect of jointly designed interventions that take advantage of local teacher expertise. There are valuable take-home lessons for all involved, underscoring how everyone can benefit when scientists take on practical problems.

There are many precedents for such productive partnerships. My office at the University of California, San Francisco (UCSF), is located at the new Mission Bay campus, where biotech buildings are springing up like mushrooms across the street. Most faculty look forward to the many synergistic interactions that are likely to arise from this proximity. I was at UCSF in 1976 when this industry began, and at that time the whole idea of university biology faculty becoming involved with the private sector seemed inappropriate and, to most of us, a waste of faculty time. But after many of our students moved on to jobs in the local biotech industry, they formed an effective bridge between the quite different cultures of industry and academia. They became the real agents of technology transfer from university laboratories and also helped to create new arrangements that now benefit the fundamental work of the university. Rather than distracting faculty from productive scholarship, as we had feared, the interactions have increased the pace of discovery.

By analogy with biotech, the formation of strong, long-lasting synergies between academic science and other critical institutions will require that some of our best students of science leave academia to become curriculum specialists inside school districts, policy analysts in state government offices, and so on. These people will form the bridges needed for science to affect a wider society. We should therefore be generating new programs to support such career transitions, while cheering on the scientists who pursue them.

– Bruce Alberts

10.1126/science.1158519

GEOLOGY

Journey to the Center of the Earth

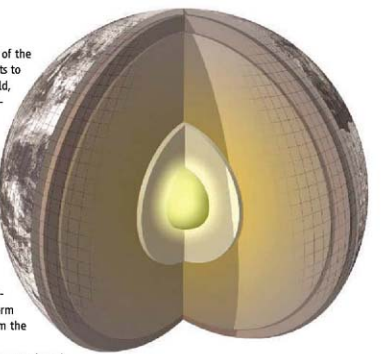

The formation of Earth's core was the major differentiation of the early planet, segregating iron and other metal-loving elements to the planet's center, setting the conditions for a magnetic field, and releasing potential energy as heat. How was the iron localized so efficiently and quickly, displacing what was probably an early, semisolid silicate-rich core?

It is generally thought that heating by impacts (some of which contained iron protocores) and enhanced radiogenic decay allowed blobs of iron metal to form and accumulate in a magma ocean in the outer Earth. Golabek *et al.* explore the iron's subsequent inward migration. Like others, they propose that enough iron accumulated to allow the dense blobs to move toward the center of Earth, displacing the silicate protocore. They also suggest, and show through numerical simulations scaled to the early Earth, that an extensive network of iron melt channels likely surrounded each sinking diapir. As these drained, they would form additional and larger daughter diapirs to scavenge iron from the upper mantle into the growing core. — BH

Earth Planet. Sci. Lett. 10.1016/j.epsl.2008.02.033 (2008).

NEUROSCIENCE

Of Landmarks and Boundaries

The striatum and the hippocampus both have important functions in learning and memory. Despite decades of intensive investigation, there are still a number of incompletely resolved questions. What sort of information is processed in each structure? How do the hippocampus and striatum cooperate to influence behavior? What

A local landmark and a distant boundary.

type of learning is performed by each? These issues are tackled in two related papers.

Using virtual reality and functional magnetic resonance imaging, Doeller *et al.* show that humans learn and remember the locations of objects relative to both local landmarks and environmental boundaries in parallel. The boundary-related system involves the right posterior hippocampus, whereas the landmark-related system involves the right dorsal striatum. When the hippocampal and striatal systems are in conflict because a landmark has been moved relative to the boundary, they do not compete directly to control behavior; instead, each system independently signals its solution to the task, with the ventromedial prefrontal cortex recruited for arbitration. Doeller and Burgess, using the same virtual reality object-location paradigm in behavioral experiments, show that striatal landmark-related processing of spatial learning obeys associative reinforcement learning, whereas hippocampal boundary-related processing does not. The latter performs purely incidental learning instead. Together, these studies provide evidence for the use of distinct learning rules in the hippocampus and striatum. — PRS

Proc. Natl. Acad. Sci. U.S.A. **105**, 10.1073/pnas.0801489105; 10.1073/pnas.0711433105 (2008).

PSYCHOLOGY

Feeling the Unseen

In uncertain situations, rapid responses may be called for, and one line of thought suggests that assessments of stimulus valence (positive or negative) occur more quickly than the evolution of specific emotions, such as the discrimination between the two negative-valence states fear and disgust. Previous work has demonstrated that valence detection is indeed fast and can be applied to stimuli that are presented so briefly (a 40-ms exposure to a picture) as to lie outside of conscious awareness. Ruys and Stapel have looked at the question of whether specific emotions can similarly be elicited unconsciously by transiently displayed (120-ms duration) pictures. Measures of cognition (a stem-word completion task), feeling (self-reports of specific emotions), and behavior (choosing to avoid fearful or disgusting movies) all indicated that the super-quick exposure evoked only a valence-based response, whereas the merely quick, yet still subliminal, stimulus was capable of evoking specific emotions. — GJC

Psychol. Sci. **19**, 385 (2008).

COMPUTER SCIENCE

A Big World After All?

From the spread of viral epidemics to the flow of information in a social network, a key question is the nature of the pathway taken. Epidemic-style models assume that propagation should occur from one individual to many others, following small-world principles. If the viral chain does not die out, it can be mapped as a tree-like structure with many branches that have short paths from the root (or original source). Liben-Nowell and Kleinberg looked at the spread of data on the Internet by examining the lists of names in two e-mail petitions and found that, rather than expanding to many individuals in a few steps, the tree structures were very narrow and several hundreds of layers deep, with large variations in the

CREDITS: (TOP TO BOTTOM) C. BECKEL/SCIENCE; DOELLER *ET AL.*, *PROC. NATL. ACAD. SCI. U.S.A.* 105, 10.1073/PNAS.0801489105 (2008)

time needed to reach the edges of the network. By running simulations on other networks, the authors confirmed that the distribution could not be modeled by a random epidemic process. However, they successfully reproduced the long, narrow trees by altering the model to allow for variations in the response time of the recipients (asynchronous response) and to allow recipients the option of either forwarding the message or group replying (back-transmission) to those already in the list. The results highlight how the transmission of data can vary from the small-world network in which the dissemination occurs. — MSL

Proc. Natl. Acad. Sci. U.S.A. **105**, 4633 (2008).

BIOMEDICINE

Ticking Down to Metastasis

The idea that the accumulation of mutations is a type of clock that can be used to chart the developmental or evolutionary history of cells or organisms is well established. Adapting this mode of analysis, Jones *et al.* have catalogued mutations that occur during the stages of colorectal cancer, focusing on the poorly understood transition from advanced carcinoma to metastasis. They model the rates of appearance of mutations found in a large-scale survey of colorectal cancer (see Wood *et al.*, Research Articles, 16 Nov. 2007, p. 1108). Mutation rates were determined by combining the numbers of mutations with estimates of cell division time, under the assumption that mutation rate and cell division time were constant in each patient. They conclude that it takes roughly 17 years for a large adenoma, which is benign, to evolve into an advanced carcinoma, which is malignant, but less than 2 years for that carcinoma to begin to metastasize. Evolution occurs through cycles of clonal expansion and mutation, and their model provides estimates of the "birth dates" of the founder cells. Although some metastasis-specific alterations were identified, the authors consider that all or most of the mutations needed for metastasis may already be present in the carcinomas. — BRJ

Proc. Natl. Acad. Sci. U.S.A. **105**, 4283 (2008).

PLANT SCIENCE

Mix-and-Match Warfare

Many secondary metabolites are produced by plants for defensive use against insect predators. Insects, in turn, develop their own countermeasures and may end up using the plant's metabolites as a signal to target, rather than to avoid, that plant. Added complications are that the suite of predators changes seasonally, and groups of plants have different vulnerabilities than do isolated plants—with the result that a plant is best served by a nimble tactical approach for the flexible deployment of its defensive weaponry.

Glucosinolates, one category of secondary metabolites, show considerable biochemical diversity owing to the enzymes that generate their derivatives. Wentzell and Kliebenstein have analyzed the diversity of glucosinolate production in *Arabidopsis*. Their results show that different pieces of the plant make different product profiles that are fine-tuned by the age of the plant and the local population density. Variability in the profile of glucosinolate derivatives among different accessions of *Arabidopsis* highlights the influence of additional modifier factors, enabling the plant to balance the risks of detection against the effectiveness of defense in its production of glucosinolate derivatives. — PJH

Plant Physiol. **146**, 10.1104/pp.107.115279 (2008).

MICROBIOLOGY

A Locus of Resistance to Activation

Chagas' disease is caused by a protozoan parasite of the Trypanosomatidae, others of which cause a range of high-morbidity and disfiguring human diseases, usually within impoverished populations. Drug treatment takes several months, is expensive, and can have side effects. Moreover, the nitroheterocyclic compounds nifurtimox and benznidazole have been the frontline drugs for more than 40 years; nitroheterocycles do not act directly upon their targets, but must first be converted by endogenous enzymes to the active compounds.

Yellow glow reveals nitroreductase in trypanosome mitochondria.

Wilkinson *et al.* have worked out how these drugs are activated. Eight months of selection in vitro generated nitroheterocyclic-resistant parasites that had lost a gene encoding a mitochondrially targeted type I nitroreductase, a flavoenzyme that reduces the nitro group and yields agents that damage DNA. Deleting a single copy of this gene enhanced resistance to nifurtimox and other nitroheterocycles severalfold. Intriguingly, knocking out both copies slowed replication and blocked differentiation into the infectious form of the parasite, which suggested that this enzyme is essential for parasite development in its mammalian host. — CA

Proc. Natl. Acad. Sci. U.S.A. **105**, 5022 (2008).

CREDIT: WILKINSON *ET AL., PROC. NATL. ACAD. SCI. U.S.A.* 105, 5022 (2008)

www.sciencemag.org

Science

1200 New York Avenue, NW
Washington, DC 20005
Editorial: 202-326-6550, FAX 202-289-7562
News: 202-326-6581, FAX 202-371-9227
Bateman House, 82-88 Hills Road
Cambridge, UK CB2 1LQ
+44 (0) 1223 326500, FAX +44 (0) 1223 326501

SUBSCRIPTION SERVICES For change of address, missing issues, new orders and renewals, and payment questions: 866-434-AAAS (2227) or 202-326-6417, FAX 202-842-1065. Mailing addresses: AAAS, P.O. Box 96178, Washington, DC 20090-6178 or AAAS Member Services, 1200 New York Avenue, NW, Washington, DC 20005

INSTITUTIONAL SITE LICENSES please call 202-326-6755 for any questions or information

REPRINTS: Author Inquiries 800-635-7181
Commercial inquiries 803-359-4578

PERMISSIONS 202-326-7074, FAX 202-682-0816

MEMBER BENEFITS AAAS/Barnes&Noble.com bookstore www.aaas.org/bn; AAAS Online Store http://www.aaasonline.com/aaas/ code AB7686; AAAS Travels: Betchart Expeditions 800-252-4910; Apple Store www.apple/episcenter/aaas; Bank of America MasterCard 1-800-833-6262 priority code FAA3YU; Cold Spring Harbor Laboratory Press Publications www.cshlpress.com/affiliates/aaas.htm; GEICO Auto Insurance www.geico.com/landingpage/go51.htm?logo=17624; Hertz 800-654-2200 CDP#343457; Office Depot https://bid.officedepot.com/portal/Login.do; Seabury & Smith Life Insurance 800-424-9883; Sidney Kimmel VIP Program 202-326-6417; VIP Money Services http://www.vipmayflower.com/domestic/index.html; Other Benefits: AAAS Member Services 202-326-6417 or www.aaasmember.org.

science_editors@aaas.org	(for general editorial queries)
science_letters@aaas.org	(for queries about letters)
science_reviews@aaas.org	(for returning manuscript review)
science_bookrevs@aaas.org	(for book review queries)

Published by the American Association for the Advancement of Science (AAAS). Science serves its readers as a forum for the presentation and discussion of important issues related to the advancement of science, including the presentation of minority or conflicting points of view, rather than by publishing only material on which a consensus has been reached. Accordingly, all articles published in Science—including editorials, news and comment, and book reviews—are signed and reflect the individual views of the authors and not official points of view adopted by AAAS or the institutions with which the authors are affiliated.

AAAS was founded in 1848 and incorporated in 1874. Its mission is to advance science and innovation throughout the world for the benefit of all people. The goals of the association are to: foster communication among scientists, engineers and the public; enhance international cooperation in science and its applications; promote the responsible conduct and use of science and technology; foster education in science and technology for everyone; enhance the science and technology workforce and infrastructure; increase public understanding and appreciation of science and technology; and strengthen support for the science and technology enterprise.

INFORMATION FOR AUTHORS
See pages 634 and 635 of the 1 February 2008 issue or access www.sciencemag.org/about/authors

EDITOR-IN-CHIEF **Bruce Alberts**
EXECUTIVE EDITOR **Monica M. Bradford**
DEPUTY EDITORS **R. Brooks Hanson, Barbara R. Jasny, Katrina L. Kelner**
NEWS EDITOR **Colin Norman**

EDITORIAL SUPERVISORY SENIOR EDITOR Phillip D. Szuromi; **SENIOR EDITOR/PERSPECTIVES** Lisa D. Chong; **SENIOR EDITORS** Gilbert J. Chin, Pamela A. Hines, Paula A. Kiberstis (Boston), Marc S. Lavine (Toronto), Beverly A. Purnell, L. Bryan Ray, Guy Riddihough, H. Jesse Smith, Valda Vinson; **ASSOCIATE EDITORS** Jake S. Yeston, Laura M. Zahn; **ONLINE EDITOR** Stewart Wills; **ASSOCIATE ONLINE EDITOR** Robert Frederick; Tara S. Marathe; **WEB CONTENT DEVELOPER** Marlyn Green; **BOOK REVIEW EDITOR** Sherman J. Suter; **ASSOCIATE LETTERS EDITOR** Jennifer Sills; **EDITORIAL MANAGER** Cara Tate; **SENIOR COPY EDITORS** Jeffrey E. Cook, Cynthia Howe, Harry Jach, Barbara P. Ordway, Trista Wagoner; **COPY EDITORS** Chris Filardo, Lauren Kmec, Peter Mooreside; **EDITORIAL COORDINATORS** Carolyn Kyle, Beverly Shields; **PUBLICATIONS ASSISTANTS** Ramatoulaye Diop, Joi S. Granger, Jeffrey Hearn, Lisa Johnson, Jeffrey Osier, Jerry Richardson, Brian White, Erika Wyman; **EDITORIAL ASSISTANTS** Carlos L. Durham, Emily Gizzie, Patricia M. Moore, Jennifer A. Seibert; **EXECUTIVE ASSISTANT** Sylvia S. Kihara; **ADMINISTRATIVE SUPPORT** Maryrose Madrid

NEWS **DEPUTY NEWS EDITORS** Robert Coontz, Elliot Marshall, Jeffrey Mervis, Leslie Roberts; **CONTRIBUTING EDITORS** Elizabeth Culotta, Polly Shulman; **NEWS WRITERS** Yudhijit Bhattacharjee, Adrian Cho, Jennifer Couzin, David Grimm, Constance Holden, Jocelyn Kaiser, Richard A. Kerr, Eli Kintisch, Greg Miller, Dennis Normile (New England), Greg Miller, Elizabeth Pennisi, Robert F. Service (Pacific NW), Erik Stokstad; **INTERN** Elsa Youngsteadt; **CONTRIBUTING CORRESPONDENTS** Jon Cohen (San Diego, CA), Daniel Ferber, Ann Gibbons, Lizzie Wade, Mitch Leslie, Marc S. Mann, Virginia Morell, Evelyn Strauss, Gary Taubes; **COPY EDITORS** Rachel Curran, Linda B. Felaco, Melvin Gatling; **ADMINISTRATIVE SUPPORT** Scherraine Mack, Faerie Groom; **BUREAUS** New England: 207-549-5911, San Diego, CA; 760-942-3252, FAX 760-942-4979, Pacific Northwest: 503-963-1940

PRODUCTION DIRECTOR James Landry; **SENIOR MANAGER** Wendy K. Shank; **ASSISTANT MANAGER** Rebecca Doshi; **SENIOR SPECIALIST** Chris Redwood; **SPECIALIST** Rick Kempa; Steve Forrester; **PRESSMAN DIRECTOR** Carol M. Tompkins; **MANAGER** Marcus Spiegler; **SPECIALIST** Jessie Mudjitaba

ART DIRECTOR Kelly Buckheit Krause; **ASSOCIATE ART DIRECTOR** Aaron Morales; **ILLUSTRATORS** Chris Bickel, Katharine Sutliff; **SENIOR ART ASSOCIATES** Holly Bishop, Laura Creveling, Preston Huey, Nayomi Kevithyagala; **ASSOCIATE** Jessica Newfield; **PHOTO EDITOR** Leslie Bitzard

SCIENCE INTERNATIONAL
EUROPE (science@science-int.co.uk) **EDITORIAL: INTERNATIONAL MANAGING EDITOR** Dinah Perkins; Register; **SENIOR ASSOCIATE EDITOR** Stella Hurtley-Jan Uppenbrink; **SENIOR EDITORS** Caroline Ash, Stella M. Hurtley, Ian S. Osborne, Stephen J. Simpson, Peter Stern; **EDITORIAL SUPPORT** Deborah Dennison, Rachel Roberts, Alice Whaley; **ADMINISTRATIVE SUPPORT** John Cannell, Kay Clements, Leslie Smith; **SALES:** **SENIOR SALES MANAGER** John Travis; **DEPUTY NEWS EDITOR** Daniel Clery; **CONTRIBUTING CORRESPONDENTS** Michael Balter (Paris), John Bohannon (Vienna), Martin Enserink (Amsterdam and Paris), Gretchen Vogel (Berlin); **INTERN** Laura Cahoon

ASIA Japan Office: Asca Corporation, Riko Ishioka, Pesako Tamura, 1-8-13, Hirano-cho, Chuo-ku, Osaka-shi, Osaka, 541-0046 Japan; +81 (0) 6 6202 6272, FAX +81 (0) 6 6202 6271; asca@po.synet.or.jp; **ASIA SALES EDITOR** Richard Stone (Beijing; rstone@aaas.org) **CONTRIBUTING CORRESPONDENTS** Dennis Normile (Japan; +81 (0) 3 3391 0630, FAX 81 (0) 3 3936 3531; dnormile@gol.com); Hao Xin (China; + 86 (0) 10 6307 4859 or 6307 3676, FAX +86 (0) 10 6307 4358; cindyhao@gmail.com); Pallava Bagla (South Asia: +91 (0) 11 2271 2896; pbagla@vsnl.com)
AFRICA Robert Koenig (contributing correspondent, robkoenig@gmail.com)

EXECUTIVE PUBLISHER **Alan I. Leshner**
PUBLISHER **Beth Rosner**

FULFILLMENT SYSTEMS AND OPERATIONS (membership@aaas.org): **DIRECTOR** Waylon Butler; **CUSTOMER SERVICE SUPERVISOR** Pat Butler; **SPECIALISTS** Laurie Baker, Latoya Casteel, LaVonda Crawford, Vicki Linton; **DATA ENTRY SUPERVISOR** Cynthia Johnson; **SPECIALIST** Tanitra Hill

BUSINESS OPERATIONS AND ADMINISTRATION DIRECTOR Deborah Rivera-Wienhold; **ASSISTANT DIRECTOR, BUSINESS OPERATIONS** Randy Yi; **SENIOR FINANCIAL ANALYSTS** Michael LoBue, Jessica Tierney; **RIGHTS AND PERMISSIONS: ADMINISTRATOR** Emilie David; **ASSOCIATE** Elizabeth Sandifer; **MARKETING DIRECTOR** John Meyers; **MARKETING MANAGERS** Allison Pate, Darryl Walter; **MARKETING ASSOCIATES** Aimee Aporte, Alison Chandler, Mary Ellen Crowley, Marcia Leach, Julianne Wielga, Wendy Wise; **INTERNATIONAL MARKETING MANAGER** Suzanne Bright; **EXECUTIVE ASSISTANT** Jennifer Reeves; **MARKETING/NUMBER SERVICES EXECUTIVE** Linda Rusk; **SITE LICENSE SALES DIRECTOR** Tom Ryan; **SALES MANAGER** Russ Edna; **SALES AND CUSTOMER SERVICE** Mehan Dossani, Iqoo Ellis, Kiki Forsythe, Catherine Holland, Phillip Smith, Phillip Tsokalidis; **ELECTRONIC SALES MANAGER** Elizabeth Hartman; **PROJECT MANAGER** Trista Snyder; **ASSISTANT MANAGER** Lisa Stanford; **SENIOR PRODUCTION SPECIALISTS** Christopher Coleman, Walter Jones; **PRODUCTION SPECIALISTS** Michele Johnston, Kimberly Oster

ADVERTISING DIRECTOR WORLDWIDE Ad Sales Bill Moran

PRODUCT Science_advertising@aaas.org): **NORTHEAST** Rick Bongiovanni: 330-405-7080, FAX 330-405-7081; **WEST COAST/CANADA** Tosha Young: 650-964-2266; **EAST COAST, CANADA** Christopher Breslin: 443-512-0330, FAX 443-512-0331; **UK/EUROPE/ASIA** Michelle Fleit: +44 (0) 1223-326-524, FAX +44 (0) 1223-325-532; **JAPAN** Mashy Yoshikawa: +81 (0) 33235 5961, FAX +81 (0) 33235 5852; **SENIOR TRAFFIC ASSOCIATE** Delandra Simms

COMMERCIAL EDITOR Sean Sanders: 202-326-6430

CLASSIFIED (advertise@sciencecareers.org): **US: RECRUITMENT SALES MANAGER** Ian King: 202-326-6528, FAX 202-289-6742; **INSIDE SALES MANAGER:** Nimo Sutherland: 202-326-6532; **RECRUITMENT:** 202-326-6543; **INSIDE SALES REPRESENTATIVE** Karen Foote: 202-326-6740; **KEY ACCOUNT MANAGER** Jorthan Abbie; **RECRUITMENT** Alexis Fleming: 202-326-6578; **SOUTHWEST** Tina Burks: 202-326-6577; **NORTHEAST** Mary McHale: 202-326-6533; **SALES COORDINATORS** Erika Foard, Rohan Edmonson, Shirley Young; **INTERNATIONAL: SALES MANAGER** Tracy Holmes: +44 (0) 1223 326525, FAX +44 (0) 1223 326532; **SALES** Marium Hoodia, Alex Polmer, Alessandra Sorgente; **SALES ASSISTANT** Rebecca Doshi; **JAPAN** Mashy Yoshikawa: +81 (0)3 3235 5961, FAX +81 (0)3 3235 5852; **ADVERTISING PRODUCTION OPERATIONS MANAGER** Deborah Tompkins; **SENIOR PRODUCTION SPECIALISTS** Robert Buck, Amy Hardcastle; **SENIOR TRAFFIC ASSOCIATE** Christine Hall; **PUBLICATIONS ASSISTANT** Mary Lagnaoui

AAAS BOARD OF DIRECTORS: RETIRING PRESIDENT, CHAIR David Baltimore; **PRESIDENT** James J. McCarthy; **PRESIDENT-ELECT** Peter C. Agre; **TREASURER** David E. Shaw; **CHIEF EXECUTIVE OFFICER** Alan I. Leshner; **BOARD** Lynn W. Enquist, Susan M. Fitzpatrick, Alice Gast, Linda P. B. Katehi, Nancy Knowlton, Cherry A. Murray, Thomas D. Pollard, Thomas A. Woolsey

Probing Stonehenge

Archaeologists broke ground at Stonehenge last week for the first time since 1964, with the aim of using modern technology to pinpoint just when builders dragged the first bluestone pillars to the site some 4500 years ago. The team, which is re-excavating a trench originally dug in the 1920s, plans to analyze short-lived organic material such as twigs or grains with mass spectroscopy. They hope to establish the arrival date of the stones to within a couple of decades.

The dig leaders, Geoffrey Wainwright of the Society of Antiquaries of London and Timothy Darvill of Bournemouth University in the U.K., are looking to bolster their theory that bluestones—dragged 250 kilometers from the Preseli Hills in Wales—were valued for their healing powers. Inscriptions in Wales reveal that locals considered the stones magical. And deformed skeletons recently dug up nearby may have been from pilgrims seeking cures. Precisely dating the different building stages of the monument is "wrapped into a series of interesting debates" about pottery, metallurgy, and spirituality in northwest Europe, says Darvill. The project is part of a broader National Geographic–sponsored effort covering nearby Neolithic sites.

Stone Axes From the Deep

An amateur Dutch archaeologist has discovered 28 Neandertal hand axes in debris scooped off the North Sea floor and dumped at a Dutch gravel yard.

The flint axes were under 30 meters of water 13 kilometers off the east coast of England and buried 5 to 10 meters below the sea floor. They were found last December by Jan Meulmeester, a cook at a retirement home who was poking through gravel piles on his day off.

The axes match similar artifacts crafted by Neandertals more than 100,000 years ago and suggest that Neandertals hunted mammoths and other creatures in a landscape long since underwater, says Hans Peeters, an archaeologist for the National Service for Archaeology, Cultural Landscapes and Built Heritage in Amersfoort. Until the end of the last Ice Age about 10,000 years ago, Britain was connected to the European mainland, and much of what is now the North Sea was rolling plains.

"I've never seen such a large group like the one found by Mr. Meulmeester," says Peeters. The gravel-dredging company has stopped work in the area, and Dutch and English officials are planning a survey to look for further traces of the sunken landscape.

CREDITS (TOP TO BOTTOM): RUSSELL BACH/JUNIUS/OWN UNIVERSITY; COURTESY OF PHIL GIBBARD; UNSEY ECEL SPAN

Rakish Rodent

Birds do it. Primates do it. Now even rodents do it—use tools, that is. Neuroscientist Atsushi Iriki and colleagues at the RIKEN Brain Science Institute near Tokyo reported online in *PLoS ONE* last month that they had trained five degus, rodents native to Chile, to use a small rake to reach beneath a fence to retrieve a sunflower seed. Through daily training sessions over 2 months, the degus went from simply pulling the rake forward to get the seed to sweeping the tool with the ease of an ice hockey player corralling a loose puck.

Iriki says the scientists believe it is the first time rodents have learned to use tools in a lab experiment. The experiments, which include detailing the neurological changes involved in acquiring tool use, should help pinpoint areas of the brain for closer study in primates. "The mental function behind tool use is the basis for many other abilities," such as constructing buildings or complex machines, Iriki says.

A BIRD FOR THE HOLY LAND

Politics is poking its beak into a contest to choose Israel's national bird. Set up by two ornithologists affiliated with the Society for the Protection of Nature in Israel (SPNI) to celebrate the Jewish state's 60th anniversary this year, it features a flock of oft-seen birds. Army brass and soldiers like the lesser kestrel, but peaceniks say that's too warlike. Israeli Arabs favor the yellow-tufted sunbird because of its alternative name, the Palestine sunbird; Israeli nationalists oppose it for the same reason.

"Most people don't realize how important Israel is for bird migration," says ornithologist Yossi Leshem of Tel Aviv University, who hopes a million Israelis will vote. President Shimon Peres will announce the results on 29 May, and national stamps, coins, and telecards with the new symbol are planned. Most of the birds on the ballot are migrants, of which some 500 million pass through the Holy Land each year. The nine finalists include the hoopoe, the owl, the spur-winged plover, and the griffin vulture, but no doves.

Palestine sunbird (*left*), kestrels.

Three Q's

As head of Quebec's provincial medical research council, neuroscientist **Alain Beaudet** lamented the dearth of collaborative programs between Canada's federal and provincial governments. On 1 July, he moves to the other side of the table as the new president of the Canadian Institutes of Health Research (CIHR), which administer $733 million per year in research grants.

Q: Do you agree with your predecessor, Alan Bernstein, that the CIHR budget can't keep up with the demands created by Canada's expanding scientific infrastructure?

He was absolutely right. … Take the federal government's decision to increase the number of fellowships. I think it's great. But what organizations will give them out? How many students are there that are worthy of receiving fellowships? What are the needs? Putting our resources and our expertise together to work in a concerted fashion is very, very important.

Q: Do CIHR partnership programs need to change?

When CIHR partners, [the agency's attitude has been] … we organize everything and you guys [the provincial partners] come in and part with your money. … I'd like to see provinces come up with a health problem specific to that province and [then have] CIHR help to tackle that problem.

Q: The recent CIHR restructuring took financial decision-making away from the governing council and handed it to a committee made of directors of the agency's 13 institutes. In such a situation, is it possible for a president to effect change?

It's clear that we have to bring the individual institutes into the fray. They've got boards that are full of very bright people. Let's use these people more. … [But] let me first get acquainted with the beast and then I'll tell you how to tame it.

CREDITS: (TOP TO BOTTOM) SOURCE; MONTREAL NEUROLOGICAL INSTITUTE AND HOSPITAL; MIT; DAVID BAY

MOVERS

A STAR'S HOMECOMING. Japan's only Nobel Prize–winning biologist is returning home after 46 years. Neuroscientist Susumu Tonegawa, who was caught up in a hiring controversy at the Massachusetts Institute of Technology (MIT) 2 years ago, will begin working part-time next April at the RIKEN Brain Science Institute outside Tokyo.

Tonegawa, 68, resigned his position as director of MIT's Picower Institute for Learning and Memory in late 2006 after an MIT panel found serious flaws in MIT's neuroscience effort. Some MIT colleagues had accused Tonegawa of blocking the appointment of a promising young researcher to another neuroscience institute on campus because she was a woman. The report was critical of his role in the matter, but no disciplinary action was taken.

Tonegawa did not return phone calls, but news reports said that as director of the institute, he hopes to entice non-Japanese to Japan to help lead brain research projects. MIT officials said he would nevertheless continue to retain his professorship and lab at MIT.

REACHING OUT. The California Academy of Sciences in San Francisco has hired David Mindell to revitalize its $6 million research program. Mindell, an evolutionary biologist at the University of Michigan, Ann Arbor, will take up a newly created post as dean of science and research collections at the 155-year-old academy, which this fall moves into a new eco-friendly building in Golden Gate Park. "Our hope is to become one of the pre-eminent research museums in the world," says Mindell, who starts the new job in July. He wants to expand research in comparative genomics, strengthen ties with local university researchers, and do more public outreach—especially about evolution.

THEY SAID IT

"In fact, some manuscripts include no plain explanation of why the work is of interest. Author responses to negative referee reports sometimes contain narratives reminiscent of short stories (perhaps by Kafka, with particular emphasis on description of conflict)."

—Reinhardt Schuhmann, managing editor of *Physical Review Letters*, in a 13 March editorial urging authors to write more clearly.

Awards >>

FOR AFRICA. Brian Greenwood, a professor of tropical medicine, and Miriam Were, a public health expert, will share an inaugural $1 million award from the Japanese government for their efforts to fight diseases in Africa.

Greenwood, a faculty member at the London School of Hygiene and Tropical Medicine in the U.K., took up malaria research after recognizing the devastating effects of the disease, particularly on children. He has studied the disease's genetic factors and its clinical effects.

Were, born in Kenya and trained at Johns Hopkins University in Baltimore, Maryland, has been an educator and administrator working on public hygiene and AIDS through community health systems. She is now chair of Kenya's National AIDS Control Council and the African Medical and Research Foundation.

The prize honors Hideyo Noguchi, who died of yellow fever 80 years ago in Africa while seeking a vaccine for the disease. It will be awarded every 5 years.

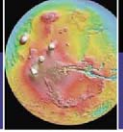

Highs and lows on Mars 165

Racetrack memories 166

Up to snuff? Wetland mitigation projects will be required to meet standards drawn from research such as this at a restoration project in Indiana.

ENVIRONMENTAL REGULATION

New Rules on Saving Wetlands Push the Limits of the Science

In one of the most significant wetlands regulations in 2 decades, the U.S. Army Corps of Engineers has spelled out what developers must do to mitigate damage from their construction projects. The new regulations are meant to make mitigation efforts more accountable, successful, and scientific. But some researchers and environmentalists believe that the rule isn't strict enough, and that too little is known about how to restore some of these fragile ecosystems, for the rule to work as intended.

In 1989, President George H. W. Bush announced a policy of no net loss of wetlands. Mitigation was a major tool to achieve the goal. It works like this: Any construction project that will harm a wetland or stream, say a shopping mall or highway, requires a permit from the corps. The agency issues some 80,000 permits a year, and each one requires developers to minimize the impact on wetlands and mitigate any unavoidable damage. Developers and public agencies spend nearly $3 billion a year on mitigation, much of it in or around wetlands they built on. In the past decade, more developers have started buying credits from "mitigation banks" set up to restore and create wetlands.

But the process didn't work well. Many projects have been flops, and the corps has failed to exert sufficient oversight, according to reports by the U.S. National Academy of Sciences' National Research Council (*Science*, 6 July 2001, p. 25) and other groups. Congress asked the agency to issue a new rule. The corps itself wasn't satisfied, says Mark Sudol, its chief regulator: "We knew we had to fix something."

The rule, to be published 10 April in the *Federal Register*, is designed to improve the track record of mitigation by recommending the use of a watershed approach and by requiring enforceable, ecologically-based performance standards. It extends mitigation policies to streams, a controversial idea given the nascent state of stream restoration science. The rule also standardizes requirements for all types of mitigation and strengthens long-term protection of sites. "They have moved forward significantly on some of the administrative issues that have dogged mitigation," says Julie Sibbing of the National Wildlife Federation in Reston, Virginia.

With a watershed approach, the corps would consult a detailed inventory of streams and wetlands, threats, and priorities for restoration before deciding whether a proposed mitigation project is adequate. But such watershed plans are costly, and only a few states have created them. In many places, scientists just don't know enough about the exact functions of particular wetlands and how to prioritize their restoration. Sudol says that his agency is weighing how regulators can make progress using the data at hand, for example, by trying to get mitigation projects located near parks or wildlife corridors.

To improve the success rate of mitigation projects, the rule—issued jointly with the Environmental Protection Agency (EPA)—requires developers and mitigation bankers to meet ecological performance standards. For example, a riparian wetland might need to encounter enough floods per year to remain healthy. Although wetland ecology varies enormously around the country, the standards must be based on the "best available science that can be measured or assessed in a practicable manner." In addition, the corps will now require backup plans in case a mitigation project fails. A developer or mitigation banker "can't just walk away," Sudol says.

But many researchers are alarmed that the rule enters uncharted territory with provisions on stream mitigation. The government was concerned that damage to streams was not being adequately addressed, says Palmer Hough, EPA's lead scientist on the rule. The mitigation for stream damage tended to be "in-lieu fees" that went to state or nonprofit programs designed to help wetlands elsewhere, some of which have been mismanaged in the past. "We won't trade streams for wetlands," says Sudol, who notes that the new rule requires stream impacts to be offset by stream mitigation.

Margaret Palmer, a stream ecologist at the University of Maryland, College Park, is troubled that the creation of new streams is part of the definition of restoration. Palmer emphasizes that there is no evidence that an engineered stream can ▶

CREDIT: MICHAEL CONROY/AP PHOTO

Alcohol and drugs
168

Reducing crops' thirst
171

replace the functions of a natural one. In addition, she cautions that the science of stream restoration is relatively immature. Sudol acknowledges that but says prudent experimentation will be valuable: "If we don't allow someone to try something to see if it works, how will we move ahead?" He notes that developers must carry out at least 5 years of monitoring and submit backup plans.

Environmentalists worry that the rule, which goes into effect in early June, gives too much discretion to the corps' 38 district offices. "It's couched in scientific terms, but almost all of that can be waived when the district engineer feels it's not practicable," says Joan Mulhern of Earthjustice, an advocacy group in Washington, D.C. Sudol prefers to describe it as a balancing act. "The corps wants to bring in science, but we still need to make timely permit decisions," he says.

Patrick Parenteau of Vermont Law School in South Royalton welcomes new provisions for public notification and comment. In addition, monitoring results will be available on the Web. At the very least, he says, the new rules will make it easier to tell whether mitigation is working and how to improve it. **–ERIK STOKSTAD**

MEDICINE

Drug Bestows Radiation Resistance on Mice and Monkeys

Radiation therapy is a mixed blessing for cancer patients: It destroys tumor cells but also inflicts harm on healthy tissues, particularly the spleen, bone marrow, and gastrointestinal tract. On page 226, researchers led by Lyudmila Burdelya of the Roswell Park Cancer Institute in Buffalo, New York, report a promising new way to protect those tissues, one they claim could help improve outcomes of radiation therapy—and perhaps even save lives in a nuclear catastrophe. The strategy may be tested in cancer patients as early as this year.

Richard Kolesnick of the Memorial Sloan-Kettering Cancer Center in New York City calls the work "a breakthrough in an issue that has challenged the scientific community." It's a fine example, he says, of "how understanding mechanisms of tissue damage can result in [the discovery of] valuable pharmacologic agents."

Radiation induces damage in healthy tissues not by directly killing cells but by prompting them to commit suicide through a process called apoptosis. Burdelya and her colleagues wondered if they could rescue radiation-blasted tissues by shutting down this cell death program, which the body normally turns on in cells with damaged DNA to keep them from multiplying.

Tumor cells persist in the body because they are able to block apoptosis, by activating a transcription factor known as nuclear factor–κB. "Many in the cancer field are trying to inhibit NF-κB in tumor cells in order to let them commit suicide," says Andrei Gudkov, a co-author and a molecular geneticist at Roswell. "We thought, 'Why not try to do the opposite in normal cells to help them survive radiation?' "

Burdelya and her colleagues knew that human gut and immune cells activate NF-κB when flagella, bacteria's whiplike tails, tickle a cell surface protein called Toll-like receptor 5. Drawing upon this insight, they developed an NF-κB-activating drug, dubbed CBLB502, by modifying a small fragment of a *Salmonella* flagella. The team found that mice and rhesus monkeys injected with CBLB502 45 minutes to 24 hours before exposure to lethal radiation were more likely to survive, or survive longer, than animals that did not receive the drug. The drug also helped prevent death in mice when administered an hour after the animals received a radiation dose. There were no obvious side effects to the drug, and in another experiment, the researchers showed that radiation was still effective in treating tumors in mice that had received CBLB502.

CREDIT: MICHAEL ANDERSON/NCI

Safeguarding cells. A drug based on a bacterial protein could help radiation therapy treat tumors more safely.

Cleveland BioLabs, a Buffalo, New York, company that owns the drug, views CBLB502 as an adjuvant to radiotherapy but also hopes to sell it to governments as a preventive medicine to be stockpiled for a nuclear war, dirty bomb, or nuclear accident. (Five of the paper's 12 authors are employees of the company, and three others, including Burdelya and Gudkov, are paid consultants.) Other research groups, some funded by the U.S. Department of Homeland Security, are pursuing different strategies for radiation-protection drugs.

Burdelya's approach may have broad application, says Preet Chaudhary, an oncologist at the University of Pittsburgh School of Medicine in Pennsylvania. "It will be interesting to test it in other conditions with excess apoptosis, such as degenerative disorders and ischemia reperfusion injury," he says. **–YUDHIJIT BHATTACHARJEE**

BIOMEDICAL COMMUNITY

HHMI's Cech Signs Off on His Biggest Experiment

When Thomas Cech, president of the Howard Hughes Medical Institute (HHMI), announced last week that he will step down in 2009 to return to research, some people were taken by surprise. For one thing, the date—1 April—seemed suspect. And why would a superstar like Cech walk away from a dream job: running the largest private biomedical research funder in the United States? Cech's answer is direct, in the style of a working scientist: At 60, he says he's accomplished what he set out to do at HHMI. "I'm ready to return to the adventure of my own research and my own teaching," he told the staff. In an interview, he added: "I'm a little surprised I've managed to hang on here as long as I have."

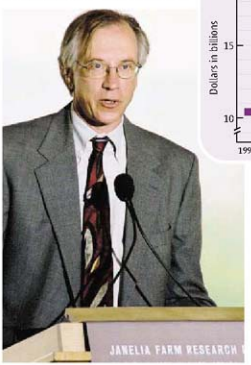

Back to Boulder. Having launched Janelia Farm, a center for neurobiology, HHMI President Thomas Cech will return to Colorado to pursue his own research.

Cech's 8 years at Hughes have been eventful. The endowment has grown by 60%, to nearly $19 billion; Cech added new programs in research and education; and he softened HHMI's elite image to make it more "democratic," observers say. He will leave behind a bold but unfinished experiment: HHMI's first research campus, with the lofty goal of figuring out how the brain is wired.

A 1989 Nobel Prize winner for work showing that RNA can act as a catalyst, Cech took the reins in 2000 from Purnell Choppin, becoming the third HHMI chief since the sale of Hughes Aircraft for $5 billion in 1985 launched a biomedical research powerhouse. Over 12 years, Choppin had built up HHMI's lead program, providing generous support to roughly 300 biomedical research investigators at host institutions. Unlike Choppin, Cech was an active researcher when he took over. He came with the agreement that he would spend a week each month running his lab at the University of Colorado, Boulder. He soon brought a casual style to HHMI headquarters in Chevy Chase, Maryland, showing up in sweaters at a place where suits and ties had been the norm.

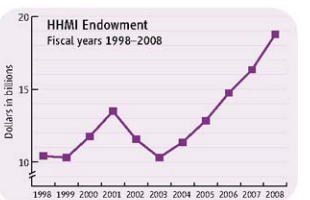

One of Cech's first tasks was to plan a new research campus together with HHMI vice presidents Gerald Rubin and David Clayton. Federal tax rules required that HHMI spend at least 3.5% per year of its growing endowment. Instead of expanding the investigator program, the three HHMI leaders decided to build Janelia Farm Research Campus, a $500 million, glass-walled center nestled in a hillside in Ashburn, Virginia, that opened in 2006 and will bring 25 interdisciplinary teams together to study neural circuits and imaging. The 15 group leaders and other staff recruited so far are "outstanding," says Bruce Stillman, president of Cold Spring Harbor Laboratory and a member of HHMI's medical advisory board, but whether it will be a "home run" will not be known for a decade (*Science*, 8 December 2006, p. 1530).

Janelia Farm's creation was not trouble-free: In the economic downturn after 2001, the value of HHMI's endowment plummeted $3 billion in 2 years (see graph). Cech decided to press ahead with construction and cover the shortfall partly by cutting investigator grants 10% for 1 year. Some HHMI investigators resented Janelia, says Stillman. Since then, he says, most "came around to be supportive," and many are collaborating with the center.

Cech also expanded the reach of HHMI's investigator program, adding about 30 slots for physician scientists. It was a way to fund translational research, an opportunity "we didn't want to ignore," Cech says. In a more fundamental change, he scrapped a process in which about 200 research institutions each nominated a few candidates for new investigators, instead inviting individuals from these institutions to apply directly. Although that has meant "enormous numbers of applications" for HHMI's latest competition, Cech says, it has attracted people from new fields, such as physical sciences. The change "was tremendously good for everybody," says Stanford neurobiologist Carla Shatz, another member of HHMI's medical advisory board. The full impact should become clear when the results are announced in May.

"My passion," according to Cech, has been HHMI's educational programs, including creating $1 million, 4-year awards for talented biology professors. His influence in education and other areas has reached beyond HHMI, notes Harold Varmus, former director of the U.S. National Institutes of Health (NIH) in Bethesda, Maryland, and now president of Memorial Sloan-Kettering Cancer Center in New York City. For example, Cech pushed the public-access debate forward by requiring that HHMI investigators' articles be free online within 6 months. He also chaired a National Research Council committee on young investigators. Offering direct help, last month, Cech launched a program to appoint up to 70 early-career scientists as HHMI investigators for 6 years.

Commanding the HHMI budget ($726 million last year), Cech says, is like directing the biomedical research budget of "a whole country." Because HHMI's board of trustees is relatively hands-off, "if we don't do something great here, we have no one to blame," says Cech. Still, it became clear last year when he turned down a chance to be president of Harvard, which would have required him to give up his lab, that running a big organization was not what he really wanted to do. He realized he would prefer to be "a musician" rather than "conductor of the orchestra," he says. In spring 2009, Cech plans to return to Boulder, where his 10-person HHMI lab is studying telomerase. The HHMI board is expected to form a search committee in the next few weeks. **–JOCELYN KAISER**

CREDITS: (PHOTO) PAUL FETTERS/HHMI; (DATA) HHMI

PLANETARY GEOLOGY

An Early Big Hit to Mars May Have Scarred the Planet for Life

Earth has its high-standing continents and low-lying ocean basins, thanks to plate tectonics. And Mars has its smooth northern lowlands and its cratered highlands. But there's no credible sign that plate tectonics ever operated on Mars, so how did a third of the planet come to be as much as 4 kilometers lower than the rest? For the past quarter-century, a leading theory has held that a giant impact battered the young planet and excavated the northern lowlands, but that idea seemed to have serious problems.

Now, two new studies purport to ease the difficulties with a giant impact. In one study, researchers reveal the true dimensions of the huge "Borealis basin," making it look much more like the crater of a giant impact. And a second group has run simulations that suggest how an impactor could have blasted out an 8000-kilometer-wide crater without melting it into an unrecognizable puddle of magma. "I think there's much to recommend [a giant impact] now with all this new work,"

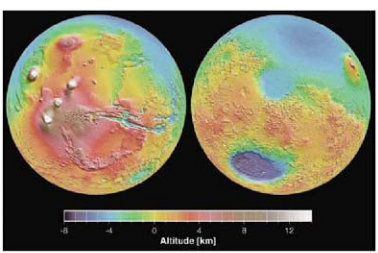

CREDIT: MARS ORBITER LASER ALTIMETER (MOLA) TEAM/GODDARD SPACE FLIGHT CENTER/NASA

Striptease. Removing the Tharsis volcanoes of Mars (reds and yellows, left panel) from part of the northern lowlands (light blue, right panel, *top*) uncovered an elliptical basin that looks like an impact crater.

says Sean Solomon, a planetary geophysicist at the Carnegie Institution of Washington's Department of Terrestrial Magnetism in Washington, D.C.

Last month, planetary geophysicist Jeffrey Andrews-Hanna of the Massachusetts Institute of Technology in Cambridge and colleagues presented their test of the giant-impact hypothesis at the Lunar and Planetary Science Conference (LPSC) in Houston, Texas. In 1984, planetary scientists Donald Wilhelms, now retired from the U.S. Geological Survey, and Steven Squyres of Cornell University first proposed that a huge impactor had blasted out the Borealis basin. Fitting a circle to the "dichotomy boundary" between the basin and the highlands, they suggested that the circle could mark the outer edge of a huge crater. But the fit was too rough to win many converts.

So Andrews-Hanna and his colleagues looked for a better way to trace out the dichotomy boundary. The great Tharsis volcanic complex had obscured much of the boundary when it smothered one-quarter of the planet with lava hundreds of millions of years after the lowlands formed. To "remove" Tharsis, they drew on measurements of martian gravity and surface height from the past decade of Mars orbiters. Subtle variations in the pull of gravity—evidenced in variations of a spacecraft's orbit—reflect the added mass of Tharsis lavas as well as the extent of the deep, less-dense crustal rock buoying up the highlands. The height of the surface constrains the volume of added lavas.

By combining the data in a model, the researchers erased Tharsis's contribution to the present surface and traced the topographic edge of the Borealis basin right under Tharsis. Rather than a circle, the best shape for the basin turns out to be a 10,650-kilometer-long ellipse, they reported at the LPSC meeting. That's a familiar look for big impact basins. The 2300-kilometer Hellas impact basin in the southern highlands, for example, is also elliptical and also underlain by a uniformly thin crust. And there's no particular reason, Andrews-Hanna said, why the giant-impact theory's only serious rival—a peculiar sort of churning deep within the planet—would produce an elliptical basin or the observed sharp boundary between thin and thick crust.

The other long-standing objection to impact excavation was the mere survival of a craterlike feature of any sort. Any object ▶

Biotech Lawyers, Rejoice

It's back to square one for would-be reformers at the U.S. Patent and Trademark Office (USPTO). Last week, a Virginia federal court rejected rules the office proposed last year that would have limited the number of so-called continuations that can extend the normal 17-year life of a patent claim with amendments and appeals. Up to one-third of U.S. patent filings in recent years have been continuations (*Science*, 28 July 2006, p. 425), and USPTO said the proposed limits would have cut their workload. Other critics say continuations give some patent holders an unfair advantage. But the Biotechnology Industry Organization said the changes would have inhibited the "financing necessary to bring innovative … life-saving products to market." Industry sued last year to block the change; a federal judge sided with them, saying the rules exceeded "USPTO's rulemaking authority."

–ELIOT MARSHALL

The Big Apple Does Science

New York City will display its scientific chops next month when a coterie of scientists, media stars, foundations, and university presidents present the World Science Festival. The 5-day event will include a play about oxygen, a dance performance inspired by string theory, a neuroscience lecture paired with a musical meditation on consciousness, and a World Science Summit modeled on the annual Davos confab. Running from 28 May through 1 June, the extravaganza is the brainchild of Columbia University physicist Brian Greene and his partner, Tracy Day, a television producer, who hope "to sustain a general public informed by the content of science."

–ANDREW LAWLER

Buffaloed

An effort to prevent the spread of brucellosis from bison in Yellowstone National Park to nearby cattle is poorly managed, says the U.S. Government Accountability Office (GAO). Although there are no documented cases of transmission, federal and Montana state agencies are 5 years behind schedule in vaccinating bison and securing a conservation easement around the park. The plan currently sanctions the slaughter of thousands of bison that leave Yellowstone, as long as the herd doesn't drop below 3000. Worried by the extensive culling, members of the House Committee on Natural Resources requested the GAO investigation. The resulting report calls for concrete objectives and greater accountability in the plan, which began in 2000.

–ELSA YOUNGSTEADT

hundreds of kilometers across that hit Mars at tens of thousands of kilometers per hour, the thinking went, would heat the planet so dramatically that any crater would disappear in a sea of globe-girdling melted rock. Now that computer models are up to the task of simulating giant impacts in detail, that thinking is changing.

As most recently reported at last December's American Geophysical Union meeting, planetary scientist Margarita Marinova of the California Institute of Technology in Pasadena and colleagues have simulated a range of giant impacts on Mars, all producing 8000-kilometer craters. They found that the melt from vertical impacts does in fact obliterate the crater but that faster, low-angle impacts do not. Simulated glancing blows at angles below 30° produce less melt overall and splash much of it into space. The giant-impact mechanism "was always thought dynamically impossible," said Andrews-Hanna at LPSC. "Now you can't dismiss the possibility."

The two studies are convincing researchers that "the giant impact lives (after all)!" as planetary geophysicist Roger Phillips of Southwest Research Institute in Boulder, Colorado, playfully writes in an e-mail. Few are entirely won over yet, but a giant impact worked out as the origin of Earth's moon. Perhaps it will also serve to explain the deepest mystery of martian geology.

–RICHARD A. KERR

APPLIED PHYSICS

At Mixed Odds, Racetrack Memory Charges From Gate

For more than a decade, physicists and engineers have been trying to replace the electronic memories that computers, cell phones, and other devices rely on. Now, on page 209, Stuart Parkin, a physicist at IBM's Almaden Research Center in San Jose, California, and colleagues demonstrate a memory that pushes magnetic bits around tiny nanoscale "racetracks." Racetrack memory might someday replace the electronic memory that can store thousands of songs and pictures in an iPod, Parkin says. But skeptics doubt it can live up to its advance billing.

It's a controversial effort that's even been funded with controversial money. Racetrack memory started creating a media buzz about a year ago, but many researchers doubt it will ever emerge as a commercially viable technology. "A lot of us don't think that this is going to reach the finish line," says Robert Buhrman, an applied physicist at Cornell University. Others have faith in Parkin, whose previous work led to huge leaps in computer hard-drive technology. "He's the right person to take on such a challenge," says Gernot Güntherodt, a physicist at RWTH Aachen University in Germany.

Memory comes in several types. A hard drive stores information in tiny magnetic bits that can be magnetized in one direction or another with a magnetic field to store the 1s and 0s of binary code. It's capacious but slow. The electronic "random access memory" (RAM) that connects directly to a computer's processor encodes information in electric charges stored on tiny capacitors or in voltages in networks of transistors. RAM is fast, but it forgets everything when powered down. The flash memory in digital cameras and other small devices works a bit like RAM but involves capacitors that can be semipermanently polarized to hold information without power. Flash bits eventually wear out, however. And all electronic technologies may soon reach their limits as engineers strive to cram ever more bits onto a chip.

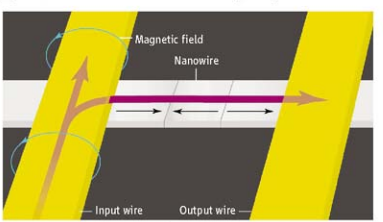

Driven. Bits consist of magnetized "domains" pushed along by flowing electrons (purple). Researchers read them by measuring the wire's resistance, which is affected by the "walls" between oppositely magnetized domains.

Racetrack memory stores bits of information on metal nanowires, in minuscule "domains" that can be magnetized to point either way along the wire. But unlike the stationary bits in a hard drive, the bits in racetrack memory move. To write a bit, electrons flowing through an input wire create a magnetic field (see figure). If the bit has a different value from the preceding one—one is a 0 and the other is a 1—then a domain wall will exist between them. Some of the electrons also flow down the nanowire, and in theory they should push the domain walls, and hence the bits, down the wire.

That's just what Parkin and colleagues showed. The team made a three-bit "shift register" that could reliably pass a sequence of bits from input to output. That's the basic function that the memory element has to perform, and there's no question that it works, says Jian-Gang "Jimmy" Zhu, an electrical engineer at Carnegie Mellon University in Pittsburgh, Pennsylvania. "It does prove the basic concept," Zhu says.

"It's demonstrating, in my mind, a paradigm shift in building magnetic memories," Parkin says. He envisions laying down scads of racetracks to make a new type of RAM. That memory could be faster, cheaper, and more robust than flash, he says. And if the little racetracks could be manufactured on end as towers, the memory could be dense enough to replace hard drives, Parkin says.

Others say that such visions may be hard to achieve. Moving the domain walls takes a lot of juice—200 million amps per square centimeter—Buhrman notes. "That's a huge current density," he says. Zhu says that to make the memory competitive, researchers will have to stand the nanowires on end. Nobody knows how to do that, he says.

Some people also question the way the research was funded. The money came in part from a federal earmark directed toward the Center for Nanoscale Science and Engineering at the University of California, Riverside. The center gave IBM $5.1 million for the work from 2004 to 2006, according to figures provided by Robert Haddon, a chemist at Riverside and director of the center. Parkin says the money amounted to only 20% or 30% of the total investment and that he didn't seek the funding: "They came to me."

In spite of the questions surrounding it, Zhu says he likes the racetrack memory concept. "It's very different, very bold," he says. Time will tell whether it leads to a revolutionary new technology or fades from memory.

–ADRIAN CHO

CREDIT: P. MILEY/SCIENCE

PARKINSON'S DISEASE

Signs of Disease in Fetal Transplants

In the 1990s, an experimental treatment for Parkinson's disease raised hopes that the devastating movement disorder might be on the verge of yielding to modern medicine. Doctors reported that by extracting dopamine-producing neurons from aborted fetuses and injecting them into the brain to replace neurons destroyed by the disease, they were able to restore some patients' mobility. But despite its early promise, the procedure has had a contentious history. From the start, abortion foes objected to using fetal tissue, and two high-profile clinical trials later found that the surgery offered little to no benefit and appeared to cause involuntary movements in some patients.

New studies add another wrinkle to this complex story, revealing that implants can survive a decade or more but in some cases appear to acquire signs of Parkinson's disease—a surprising finding that could shed light on the disease's mechanisms.

Three independent research groups report online this week in *Nature Medicine* findings from postmortem examinations of a total of six brains from Parkinson's patients who received the fetal transplant surgery between 9 and 16 years earlier. They are the first postmortem studies done this long after the surgery. All three studies found that many transplanted cells—identified by their pigmentation and staining for an enzyme involved in dopamine production—were apparently alive and well-integrated in the patients' brains. But two of the teams—one led by neuroscientist Jeffrey Kordower at Rush University Medical Center in Chicago, Illinois, the other by Patrik Brundin at the Wallenberg Neuroscience Center in Lund, Sweden—found that a small proportion of the surviving cells showed a hallmark of Parkinson's pathology: clumps of protein containing α-synuclein and ubiquitin. The third team, led by Ole Isacson at Harvard University, saw no signs of Parkinson's pathology in the transplanted cells in the brains they examined.

"I think it's extremely intriguing," says Stanley Fahn, a neurologist at Columbia University. The Brundin and Kordower groups' findings suggest that the disease can spread from the host brain to much younger neurons with different genetics, Fahn says. "We know that age is the most important risk factor for Parkinson's disease, but here these neurons are only 14 years old," he says. "It opens up the possibility of some new pathogenic mechanism we hadn't thought of before."

The reason for the discrepancy with Isacson's group's findings isn't clear, Fahn and others say. Differences in surgical techniques or differences in the patients' immune reactions to the transplanted fetal cells might be important factors, says D. Eugene Redmond, a veteran Parkinson's researcher at Yale University.

Researchers are divided about what bearing, if any, the findings have on expectations for future cell-transplant therapies, including possible stem cell treatments. "Personally, I think it's encouraging," says Redmond, who points out that all three studies documented long-term survival of transplanted neurons. "If you could provide a benefit, … even if it only lasts 10 or 12 years, I think most people would see that as a great improvement."

Fetal transplant surgery is rarely done now, but some researchers, including Brundin and Isacson, still think the method holds promise and can be improved. A consortium of North American and European researchers is planning a clinical trial to see if the surgery offers consistent benefits and to help pave the way for stem cell transplants, should they become available. **–GREG MILLER**

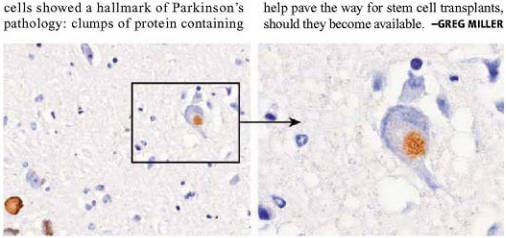

CREDIT: J.-Y. LI ET AL., *NATURE MEDICINE* (6 APRIL 2008)

Sign of trouble? Clumps of α-synuclein (brown) inside transplanted fetal neurons suggest that Parkinson's disease can spread from the host brain into younger cells with different genetics.

Talk It Out

Sixty U.S. research universities want the next Administration to create an ongoing platform to discuss the needs of academic researchers. And the current science adviser thinks it's a good idea.

A white paper (www.aau.edu/reports/SAAS_08.pdf) from the Association of American Universities (AAU) calls for a committee comprised of top federal science officials and university presidents that would study problems with the current "partnership" and suggest changes. "There's no mechanism for a continuing dialogue on issues that cut across agencies," explains AAU's Tobin Smith, citing differing rules on grants management as well as broader policies relating to regulatory requirements and funding.

The panel would be a new breed of advisory cat: Existing oversight bodies are made up of either outsiders, such as the President's Council of Advisors on Science and Technology, or insiders, like the National Science and Technology Council. But presidential science adviser John Marburger says that "the issues raised in the AAU report are important ones" and that "the tasks AAU is suggesting would be possible in such a committee." **–JEFFREY MERVIS**

Stern Swan Song

U.S. lawmakers pledged last week to fight for more money for NASA's beleaguered science program, even as outgoing NASA science chief S. Alan Stern (*Science*, 4 April, p. 31) warned in a farewell letter about the rising costs of individual projects. Senator Barbara Mikulski (D–MD), who chairs the panel responsible for NASA funding, told NASA Administrator Michael Griffin that she would push again this year to win $1 billion more for the agency in 2009, in part to take the pressure off the science budget. A similar effort died in conference last year.

On the same day, a parade of witnesses told the House Science and Technology Committee that NASA must keep the fiscal lid on its launcher to replace the space shuttle. It's a $3.5 billion item in the 2009 budget that many fear will drain money from science. Meanwhile, Stern said in his letter that he resigned "only after several months of hard thought and reflection about the consequences of spiraling mission costs that [the Science Mission Directorate] could not control." The issue, he added, "became an important matter of principle that trumped even my boss," referring to Griffin. Asked what he will do now, Stern told *Science*, "Find a job."

–ANDREW LAWLER

Tackling Alcoholism With Drugs

New treatments, some now in clinical trials, reflect a growing awareness that people with different genetic profiles and drinking histories may need different therapies

Jennifer started drinking more heavily in her early 30s, about the time her marriage started going sour. She split up with her husband and moved with her daughter from California to live with her mother in the Washington, D.C., suburbs. Sometimes while her daughter was at school, Jennifer would polish off a 1.5-liter bottle of wine and then another at night. She blacked out from drinking about once a week, she says, and twice ended up in the emergency room in the throes of alcohol withdrawal. Her life was spinning out of control.

Last year, at age 36, she found herself in a hospital at the National Institutes of Health in Bethesda, Maryland, where she had volunteered for a study on a potential drug treatment for alcoholism. She got a physical exam, filled out a series of questionnaires, and endured a test in which a researcher gave her a small glass of vodka and asked her to hold and sniff it—no drinking allowed. "My hands got sweaty, and I started to salivate," she says. "I imagined myself being on the deck on a warm day having cocktails with friends."

For the next 4 weeks, Jennifer would stay in the hospital, taking a pill once a day—either a placebo or a drug that dampens stress responses in the brain. The study, led by Markus Heilig, director of clinical research at the National Institute on Alcohol Abuse and Alcoholism (NIAAA), was designed to test a drug Heilig hopes will help people he describes as "anxious alcoholics." Instead of drinking for the rewarding buzz, anxious alcoholics drink for relief—from either the mental stress of life events or the physiological stress caused by abstaining from alcohol when the body has come to depend on it, Heilig says.

His study is one of several recent efforts that are raising hopes of new and improved treatments for alcoholism that work by restoring balance to various biochemical pathways in the brain that are thrown off kilter by extended heavy drinking. Much of the work also reflects a growing realization that there may be different types of alcoholism and that people with different genetic profiles and drinking histories may respond better to different types of drugs.

"It's a fascinating time in our field," says Selena Bartlett, who directs the Preclinical Development Group at the Ernest Gallo Clinic and Research Center at the University of California, San Francisco. "It feels like we're heading for a sea change for new therapies for alcoholism."

Why drugs?

Alcohol dependence afflicts 4% of the adult population and is the third leading cause of preventable death in the United States, according to NIAAA. Yet only 10% to 15% of those affected get treatment, mostly in group counseling or support sessions, says Mark Willenbring, NIAAA's director of treatment and recovery research. There's a lingering perception in the general public and among some primary care physicians that alcoholism is a problem best remedied with willpower, not medicine. Willenbring disagrees. "That's like saying 'Why do we treat diabetes with insulin? Why don't we just have people … learn to eat right and exercise?' " Behavioral interventions help many people, Willenbring and other clinicians say, but they often work better when combined with drugs that help loosen the grip of addiction.

Three drugs are currently approved for treating alcoholism in the United States. The oldest, disulfiram (better known as Antabuse), has fallen out of favor with many doctors. It makes people violently ill if they drink, providing a powerful disincentive but one that can easily be skirted by anyone with enough foresight to stop taking it before a binge. Naltrexone, approved in 1994, is more widely used. The ultimate buzz killer, it blocks opioid receptors in the brain to prevent the euphoric effects of alcohol. The third drug, acamprosate, approved in 2004, blocks receptors for the neurotransmitter glutamate and is thought to quell hyperactive glutamate signaling caused by alcohol dependence. Acamprosate has shown modest benefits in Europe, where clinicians have used it to treat alcoholism

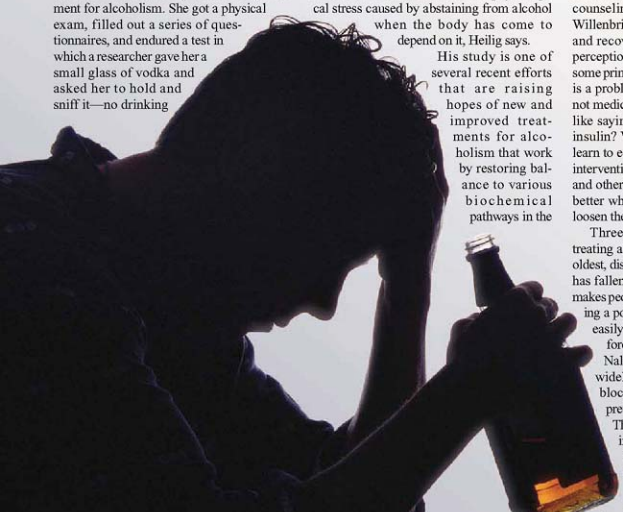

CREDIT: SCOTT GIBSON/CORBIS

Antialcoholism Drugs

Drug (trade name)	Manufacturer	Mechanism	Notes
Disulfiram (Antabuse)*	PLIVA	Interferes with alcohol metabolism	Makes patients violently ill when alcohol is consumed.
Naltrexone (Depade, ReVia, Vivitrol)*	Several companies	Blocks opioid receptors	Curtails euphoria; monthly injection approved in U.S. in 2006.
Acamprosate (Campral)*	Merck Santé	Inhibits glutamate signaling	Thought to reduce withdrawal symptoms; efficacy differs in European and U.S. trials.
Topiramate (Topamax)	Ortho-McNeil Neurologics	Inhibits glutamate signaling, enhances GABA signaling	Approved for epilepsy and migraine; encouraging results in two trials for alcoholism.
Ondansetron (Zofran)	GlaxoSmithKline	Blocks $5HT_3$ serotonin receptors	Approved for treating nausea; reduced drinking in early-onset alcoholics in two studies.
Baclofen (Baclofen)	Several companies	Stimulates GABAB receptors	Approved for treating spasticity; reduced drinking in several small trials for alcoholism.
Varenicline (Chantix)	Pfizer	Weakly activates nicotinic acetylcholine receptors	Approved for smoking cessation; human tests for alcoholism now beginning.
LY686017	Eli Lilly and Co.	Blocks NK1 receptors for substance P	Reduced stress and alcohol craving in preliminary test with hospitalized alcoholics.

* Approved in U.S. for treating alcoholism.

for nearly 20 years, but it did no better than a placebo in a large U.S. trial published in 2006 in the *Journal of the American Medical Association* (*JAMA*). It's a mixed bag, says Stephanie O'Malley, an alcoholism researcher at Yale University. "We have effective treatments, but they don't help everyone," she says. "There's lots of room for improvement."

In the case of naltrexone, genetics may offer a clue to why some alcoholics respond better than others, says Charles O'Brien, a clinician and psychopharmacologist at the University of Pennsylvania who pioneered the drug's use for treating alcoholism. O'Brien's team reported in 2003 that alcoholics with a particular variant of the μ-opioid receptor gene respond better to naltrexone treatment. An independent study, reported in the February *Archives of General Psychiatry*, confirmed this finding in a larger sample of 911 alcoholics. In that study, 87% of patients with the variant either abstained from alcohol or tippled only moderately during the 16-week study period. Among patients without the variant, only 55% had a similar outcome, regardless of whether they got naltrexone or a placebo.

"This is a milestone in pharmacogenetics," says Rainer Spanagel, a psychopharmacologist at the Central Institute of Mental Health in Mannheim, Germany. For all the talk about using patients' genetics to select the best drugs, there are only a handful of success stories so far in all of medicine, Spanagel says. Some researchers offer more tempered enthusiasm, however, pointing out that one smaller study failed to find a connection between the opioid receptor gene variant and response to naltrexone.

CREDIT: B. REED/LOS ANGELES NEUROANALYSIS

Meet the candidates

Other drugs that are generating a buzz among alcoholism researchers take aim at a wide variety of molecular targets (see table). One of the more promising contenders is topiramate, an anticonvulsant currently approved for treating epilepsy and migraines. In two double-blind randomized controlled trials, one published in 2003 in *The Lancet* and a larger follow-up published last October in *JAMA*, researchers led by psychiatrist and psychopharmacologist Bankole Johnson of the University of Virginia, Charlottesville, reported that alcoholics who took topiramate daily had fewer heavy drinking days and more abstinent ones. In the *JAMA* study, the trend toward sobriety seemed to be growing even stronger at the end of the 14-week trial in the topiramate group—a very encouraging sign, says NIAAA's Willenbring. "The level of effectiveness seemed to be at least as good as naltrexone and maybe better."

> *"It feels like we're heading for a sea change for new therapies for alcoholism."*
>
> —SELENA BARTLETT, UNIVERSITY OF CALIFORNIA, SAN FRANCISCO

Topiramate alters the activity of glutamate, GABA, and other neurotransmitters, but exactly how it dampens the desire to drink isn't known. Animal studies have suggested that the drug reduces the release of dopamine from neurons in the brain's reward circuitry, and Johnson hypothesizes that it may work by inhibiting the rewarding surge of dopamine an alcoholic gets from knocking back a drink.

Another drug suspected to dampen hyperactive reward mechanisms is just entering its first tests in human subjects. In a 2007 paper in the *Proceedings of the National Academy of Sciences*, Bartlett and her Gallo Center colleagues reported that a drug called varenicline substantially reduces drinking in alcohol-dependent rats. Varenicline, which is sold as a smoking-cessation aid, weakly stimulates receptors for the neurotransmitter acetylcholine but at the same time keeps them from getting overexcited by an influx of nicotine or, perhaps, alcohol. As with topiramate, the mechanism is murky, but Bartlett and others speculate that varenicline's moderating influence on acetylcholine receptors may exert an overall calming influence on the brain's reward circuitry, preventing huge highs without revoking the ability to feel pleasure. "It may stabilize those systems in a way that makes the patients happy enough to stay on the drugs," says Heilig, who suspects that the pleasure-blocking effects of naltrexone may explain why many patients who take it don't stick with their drug regimen. Heilig is collaborating with Bartlett on human studies with varenicline that are about to begin at NIAAA. O'Malley's group has already started similar work at Yale.

Stress effects

At the same time, Heilig suspects that the rewarding aspects of drinking are only part of the story. Epidemiological and clinical studies have identified two basic types of alcoholics, he says. So-called reward drinkers are the ones

who get a big rush from drinking. "If you think back to high school, … in every class there's two guys who when they got alcohol, they got wild and got up on the table and started doing crazy things," Heilig says. They are the ones who tend to have a family history of alcoholism and get into trouble with alcohol in their teens or early 20s. They're also the ones who respond best to naltrexone, Heilig says. The second type, the anxious alcoholics, often start out as moderate drinkers and get into trouble in their 30s or 40s. They drink mainly to relieve anxiety and stress, and they tend to respond poorly to naltrexone, Heilig says.

More than a decade of rodent studies, many of them conducted in the laboratory of George Koob, a neurobiologist at The Scripps Research Institute in San Diego, California, have provided the rationale for treating anxious alcoholics with drugs that target stress mechanisms. (Heilig was a postdoctoral fellow with Koob before moving to NIAAA.) Koob and others have found hyperactive stress signaling in the brains of alcohol-dependent rodents, including increased sensitivity to corticotropin-releasing factor (CRF), a hormone that kicks off a cascade of stress responses. Drugs that block CRF curtail excessive drinking in alcohol-dependent rodents and reduce the likelihood that a stressful event—such as an electric shock—will cause a recovering rodent alcoholic to relapse, researchers have found.

Human studies have also hinted at a link between stress mechanisms and alcoholism. In 2006, German researchers reported in *Molecular Psychiatry* that binge drinking is more common in people with certain variations of the gene that encodes the receptor for CRF. Adolescents who possess a particular one of these gene variants are more likely to engage in heavy drinking after a stressful life event, the same research team reported in *Biological Psychiatry* in January.

Based on the growing body of animal and human research, Koob, Heilig, and like-minded researchers suspect that drugs that block the CRF receptor would be extremely promising for treating alcoholism. Unfortunately, no such drugs are currently approved for human use. "Drugs are in development, … but that's still several years away," Heilig says.

In the meantime, Heilig's recent study with anxious alcoholics investigated a drug that blocks a different stress pathway. It blocks a receptor for substance P, a neurotransmitter involved in signaling pain and stress. (The drug, dubbed LY686017 by its creator, Eli Lilly and Co., had proved safe in clinical trials for depression but not effective enough to merit further development, Heilig says.) Heilig and co-workers recruited 50 recovering alcoholics, including Jennifer, all of whom scored high on questionnaires that measure anxiety.

During the monthlong study, the researchers took blood samples to monitor stress-hormone levels in the volunteers and queried them about their alcohol cravings. Near the end of the study, they subjected them to a mock interview intended to evoke the type of social stress that can drive a recovering alcoholic back to the bottle. Volunteers were told to imagine that they were applying for their dream job and had 5 minutes to convince the hiring committee—three stone-faced research assistants in white coats—that they were the right person for the job. Then they were asked to perform a daunting test of mental arithmetic. This ordeal caused a smaller outpouring of stress hormones and evoked milder cravings for alcohol in the patients who'd been on a daily dose of LY686017, Heilig and colleagues reported online 14 February in *Science*.

Downward spiral. In the 1962 movie ***Days of Wine and Roses***, Lee Remick plays an alcoholic who gradually became addicted. New therapies may offer better results in such cases.

The researchers also conducted a brain-scanning experiment with the volunteers. Recent research in press at the *Journal of Studies on Alcohol and Drugs* suggests that alcoholics exhibit exaggerated responses in certain brain regions when they look at unpleasant images (such as photos of car crashes) and exhibit diminished responses to positive images (photos of children or animals, for example). This was also true of the subjects who received the placebo in Heilig's experiment, but the ones who received the drug showed the opposite effect. Taken as a whole, the study provides preliminary evidence that LY686017 suppresses the stress and negative emotions that drive anxious alcoholics to drink, Heilig says.

When the study was over, Jennifer was told that she'd been among those who received the drug. She says she'd noticed a difference in her reaction when she took the vodka-sniffing test again at the end of the study. "This time, I wasn't romanticizing it … [and] picturing good times," she says. "It didn't make me want to go find some ice cubes and cranberry juice like the first time did."

Other researchers agree that the work looks promising but caution that LY686017 has not yet been shown to reduce drinking in anybody with a drinking problem—all of the subjects were hospitalized and on enforced abstinence. "It reportedly reduced alcohol craving, which may be very important, but you've just got to test it in an outpatient clinical trial to see whether it actually reduces drinking," says O'Brien. That's the next step, Heilig says: "Two companies are taking this to full-scale clinical trials. After that, we'll have some answers."

Even if those trials go well, questions will still remain—as they do for all of the drugs in development—about how long patients would need to be medicated. There are simply not enough data at this point to know whether a recovering alcoholic would have to take medication indefinitely or whether a shorter drug regimen would lead to the desired outcome. Even the desired outcome is somewhat controversial. Although some studies have found that a small minority of former alcoholics are able to drink moderately without relapsing, many experts argue that abstinence is always the safest bet.

Despite such uncertainties, veteran alcoholism researchers are convinced that there are brighter days ahead. Willenbring predicts that in the next 5 to 10 years the field will have its "Prozac moment": "I think we're going to have a medication that's perceived as effective, that's well-marketed by a pharmaceutical company, and that people receive in a primary-care setting or general-psychiatry setting." If so, the abysmally low proportion of people who get effective treatment for alcoholism may finally begin to rise.

–GREG MILLER

CREDIT: WARNER BROS/THE KOBAL COLLECTION

Drying out. Australian farmers know all too well the devastating effects of drought, which has greatly reduced harvests.

PLANT GENETICS

The Blue Revolution, Drop By Drop, Gene by Gene

Researchers probe the secrets of how plants cope with water stress to improve crop yields

Eight years ago, then–U.N. Secretary-General Kofi Annan called for a "Blue Revolution" in agriculture. With Earth's water resources under strain, population growth booming, and desertification increasing, the need to wring more crops out of dry land is becoming urgent, Annan said in his April 2000 Millennium Address.

It was a call to arms for plant genomicists. But they are fighting a battle on many fronts. "Drought stress is as complicated and difficult to plant biology as cancer is to mammalian biology," says Jian-Kang Zhu, a molecular geneticist at the University of California, Riverside. Plants have evolved complex mechanisms to deal with water shortages, which vary in timing and severity from place to place, season to season.

Researchers armed with the latest sequencing and gene-expression technologies are making progress in rounding up the genes that can help plants stand up to dry conditions, both in the greenhouse and in the field. "We do know a bit more about what the effects [of stress] are in biochemical detail," says Hans Bohnert, a biochemist at the University of Illinois, Urbana-Champaign. But some skeptics doubt that it will be possible to manipulate one or a few genes to get tougher breeds. "There isn't a single, magical drought-tolerance trait," says Mark Tester, a plant physiologist at the Australian Centre for Plant Functional Genomics in Glen Osmond.

Others counsel patience. Companies and governments are evaluating promising new strains of corn, rice, and other crops—some genetically modified (GM) and some the products of conventional breeding—in the field. Australian farmers, for example, are eagerly awaiting results of a field trial of GM, drought-tolerant wheat that has just been harvested. There's been "a constant increase in interest, particularly from the private sector," says Roberto Tuberosa of the University of Bologna in Italy. "Drought and tolerance to water stress are very hot topics at this moment."

Drop by drop

During the green revolution, researchers and breeders focused on improving productivity by providing optimal environments—fertilizing poor soils, irrigating dry lands, destroying weeds and pest insects—and developing high-yielding crops that thrive under those conditions. But looming water shortages are changing the equation. Agriculture consumes 70% of the water people use, and its needs will increase 17% by 2025, according to the International Water Management Institute (IWMI), based in Sri Lanka. But competition from urbanization and development means that "less water is becoming available for agriculture," says Henry Nguyen, a plant geneticist at the University of Missouri, Columbia.

Given this anticipated shortfall, IWMI's *Comprehensive Assessment of Water Management in Agriculture*, released in 2003, called for a 40% improvement by 2025 in yields of crops where water is the limiting factor. Unfortunately, historically, improvements have inched along by only about 10% per decade, says John Passioura of CSIRO Plant Industry in Canberra, Australia, and it's not clear that even that pace can be sustained.

Climate change also has agronomists worried. Rainfall in some areas is declining and becoming more erratic, wreaking havoc on markets. A case in point: A drought in Australia has cut world supplies of wheat and barley, leading to a spectacular price hike in those crops. And rice farmers in northern Italy have been forced to shift from growing rice in paddies to flooding their fields for very short periods.

Plants have mechanisms to cope with drought. In some places, local crop varieties have evolved to survive, if not thrive, as long as water shortages are not too severe. How efficiently a plant draws water from the soil, how

Rain or shine. In China, movable shelters shield drought-tolerant rice from rain during field trials.

CREDITS: (TOP TO BOTTOM) MARK MADISON/GETTY IMAGES; NATIONAL KEY LABORATORY OF CROP GENETIC IMPROVEMENT/HUAZHONG AGRICULTURAL UNIVERSITY

well cells retain water, how much water is released through leaf openings called stomata, the timing of flowering relative to the seasonal onset of drought—all factor in drought tolerance. Roots produce molecules that allow them to suck water out of ever-drier soils; leaves respond by closing stomata. Cells mop up free radicals produced during dehydration or produce molecules that preserve their ability to hold on to what water they have.

Researchers are employing two strategies to decipher and harness these responses to drought. Some take a relatively traditional approach, growing and crossing varieties and evaluating how the progeny vary in their ability to deal with stress. They then select and grow the best-adapted plants. For these breeders, genome studies have identified DNA markers that speed the identification and selection of plants worthy of further study.

Some researchers head straight for the genes. In 1998 at the University of Arizona, Tucson, Bohnert and his colleagues began teasing apart the genetics of stress response using the model plant *Arabidopsis*, whose genome was sequenced in 2000. They evaluated thousands of mutant *Arabidopsis* strains, each of which contained a fluorescence protein attached to a stretch of regulatory DNA known to be involved in the plant's responses to stress. Lack of fluorescence would indicate that the responses were switched off, perhaps because a gene in the pathway that triggers them had been mutated.

The genetic technology they used enabled them to home in on the mutated gene or DNA region. They then manipulated the activity of these genes in transgenic plants to better understand the gene's role in weathering tough conditions. Other groups have done broad-scale surveys of genes and proteins active when plants are under stress, coming up with many promising candidates.

But precious few of these leads have panned out, possibly because drought responses are extremely complex. "We still do not have all the pieces of the puzzle, not even the key pieces," says Zhu, who worked with Bohnert. His work, for example, is showing that beyond genes, small RNAs help regulate stress responses in ways he does not yet fully understand. "There are now several hundred papers published, tweaking individual genes," says Bohnert. "Under controlled conditions, one can see an effect but not in the field."

Gene by gene

A few genes have helped in the field, however. After looking at expression patterns of 1500 genes in *Arabidopsis* plants grown under drought conditions, Donald Nelson, now at Monsanto in Mystic, Connecticut, and his colleagues found 40 that appear to be involved in drought adaptation. They looked at effects of the most promising ones by causing each to be permanently turned on in GM plants. *Arabidopsis* with a constantly active *NF-YB1* gene didn't wilt as much as wild-type *Arabidopsis* and maintained higher photosynthetic rates.

Nelson tracked down the equivalent gene in maize and switched it on permanently. Simulated drought conditions typically reduced maize yield by more than 50%. Under those conditions, the GM maize produced as much as 50% more than unmodified plants, they reported online 8 October 2007 in the *Proceedings of the National Academy of Sciences*.

Subsequent field studies show that the transcription factors produced by these genes increase yields by an average of 10% to 15% under a variety of stress conditions, Paul Chomet, also at Monsanto in Mystic, Connecticut, reported in Washington, D.C., in February at the 50th Annual Maize Genetics Conference. This work was "a proof of concept," Chomet said. Monsanto now has a large-scale program screening for genetic enhancements that can improve yield despite water shortages, with one new variety about to enter the regulatory pipeline. (The company has also just agreed to develop this and other drought-tolerant technologies with the African Agricultural Technology Foundation through a royalty-free agreement that will make these crops available to small farmers.) This effort is much more challenging, than, say, developing GM Bt maize, in which "you flip a switch and Bt works," he pointed out. "With drought, we are trying to dial into the physiology of the plant."

Yafan Huang has also tried dialing into the physiology of the plant. In 1996, Peter McCourt of the University of Toronto in Canada and his colleagues discovered a mutant *Arabidopsis* that was overly sensitive to the plant hormone abscisic acid, which influences plant development and activates stress responses, including closing stomata to inhibit water loss. Two years later, McCourt's group demonstrated that the mutated gene, *ERA1*, typically countered abscisic acid's propensity to close stomata. Mutants lacking a functional *ERA1* were more sensitive to the hormone and their stomata more prone to closure—a change that helped the mutants withstand drought stress (*Science*, 30 August 1996, p. 1239; 9 October 1998, p. 287).

Encouraged by this discovery, McCourt and Huang, of Performance Plants Inc. in Kingston, Canada, fiddled with this same gene in canola. They created a line of canola that carried antisense DNA that disables the

More crop per drop. Tests of genetically modified rice (*top right*), canola (*middle right*), and corn (*bottom right*) show that they withstand dry spells better than unmodified controls (*left*).

CREDITS: (TOP TO BOTTOM) NATIONAL KEY LABORATORY OF CROP GENETIC IMPROVEMENT, HUAZHONG AGRICULTURAL UNIVERSITY; ANGELA SAMPLE, COURTESY OF MONSANTO

Getting to the Root of Drought Responses

Plants are bit like giant straws. Water in the ground gets "sucked" up the corn stalk or tree trunk and leaks out of microscopic pores, primarily in the leaves. The pores, called stomata, must open to let in carbon dioxide for photosynthesis, but the water loss—up to several cubic meters a day for a tree—can be severe, especially in drought-ridden areas. Not surprisingly, researchers seeking to develop drought-resistant crops have homed in on ways to keep stomata shut down (see main text). But Henry Nguyen, a plant geneticist at the University of Missouri, Columbia, thinks they should also be looking at the bottom end of the straw. He and Missouri colleague Robert Sharp are establishing a drought research center at Missouri that will concentrate on root biology. "From a drought research [perspective], this will be a new frontier," says Nguyen.

It's been difficult to unearth how roots cope with arid conditions. Unlike leaves, their workings are hard to observe. Nguyen is peering deep inside the roots, at the genes themselves. His group has surveyed gene-expression patterns in different parts of maize roots under various stresses and plans to compare them with expression patterns in soy roots. Early analyses suggest that different biochemical pathways underlie drought adaptations in the two species, he says.

Lewis Lukens, a plant geneticist at the University of Guelph in Canada, and his graduate student Tina Wambach are finding different patterns of gene expression in the roots of plants from different inbred lines of maize, some of which grow more than others when water is in short supply. Lukens and Wambach looked at gene activity in a half-dozen of the more diverse responders. They grew seedlings suspended in water solution to see what was happening, get relatively pure samples of RNA, and precisely control water availability. They started the seeds in normal conditions, then subjected them to "drought" stress for 24 hours, sampling root tissue during prestress, "drought," and recovery periods.

To Lukens's surprise, the number of activated genes varied threefold across the different inbred lines. In one, 4500 genes out of 40,000 changed their expression; whereas in another, only 2000 did so. Furthermore, "there were very few changed genes shared across all the genotypes," says Lukens. Even when the same gene was activated, it was revved up to varying degrees, he reported in February in Washington, D.C., at the 50th Annual Maize Genetics Conference.

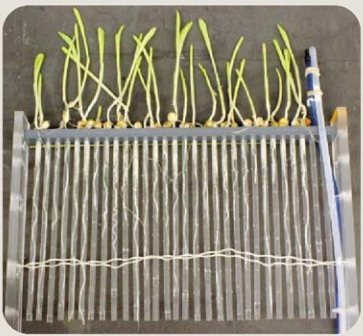

In full view. Maize seedlings grown hydroponically varied in their roots' resistance to water stress.

Although the diversity of responses was initially confusing, Lukens later discovered that many of the genes were active in the same enzymatic pathways. "We saw much more conservation," with about 40% of the pathways shared across all the lines, he notes. It seems that many lines had adapted in a similar way, but the activity of different genes in particular pathways changed. Lukens hopes that by crossbreeding lines that show different patterns of gene expression in the same pathway, breeders may come up with hybrids with even better drought tolerance than either of the parent lines. Meanwhile, "the next step is to do the genetics and identify the regions of the genome that explain that diversity," he says. **–E.P.**

ERA1 gene in drought conditions. In both lab and field studies, the plants produced significantly more seeds than wild-type canola, they reported in 2005. The work "for the first time showed it was possible to engineer a single gene and have an effect," says Nguyen. Moreover, when water supplies were adequate, the GM canola yields were on par with the non-GM canola, which is key to any drought-tolerant crop's commercial success. Both results have held up through three more years of field studies.

Ultimately, "whether the Performance Plant work will advance drought hardiness is hard to say," says Lewis Lukens, a plant geneticist at the University of Guelph in Canada. But, Huang notes, tests are under way for similarly modified corn and other plants. Several companies are evaluating whether to use Performance Plant technology in their drought-resistant lines.

Control over stomata is also key to a drought-tolerant rice being developed in China. Instead of shutting down a gene, researchers at the National Center for Plant Gene Research in Wuhan cause a different one to be overactive. This gene, called *SNAC1*, enhances the ability of abscisic acid to shut the stomata. Under severe drought conditions, the GM rice produced 22% to 34% more seeds than non-GM rice and produced about the same number of seeds under normal conditions, Lizhong Xiong and colleagues reported in 2006. The rice tested is not one widely grown commercially, and thus the work is a "proof of idea," says Xiong. His team is now generating new transgenic plants from commercial rice varieties.

Meanwhile, in Australia, Molecular Plant Breeding CRC just finished a small field trial in a dry part of Victoria of several transgenic wheat lines designed to withstand drought. Each line contains one of six different genes for drought tolerance derived from maize, *Arabidopsis*, a moss, or a yeast. The company will not reveal the nature of the genes, and the test is just to see if the transgenic lines outperform the control lines under field conditions, says Michael McLean, a spokesperson for Molecular Plant Breeding CRC in Bundoora.

"Clearly, recently we have seen some very promising advances in terms of drought tolerances in crop plants," says Nguyen. "Now it's a question of how to optimize the system." And Tester is also optimistic: Ultimately, "I think there will be a palette of genes from which breeders and crop scientists will select for putting together the drought tolerance for a particular region."

The revolution Kofi Annan called for in 2000 hasn't yet occurred, but the seeds have at least been planted.

–ELIZABETH PENNISI

CREDIT: TINA WAMBACH

Sticky success. Digging asphalt from a seep, researchers recreated samples of Olmec sealant (*inset*).

Following an Asphalt Trail to Ancient Olmec Trade Routes

When archaeologists teach about the Olmec culture, they flash images of massive stone heads, sculpted for a sophisticated elite who ruled the swampy lowlands of Mexico from 1200 to 400 B.C.E. But a poster by archaeologist Carl Wendt of California State University, Fullerton, throws the spotlight on Olmec commoners. Once dismissed as simple maize farmers, the ordinary Olmec apparently mastered a sophisticated technique for making asphalt, crucial to sealing wooden boats, and they traded the valuable substance to others.

This research will shed new light on previously invisible trade routes, says Olmec expert David Grove of the University of Florida, Gainesville. Because Wendt can distinguish asphalt from various sources, Grove notes, the work "adds a significant new 'artifact' [asphalt] to the small list of artifacts that can be used in the study of trade in Mesoamerica at 1000 B.C.E."

Earlier archaeologists paid little attention to asphalt, occasionally noting its presence on sacred figurines, tool handles, and potsherds. But during excavations at the Olmec site of Paso los Ortices, Wendt discovered a pit containing 250 kilograms of asphalt slabs. He wondered how the Olmec processed asphalt, what they used it for, and whether elites controlled its manufacture.

To find out, his team studied thin sections of asphalt lumps from Olmec sites with a petrographic microscope. They noted even patterns of sand particles and impressions of decomposed plants, suggesting that these silica-rich materials were intentionally mixed in during heating to add structure to the asphalt. The team also identified and sampled more than 50 asphalt seepages in the Olmec region.

Then they experimented, adding different plant additives and heating samples in clay pots over fires to produce an asphalt that was both flexible enough to apply to figurines and other objects and yet hard enough to resist melting in the sun. "We had a bear of a time trying to get it to that state," says Wendt. Some samples were simply too watery. But Wendt and his team processed other, stickier samples in just a few hours; they found that the leaves of a plant the local inhabitants use to wrap tamales produced the best asphalt.

The result is a very early example of materials processing, says Philip Arnold, an archaeologist at Loyola University in Chicago, Illinois, and it's "like a culinary art: You have to understand the properties of individual ingredients and how they work together."

Wendt's evidence now suggests that commoners produced their own asphalt, because the seeps were too numerous for easy management by Olmec lords. Moreover, Wendt's studies at the small Olmec site of El Remolino, dated between 1200 and 850 B.C.E., revealed that commoners extensively processed and used asphalt in their households.

But what did they use it for? Other emerging data provide some clues. In January on the Veracruz coast, a team led by Alfredo Delgado Calderón of the Instituto Nacional de Anthropología e Historia, Veracruz, unearthed remains of a 2200-year-old port and two canoes. The wood had rotted away, but the team found a 1- to 8-centimeter-thick asphalt lining that had once sealed the entire interior of the canoes.

Wendt suggests that Olmec commoners processed asphalt primarily to waterproof their boats. That idea fits well with new thinking about the Olmec. For years, archaeologists had agreed that the Olmec economy was founded on maize agriculture, but recent studies reveal that the Olmec situated their villages along rivers and hunted wetland game. "Rivers are their transportation, communication, and trade routes," says Wendt. "So to have effective watercraft is going to be critical."

Wendt is now studying the Olmec trade in asphalt, using chemical analyses to trace samples to their seepage of origin. This "provides a wonderful economic geography that has not been available for Olmec studies," says Arnold. "It helps us to contour the Olmec political economy."

Herring and Nuts for The 'Salmon People'

Archaeologists have long regarded the ancient inhabitants of the northwest coast of North America as the people of the salmon, crediting abundant salmon runs for the rise of large villages and complex societies over the past 6000 years. Moreover, researchers thought that the huge surpluses of dried and smoked salmon brought leisure, spurring rich

Nuts about starch. Ancient northwest coast peoples leached acorns in pits to make them tastier.

CREDITS: (TOP TO BOTTOM) CARL J. WENDT; DALE CROES/SOUTH PUGET SOUND COMMUNITY COLLEGE

Signs of the First Whale Hunters

Europeans who explored the Bering Sea in the 18th century marveled at the daring and prowess of Eskimo whalers, who hunted 90-ton cetaceans from open, skin-covered boats called umiaks, using little more than stone-tipped weapons and sealskin floats. But when and where did this cooperative hunting tradition begin? Clear evidence has been elusive—until now.

At the meeting, Arctic experts gasped audibly as Daniel Odess, curator of archaeology at the University of Alaska Museum in Fairbanks, showed photos of his team's find: a piece of walrus ivory inscribed with several pictures, including two dramatic images of teams of sea hunters in umiaks pursuing whales. The ivory was found in Chukotka, in the northeast corner of the Russian Federation. It was in direct contact with wood radiocarbon-dated to 3000 years ago, making it the oldest known evidence of whaling.

"An actual picture like that is probably the closest thing that we can ever get to direct evidence for whaling," says Christyann Darwent, a zooarchaeologist at the University of California, Davis. "It's an astounding find."

Until now, the earliest evidence for whaling came from 2000-year-old sites on St. Lawrence Island in Alaska. The new find emerges from a site called Un'en'en, perched on the crest of a steep slope overlooking a protected bay in the Bering Sea. "It would have been an excellent lookout for hunters," says Odess. "Today, gray whales come right into the beach there to scratch barnacles off." The project's co-director, archaeologist Sergey Gusev of the Russian Research Institute for Cultural and Natural Heritage, discovered the site in 2005, noting some unusual stone tools, and invited Odess and others to help excavate in 2007.

The team focused on a pit-house measuring at least 45 square meters—large by Arctic standards. They recovered fragments of worked and unworked whale bone, including baleen from two large whale species, most likely gray whale and bowhead. In addition to making tools normally associated with hunting seals, the people of Un'en'en knapped large, heavy-duty blades to tip lances. Many of these had broken, likely from impacts with large and heavy animals. Overall, these artifacts suggest whaling, but they could also reflect simple scavenging of whale carcasses, says Odess.

Then, near the very end of the dig, a Russian crew member found a 50-cm-long piece of incised walrus ivory in situ. The ivory bore traces of what seems to be red ochre and featured pictures of individual animals plus three major narrative scenes. Two of these complex images depicted groups of ancient whalers voyaging at sea in four- and five-passenger umiaks—the earliest known evidence for this skin boat.

It makes sense that whaling arose early in this area, notes archaeologist Owen Mason of GeoArch Alaska in Anchorage. "This is putting it out there that Siberia was the place for early whaling, and that's where the nutrient hot spots [that attracted whales] were," he says.

The third narrative scene portrayed death by violence, with two men attacking a lone individual. Odess suggests that this may depict early warfare in the Arctic, as people began competing for the best whaling places. "If you take a whale, you get literally a ton of food, so you can store it," Odess notes. "But you create the need to stay there and defend it from others. So whaling and warfare certainly are linked together." **–H.P.**

Whaler's art. Two scenes carved in walrus ivory, found overlooking the Bering Sea, are the first evidence of humans hunting whales.

traditions of wood carving, ceremony, and dance. Salmon, in this view, served as the staff of life and the chief driver of cultural development.

But a stream of new studies now complicates this picture. New excavations reveal a surprising dependence on both plant foods and other kinds of seafood. These early Native Americans did eat large quantities of salmon, but some also processed acorns, harvested a potatolike tuber called the wapato, and feasted on cod, halibut, and herring. "People on the northwest coast went after everything that is around," says zooarchaeologist Virginia Butler of Portland State University in Oregon, "but because we've had this salmon view, it's obscured it."

Take plants, for example. A specialized wapato-processing site has recently been unearthed in British Columbia, suggesting a heavy reliance on this starchy tuber. And another source of carbohydrates has turned up at the Sunken Village site along the Lower Columbia River. There, a team led by archaeologist Dale Croes of South Puget Sound Community College in Olympia, Washington, and Akira Matsui of the National Cultural Properties Research Institute in Japan recently mapped 114 shallow pits littered with the remains of Oregon white oak acorns. The team's studies revealed that aquifers at the site regularly flush water through the pits. By simply storing acorns there over winter, ancient people leached the bitter tannins from the nuts, making them more edible. Based on the pit sizes, Croes and colleague Bethany Mathews estimate that people processed as many as 2.5 million acorns at the site each year. "You just don't think of acorns as being a way of making a living here," says Croes. "It's poorly understood that plant foods are a major part of the economies."

As for fish, zooarchaeologist Madonna Moss of the University of Oregon, Eugene, presented new analyses of two sites on Prince of Wales Island in southern Alaska, highlighting the variability in ancient northwest coast fisheries. People did indeed fish salmon at the Coffman Cove Village Site, which is located next to a salmon stream and dates from 5500 to 700 years ago, says Moss; nearly 90% of the fish bone there is salmon. But at a second site, situated just a few hundred meters away and occupied from 2000 to 3000 years ago, cod and its by-catch of rockfish and sculpin accounted for 81% of fish bone through time, compared with only 5% salmon bone. "Studying either site in isolation would give a false impression," says Moss.

Moss suspects that the early islanders prized Pacific cod as a late-winter or early spring fishery. In recent times, local Tlingit families smoked and stored Pacific cod. Moreover, Coffman Cove lay next to an important cod fishing ground, where the topography of the ocean floor forces schools of cod to rise to shallower depths. In southern Alaska, says Moss, salmon is certainly an important resource, "but it's not the whole story."

–HEATHER PRINGLE

Heather Pringle writes about archaeology from Vancouver, Canada.

CREDIT: UN'EN'EN EXCAVATION TEAM

LETTERS

edited by Jennifer Sills

Retraction

IN THE REPORT "DARWINIAN SELECTION ON A SELFING LOCUS" (*1*), WE CONCLUDED THAT A species-wide selective sweep was associated with the rise of selfing in *A. thaliana*. We have reinvestigated the sequence and structure of alleles at the *S* pseudo locus and now find that spurious PCR amplification by the primers and/or by DNA contaminations resulted in our report of the Ψ*SCR1* and Ψ*SCR2/3* sequence from the accessions with haplotype B (CS902 ecotype) and haplotype C (CS1044, CS6751, and CS6764 ecotypes). Instead, haplogroup C either does not have an *SCR* allele, or if it is present it is so divergent as to be undetectable by PCR or Southern blotting. In CS902, which has a haplotype group B at the *S* pseudolocus, we and other groups (*2*) have isolated a distinct and novel *SCR* allele. When these corrections are made to the data, the species-wide nature of the selective sweep can no longer be supported.

We have, however, conducted further experiments and reanalysis to characterize these alleles and resolved discrepancies with previous studies (*2*, *3*). We describe this reanalysis in a paper in the journal *Molecular Ecology* (*4*). In this paper, we report that Ψ*SCR1* and its derivative alleles spread to 94% frequency in a collection of 297 accessions. We conclude that a selective sweep did occur but was confined to European populations of *A. thaliana*, and that selfing appears to have evolved independently within this species. Moreover, our finding of three *SRK* haplotype groups, plus the very low diversity in the Ψ*SCR1* locus in most of the European accessions is still supported. Nevertheless, given that one of our previous conclusions is no longer tenable and in the interests of maintaining the integrity of the scientific literature, we retract the Report. Dr. Purugganan, as the senior author of the paper, takes full responsibility for these genotyping errors and apologizes for any difficulties it may have caused.

P. Awadalla (*1*) did not sign this Retraction because he does not support the interpretation of K.K.S. and M.D.P. above and thereafter (*4*) as sufficient evidence of a European sweep, and he was not involved in any data collection (*1*, *4*). However, he agrees that Shimizu *et al.* (*1*) should be retracted.

KENTARO K. SHIMIZU,[1] JENNIFER M. REININGA,[2]* ANA L. CAICEDO,[3] CHARLOTTE A. MAYS,[4] RICHARD C. MOORE,[5] KENNETH M. OLSEN,[6] STEPHANIE RUZSA,[4] GRAHAM COOP,[7] CARLOS D. BUSTAMANTE,[8] MICHAEL D. PURUGGANAN[9]

[1]Institute of Plant Biology, University of Zurich, Zurich, Switzerland. [2]Institute for Genome Sciences and Policy, Duke University, Durham, NC 27708, USA. [3]Department of Biology, University of Massachusetts, Amherst, MA 01003, USA. [4]Department of Genetics, North Carolina State University, Raleigh, NC 27695, USA. [5]Department of Botany, Miami University, Oxford, OH 45056, USA. [6]Department of Biology, Washington University, St. Louis, MO 63130, USA. [7]Department of Human Genetics, University of Chicago, Chicago, IL 60637, USA. [8]Department of Biological Statistics and Computational Biology, Cornell University, Ithaca, NY 14853, USA. [9]Department of Biology, New York University, New York, NY 10003, USA.

*In the 2004 Report, Jennifer M. Reininga's name was listed as Jennifer M. Cork.

References

1. K. K. Shimizu *et al.*, *Science* **306**, 2081 (2004).
2. C. Tang *et al.*, *Science* **317**, 1070 (2007).
3. S. Sherman-Broyles *et al.*, *Plant Cell* **19**, 94 (2007).
4. K. K. Shimizu, R. Shimizu-Inatsugi, T. Tsuchimatsu, M. D. Purugganan, *Mol. Ecol.* **17**, 704 (2008).

Vegetation's Role in Coastal Protection

WE ARE CONCERNED ABOUT THE ASSERTION in the Report by E. B. Barbier *et al.* that vegetation reduces coastal damage during extreme events ("Coastal ecosystem–based management with nonlinear ecological functions and values," 18 January, p. 321). Although the intended point was that ecosystem services do not linearly scale with habitat size, the conclusions drawn from the chosen example of wave attenuation are speculative. Figure S1, A to F, shows wave attenuation curves that are typical, with or without vegetation on the surface.

CREDIT: JIM REED/CORBIS

Several other recent papers have also argued that vegetation reduces the impact of extreme events such as the Asian tsunami (*1*, *2*) or Hurricane Katrina (*3*, *4*). As in these studies, the evidence collected by Barbier *et al.* is based on correlation or visual description.

In the examples where vegetation appears to have protected the coast, there is no clarification as to the mechanism involved. It has been inductively proven that coastal plants can "engineer" land elevation (topography and bathymetry) through succession, but this is a long-term process that occurs before the event (e.g., the sand dune example in Barbier *et al.*). It has not yet been determined whether vegetation can resist waves over a few meters in height during an extreme event (*5*). Thus, an important question is whether vegetation structure reduces coastal damage directly through wave attenuation or indirectly by altering the geography of the landscape.

The difference has serious management and policy implications. If we emphasize direct structural value, we may end up with coastlines populated with invasive species or anthropogenic structures that kill more people than the waves themselves during extreme

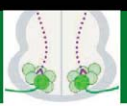

No axon mingling allowed

185

Cells at high resolution

187

events (*6*, *7*). And we still cannot guarantee that the surge (the real killer) or erosion [often enhanced by attenuation (δ)] will be reduced.

RUSTY A. FEAGIN

Spatial Sciences Laboratory, Department of Ecosystem Science and Management, Texas A&M University, College Station, TX 77845, USA, and Fitzwilliam College, University of Cambridge, Cambridge CB3 0DG, UK. E-mail: feaginr@tamu.edu

References

1. F. Danielsen *et al.*, *Science* **310**, 643 (2005).
2. E. B. Barbier, *Front Ecol. Env.* **4**, 124 (2006).
3. R. Costanza, W. J. Mitsch, J. W. Day Jr., *Front. Ecol. Env.* **4**, 465 (2006).
4. J. W. Day Jr. *et al.*, *Science* **315**, 1679 (2007).
5. I. Möller, *Estuarine Coast. Shelf Sci.* **69**, 337 (2006).
6. K. Kathiresan, N. Rajendran, *Estuarine Coast. Shelf Sci.* **65**, 601 (2005).
7. A. M. Kerr, A.H. Baird, *Bioscience* **57**, 102 (2007).
8. I. Möller, T. Spencer, *J. Coast. Res.* **SI36**, 506 (2002).

Response

FEAGIN RAISES AN EXCELLENT QUESTION, but misunderstands our findings on the wave attenuation function of key coastal interface systems. The wave attenuation shown in fig. S1A can be attributed nearly entirely to mangrove vegetation. As we explain in the Report's Supporting Online Material, this figure for attenuation of swells with 5- to 8-s periods on the Vietnam coast is based on a field study of a mangrove swamp with various tree sizes fronted by an intertidal shoal (*1*). Small outer mangroves had almost no effect on wave heights of 0.9 m, but passage through taller, denser mangroves inshore reduced wave height to between 0.05 and 0.1 m. The 90% reduction in wave height, as shown in fig. S1A, occurred across a wide tidal flat (gradient 0.5/1000 m) and is attributed to the extent and structure of the vegetation rather than to topographic changes (*1*). We show similar results for salt marshes, with wave height declining exponentially with the distance that the vegetation extends inland from the shoreline (fig. S1B).

Contrary to Feagin's assertion, we do not argue that the storm protection value of mangroves or any other coastal interface system relies solely on vegetation as a buffer against extreme events such as tsunamis or hurricanes; in fact, we suggest otherwise in our Supporting Online Material. We agree with Feagin that mangroves are unlikely to stop a tsunami wave larger than 6 m, as ecohydrological studies have shown (*2*–*5*). Wave attenuation by mangroves is "qualitatively different" for "large, infrequent disturbances" such as tsunamis, hurricanes (typhoons), and tidal bores, compared with "small, frequent disturbances" such as tropical storms, coastal floods, and tidal waves (*4*). Yet even with respect to extremely large events, such as the 2004 Indian Ocean tsunami, mangroves may act as natural barriers to some degree (*5*).

Finally, the storm protection value of mangroves used in our Report was estimated from 39 economically damaging coastal storm events from 1975 to 2004 affecting one or more of the 21 coastal provinces of Southern Thailand (*6*, *7*). Of these events, only four could be considered extreme storm events: three typhoons and the 2004 Indian Ocean tsunami. Moreover, the frequency of smaller storm events appears to be increasing; between 1975 and 1987, Thailand experienced on average 0.54 coastal natural disasters per year. Between 1987 and 2004, the incidence increased to 1.83 disasters per year (*6*). It is against these small, frequent, and economically damaging events that we are likely to see mangroves and other coastal interface habitats offer the greatest benefit in terms of storm protection, which tends to vary nonlinearly with habitat attributes.

EDWARD B. BARBIER,[1]* EVAMARIA W. KOCH,[2] BRIAN R. SILLIMAN,[3] SALLY D. HACKER,[4] ERIC WOLANSKI,[5] JURGENNE H. PRIMAVERA,[6] ELISE F. GRANEK,[7] STEPHEN POLASKY,[8] SHANKAR ASWANI,[9] LORI A. CRAMER,[10] DAVID M. STOMS,[11] CHRIS J. KENNEDY,[1] DAVID BAEL,[8] CARRIE V. KAPPEL,[12] GERARDO M. E. PERILLO,[13] DENISE J. REED[14]

[1]Department of Economics and Finance, University of Wyoming, Laramie, WY 82071, USA. [2]Horn Point Laboratory, University of Maryland Center for Environmental Science, Cambridge, MD 21613, USA. [3]Department of Zoology, University of Florida, Gainesville, FL 32611, USA. [4]Department of Zoology, 3029 Cordley Hall, Oregon State University, Corvallis, OR 97331, USA. [5]Australian Centre for Tropical Freshwater Research, James Cook University and Australian Institute of Marine Science, Townsville, QLD 4810, Australia. [6]Aquaculture Department, Southeast Asian Fisheries Development Center, Tigbauan, Iloilo 5021, Philippines. [7]Environmental Sciences and Resources, Portland State University, Portland, OR 97207, USA. [8]Department of Applied Economics, University of Minnesota, St. Paul, MN 55108, USA. [9]Department of Anthropology, University of California, Santa Barbara, CA 93106, USA. [10]Department of Sociology, Oregon State University, Corvallis, OR 97331, USA. [11]Bren School of Environmental Science and Management, University of California, Santa Barbara, CA 93106, USA. [12]National Center for Ecological Analysis and Synthesis, University of California, Santa Barbara, CA 93101, USA. [13]CONICET–Instituto Argentino de Oceanografía, Bahía Blanca, Argentina. [14]Department of Earth and Environmental Sciences, University of New Orleans, New Orleans, LA 70148, USA.

*To whom correspondence should be addressed. E-mail: ebarbier@uwyo.edu

References

1. Y. Mazda, M. Magi, M. Kogo, P. N. Hong, *Mangroves Salt Marshes* **1**, 127 (1997).
2. E. Wolanski, in *Coastal Protection in the Aftermath of the Indian Ocean Tsunami. What Role for Forests and Trees?* S. Braatz, S. Fortuna, J. Broadhead, R. Leslie, Eds. (FAO, Bangkok, 2007), pp. 157–179.
3. E. Wolanski, *Estuarine Ecohydrol.* (Elsevier, Amsterdam, 2007).
4. D. Alongi, *Estuarine Coast. Shelf Sci.* **76**, 1 (2008).
5. R. Cochard *et al.*, *Perspect. Plant Ecol. Evol. Syst.* **10**, 2 (2008).
6. E. Barbier, *Econ. Pol.* **22**, 177 (2007).
7. EM-DAT, *EM-DAT: The OFDA/CRED International Disaster Database* (Université Catholique de Louvain, Brussels, 2005); www.emdat.be.

A Quaternary Question

IN THE NEWS FOCUS BY R. A. KERR ("A TIME war over the period we live in," 25 January, p. 402), stratigraphers wish to rid the geological time scale of the Quaternary, on the grounds that "boundaries on the time scale are not delineated by climate changes." How very odd, then, that the end of the Pleistocene—a unit that stratigraphers are happy to keep—is defined by their governing body, the International Commission on Stratigraphy, as "Exactly 10,000 Carbon-14 years BP. Near the end of the Younger Dryas cold spell" (*1*). So, a chronologically arbitrary round number tied to the end of a merely millennium-long cold snap is somehow acceptable as a geological unit, but the climatically bounded Quaternary is not? What am I missing?

DAVID J. MELTZER

Department of Anthropology, Southern Methodist University, Dallas, TX 75275–0336, USA.

Reference

1. www.stratigraphy.org/geowhen/stages/Pleistocene.html

Response

THE INTERNATIONAL UNION FOR QUATERNARY Research (INQUA) Commission on Stratigraphy determined at the 1969 INQUA Congress in Paris that the Holocene should be delineated as "exactly 10,000 Carbon-14 years BP," as correctly stated by Metzer. However, this is not a definition but a duration of a chronostratigraphic unit. A true definition of a chronostratigraphic boundary includes (i) a unique physical point in a stratigraphic section and (ii) supporting criteria by which the boundary can be identified. No

definition was created for the base Holocene at the 1969 INQUA Congress. In fact, little was done regarding this unit for nearly 40 years! A Working Group of the current ICS Subcommission on Stratigraphy (*1*) is in the process of writing a definition of the base Holocene that includes an archived core to serve as the unique physical point, as well as criteria such as values for deuterium excess, $\delta^{18}O$, dust concentration, a range of chemical species, and annual layer thickness. The Report of the Working Group is expected to be completed within 1 to 2 months and circulated for approval. Thus, the base Holocene will soon have a clear definition.

With regard to the "climatically bounded Quaternary," I would point out that the boundary of the Quaternary is currently under discussion by the Quaternary Subcommission on Stratigraphy and the Neogene Subcommission on Stratigraphy (*2*). The latter group prefers that the base Quaternary and base Pleistocene continue to be defined by the physical marker for the base Pleistocene. Quaternarists advocate the lowering of the base Quaternary (and base Pleistocene) to the physical marker of the (upper Pliocene) Gelasian Stage. These issues will be discussed at the International Geological Congress in Oslo in August 2008.

WILLIAM A. BERGGREN

Department of Geology and Geophysics, Woods Hole Oceanographic Institute, Woods Hole, MA 02543, USA.

References and Notes

1. P. Gibbard, *Annual Report of the Subcommission on Quaternary Stratigraphy*, in the *ICS Annual Report for 2007* (www.stratigraphy.org/report07.pdf).
2. Follow link to Global Boundary Stratotype Sections and Points at www.stratigraphy.org/.
3. I thank S. Finney for pointing me in the right direction for an update on the Holocene issue.

Soil Erosion: Data Say C Sink

IN THE LETTER "SOIL EROSION: A CARBON sink or source?" (R. Lal and D. Pimentel, 22 February, p. 1040) and in its Response (K. Van Oost *et al.*, 22 February, p. 1042), the authors note that soil erosion is a serious threat to land health. Nevertheless, evidence points toward a carbon (C) sink term induced by erosion. Mechanistically, accelerated soil erosion reduces the C source term because there is less C to decompose at the eroded site. Although erosion may reduce productivity (as discussed by Lal and Pimentel), any plant production, whether reduced or fertilized, contributes to C uptake (causing a sink), which can be quite high even in nonfertilized settings (*1*). As we attempt to account for transported C and its fate in depositional settings, we must consider larger temporal and spatial scales, whether colluvial (*2*–*4*), impoundment (*4*), or export to the ocean (*5*). This scaling requires careful accounting (*6*, *7*), in part because CO_2 exchange is dominated by large flux terms for plant and microbial processes (*8*) and in part because erosion events are highly episodic in time and discontinuous in space.

Letters to the Editor

Letters (~300 words) discuss material published in *Science* in the previous 3 months or issues of general interest. They can be submitted through the Web (www.submit2science.org) or by regular mail (1200 New York Ave., NW, Washington, DC 20005, USA). Letters are not acknowledged upon receipt, nor are authors generally consulted before publication. Whether published in full or in part, letters are subject to editing for clarity and space.

To make the accounting more tractable, Van Oost *et al.* used baselines in time (1953 from ^{137}Cs) and space (uneroded or unperturbed landscapes). Although Lal and Pimentel claim that the budget does not reflect (i) reduced productivity of eroded lands or (ii) a full accounting of C in transport and redeposition, in fact, the data were grounded with baseline controls that confirmed the sink term noted by other investigators.

Indeed, the relationship between C removed (by erosion) and C replaced (by plant production) suggests that ~25% (of eroded C) was replaced over the 50-year period, although much more C may be fixed by new photosynthate without persisting in soil (*1*). End members for C replacement are particularly interesting: Some soils and their C pools are more resilient to disturbance, perhaps owing to larger nutrient, water, and biotic capacities. Although the study by Van Oost and colleagues concluded that a relatively small C sink (globally ~0.1 Pg C per year) resulted from cropland erosion over recent decades, additional terms for (i) stimulating plant production in depositional areas (*4*) and (ii) including other extensive human-altered landscapes (such as those that are deforested or urbanized) must now be evaluated and are likely to indicate a somewhat larger global C sink from enhanced erosion.

JENNIFER W. HARDEN,[1] ASMERET ASEFAW BERHE,[2] MARGARET TORN,[3] JOHN HARTE,[2] S. LIU,[4] R. F. STALLARD[5]

[1]U.S. Geological Survey, Menlo Park, CA 94025, USA. [2]Division of Ecosystem Sciences, University of California, Berkeley, CA 94720, USA. [3]Lawrence Berkeley National Laboratory, Berkeley, CA 94720, USA. [4]SAIC, contractor to U.S. Geological Survey Earth Resources Observation and Science Center, Sioux Falls, SD 57198, USA. [5]U.S. Geological Survey, Boulder, CO 80303, USA.

References

1. A. A. Berhe, J. Harte, J. W. Harden, M. S. Torn, *BioScience* **57**, 337 (2007).
2. J. W. Harden *et al.*, *Global Biogeochem. Cyc.* **13**, 885 (1999).
3. S. G. Liu, N. Bliss, E. Sundquist, T. G. Huntington, *Global Biogeochem. Cyc.* **17**, 1074 (2003).
4. R. F. Stallard, *Global Biogeochem. Cyc.* **12**, 231 (1998).
5. E. T. Sundquist, *Science* **259**, 934 (1993).
6. J. T. Sanderson, F. S. Chapin, J. W. Harden, J. C. Neff, M. E. Harmon, *Ecol. Appl.* **12**, 937 (2002).
7. F. S. Chapin III *et al.*, *Ecosystems* **9**, 1041 (2005).
8. S. E. Trumbore, *Global Change Biol.* **12**, 141 (2006).

CORRECTIONS AND CLARIFICATIONS

Reports: "Ceramide triggers budding of exosome vesicles into multivesicular endosomes" by K. Trajković *et al.* (29 February, p. 1244). Two papers on ESCRT-independent transport should have been cited on page 1245. The text beginning "the pathway for intraendosomal transport of PLP may be ESCRT-independent" should continue "similar to the transport of Pmel17 into melanosomes" and cite A. C. Theos *et al.*, *Dev. Cell* **10**, 343 (2006). The text beginning "the release of CD63 (with enhanced GFP fusion, EGFP-CD63) was not affected by coexpression with dominant-negative Vps4 (fig. S9)" should continue "as shown previously" and cite Y. Fang *et al.*, *PLoS Biol.* **5**, e158 (2007).

Reports: "The premetazoan ancestry of cadherins" by M. Abedin and N. King (15 February, p. 946). Values in Table 1 for normalized cadherin abundance were changed in error. The correct percentages are as follows: for the choanoflagellate *Mbre*, 0.25; for *Nvec*, 0.26; for *Dmel*, 0.12.

Association Affairs: "Science and technology for sustainable well-being" by J. P. Holdren (25 January, p. 424). In Table 4, the heading reading "Primary energy (terawatt-hours)" should have read "Net electricity (terawatt-hours)." In ref. 73, the positions held by G. Schultz, H. Kissinger, W. Perry, and S. Nunn were incorrectly described. The text should have read "Schultz and Kissinger served as U.S. secretary of state, Perry was secretary of defense, and Nunn was chair of the Senate Armed Services Committee."

ECOLOGY

Return to Natural History

Raphael D. Sagarin

At first glance, *Return to Warden's Grove* appears to be a simple book about a small, relatively unremarkable bird and a relatively unknown scientist in a tiny patch of habitat—all dwarfed by the vast setting of Canada's Northwest Territories. But like the mass-market publisher that reportedly rejected Christopher Norment's manuscript as "yet another 'man goes into nature and gets enlightened' deal," one would be mistaken to underestimate the scope and current importance of this natural history memoir. The life history of the Harris's sparrow (*Zonotrichia querula*) is the framework for a story that, almost by surprise, takes the reader on a grand tour of key themes that define our current juncture in the life sciences.

Norment (a professor of biology and environmental science at SUNY Brockport) is quietly confident in his writing. Readers won't find the gonzo natural history of Robert Sapolsky's uproarious *A Primate's Memoir* (*1*), nor the comically grotesque elaborations of tropical diseases that punctuate Tim Flannery's astounding *Throwim Way Leg* (*2*). But it is because of the understated voice and the near total lack of drama in the focal species that this book works. The construction of the book, as with any good natural history study, wanders along a spiral path that continually returns upon itself, each time with greater insight and broader vision. Norment traces this spiral around Warden's Grove, starting with a youthful expedition to the Northwest Territories, building in three successive field seasons as a graduate student years later, and only reaching its full expansive scope in this complete retelling 16 years after taking his last field notes.

Norment is fascinated with the ecological concept of the ecotone—typically a zone of transition between habitat types. Here, Norment uses ecotones to describe all sorts of transitions: the choice nesting habitats of the sparrows between forest and tundra, the fissure in his personal life between devoted family man and far-afield scientist, and the space between the civilized world and the vast northern wildernesses in which he finds scientific data and personal solace. In constantly deconstructing these different ecotones, Norment ends up building a thoughtful exploration of feeling both drawn to the natural world and pulled away from it by the competing and sometimes self-contradictory demands of science and society.

Return to Warden's Grove
Science, Desire, and the Lives of Sparrows
by Christopher Norment
University of Iowa Press, Iowa City, IA, 2008. 231 pp. $26. ISBN 9781587296338. Iowa Series in Literary Nonfiction.

But Norment also reminds us with an incredible anecdote that these ecotones are anything but fixed boundaries. During his first long northern expedition at Warden's Grove, a Soviet nuclear-powered satellite crashed just a few kilometers from his campsite, and with it came hazmat teams, government agents, and media hordes. The intrusion shattered the ecotone between wild and civilized in Norment's mind, but it seems also to have opened his worldview and challenged him to integrate his views of society with his observations of nature.

In this regard, Norment's account benefited from the decade-and-a-half delay since he finished his fieldwork at Warden's Grove. At the time of his graduate studies, the long-standing split between molecular biology and ecology was in its deepest abyss, and ecology itself had settled into self-satisfied cycling between experimental and theoretical reductionism. The disdain for descriptive natural history was curtly summarized for the author in a job interview question, "What good is your research?"

Harris's sparrow.

Yet even as the question haunted Norment through the years, the answer has been emerging everywhere in biology. Climate change and other large-scale anthropogenic changes are shifting and shattering natural ecotones. This in turn is driving an ecotonal shift in science itself: both the boundaries between branches of sciences and the boundaries between science and other societal pursuits are moving radically or disappearing altogether. The urgency of environmental change is forcing us to reconcile our work on lab benches, computers, and experimental plots with the rapidly changing ecology of the real world around us. At the same time, the undisputable and ubiquitous role of human behavior in this change requires us to examine human social, economic, and political linkages to our work.

All this integration will require balance: of mechanistic hypothesis-testing and unbounded discovery, of small-scale observation and large-scale synthesis, and of quantitative and qualitative understandings of the world. Norment's book, while reflective of earlier forays along these ecotones [such as Ed Ricketts and John Steinbeck's *Sea of Cortez* (*3*)] is a modern field guide to how we might achieve such a balance. Even as he teeters on the edge of metaphysics when discussing an intuitive sense of where to find sparrows' nests, he backs up his speculations by roping a graduate student into an amusing (but scientific) test of his nest-finding sense. And even as he waxes poetically on the idiosyncrasies of the little sparrows and the beauty of their habitat, he ends up producing an impressive scientific understanding of their physiology and ecology. What comes out clearly above all in *Warden's Grove* is the "goodness" of natural history work. We are at a time when we need more than ever solid, thoughtful observation of places far and near and of organisms as complex as humans and as unassuming as Harris's sparrows.

References
1. R. M. Sapolsky, *A Primate's Memoir* (Scribner, New York, 2001).
2. T. F. Flannery, *Throwim Way Leg: Tree-Kangaroos, Possums, and Penis Gourds—On the Track of Unknown Mammals in Wildest New Guinea* (Text, Melbourne, Australia, 1998).
3. J. Steinbeck, E. F. Ricketts, *Sea of Cortez: A Leisurely Journal of Travel and Research…* (Viking, New York, 1941).

The reviewer is at the Marine Science and Conservation Division of the Nicholas School of Earth Sciences and Environment, Duke University, LSRC A207, Research Drive, Durham, NC 27708, USA. E-mail: rds25@duke.edu

10.1126/science.1155994

MATHEMATICS

Connecting the Dots

Stephan Mertens

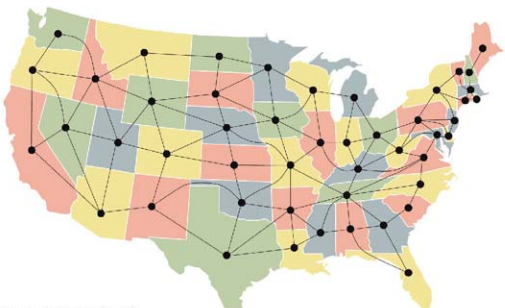

All you need is four (colors).

Networks are everywhere. The highway system, the power grid, and the Internet are networks made of tangible links. The links that form the World Wide Web are not tangible, but clickable. More often, links represent interactions. The metabolic system is woven by all the chemical reactions inside a cell. Various social networks emerge through links among actors that appeared in the same movie, people who are friends, or people who talked to each other on the phone. Some people believe that this "who-called-whom" network could be used to track down another social network: a group of terrorists planning the next attack (*1*).

The reason why almost every system can be described in terms of a network is the almost absurd simplicity of the concept: a network is just a collection of nodes joined by links, a set of dots and lines that we can draw on a sheet of paper. This idea seems to be far too general to teach us anything about complex systems that goes beyond the obvious. Surprisingly, the opposite is true: we can learn a lot by just analyzing dots and lines. Network theory helps to explain many exciting and nontrivial facts about networks, facts that translate back into properties of complex systems. We have all heard about the six degrees of separation. Network theory helps to explain why the Internet can easily cope with failures of nodes and links, but the power grid cannot. It shows how fast rumors or diseases spread in social networks and why the rich get richer. The story of these discoveries has been told in several books (*2*–*4*), but the actual mathematics behind them has received much less attention. That gap has now been filled. In *Nets, Puzzles, and Postmen*, Peter Higgins offers a popular account of the mathematics of networks. Readers willing to expose themselves to mathematical reasoning will find themselves rewarded with numerous insights into the structure of networks.

Nets, Puzzles, and Postmen
An Exploration of Mathematical Connections
by Peter M. Higgins
Oxford University Press, Oxford, 2007. 255 pp. $29.95, £15.99. ISBN 9780199218424.

Here is a brief example. In every network, there are at least two nodes that have the same number of links. Translated to a social network, this means that at any party there will be two people with the same number of friends at the gathering. For a proof of this fact, party style, suppose that there are n guests at the party. The number of friends that a guest can have at the party ranges from 0 to $n-1$. Label n martini glasses with these numbers, and ask each guest to put an olive in the glass that represents the number of his or her friends. Now there are n olives and n glasses. Glass $n-1$ will contain an olive only if there is a guest X who is a friend of everybody else. In this case, glass 0 must be empty, because everybody is friends with X. If, on the other hand, someone put an olive in glass 0, there can't be anyone who is friends with everybody, and glass $n-1$ must be empty. In effect, there are only $n-1$ glasses for n olives, so at least one glass will contain more than one olive. The guests who put their olives in this glass have the same number of friends. QED.

The book rarely gets more complicated than this, even when Higgins (a mathematician at the University of Essex) explains quite sophisticated facts about networks. Among my favorites is his discussion of the four-color theorem. The theorem posits that four colors are enough to color any map in a way that no two adjacent countries receive the same color. The proof of the theorem in 1976 made headlines not only because it settled an old and famous problem but because it was the first mathematical proof that made extensive use of a computer (*5*). Unfortunately, the computerized proof fails to provide the insight of why the theorem is actually true. However, the fact that five colors are always sufficient can be proven in a classical and revealing way. Higgins carefully leads the reader through that proof, from planar networks over Euler's formula to Kempe's compelling discharging argument. I also enjoyed the author's exposition of how to turn a two-way traffic system into a one-way setup and still be able to get from anywhere to anywhere else.

The list of surprising properties of networks Higgins presents is long. Readers will find their own favorites, whether they are more into puzzles such as sudoku and "instant insanity" or prefer real-world applications such as reassembling RNA chains and optimizing the flow through a pipeline system. After finishing *Nets, Puzzles, and Postmen*, the odds are the reader will want to know even more about networks. In that case, I recommend Richard Trudeau's little book (*6*), which nicely bridges the gap between Higgins's mathematical exploration and a full-blown textbook.

References

1. B. Hayes, *Am. Sci.* **94**, 401 (2006).
2. A.-L. Barabasi, *Linked: The New Science of Networks* (Perseus, Cambridge, MA, 2002).
3. M. Buchanan, *Nexus: Small Worlds and the Groundbreaking Science of Networks* (Norton, New York, 2002).
4. D. J. Watts, *Six Degrees: The Science of a Connected Age* (Norton, New York, 2003).
5. R. J. Wilson, *Four Colors Suffice: How the Map Problem Was Solved* (Princeton Univ. Press, Princeton, NJ, 2002).
6. R. J. Trudeau, *Introduction to Graph Theory* (Dover, New York, 1993).

10.1126/science.1154162

The reviewer is at the Santa Fe Institute and the Institut für Theoretische Physik, Otto von Guericke University, 39106 Magdeburg, Germany. E-mail: mertens@ovgu.de

CREDIT: STEPHAN MERTENS

SCIENCE AND GOVERNMENT

Science and the Candidates

The U.S. science community has converged at record speed with the unified goal of raising the profile of science in our national dialogue.

Sheril R. Kirshenbaum,[1]* Chris Mooney,[2] Shawn Lawrence Otto,[3] Matthew Chapman,[4] Austin Dacey,[5] Rush Holt,[6] Lawrence Krauss[7]

In just a few months, many in the U.S. science and engineering establishment, along with members of the business community and journalism world, have joined the ScienceDebate2008 initiative (*1*), a collective call for the U.S. presidential candidates to engage in a public debate on science and technology policy. The need for such a debate could not be more obvious; on issues ranging from the environment to medicine and health, reliable scientific information is fundamental to good policy-making (*2*). At the same time, scientific research and technological innovations fuel economic growth and ensure national competitiveness (*3*). It has been widely argued that climate change and economic competitiveness as they relate to science and technology are among the most critical challenges facing the United States (*3*, *4*). However, we rarely hear any detailed discussion of these issues from the presidential candidates.

The extraordinary speed at which ScienceDebate2008 became a national cause célèbre demonstrates that the U.S. scientific establishment can be quickly organized when motivated. Within weeks, the National Academy of Sciences, the National Academy of Engineering, the Institute of Medicine, the American Association for the Advancement of Science, the Council on Competitiveness, dozens of Nobel laureates and presidents of major universities, former presidential science advisers, and thousands of distinguished scientists, engineers, and concerned citizens joined the effort. We see this as strong evidence that the U.S. science community has been yearning for a stronger voice during an administration that has been repeatedly criticized by scientists (*5*).

Among the motivations we have heard for taking up this cause are the following: continuing inaccurate media coverage, poor science education, widespread public science illiteracy (*6*), flat funding and/or cutbacks to research funding and consequent contraction of opportunity, lack of credible public policy response to climate change and other environmental issues, and governmental suppression of science information. In a climate of declining support for science, the United States risks losing its competitive advantage to emerging science superpowers. Although science and engineering have been responsible for half of U.S. economic growth over the past half-century (*3*), by 2010, according to some estimates, 90% of all scientists and engineers will live in Asia (*7*).

Our economy depends on the ability to innovate, these supporters argue, which in turn relies on a strong foundation of government investment in research and education, yet such federal investments are shrinking as a share of the U.S. economy (*8*). Concurrently, nations such as China and South Korea are boosting governmental support of research by 10% or more annually. At the same time, the absent U.S. response to the overwhelming conclusions of the Intergovernmental Panel on Climate Change (IPCC) has caused widespread concern over continued planetary viability. U.S. science has continually found itself frustrated by developments at the intersection with politics and society and now appears ready—as demonstrated by the response to this initiative—for a far greater investment of resources in public outreach.

ScienceDebate2008 might not have emerged if not for the collective efforts of individuals largely outside of science. Two screenwriters, a journalist, a philosopher, and two scientists built a bipartisan coalition of leaders in government, in academia, and among journalists and the religious and business establishments. The initial announcement came not from the major media (which initially paid little attention), but rather via the organization of a large coalition of science bloggers and other Web-based forums, such as the launch of a page on Facebook.com, coupled with a robust Web presence that tracks daily progress. At a time when scientists are greatly dissatisfied with increasingly fragmented media and their moribund treatment of science (*9*), "netroots" efforts provide a new means of outreach. Future initiatives to bring science into a closer relationship with society and the public may benefit from a similar approach.

A science debate among presidential candidates has not yet occurred. There are several dates when such a debate could take place; as of this writing, none have been agreed to by the candidates. After a decade of what could be seen as antiscience in our nation's public discourse, and in a mainstream media culture more suited to sound bites than paragraphs, politicians are understandably reluctant to engage. But that reluctance is the very reason for this effort and for similar efforts. In an increasingly scientific world, science will become ever more intertwined with policy issues. Scientists must embrace every opportunity to engage in broader public discourse as ambassadors, popularizers, inspirers, educators, and, especially, policy-makers.

Our primary mission, to raise the profile of science in our national dialogue and in the minds of policy-makers and the public, remains. The effort has made the candidates aware of how critical science policy issues are in our global society whether they show the courage to debate them or not, and their response to this initiative will be on record and will form a basis for future development. Looking ahead, the science debate initiative may provide a means of injecting science into political discourse in the next cycle of congressional races and the presidential race of 2012.

[1]Nicholas Institute for Environmental Policy Solutions, Duke University, Durham, NC 27708, USA. [2]Contributing Editor, *Science Progress*, Washington, DC 20005, USA. [3]Chief Executive Officer, ScienceDebate2008. [4]President, ScienceDebate2008. [5]Center for Inquiry, Amherst, NY 14228, USA. [6]U.S. Congressman (D–NJ), House of Representatives, Washington, DC 20515, USA. [7]Director, Center for Education and Research in Cosmology and Astrophysics, Case Western Reserve University, Cleveland, OH 44106, USA.

*Author for correspondence. E-mail: sheril.kirshenbaum@duke.edu

References

1. Science Debate 2008, www.sciencedebate2008.com/.
2. C. Mooney, "Dr. President," *Seed*, posted 23 October 2007.
3. National Academy of Sciences, National Academy of Engineering, Institute of Medicine, *Rising Above the Gathering Storm: Energizing and Employing America for a Brighter Economic Future* (National Academies Press, Washington, DC, 2005).
4. IPCC, Fourth Assessment Report, Climate Change 2007: Synthesis Report; available at www.ipcc.ch/ipccreports/ar4-syr.htm.
5. S. Shulman *et al.*, *Scientific Integrity in Policymaking: An Investigation into the Bush Administration's Misuse of Science* (Union of Concerned Scientists, Cambridge, MA, 2004).
6. P. Tulip, G. Wurzburg, "Primary and secondary education in the United States" (Economics Department Working Paper No. 585, Organization for Economic Cooperation and Development, Paris, 2007).
7. Business Roundtable, *Tapping America's Potential: The Education for Innovation Initiative* (Business Roundtable, Washington, DC, 2005).
8. National Science Foundation, NSF Funding by Directorate, FY 1998–2007; www.nsf.gov.
9. M. C. Nisbet, C. Mooney, *Science* **316**, 56 (2007).

10.1126/science.1158281

NEUROSCIENCE

Refreshing Connections

The exchange of desensitized glutamate receptors with unoccupied ones can counteract the effects of desensitization at the synapse.

R. Angus Silver and Roby T. Kanichay

There are approximately 10^{11} neurons in the human brain, which communicate rapidly via ~10^{14} specialized connections called synapses. The strength of a synaptic connection depends on its prior activity. This plasticity occurs over a wide range of time scales—from milliseconds to months or even years—and is thought to form the basis of information processing and storage in the brain. On page 201 of this issue, Heine *et al.* (*1*) present a conceptually new mechanism that can shape plasticity on a millisecond time scale, changing our view of synaptic dynamics.

Excitatory neurons communicate by releasing the neurotransmitter glutamate from vesicles on the presynaptic side and activating AMPA receptors in the postsynaptic density (a specialized region of the postsynaptic membrane, opposite the glutamate release site, where receptors are clustered). The resulting excitation of the postsynaptic neuron is integrated with signals from other neurons and can cause the postsynaptic neuron to fire action potentials, which triggers neurotransmitter release onto downstream neurons. Short-term depression of the synaptic response reduces the strength of a connection in a frequency-dependent manner and acts as a low-pass filter to sustained signals, yet it conveys relative changes in firing rate independent of the absolute input rate (*2*). Short-term depression arises predominantly from presynaptic depletion of vesicles (*3*) and reduced responsiveness of AMPA receptors following exposure to glutamate (desensitization) (*4*, *5*). Heine *et al.* propose that AMPA receptors move within the postsynaptic membrane so rapidly that desensitized synaptic receptors exchange with unoccupied receptors located outside the synapse in tens of milliseconds, refreshing the sensitivity of the postsynaptic density to glutamate.

To investigate the effects of AMPA receptor diffusion on short-term depression, Heine *et al.* measured the movement of single AMPA receptors in cultured neurons by labeling them with quantum dots (fluorescent nanocrystals of semiconductor material). They then examined the effects of reducing receptor mobility on evoked excitatory postsynaptic currents (EPSCs) in synaptically connected pairs of neurons. Short-term plasticity was assayed from the relative amplitude of the second of two successive EPSCs. Cross-linking AMPA receptors with a specific antibody reduced the amplitude of the second EPSC, indicating that reduced receptor mobility increases short-term depression.

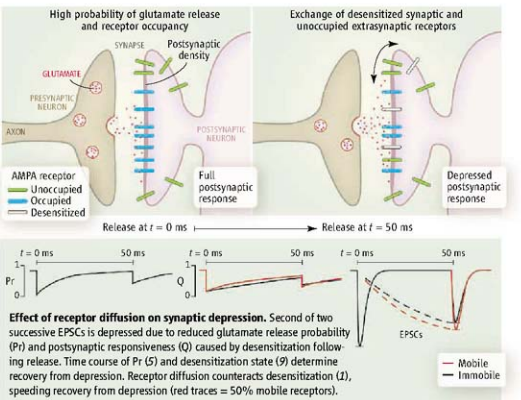

Effect of receptor diffusion on synaptic depression. Second of two successive EPSCs is depressed due to reduced glutamate release probability (Pr) and postsynaptic responsiveness (Q) caused by desensitization following release. Time course of Pr (*5*) and desensitization state (*9*) determine recovery from depression. Receptor diffusion counteracts desensitization (*1*), speeding recovery from depression (red traces = 50% mobile receptors).

Because it is difficult to disentangle the pre- and postsynaptic components of short-term depression (see the figure), the authors used various methods to activate postsynaptic AMPA receptors directly. Cross-linking increased the depression when AMPA receptors were activated by local application of glutamate through iontophoresis and, to a lesser extent, by "uncaging" of glutamate with two-photon laser photolysis. Interestingly, synaptically induced calcium influx into the postsynaptic neuron reduced receptor mobility and increased depression of iontophoretically activated currents, suggesting that AMPA receptor exchange can be regulated by synaptic activity. Mathematical modeling shows that receptor diffusion is sufficiently fast to refresh the postsynaptic density during receptor desensitization, with effects largest at small synapses containing a large fraction of mobile receptors. These results suggest that the number of receptors in the postsynaptic density fluctuates, but the contribution to EPSC amplitude variability will be small relative to stochastic vesicular release (*6*).

To understand how receptor diffusion affects synaptic transmission, both pre- and postsynaptic mechanisms must be considered. For receptor desensitization to affect short-term plasticity, glutamate release must occur at the same synaptic contacts in quick succession. If the probability of releasing glutamate at a synaptic contact is intermediate (50%), only half the contacts activated by a second presynaptic action potential will have been exposed to glutamate following the first. AMPA receptors are not usually saturated by glutamate (*7*, *8*) and onset of desensitization is usually slow (*9*) compared to the brief presence of glutamate (*10*). Hence, only a fraction (<50%) of receptors will desensitize at these synapses. The expected reduction in postsynaptic sensitivity due to desensitization is therefore 25% and falls to 10% after 50 ms as desensitization recovers with a time constant of 30 to 60 ms (*9*). Given the exchange fraction at 50 ms (*1*), receptor diffusion rescues ~30% of the desensitized component (3% of the cur-

Department of Neuroscience, Physiology and Pharmacology, University College London, Gower Street, London WC1E 6BT, UK. E-mail: a.silver@ucl.ac.uk

CREDIT: ADAPTED FROM R. ANGUS SILVER

rent). These back-of-the-envelope calculations suggest that receptor diffusion will have little effect at synapses with low to intermediate release probabilities and receptor occupancies.

The larger effects of AMPA receptor diffusion on short-term depression observed by Heine *et al.* could arise from higher receptor occupancies due to glutamate release from multiple vesicles per contact, a higher fraction of mobile receptors, and/or slower recovery from desensitization at the synapse. In general, larger effects of receptor diffusion will occur at synapses where a large fraction of receptors desensitize, as expected for connections with high release probabilities and receptor occupancies (see the figure). Receptor diffusion could explain the lack of desensitization at such synapses (e.g., at the climbing fiber synapse) (*6*). Desensitization is prominent where the presence of glutamate in the synapse is prolonged (*4*, *11*) and where strongly desensitizing AMPA receptors are expressed (*12*). However, counteracting desensitization with diffusion also requires abundant extrasynaptic AMPA receptors, which are not present in all neurons (*8*, *11*).

Although further studies are required to determine the contribution of rapid AMPA receptor diffusion to short-term depression at different synapses in the brain, the present study changes our concept of the postsynaptic density, from an array of receptors that is fixed on a time scale of minutes, to a highly dynamic structure with the potential to rapidly refresh itself from the surrounding sea of extrasynaptic receptors.

References and Notes

1. M. Heine *et al.*, *Science* **320**, 201 (2008).
2. L. F. Abbott *et al.*, *Science* **275**, 220 (1997).
3. W. J. Betz, *J. Physiol.* **206**, 629 (1970).
4. L. O. Trussell, G. D. Fischbach, *Neuron* **3**, 209 (1989).
5. C. Saviane, R. A. Silver, *Nature* **439**, 983 (2006).
6. R. A. Silver *et al.*, *J. Physiol. (London)* **510**, 881 (1998).
7. G. Liu *et al.*, *Neuron* **22**, 395 (1999).
8. D. A. DiGregorio *et al.*, *J. Neurosci.* **27**, 8344 (2007).
9. D. Colquhoun *et al.*, *J. Physiol.* **458**, 261 (1992).
10. J. D. Clements, *Trends Neurosci.* **19**, 163 (1996).
11. D. A. DiGregorio *et al.*, *Neuron* **35**, 521 (2002).
12. J. Mosbacher *et al.*, *Science* **266**, 1059 (1994).
13. We thank the Silver lab, M. Farrant, and D. Attwell for comments. R.A.S. holds a Wellcome Trust Senior Research Fellowship. R.T.K. is supported by the Wellcome Trust Neuroscience Graduate Program.

10.1126/science.1157589

GEOCHEMISTRY

Toward New Uses for Hematite

New results suggest how the photocatalytic performance of hematite may be improved.

Carrick M. Eggleston

The iron mineral hematite (see the figure) is common on Earth and has also been found on Mars (*1*). It acts as an adsorbent for natural and contaminant aqueous solutes in soils and sediments, is important in the redox cycling of iron and other metals, and acts as a respiratory electron acceptor for metal-reducing bacteria that may stem from early in the history of life (*2*). Hematite is also probably the cheapest semiconductor that absorbs substantial amounts of visible light, and is therefore a candidate component of inexpensive "artificial photosynthesis" systems for generating chemical fuels from sunlight (*3*). The results reported by Yanina and Rosso on page 218 of this issue (*4*) may bring these applications a step closer to reality.

Until recently, studies of hematite photocatalysis have given little cause for optimism. Hematite can use light energy to oxidize water, but does so inefficiently. In semiconductors like hematite, a gap exists between the valence band (electronic states occupied by electrons) and the conduction band (unoccupied electronic states). This gap normally contains no electronic states. When hematite absorbs light, electrons are elevated in energy from the valence band to the conduction band, leaving behind holes (electron vacancies) in the valence band that can move to surfaces and oxidize water. These holes are often filled

Hematite gets down to work. Hematite (α-Fe_2O_3) is a natural mineral found on Earth and other planets; the specimen shown here is from Ouro Preto, Brazil. Results by Yanina and Rosso suggest ways in which the mineral may be used in photocatalytic applications.

before they can oxidize water. The electrons that fill the holes come from a poorly understood electronic state at an energy within the gap (an "intragap" state) (*5*).

Yanina and Rosso now show that hematite crystals—in the form of plates with narrow "edge" surfaces and larger "basal" surfaces—can, by means of conduction through the solid, reductively dissolve on edge surfaces while simultaneously oxidizing Fe^{2+} that interacts with basal surfaces so that the basal surfaces grow. Different crystal faces have different potentials at a given pH, which cretaes potential gradients within the crystal that can drive conduction from one crystal face to another. Their results are relevant to electrical processes in both natural and synthetic crystals generally and suggest, in particular, that the intragap state might be associated with the edge surfaces of hematite. This is important because surfaces can be modified, whereas states inherent only to the bulk structure could form an insurmountable obstacle to improving the photocatalytic efficiency of hematite.

Crystals will take advantage of any available kinetic pathway to evolve toward an equilibrium shape, and Yanina and Rosso have demonstrated one such pathway. Synthesis procedures already exist, however, for making hematite particles in spindles versus platelets by modifying surfaces with adsorbed molecules (*6*). Electric fields have also previously been observed in anisotropic solids (*7*). Earlier studies of hematite (*8*) noted dark currents and open-circuit potentials that were attributed to electrode corrosion. Yanina and Rosso show where this corrosion reaction probably happens. More important, they put many of these disparate pieces together to form a coherent picture of internal electrical currents between surfaces through conductive solids.

To discuss why their result is important for enhancing hematite photocatalysis, we take a closer look at the potentials reported by Yanina and Rosso for different hematite surfaces. The reported potentials do not coincide with either the valence or the conduction

Department of Geology and Geophysics, University of Wyoming, Laramie, WY 82071, USA. E-mail: carrick@uwyo.edu

CREDIT: WALTER GEIBESPIELER/CORBIS

bands, but instead bracket the range of potentials reported for the intragap state (*5*). Only when sufficient electrons are available from aqueous solutes do the basal surfaces reach the more negative potential characteristic of the hematite conduction band.

Under these circumstances, one would expect the basal surface to reductively dissolve. Yanina and Rosso show that this is true only if the basal surface is the only one exposed to solution. When both basal and edge surface are exposed to solution, the basal surface does not reductively dissolve but instead oxidizes aqueous Fe^{2+}. Reductive dissolution takes place at edge surfaces, not basal surfaces. Possible interpretations are that a state within bulk hematite—such as the intragap state—acts as an oxidant for basal surfaces and as a reductant for edge surfaces, or that the edge surfaces act directly as an oxidant for species at basal surfaces. Yanina and Rosso's result forces us to include the second interpretation among the possibilities.

Objections will be raised to the second interpretation because the intragap state is thought to be a bulk phenomenon, not a surface state (*5*). However, the two interpretations need not be mutually exclusive. Yanina and Rosso point out significant differences between hydroxyls on edge surfaces as compared to basal surfaces. Hematite crystals generally contain some hydroxyl as an impurity, and hydroxyl defects within hematite crystals may have similar electronic properties to hydroxyls on edge surfaces. If so, then the way is open to synthesizing hematites without an intragap state to limit photocatalytic efficiency. Bulk hydroxyl defects can be minimized using scrupulously dry synthesis techniques, and edge surfaces can be modified using a suitable adsorbate to create surface states at more negative potentials than those of unmodified edge surfaces.

More work will be needed to see whether edge surface modifications improve hematite photocatalytic efficiency, but recent results are encouraging. Kay *et al.* have reported a new efficiency benchmark for photocatalytic water splitting by hematite (*9*) using nanocrystalline hematite films made by chemical vapor deposition (a nonaqueous process presumably resulting in low water content) and with a preferred orientation exposing edge surfaces to light. As for surface modification, Wang *et al.* have shown that photocurrents for hematite coated with $SrTiO_3$ are much higher than for hematite or $SrTiO_3$ alone (*10*). Maybe we can make hematite work for us after all.

References

1. S. W. Squyres *et al.*, *Science* **306**, 1709 (2004).
2. M. Vargas *et al.*, *Nature* **395**, 65 (1998).
3. M. Grätzel, *Nature* **414**, 338 (2001).
4. S. V. Yanina, K. M. Rosso, *Science* **320**, 218 (2008).
5. G. Horowitz, *J. Electroanal. Chem.* **159**, 421 (1983).
6. N. Galvez *et al.*, *Clays Clay Min.* **47**, 304 (1999).
7. L. Y. Liu, C. Warde, *IEEE Trans. Electr. Dev.* **33**, 1593 (1986).
8. R. Shinar, J. H. Kennedy, *J. Electrochem. Soc. Electrochem. Sci. Technol.* **130**, 392 (1983).
9. A. Kay *et al.*, *J. Am. Chem. Soc.* **128**, 15714 (2006).
10. Y. Wang *et al.*, *J. Phys. D Appl. Phys.* **40**, 3925 (2007).

10.1126/science.1157189

NEUROSCIENCE

Axons Seek Neighborly Advice

Cell contact-dependent communication between adjacent motor and sensory neurons prevents miswiring of developing neural circuits.

Keith K. Murai[1]* and Elena B. Pasquale[2]*

Coordinating motor and sensory pathways in the nervous system ensures efficient execution of bodily movements. Motor neurons in the spinal cord extend axons that drive muscle contraction in the periphery. Sensory neurons (in dorsal root ganglia) adjacent to the spinal cord send feedback to the motor neurons about muscle position/stretch, touch, and pain. Anatomical coupling of the two pathways begins as axons from motor and sensory neurons join paths near the spinal cord and project together in related, but distinct, bundles on their way to muscle and dermis. Despite the known precision of sensory-motor connectivity, the mechanisms yielding this organization have remained unclear. On page 233 of this issue of *Science*, Gallarda *et al.* (*1*) report that subpopulations of motor and sensory axons directly communicate with each other to prevent a biological short-circuit of this system.

Classical tracing and transplantation studies have shown that motor and sensory neurons exhibit closely associated projection patterns and can influence each other's outgrowth (*2*–*4*), but direct molecular evidence for their reciprocal communication during development has been lacking. Using advanced mouse genetics, Gallarda *et al.* simultaneously illuminated these pathways by expressing marker proteins. They observed that late-developing motor axons projecting to muscles of the trunk develop in close proximity to axons of sensory neurons from the dorsal root ganglia. Even at initial phases of growth, axial motor and sensory axons avoid each other before fully segregating within the same nerve. Interestingly, axons from axial motor neuron explants and sensory neuron explants refuse to intermingle, thus recapitulating their behavior in vivo. Moreover, motor neuron growth cones (the leading tips of axons) collapse on contact with sensory axons. These results suggest that molecular recognition events prevent inappropriate mixing of axons during development.

Among the factors that can mediate this type of recognition are the ephrins and Eph receptors, cell surface-associated ligands and receptors whose interaction at sites of cell-cell contact facilitates intercellular communication (*5*). In general, these two protein families guide axons to their targets by enabling growth cones to communicate with surrounding cells. In the peripheral motor system, EphA4 signaling ensures proper pathway selection of motor axons to the limb (*6*–*8*). Compartmentalized Eph receptor expression within developing nerves, such as EphA4 in spinal nerves and EphB2 in the optic nerve of the chick embryo (*9*, *10*), suggests that these proteins play an additional role in separating axon populations. However, their involvement in axon segregation has not been demonstrated.

Gallarda *et al.* analyzed the projections of axial motor and sensory neurons in mice lacking EphA3 and EphA4 and discovered that these receptors control the repulsion of axial motor axons from neighboring ephrin-A–expressing sensory axons. This repulsive signaling not only inhibits the intermingling of motor and sensory axons, but also blocks motor axons from projecting in the wrong direction along sensory axons and infiltrating the dorsal root ganglia (see the figure). Ultimately, these EphA-mediated guidance events

[1]Centre for Research in Neuroscience, Department of Neurology and Neurosurgery, McGill University Health Centre, Montreal General Hospital, 1650 Cedar Avenue, Montreal, QC H3G 1A4, Canada. [2]Burnham Institute for Medical Research, La Jolla, CA 92037; and Pathology Department, University of California at San Diego, La Jolla, CA 92093, USA.

*To whom correspondence should be addressed. E-mail: keith.murai@mcgill.ca; elenap@burnham.org

prevent axial motor axons from contaminating the physiology of the sensory system.

Remarkably, sensory axons serve as a developing barrier that constrains the growth of axons from axial motor neurons. However, EphA3 and EphA4 signaling is just part of the story, because loss of these receptors only influences the development of late-forming axial motor axons, whereas the initial organization of sensory and nonaxial motor axons is unaffected. Furthermore, the cues that separate axon populations proximal to the spinal cord are likely different from those in the periphery. Hence, the work of Gallarda *et al.* highlights the molecular complexity of the nervous system, where axon pathway selection within nerves depends on multiple cues operating in different anatomical regions. As proposed for the olfactory system, sensory and motor axon segregation may be controlled by the combinatorial activities of adhesion molecules and repulsive molecules differentially expressed in discrete axon subpopulations (*11*).

Many questions still remain to be answered. It is known that target-derived factors coordinate genetic programs that control selective sensory input onto motor neurons (*12*, *13*). However, the programs that initiate the cooperative growth of motor and sensory pathways are mostly unknown. Several aspects of Eph function in sensory-motor circuit development also require attention. For example, the function of ephrin-A's that are expressed with EphA receptors on motor axons needs to be addressed (*1*, *8*, *14*, *15*). It will also be important to clarify the relative contribution of ephrin-A's on sensory axons versus those in the surrounding mesenchyme in guiding axial motor neurons. This may help explain discrepancies with previous findings showing that axial motor axons are attracted to ephrin-A5 in the surrounding mesenchyme of the chick embryo (*7*). Species-related differences in downstream signaling molecules that mediate EphA repulsive signals, such as Ephexins, may account for these different observations (*16*). The contribution of other Eph receptors and ephrins in generating the sensory-motor circuit also awaits investigation. Finally, it will be important to know whether insufficient or improper use of Eph-dependent mechanisms leads to altered neural connectivity after nervous system injury. Findings such as those presented by Gallarda *et al.* will continue to guide our understanding of developmental and remodeling events that control neural circuit assembly and function.

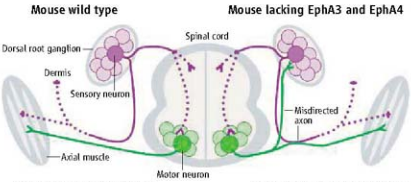

Cooperative motor-sensory axon guidance. Axons from axial motor neurons project away from the spinal cord and establish an aligned, but segregated, relation with sensory neuron axons along their path to muscle and dermal targets. However, axial motor axons from mice that do not have the EphA3 and EphA4 receptors lack repulsion from sensory axons near the spinal cord and inappropriately invade dorsal root ganglia.

References

1. B. W. Gallarda *et al.*, *Science* **320**, 233 (2008).
2. L. Landmesser, *J. Physiol.* **284**, 391 (1978).
3. M. G. Honig *et al.*, *Development* **125**, 995 (1998).
4. L. Landmesser, M. G. Honig, *Dev. Biol.* **118**, 511 (1986).
5. L. Luo, J. G. Flanagan, *Neuron* **56**, 284 (2007).
6. F. Helmbacher *et al.*, *Development* **127**, 3313 (2000).
7. A. Kania, T. M. Jessell, *Neuron* **38**, 581 (2003).
8. J. Eberhart *et al.*, *J. Neurosci.* **24**, 1070 (2004).
9. C. Soans *et al.*, *Oncogene* **9**, 3353 (1994).
10. J. A. Holash, E. B. Pasquale, *Dev. Biol.* **172**, 683 (1995).
11. S. Serizawa *et al.*, *Cell* **127**, 1057 (2006).
12. S. Arber *et al.*, *Cell* **101**, 485 (2000).
13. J. H. Lin *et al.*, *Cell* **95**, 393 (1998).
14. H. Iwamasa *et al.*, *Dev. Growth Differ.* **41**, 685 (1999).
15. T. Marquardt *et al.*, *Cell* **121**, 127 (2005).
16. M. Sahin *et al.*, *Neuron* **46**, 191 (2005).

10.1126/science.1157605

BIOCHEMISTRY

Anatomy of a Fungal Polyketide Synthase

Cutting a fungal polyketide synthase into pieces reveals the function of all its catalytic domains.

Kira J. Weissman

Fungi are among nature's most proficient chemical factories, churning out valuable medicines, including the antibiotic penicillin and the cholesterol-lowering statins. Other fungal products, such as the potent carcinogen aflatoxin B1, are less benign. Many of these diverse compounds are polyketides, constructed by enzymes called polyketide synthases from a small set of building blocks. In fungal polyketide synthases, several catalytic domains are joined together like beads on a string (see the figure, bottom panel); the number of domains determines the complexity of the final structure. On page 243 of this issue, Crawford *et al.* (*1*) meticulously dissect the aflatoxin B1 polyketide synthase of *Aspergillus parasiticus*, elucidating the function of each catalytic site.

Aflatoxin B1 is an oxidation product of the much simpler molecule norsolorinic acid (NSA) (see the figure) (*2*). NSA is built by joining one unit of hexanoate to seven units of acetate (the decarboxylation product of malonate). The resulting polyketide chain is zipped up to form a series of three adjoining rings with a hexanoate tail. All catalytic sites required to construct NSA are present in a polyketide synthase called PksA, but some 15 additional steps are needed to transform NSA to aflatoxin B1 (*3*).

Sequence analysis of PksA and related "nonreducing" polyketide synthases from other fungi (*4*) readily identifies specific regions to link building blocks [ketosynthase (KS)], recruit malonate units [malonyl-CoA:acyl carrier protein transacylase (MAT)], and release the final product [thioesterase/cyclase (TE/CLC)] (*5*). The location of the acyl carrier protein (ACP), which serves as the attachment point for intermediates, is also evident. However, no obvious candidates turn up for selecting hexanoate and for driving cyclization.

Attempts to analyze fungal PKS machinery have been hampered by the giant size and complexity of the proteins. Working on the

Department of Pharmaceutical Biotechnology, Saarland University, 60041 Saarbrücken, Germany. E-mail: k.weissman@mx.uni-saarland.de

CREDIT: KEITH A. HUBA

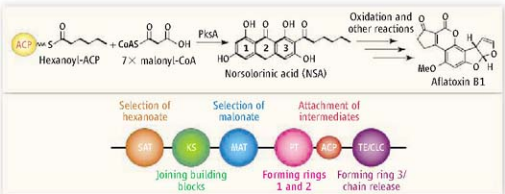

Assembly line. The polyketide synthase PksA builds NSA from one unit of hexanoate (from hexanoyl–ACP) and seven units of malonate (from malonyl–CoA). NSA is then transformed into the carcinogen aflatoxin B1 by a series of oxidative reactions (**top**). Crawford *et al.* have determined the function of all domains within PksA (**bottom**).

assumption that the domains were once discrete proteins that became linked together during evolution, several groups have tried to cut fungal polyketide synthases into more manageable pieces. A simple approach (*6*, *7*) has been to assume that sequences not present in similar, discrete enzymes are linker regions and that the remaining sequences are the domains. In vitro studies of the MAT and ACP domains from PksA obtained by this method confirmed their expected activities (*6*).

However, the Udwary-Merski algorithm (UMA) (*8*) has proved even more successful. UMA searches amino acid sequences for three indicators of structured protein domains (secondary structure, local hydrophobicity, and family homology), better distinguishing folded regions from linkers. One of UMA's first achievements was to predict the location of the two missing activities in PksA: a starter unit–ACP transacylase (SAT) domain at the N terminus and a putative product template (PT) domain just upstream of the ACP. Subsequent experiments with the discrete SAT domain proved its function in recruiting hexanoate (*9*).

Using UMA as a guide, Crawford *et al.* have now further deconstructed PksA into seven different chunks (monodomains, didomains and tridomains) and then recombined the pieces in vitro (*1*); every reaction contained the tridomain SAT-KS-MAT required for loading and condensation. Guided by the assumption that differences from wild-type behavior could be attributed to the missing domain(s), analysis of the resulting products enabled the authors to determine each domain's role. With high-resolution mass spectrometry, the authors detected predicted intermediates attached to the ACP domain, further supporting the assigned domain functions. As expected, a reaction mixture containing all domains resulted mainly in NSA.

In 2000, Staunton argued that cyclization of polyketone chains might begin during the chain-extension process (*10*): In this way, the polyketide synthase would avoid the task of protecting a long, reactive chain from spontaneous ring formation and establish the regiochemistry of all subsequent cyclizations. However, the mass spectrometry data reported by Crawford *et al.* suggest that PksA constructs full-length chains on its ACP before installing any rings. Tang and co-workers recently reached the same conclusion from studies of another nonreducing fungal PKS interacting with a discrete enzyme. The enzyme consistently acted at a specific carbon of the intermediate attached to the ACP, evidence that it was able to count along the fully extended chain to locate the correct site (*7*). Apparently, nature's view of economy of catalytic mechanism does not always agree with ours.

PksA has close relatives in many other fungi, so the results of Crawford *et al.* are likely to be generalizable. However, the nonreducing polyketide synthases are the simplest polyketide synthases in fungi. The partially reducing polyketide synthases incorporate ketoreductase domains that act only during selected extension cycles, whereas the highly reducing polyketide synthases contain several additional catalytic sites. Neither system uses SAT or PT domains, and thus the basis for their complex programming is unclear. Application of the dissection approach to these polyketide synthases may soon provide some answers. UMA's work is just beginning.

References

1. J. M. Crawford *et al.*, *Science* **320**, 243 (2008).
2. R. E. Minto, C. A. Townsend, *Chem. Rev.* **97**, 2537 (1997).
3. K. M. Henry, C. A. Townsend, *J. Am. Chem. Soc.* **127**, 3724 (2005).
4. R. J. Cox, *Org. Biomol. Chem.* **5**, 2010 (2007).
5. A. Watanabe *et al.*, *Tetrahedron Lett.* **39**, 7733 (1998).
6. Y. Ma *et al.*, *ChemBioChem* **7**, 1951 (2006).
7. S. M. Ma *et al.*, *J. Am. Chem. Soc.* **130**, 38 (2008).
8. D. W. Udwary *et al.*, *J. Mol. Biol.* **323**, 585 (2002).
9. J. M. Crawford *et al.*, *Proc. Natl. Acad. Sci. U.S.A.* **103**, 16728 (2006).
10. J. Staunton, K. J. Weissman, *Nat. Prod. Rep.* **18**, 380 (2001).

10.1126/science.1157677

BIOCHEMISTRY

Zooming Into Live Cells

Fabien Pinaud and Maxime Dahan

High-resolution optical imaging is providing real-time data on molecular processes in live cells.

Flying high over a city, a visitor from outer space on a mission to study the organization of urban life is likely to first notice a mostly static structure, intersected by a few traffic axes. But landing next to a main street, he will find a much more complex and dynamic situation, with people moving in various directions and interacting in groups. Advances in high-resolution light microscopy now allow researchers to undertake similar journeys into the complexity of live cells. As reported by Westphal *et al.* on page 246 of this issue (*1*), optical techniques are now producing image sequences in which the dynamics of molecules or supramolecular assemblies are recorded with nanometer-scale accuracy in real time. By opening a window to molecular-scale processes, the techniques promise to elucidate many aspects of cell organization.

Light microscopy is an essential tool in biology, offering a sensitive, noninvasive approach to probing cells. The resolution of lens-based microscopes was, however, long thought to be limited to about half the wavelength λ of the light used (~250 to 300 nm for visible light). Many questions have remained unanswered because the assembly of many cellular structures takes place on a scale much smaller than λ/2 and therefore cannot be resolved by conventional microscopy.

Recent studies have shown that the resolution does not have to be limited to λ/2 (*2*). A

Laboratoire Kastler Brossel, CNRS UMR8552; Physics and Biology Department, Ecole Normale Supérieure; Université Pierre et Marie Curie-Paris 6, 46 rue d'Ulm, 75005 Paris, France. E-mail: maxime.dahan@lkb.ens.fr

key step is to find a means to reduce the number of fluorescently labeled molecules that are excited simultaneously at every acquisition step of the image. In one approach, the effective size of the exciting beam is reduced by stimulated emission depletion (STED), in which a doughnut-shaped quenching beam is wrapped around the excitation spot (see the first figure, left panel) (*3*). The result is akin to sharpening a pencil to draw finer lines. By scanning the "sharpened" spot over the sample, an image is built pixel by pixel, with a resolution currently down to 20 nm.

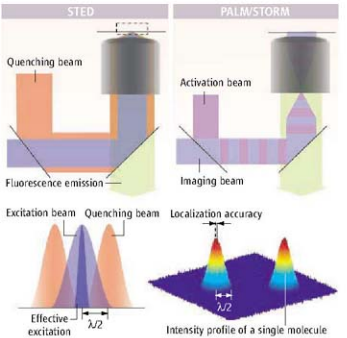

Higher resolution. In STED microscopy (**left**), an excitation beam overlaps with a doughnut-shaped quenching beam. At the focal point, the effective excitation is much narrower than λ/2. With PALM or STORM (**right**), the sample is illuminated with an activation light and an excitation beam. Single activated molecules can be localized with an accuracy well below λ/2.

In another approach, microscopy techniques (termed PALM and STORM) take advantage of molecules that can be turned on and off with different light sources (*4*, *5*). Using low activation intensity, a small and random subset of molecules in the field of view is activated. Next, a conventional image is taken, in which activated emitters appear as sparse spots. The molecules are then deactivated through photobleaching or by switching back to their off state. Each spot has a diffraction-limited extension of ~λ/2, but its center can be localized with much higher accuracy (see the first figure, right panel)—in practice down to 10 to 40 nm. By repeating the activation-imaging-deactivation cycle many times, a composite image made up of the positions of all individual molecules is created, much like in a pointillist painting.

High-resolution microscopy has recently been extended to three-dimensional (*6*) and multicolor imaging (*7*–*9*). It has allowed imaging of membrane proteins (*10*), cytoskeletal elements (*9*), and vesicles (*11*) in fixed samples with unmatched resolution.

Westphal *et al.* now extend STED microscopy to live cell imaging. By working on small regions of interest and finely tuning the size of the STED excitation spot, they find a suitable compromise between the number of detected photons and the scanning speed to achieve video-rate intracellular imaging with a resolution of ~60 nm. With such resolution, they record the motion of individual fluorescently labeled presynaptic vesicles in live neurons (see the second figure). The data reveal complex, continuous intracellular trafficking of the vesicles, with confined movements in nerve terminals. The experiments closely follow advances in PALM techniques that permitted in vivo tracking of membrane proteins (*12*, *13*).

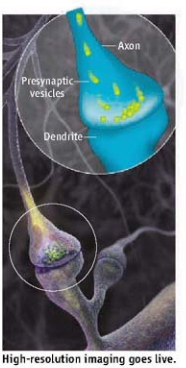

High-resolution imaging goes live. Westphal *et al.* have used STED microscopy to track presynaptic vesicles in live neurons in real time.

High-resolution microscopy provides many possibilities for biomedical research. The detailed organization of subcellular structures such as small membrane microdomains, cytoskeletal scaffolds, and multiprotein factories can be directly visualized. But one of the most exciting prospects is the possibility to follow, in real time, the dynamics at play in assembling, maintaining, and taking apart such structures. Indeed, it is becoming increasingly clear that most, if not all, cellular structures are maintained by continuous exchanges of transiently interacting and dissociating molecules (*14*). The kinetics of these exchanges, together with the structure-function relationship, can now be characterized in situ.

High-resolution microscopy will also transform the way interactions are probed in living cells, because it provides a much higher confidence level to determine if two molecules are very close to each other (and thus are potentially interacting with one another). This is particularly important for interactions mediated through supramolecular complexes larger than ~10 nm, a distance above which molecular proximity measurements based on energy transfer between fluorophores become impractical (*15*).

Looking in real time at individual molecular assemblies does not come without technical and conceptual challenges. Cellular targeting of brighter and highly photostable fluorescent probes (*16*) will be required to study fast and complex dynamics over extended time periods. Analysis and processing of the large data sets collected from thousands of single molecules will demand substantial computer resources. Furthermore, as observed in many single-molecule experiments, the dynamics of individual objects in live cells is highly heterogeneous. Understanding the causes and implications of this heterogeneity will imply concerted experimental and modeling efforts. Ultimately, we expect high-resolution microscopy to illustrate that there is no average molecule, much as single-cell experiments debunked the myth of the average cell (*17*).

References and Notes

1. V. Westphal *et al.*, *Science* **320**, 246 (2008); published online 21 February 2008 (10.1126/science.1154228).
2. S. W. Hell, *Science* **316**, 1153 (2007).
3. S. W. Hell, J. Wichmann, *Opt. Lett.* **19**, 780 (1994).
4. E. Betzig *et al.*, *Science* **313**, 1642 (2006).
5. M. J. Rust *et al.*, *Nat. Methods* **3**, 793 (2006).
6. B. Huang *et al.*, *Science* **319**, 810 (2008).
7. M. Bates *et al.*, *Science* **317**, 1749 (2007).
8. G. Donnert *et al.*, *Biophys. J.* **92**, L67 (2007).
9. H. Shroff *et al.*, *Proc. Natl. Acad. Sci. U.S.A.* **104**, 20308 (2007).
10. R. R. Kellner *et al.*, *Neuroscience* **144**, 135 (2007).
11. K. I. Willig *et al.*, *Nature* **440**, 935 (2006).
12. S. Manley *et al.*, *Nat. Methods* **5**, 155 (2008).
13. S. T. Hess *et al.*, *Proc. Natl. Acad. Sci. U.S.A.* **104**, 17370 (2007).
14. E. Karsenti, *Nat. Rev. Mol. Cell Biol.* **9**, 255 (2008).
15. E. A. Jares-Erijman, T. M. Jovin, *Nat. Biotechnol.* **21**, 1387 (2003).
16. B. N. G. Giepmans *et al.*, *Science* **312**, 217 (2006).
17. J. M. Levsky, R. H. Singer, *Trends Cell Biol.* **13**, 4 (2003).

F.P. acknowledges the support of a Marie Curie Intra-European Fellowship.

10.1126/science.1156510

RETROSPECTIVE

Arthur C. Clarke (1917–2008)

A giant of science fiction literature wrote with scientific precision and imaginative insight about Earth and space sciences.

Joseph N. Pelton[1] and John Logsdon[2]

Scientific giants give us powerful understanding of how nature works. Newton identified gravity; Curie provided knowledge of radioactivity; Einstein, the space-time continuum; Hubble, a yardstick to measure the size of the "Big Bang universe." Other powerful figures in human history contribute primarily by their insights into what might be. They span an incredibly broad range of art, literature, invention, and scientific inquiry. Leonardo Da Vinci is an obvious prototype, whose work and thoughts have transcended time.

Sir Arthur C. Clarke was clearly one of these "others." He was able, decade after decade, to generate prescient insights into the scientific and social worlds. He skipped merrily and with equal aplomb from the world of imagination to that of science and technology. He was the essence of wit. But there was more than wit and insight to his work. Unlike his contemporaries—Ray Bradbury, Isaac Asimov, and Robert Heinlein among them—Arthur Clarke remained an optimist about the human ability to make life better through the peaceful use of science and technology. That he was often disappointed in reality did not temper that optimism. Though he was not a religious man, there was an underlying positive spirituality to his writings that set him apart. He was convinced that human destiny involved leaving the Earth for other places in the solar system and beyond, and that the results of space exploration would improve the human condition.

Clarke was already experimenting with rockets when he was 13 years old. By the time he was 17, he was developing sound transmission using light waves. At the age of 18 he aced the United Kingdom Civil Service exams and acquired the sobriquet "The Fastest Slide Rule in Whitehall." He joined the Royal Air Force (RAF) in 1941 and made key contributions to the development of radar during World War II. In October 1945, mustering out of the RAF at the advanced age of 28, he published in *Wireless World* magazine an article entitled "Extra-Terrestrial Relays." Well inside the issue—not the cover story—he set forth with mathematical clarity the key elements of deploying a global communications satellite network in a 36,000 kilometer orbit that would enable global coverage with just three satellites. His lordly compensation for this multibillion dollar idea was £15 (then ~US $65), and lifetime recognition as the pioneer of an idea that changed the world.

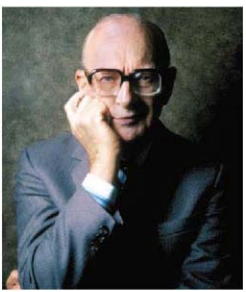

CREDIT: WILLIAM COUPON/CORBIS

Not one to dawdle, Arthur Clarke graduated in 1948 from King's College, London, taking only 2 years to complete his studies. He sold his first science fiction story in 1945, and by 1953 his career as a science fiction giant was firmly launched with the publication of *Childhood's End*. A stream of books poured forth year after year. During his prodigious career he won virtually every major science fiction writing award. *Rendevous with Rama* (1973) alone won the Hugo, Nebula, John W. Campbell Memorial, and Jupiter Awards. The science fiction works that sustained him financially never strayed far off the path of scientific possibility. He remained contemptuous of science fiction that was inconsistent with the basic laws of physics.

Clarke's books are equally divided between science fact and science fiction. His 1951 exposition of the emerging field of astronautics, *The Exploration of Space*, was a Book-of-the-Month selection in the United States and introduced many around the world to the possibilities linked to sending men and machines into orbit and beyond.

In 1954, Arthur Clarke made his first trip to Sri Lanka; he settled there on a permanent basis in 1956. Even then, Clarke sensed that he would never go into space. His alternative was exploring the mysterious world of the oceans. He was an avid scuba diver, until his health gave out, and fascinated with the ocean and exploring their mysteries in his books.

But his consuming interest was undoubtedly outer space. Through his collaboration with film director Stanley Kubrick on the 1968 movie *2001: A Space Odyssey*, and the accompanying book, his ideas on the origins and future of humanity reached millions. He was quite proud of the fact that his writings helped inspire many young people to become astronauts, including several of those who traveled to the moon during the Apollo program. Arthur Clarke not only wrote about space in entertaining ways, he also presented a vision of a compelling future away from the home planet.

Perhaps Clarke's most riveting character was HAL—the computer in *2001*—a machine that not only developed awareness but even the ability to commit murder. The importance of HAL in Clarke's writing was no fluke. He felt that artificial intelligence was the most important invention of our time.

Arthur Clarke was no one-act wonder. He wrote over 100 books and hundreds of articles with both scientific precision and literary genius. He wrote about every aspect of Earth and space science. His range of interests included communications, education, the environment, energy technologies, climate, genetic engineering, space science, advanced materials, robotics, astrophysics, advanced transportation systems, nonlinear math, and just about every other imaginable technology.

How can we appropriately remember this giant? We can recall, "The only way of discovering the limits of the possible is to venture a little way past them into the impossible," one of his three laws from *Profiles of the Future* (1962). We could also designate the geosynchronous orbit the "Clarke Orbit" and perhaps create an Arthur C. Clarke Center for Imagination.

Now, after 90 full years, Arthur C. Clarke is launched into the cosmos for a well-deserved rest. This is no mere literary allusion. Clarke, who had no false sense of modesty about his achievements, arranged for a lock of his hair to be launched into space so that he could share his DNA with the universe.

[1]The Space & Advanced Communications Research Institute, George Washington University, Washington, DC 20052, USA. [2]The Space Policy Institute, George Washington University, Washington, DC 20052, USA. E-mail: logsdon@gwu.edu

10.1126/science.1158220

Magnetic Domain-Wall Racetrack Memory

Stuart S. P. Parkin,* Masamitsu Hayashi, Luc Thomas

Recent developments in the controlled movement of domain walls in magnetic nanowires by short pulses of spin-polarized current give promise of a nonvolatile memory device with the high performance and reliability of conventional solid-state memory but at the low cost of conventional magnetic disk drive storage. The racetrack memory described in this review comprises an array of magnetic nanowires arranged horizontally or vertically on a silicon chip. Individual spintronic reading and writing nanodevices are used to modify or read a train of ~10 to 100 domain walls, which store a series of data bits in each nanowire. This racetrack memory is an example of the move toward innately three-dimensional microelectronic devices.

There are two main means of storing digital information for computing applications: solid-state random access memories (RAMs) and magnetic hard disk drives (HDDs). Even though both classes of devices are evolving at a very rapid pace, the cost of storing a single data bit in an HDD remains approximately 100 times cheaper than in a solid-state RAM. Although the low cost of HDDs is very attractive, these devices are intrinsically slow, with typical access times of several milliseconds because of the large mass of the rotating disk. RAM, on the other hand can be very fast and highly reliable, as in static RAM and dynamic RAM technologies. The architecture of computing systems would be greatly simplified if there were a single memory storage device with the low cost of the HDD but the high performance and reliability of solid-state memory.

Racetrack Memory

Because both silicon-based microelectronic devices and HDDs are essentially two-dimensional (2D) arrays of transistors and magnetic bits, respectively, the conventional means of developing cheaper and faster devices relies on reducing the size of individual memory elements or data storage bits. An alternative approach is to consider constructing truly 3D devices. One such approach is "racetrack" memory (RM) (*1*), in which magnetic domains are used to store information in tall columns of magnetic material arranged perpendicularly on the surface of a silicon wafer (Fig. 1). Magnetic domain walls (DWs) (*2*) are formed at the boundaries between magnetic domains magnetized in opposite directions (up or down) along a racetrack (Fig. 2). Each domain has a head (positive or north pole) and a tail (negative or south pole). Successive DWs along the racetrack alternate between head-to-head and tail-to-tail configurations. The spacing between consecutive DWs (that is, the bit length) is controlled by pinning sites fabricated along the racetrack. There are several means of creating such pinning sites; for example, by patterning notches along the edges of the racetrack or modulating the racetrack's size or material properties. Besides defining the bit length, pinning sites also give the DWs the stability to resist external perturbations, such as thermal fluctuations or stray magnetic fields from nearby racetracks.

RM is fundamentally a shift register in which the data bits (the DWs) are moved to and fro along any given racetrack to intersect with individual reading and writing elements integrated with each racetrack (Fig. 1). The DWs in the magnetic racetrack can be read with magnetic tunnel junction magnetoresistive sensing devices (*3*) arranged so that they are close to or in contact with the racetrack. Writing DWs can be carried out with a variety of schemes (*1*), including using the self-field of currents passed along neighboring metallic nanowires; using the spin-momentum transfer torque effect (*4*, *5*) derived from current injected into the racetrack from magnetic nanoelements; or using the fringing fields from the controlled motion of a magnetic DW in a proximal nanowire writing element (*1*).

Uniform magnetic fields cannot be used to shift a series of DWs along the racetrack: Neighboring DWs would move in opposite directions and so eventually annihilate each other. Magnetic memory devices using non-uniform local magnetic fields to manipulate DWs were studied several decades ago (*6*, *7*) but were abandoned because of their complexity and cost.

In RM, DWs are shifted along the racetrack by nanosecond current pulses using the phenomenon of spin-momentum transfer (*4*, *5*). When a current is passed through a magnetic material, it becomes spin-polarized because of spin-dependent diffusive scattering, and so carries spin angular momentum (*3*, *8*). When the spin-polarized current is passed through a DW, the current transfers spin angular momentum to the wall, thereby applying a torque to the moments in the DW, which can result in motion of the wall

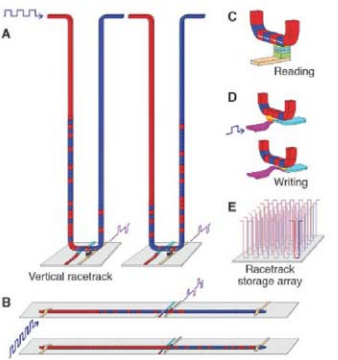

Fig. 1. The racetrack is a ferromagnetic nanowire, with data encoded as a pattern of magnetic domains along a portion of the wire. Pulses of highly spin-polarized current move the entire pattern of DWs coherently along the length of the wire past read and write elements. The nanowire is approximately twice as long as the stored DW pattern, so the DWs may be moved in either direction. **(A)** A vertical-configuration racetrack offers the highest storage density by storing the pattern in a U-shaped nanowire normal to the plane of the substrate. The two cartoons show the magnetic patterns in the racetrack before and after the DWs have moved down one branch of the U, past the read and write elements, and then up the other branch. **(B)** A horizontal configuration uses a nanowire parallel to the plane of the substrate. **(C)** Reading data from the stored pattern is done by measuring the tunnel magnetoresistance of a magnetic tunnel junction element connected to the racetrack. **(D)** Writing data is accomplished, for example, by the fringing fields of a DW moved in a second ferromagnetic nanowire oriented at right angles to the storage nanowire. **(E)** Arrays of racetracks are built on a chip to enable high-density storage.

IBM Almaden Research Center, San Jose, CA 95120–6099, USA.

*To whom correspondence should be addressed. E-mail: parkin@almaden.ibm.com

(*9*–*15*). The direction of motion of the DWs is independent of the magnetic charge of the DW, whether head to head or tail to tail, so that an entire sequence of DWs can be shifted along the racetrack. The magnetic columns need to be sufficiently narrow (<~100 nm) for the spin momentum transfer interaction of the current with the DW to dominate over the self-field of the current. Thus, the racetracks are composed of nanowires of magnetic material approximately 100 nm or less in diameter and one to several tens of micrometers tall, thereby accommodating ~10 to 100 DWs per racetrack. The cost of storing one data bit in the RM is lowered as the number of DWs (n) that are stored in an individual racetrack increases, and, moreover, the average time needed to read a particular bit is independent of n if the distance between DWs is kept constant.

Fabricating the 3D RM is a substantial challenge (*16*). However, RM can also be built in a 2D geometry (Fig. 1B), which is much simpler. Moreover, even though a 2D RM has lower density than a 3D RM, its density is superior to that of nearly all other solid-state memories, including the densest flash memory (*16*) (table S1). The planar geometry is also more suitable for exploring the RM physics in a laboratory environment.

One of the most challenging aspects of RM is the controlled and reliable motion of a series of DWs, which are the data bits, backward and forward along the racetrack. The ultimate performance of RM will depend both on the current density required to move DWs and the velocity at which the DW pattern can be shifted along the racetrack. Thus, a detailed understanding of the magnetization dynamics of DWs and their interaction with spin-polarized current is key for the successful development of RM.

DW Data Bit

Current-driven DW motion has been studied in just a small number of magnetic materials, both "soft" and "hard" (*17*–*30*), in in-plane and perpendicularly magnetized nanowires, respectively. In hard materials, the magnetization direction is determined largely by the direction of the magnetic anisotropy fields, which are intrinsic to the material. In contrast, the magnetization direction in magnetically soft nanowires is defined by the geometrical shape and form of the nanowire. Here we focus on horizontal racetracks with rectangular cross-sections fabricated from thin films of soft magnetic alloys composed of iron, nickel, and cobalt. In these cases, the internal structure of the DW and its width are largely derived from magnetostatic fields determined by the shape of the racetrack (*2*). In particular, the DW width scales approximately with the nanowire width.

For the nanowire dimensions studied—widths ranging from 100 to 500 nm and thicknesses ranging from 10 to 50 nm—the DW states with the lowest energies have either transverse (T) or vortex (V) wall structures (*31*, *32*) (Fig. 2, A and B). The vortex structure is favored in thicker or wider nanowires because it is flux closed with reduced surface charge (and, thereby, demagnetizing fields) at the nanowire edges. In larger nanowires, even more complex DW structures can be found (Fig. 2B). It is common to find both T and V DW structures in a given nanowire, for a wide range of nanowire widths and thicknesses, even when the DW energies are substantially different (Fig. 2A).

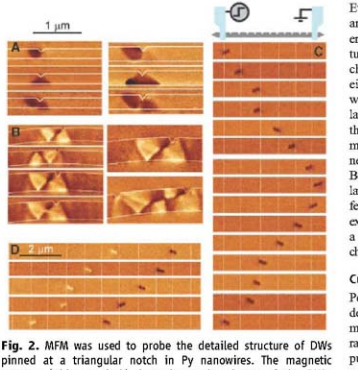

Fig. 2. MFM was used to probe the detailed structure of DWs pinned at a triangular notch in Py nanowires. The magnetic contrast (white or dark) depends on the charge of the DWs, whether head to head or tail to tail. Solid white lines show the nanowire's topography as determined by atomic force microscopy. **(A)** Structure of tail-to-tail DWs observed in thin 10-nm-thick nanowires with widths of 200 nm (left) and 300 nm (right). From top to bottom, images show DWs with anticlockwise transverse, clockwise transverse, and anticlockwise vortex structures. **(B)** Structure of head-to-head DWs observed in 40-nm-thick nanowires with widths from 200 to 400 nm. The leftmost four images show examples of vortex DWs with clockwise and anticlockwise chiralities, both with negative core polarity (top two images on the left, for a nanowire width of 200 nm), and clockwise vortex walls with negative and positive core polarities (bottom two images on the left, width 300 nm). The two images on the right show examples of structures found in a 400-nm-wide nanowire: a vortex wall with clockwise chirality and negative polarity (top) and a more complex structure comprising two vortices and one antivortex for a DW pinned between two neighboring notches (bottom). **(C)** MFM was used to image the motion of a single tail-to-tail vortex DW. The cartoon at top shows a schematic of the experiment. A nanowire comprising a series of notches was connected to electrical contacts at each end to allow for injection of current pulses. Experimental results are shown for a 40-nm-thick, 100-nm-wide permalloy nanowire with 11 triangular notches located 1 μm apart; a part of the nanowire with six notches, indicated by vertical white dotted lines, is shown. Single current pulses, 8V (26 mA) and 14 ns long, were applied between each image sequentially from top to bottom. For the first eight images, pulses with negative polarities were applied. For the last seven images, pulses with positive polarities were applied. **(D)** The motion of two DWs in the same nanowire as (C). Positive current pulses (26 mA, 14 ns long) were applied between successive images sequentially from top to bottom.

Even when only vortex DWs are energetically stable, several metastable vortex structures can be observed: The chirality of the vortex can be either clockwise or anticlockwise, and the vortex core polarity (that is, the direction of the out-of-plane vortex core magnetization) can be either negative or positive (Fig. 2B). Both the chirality and the polarity of the vortex strongly affect the DW dynamics. For example, the pinning strength of a notch depends on the DW chirality (*33*).

Current-Driven DW Motion

Perhaps the key concept underlying RM is the controlled movement of DWs along the racetrack by means of short pulses of spin-polarized current. This concept is demonstrated in Fig. 2C for permalloy (Py, $Ni_{81}Fe_{19}$) nanowires by measurement of the position, quasi-statically with magnetic force microscopy (MFM), of one or more DWs created in the nanowires. A sequence of MFM images was recorded after the injection of single current pulses or trains of pulses of varying length and magnitude along the nanowire. The DWs don't move until a critical current threshold is exceeded. In Fig. 2C, the controlled motion of vortex DWs between successive notches is clearly shown for 14-ns-long pulses corresponding to a current density of $\sim 3 \times 10^8$ A/cm^2. Depending on the current direction, the DWs are moved in either direction along the nanowire, but the DWs' motion is in the direction of the electron flow (that is, opposite to the current direction). Under these experimental conditions, the motion of the DWs is not reliable: In some cases, the DWs don't move, move only across a notch, or, on the contrary, skip a notch.

Under the same experimental conditions it is also possible to controllably move two DWs (Fig. 2D). The two DWs move in the same direction—with the electron flow—even though they have opposite magnetic charge. This demonstrates the feasibility of shifting a series of DWs with opposite charges along the racetrack. However, an important drawback of

these studies is that the threshold current density is so high that the nanowire temperature increases because of severe Joule heating from the current pulses. The heat capacity of the nanowire is so small that its equilibrium temperature is reached very quickly, within ~2 to 20 ns depending on the thermal link to the underlying substrate. In extreme cases, the nanowire's temperature can approach that of the Curie temperature of Py (~850 K). This obviously has deleterious results, including the possibility of the creation or annihilation of pairs of DWs. Reversals in the chirality (*33*) or polarity of the DWs and transformations of the DW structure (*20*) can also be seen at these high current densities, influenced not only by thermal perturbations but also by spin-momentum transfer itself. Thus, for the successful operation of RM, it is important to reduce the critical current density for moving DWs.

Critical Current for DW Motion

Understanding the origin of the critical current and its dependence on the racetrack's material and geometry has been a challenge for experimental and theoretical physicists in the past few years. Let us first compare DW motion driven by current and magnetic field. The field analog of the critical current density J_c is the propagation (or coercive) field H_p, below which no motion occurs. The origin of this propagation field is extrinsic: For an ideal racetrack, without any defects or roughness, DWs would move for any nonzero applied field, albeit very slowly. Thus, nonzero values of the propagation field are directly related to defects, which provide local pinning sites for the DW. In fact, H_p is proportional to the pinning strength, which can be tuned, for example, by fabricating notches with variable depths.

Intuitively, one would expect current-driven DW motion to follow the same behavior: The stronger the pinning, the larger the critical current. However, the original theories of spin-transfer torque suggested the existence of an intrinsic critical current density, even for an ideally smooth nanowire (*11*, *12*, *14*). In these theories, for currents smaller than this threshold value, DWs move only a short distance before stopping as they reach a dynamical equilibrium (for which the influx of spin angular momentum is compensated by damping). The critical current is independent of pinning strength (except for extremely strong pinning) and depends only on the racetrack's geometry and material parameters. More recently, it has been proposed that in addition to this original adiabatic spin-transfer torque term, there is another contribution that behaves as a magnetic field localized at the DW, which is often described as a nonadiabatic term. Even though the origin of this term is still under debate (*13*–*15*), its mere existence has dramatic effects on the current-driven DW dynamics. Indeed, the critical current becomes extrinsic; that is, it scales with the pinning strength. Thus, it follows that the critical current could be controlled by engineering pinning sites along the racetrack.

The relationship between critical current and pinning strength for vortex DWs is shown in Fig. 3A. These data suggest the existence of two different regimes. For relatively weak pinning (below ~15 Oe), the critical current density scales linearly with the pinning field. For the lowest pinning strength (~5 Oe), the critical current is on the order of 10^8 A/cm^2. For stronger pinning (>15 Oe), the critical current appears to saturate and becomes independent of pinning strength. In this regime, however, DW motion requires very high current densities resulting in significant Joule heating, and experimental data are thus difficult to interpret. These data suggest the existence of a nonadiabatic term in the spin-transfer torque. Indeed, the critical current in the low pinning regime seems to tend to zero for zero pinning, suggesting a purely extrinsic origin [a similar dependence was observed in multilayers with perpendicular anisotropy (*29*)]. However, we cannot rule out the existence of a nonzero critical current for very low pinning (<5 Oe). Further work is needed to achieve such an extremely low pinning.

To date, the critical current to move a transverse DW in zero field has not yet been determined. It appears, as is consistent with theoretical models, that the threshold current for the motion of a transverse DW is higher than that for a vortex DW. It could be that in nanowires of appropriate dimensions (such as those with squarer cross-sections), transverse DWs can be moved.

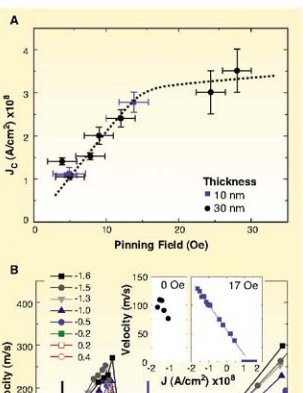

Fig. 3. (**A**) Critical current for depinning a vortex DW near zero field versus depinning field, measured on 10- and 30-nm-thick and 100- to 300-nm-wide Py nanowires using current pulses 20 to 100 ns long. The dotted line is a guide to the eye. (**B**) DW velocity plotted against magnetic field for various current densities flowing across the DW for Py nanowires 10 nm thick and 300 nm wide. Current densities indicated in the figure are in units of 10^8 A/cm^2. Solid and open symbols represent negative and positive currents, respectively. Negative current corresponds to electrons flowing along the field-driven motion of DWs. (Insets) DW velocity versus current density at fixed magnetic fields.

DW Velocity

The maximum DW velocity that can be achieved is an important parameter that will ultimately determine the speed of RM. We have measured the DW velocity as a function of magnetic field and current density by using time-resolved resistance measurements (*21*, *24*, *34*). Figure 3B shows the dependence of the DW velocity on magnetic field and current density. The DW velocity peaks at a relatively low magnetic field (~10 Oe), above which a negative DW mobility is observed (that is, the velocity decreases when the field increases). This drop in the DW velocity is associated with a change in the DW propagation mode and is known as the Walker breakdown (*34*–*36*).

Depending on the field, the DW moves with or without changing its structure. These different regimes are delineated by the Walker breakdown field. Above this field, as the DW moves, its structure transforms in a highly coherent manner, periodically switching between different states. This was observed recently as a periodic variation in the resistance of a moving DW (*34*). It was found that the oscillation period increased linearly with field but was little influenced by current, even though the DW's velocity was substantially changed. These results give direct evidence for the precessional nature of the DW's dynamics.

When spin-polarized currents are injected into the nanowire, the DW's velocity can be substantially modified (*21*, *22*). The right panel of the inset in Fig. 3B shows that the field-driven DW's velocity varies linearly with current. Its velocity is increased or decreased here by up to 110 m/s when the electron flow is in the same or in the opposite direction to the pressure applied by the magnetic field. For magnetic fields smaller than

~5 Oe, field alone cannot drive the DW along the nanowire because of local random pinning from edge and surface roughnesses. However, current can move the DW even in the absence of any magnetic field. The left panel of the inset in Fig. 3B shows the dependence of the velocity on the current density near zero field. The velocity exhibits a maximum value of ~110 m/s at a current density of $\sim 1.5 \times 10^8$ A/cm^2 (*24*). Such velocities are high enough for the RM to operate at clock rates that are competitive with those of existing technologies (table S1).

Resonant Amplification of DW Motion

In order to build a RM with stable bits, the DWs are located at specially fabricated pinning sites, suitably spaced along the racetrack. This means, however, that the current densities needed to move the DWs between these sites might be too high for practical use, in particular for nanowires formed from a single layer of Py. A novel method for lowering the critical current density of pinned DWs was recently demonstrated, which involves using short current pulses with particular lengths, matched to the innate precessional frequency of the pinned DW (*23*, *26*). It has long been realized that many properties of a DW can be described as if the DW has a mass (*37*); just like a mechanical oscillator, a DW confined in a potential well resonates at a natural frequency when subjected to an excitation. This means that the amplitude of the DW's oscillatory motion can be resonantly amplified by properly engineering the profile of the current excitation, thereby substantially reducing the critical current (Fig. 4).

Insight into the DW's response to current excitation is obtained from a 1D model of the DW dynamics (*37*). The model is based on the Landau-Lifshitz-Gilbert equation, which describes the magnetization dynamics, including the DW's interaction with current.

When a small current is applied, the DW's position within the potential well and its energy undergo damped oscillations, eventually reaching a stationary state but with an increased energy proportional to the current (Fig. 4A, c). When the current is turned off, the DW oscillates toward its original equilibrium position at the bottom of the pinning potential. The details of the DW's trajectories during and after current excitation are strongly influenced by the duration of the current excitation (Fig. 4A. d and e). When the current pulse length is matched to approximately a half integer of the DW's precessional period τ_p (such as 1/2, 3/2, 5/2, etc.), the DW can have sufficient energy to be driven out of the pinning site; whereas for pulses just a half-integer period longer (or shorter), the DW's energy is lower and it remains confined. Thus, the probability of depinning a DW from a pinning site oscillates with the current pulse length, which is a direct manifestation of the current-induced precessional excitation of the DW.

Experimental observation of this effect is shown in Fig. 4A, a and b, for two nanowires

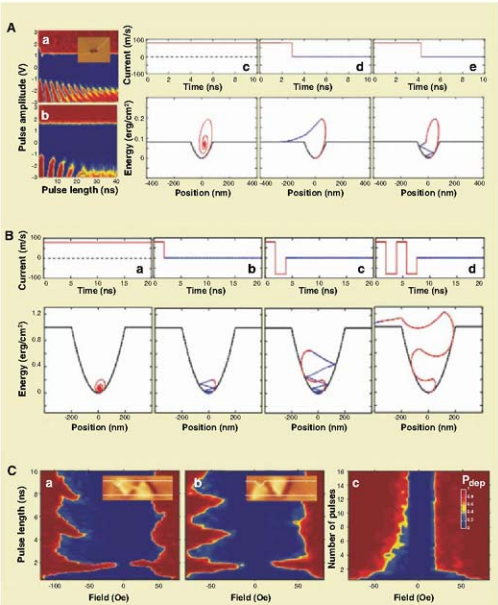

Fig. 4. Resonant amplification of DW motion can be used to reduce the current density required to move DWs from pinning sites. **(A)** Experimental observation of the DW oscillation confined in a potential well. (**a**) Probability of DW motion versus pulse length and amplitude, measured in an L-shaped nanowire (200 nm wide and 40 nm thick). The DW is weakly pinned at a local defect in the bend. A magnetic field of ~25 Oe was applied to assist DW motion. When the electron flow is along the field-driven motion direction (positive voltages), the DW is depinned only when the current density exceeds a threshold value, which does not depend on the pulse length. In contrast, when the electron flow opposes the DW motion direction, oscillations of the depinning probability are observed. (**b**) Probability map measured under the same conditions for a wire 100 nm wide and 40 nm thick. (**c** to **e**) Current-driven dynamics of a DW pinned in a shallow parabolic potential well, calculated with a 1D analytical model. The top panels show the current profile versus time for dc currents (c), a pulse at resonance [(d), pulse length 2.9 ns] and a pulse out of resonance [(e), pulse length 4.3 ns]. The bottom panels show the DW energy as a function of its position during (red) and after (blue) the current pulse. Also shown is the parabolic pinning potential well (black). **(B)** Analytical calculations of the dynamics of a DW pinned in a deep potential well. The DW trajectory in the energy/position space is plotted for dc current (**a**), a single pulse at resonance (length = 1.9 ns) (**b**), one bipolar pulse at resonance (**c**), and two bipolar pulses at resonance (**d**). **(C)** Experimental maps of the depinning probability for clockwise (**a**) and anticlockwise (**b**) head-to-head DWs pinned at the righthand side of a triangular notch in a nanowire 200 nm wide and 40 nm thick. The insets show the corresponding MFM images. The depinning probability is measured as a function of the external field and the pulse length for a series of 16 bipolar pulses, with an amplitude of 1 V. (**c**) Depinning probability (P_{dep}) map as a function of the applied field and the number of bipolar pulses applied at resonance (pulse length, 1.9 ns) for the anticlockwise DW shown in (b).

with different widths. The DW is pinned at a local defect in the curved region of the L-shaped nanowires. For negative voltages, the depinning probability oscillates with the current pulse length according to the mechanism described above (*23*), but with a longer period in the narrower wire because of the higher mass of the DW in the latter case. A magnetic field was applied to aid the DW's motion so that the oscillatory depinning effect was observed only for one current direction (here, negative).

When the pinning potential is deeper, a single current pulse with the same amplitude as in the previous example does not allow the DW to be depinned (Fig. 4B, b). However, just like a mechanical oscillator, the DW's energy can be resonantly enhanced by applying a series of current pulses synchronized with the oscillatory motion of the DW. This is illustrated in Fig. 4B, c and d, for the case of current pulses each exactly 1/2 τ_p long, but with successive pulses of opposite polarities. The DW energy increases with each successive pulse until it is larger than the potential depth and the DW can be depinned. This takes places at much lower currents than is otherwise possible with dc current or a single current pulse (*26*).

Experimental evidence of the resonant amplification of DW motion is shown in Fig. 4C. Vortex DWs with either clockwise (a) or anticlockwise (b) chiralities are pinned at the righthand side of a triangular notch, which provides strong pinning. The probability of DW motion is shown as a function of the applied field and the pulse length, for a series of 16 bipolar pulses of fixed amplitude of 1 V (~10^8 A/cm^2). When the pulse length equals 1/2 τ_p (~2 ns), the DWs are depinned with greater probability. Resonant amplification also occurs when the length of the pulse is increased by integer multiples of the resonance period but with progressively reduced efficiency. The shorter the current pulse, the more efficient is the phenomenon. Moreover, the phenomenon is only weakly dependent on the pinning potential [the resonance frequency depends on the square root of the slope of the potential well (*23*)] and on the DW's structure (for example, the chirality and polarity of vortex DWs). These attributes make the possibility of resonant DW depinning very useful for RM.

For the resonant amplification of DW motion to be useful in RM, it is important that depinning be achieved for a short series of pulses. Figure 4C, c shows experimental mapping of the depinning probability at resonance as a function of the applied field and the number of pulses for a series of bipolar pulses (1 V, 1.9 ns long) for the same DW as in Fig. 4C, b. Resonant amplification (in this case leading to the reduction of the depinning field) is substantial for just a single bipolar pulse and saturates for short trains of pulses (two to eight, depending on the depinning direction).

Outlook

There is much discussion about the possibility of developing 3D silicon microelectronic devices to overcome the limitations of the further scaling of complementary metal oxide semiconductor transistors. These typically involve the thinning and stacking of several silicon chips in packages or the use of silicon through-wafer vias. RM is a 3D technology that is relatively simple in concept and potentially inexpensive to fabricate (*16*). By using the essentially unused space above the surface of a silicon wafer for storing data (in columns of magnetic material) and by "bringing" these data to the surface of the wafer for reading and manipulating the data, an intelligent 3D memory chip can be built with unsurpassed data storage capacities. Moreover, RM, by storing data as the direction of a magnetization vector, has no obvious fatigue or wearout mechanism, which plagues many nonvolatile memory technologies today that store information by physically moving atoms (such as phase-change or ferroelectric memory).

RM encompasses recent advances in the field of metal spintronics (*3*). Magnetoresistive devices based on the manipulation of the flow of spin-polarized current through metallic heterostructures composed of sandwiches of thin ferromagnetic electrodes separated by ultrathin metallic [typically copper (*38*)] or dielectric layers [the most useful being MgO (*39*)] have proven to be invaluable for sensing data bits in magnetic HDDs. Indeed, the first device—the spin valve—enabled a thousandfold increase in the storage capacity of such drives in the past decade (*3*). The second device—the magnetic tunnel junction (MTJ)—is in the process of supplanting the spin valve because of its higher signal. MTJs also form the basis of modern magnetic RAMs (MRAMs), in which the magnetic moment of one electrode is used to store a data bit. Whereas MRAM uses a single MTJ element to store and read one bit, and HDDs use a single MTJ to read all ~100 GB of data in a modern drive, RM uses one device to read ~10 to 100 bits. Depending on the number of DWs per racetrack and the velocity of the DW, the average access time of RM will be 10 to 50 ns, as compared to 5 ms for an HDD and perhaps ~10 ns for advanced MRAM.

RM uses spin-polarized current not only for sensing but also for manipulating magnetic information. Recent experiments establish its basic principles. DWs can be moved with nanosecond-long current pulses over distances of several micrometers and at high velocities exceeding 100 m/s (*24*). Moreover, DW motion using current alone enables moving a series of adjacent DWs (of alternating charge) in lockstep in one direction or the other by using current pulses of one sign or the other. However, there remain important challenges to overcome. Among these are the demonstration of the highly reliable motion of a series of ~10 to 100 DWs along the racetrack, and the reduction of the current density required for DW motion below the dc threshold values currently needed at room temperature, while maintaining high DW velocity. Further understanding of the interaction of spin-polarized current with magnetic moments is essential. Exploring a wide variety of materials and heterostructures may provide new insight into DW dynamics driven by current, making possible DW-based memory and possibly logic devices that were previously inconceivable.

References and Notes

1. S. S. P. Parkin, U.S. Patents 6,834,005, 6,898,132, 6,920,062, 7,031,178, and 7,236,386 (2004 to 2007).
2. A. Hubert, R. Schäfer, *Magnetic Domains: The Analysis of Magnetic Microstructures* (Springer, Berlin, 1998).
3. S. S. P. Parkin *et al.*, *Proc. IEEE* **91**, 661 (2003).
4. J. Stonczewski, *J. Magn. Magn. Mater.* **159**, L1 (1996).
5. L. Berger, *Phys. Rev. B* **54**, 9353 (1996).
6. R. E. Matick, *Computer Storage Systems and Technology* (Wiley, New York, 1977).
7. S. Middelhoek, P. K. George, P. Dekker, *Physics of Computer Memory Devices* (Academic Press, London, 1976).
8. N. F. Mott, H. Jones, *Theory of the Properties of Metals and Alloys* (Oxford Univ. Press, Oxford, 1936).
9. L. Berger, *Phys. Rev. B* **33**, 1572 (1986).
10. L. Berger, *J. Appl. Phys.* **63**, 1663 (1988).
11. G. Tatara, H. Kohno, *Phys. Rev. Lett.* **92**, 086601 (2004).
12. Z. Li, S. Zhang, *Phys. Rev. Lett.* **92**, 207203 (2004).
13. S. Zhang, Z. Li, *Phys. Rev. Lett.* **93**, 127204 (2004).
14. A. Thiaville, Y. Nakatani, J. Miltat, Y. Suzuki, *Europhys. Lett.* **69**, 990 (2005).
15. S. E. Barnes, S. Maekawa, *Phys. Rev. Lett.* **95**, 107204 (2005).
16. See supporting material on *Science* Online.
17. N. Vernier, D. A. Allwood, D. Atkinson, M. D. Cooke, R. P. Cowburn, *Europhys. Lett.* **65**, 526 (2004).
18. A. Yamaguchi *et al.*, *Phys. Rev. Lett.* **92**, 077205 (2004).
19. E. Saitoh, H. Miyajima, T. Yamaoka, G. Tatara, *Nature* **432**, 203 (2004).
20. M. Kläui *et al.*, *Phys. Rev. Lett.* **94**, 106601 (2005).
21. M. Hayashi *et al.*, *Phys. Rev. Lett.* **96**, 197207 (2006).
22. G. S. D. Beach, C. Knutson, C. Nistor, M. Tsoi, J. L. Erskine, *Phys. Rev. Lett.* **97**, 057203 (2006).
23. L. Thomas *et al.*, *Nature* **443**, 197 (2006).
24. M. Hayashi *et al.*, *Phys. Rev. Lett.* **98**, 037204 (2007).
25. S. Lepadatu *et al.*, *Appl. Phys. Lett.* **90**, 232505 (2007).
26. L. Thomas *et al.*, *Science* **315**, 1553 (2007).
27. M. Yamanouchi, D. Chiba, F. Matsukura, H. Ohno, *Nature* **428**, 539 (2004).
28. D. Ravelosona, D. Lacour, J. A. Katine, B. D. Terris, C. Chappert, *Phys. Rev. Lett.* **95**, 117203 (2005).
29. D. Ravelosona, S. Mangin, J. A. Katine, E. E. Fullerton, B. D. Terris, *Appl. Phys. Lett.* **90**, 072508 (2007).
30. M. Feigenson, J. W. Reiner, L. Klein, *Phys. Rev. Lett.* **98**, 247204 (2007).
31. Y. Nakatani, A. Thiaville, J. Miltat, *J. Magn. Magn. Mater.* **290–291**, 750 (2005).
32. R. D. McMichael, M. J. Donahue, *IEEE Trans. Magn.* **33**, 4167 (1997).
33. M. Hayashi *et al.*, *Phys. Rev. Lett.* **97**, 207205 (2006).
34. M. Hayashi, L. Thomas, C. Rettner, R. Moriya, S. S. P. Parkin, *Nat. Phys.* **3**, 21 (2007).
35. N. L. Schryer, L. R. Walker, *J. Appl. Phys.* **45**, 5406 (1974).
36. G. S. D. Beach, C. Nistor, C. Knutson, M. Tsoi, J. L. Erskine, *Nat. Mater.* **4**, 741 (2005).
37. A. P. Malozemoff, J. C. Slonczewski, *Magnetic Domain Walls in Bubble Material* (Academic Press, New York, 1979).
38. S. S. P. Parkin, R. Bhadra, K. P. Roche, *Phys. Rev. Lett.* **66**, 2152 (1991).
39. S. S. P. Parkin *et al.*, *Nat. Mater.* **3**, 862 (2004).

40. We thank K. Roche and B. Gallagher for their contributions to this paper, R. Moriya and C. Rettner for help with sample preparation, and our colleagues in the Magnetoelectronics group at Almaden for many useful discussions.

Supporting Online Material

www.sciencemag.org/cgi/content/full/320/5873/190/DC1
Materials and Methods
SOM Text
Tables S1 and S2
References

10.1126/science.1145799

Amplification of Cretaceous Warmth by Biological Cloud Feedbacks

Lee R. Kump[1]* and David Pollard[2]

During supergreenhouse intervals of the geologic past, both tropical and polar temperatures were considerably warmer than today, and the gradient between the two was reduced. To even approach these equable climate states with climate models, atmospheric CO_2 levels must be specified that significantly exceed most proxy estimates for the Cretaceous and the Eocene (*1*). Thus, climate modelers have invoked viable but hard-to-evaluate hypotheses of elevated atmospheric methane levels, greater poleward oceanic heat transport, and enhanced polar stratospheric clouds (*2*).

An unexplored alternative involves planetary albedo, the fraction of the incoming solar radiation that is reflected to space, which is largely dependent on cloud cover and cloud albedo. A major determinant of cloud properties is the abundance of cloud condensation nuclei (CCN). When CCN are abundant, many small cloud droplets form, creating optically dense, high-albedo clouds; when abundance is low, fewer and larger droplets form, creating optically thinner, lower-albedo, and, importantly, shorter-lived clouds (*3*). Today, pollution dominates continental CCN, producing abundances of thousands per cm^3. In remote oceanic regions, biological release of dimethylsulfide is the major pathway for CCN production. Andreae (*4*) concludes that biological productivity determined the CCN concentrations over prehuman unpolluted land and sea, ranging from a few tens per cm^3 in low-productivity regions to a few hundred per cm^3 in high-productivity regions, supporting the notion of a prominent role for the biota in climate regulation on the prehuman Earth (*5*). If CO_2-induced warming during supergreenhouse intervals reduced global primary productivity by temperature stress and enhanced vertical stratification of the ocean, causing a reduction in CCN concentration, would lower cloud amounts and albedo have caused further warming?

To explore this hypothesis, we used a global climate model (GENESIS version 3.0) (GCM) to simulate middle Cretaceous [~100 million years ago (Ma)] climate with various atmospheric CO_2 amounts. This GCM has a slab mixed-layer ocean and prognostic cloud water amounts, and version 3 uses the National Center for Atmospheric Research (NCAR) Community Climate Model 3 (CCM3) radiation code with prescribed cloud droplet radii r_e (*3*). Cloud droplet radii mainly affect cloud optical depth, infrared emissivity, and precipitation efficiency, P_e, the rate at which cloud water is converted to precipitation. Modern large-scale observations and theory suggest that for ~10- to 100-fold global reductions in past aerosol and CCN amounts, ~30% (over ocean) to ~100% (over land) increases in liquid droplet radii are plausible (*3*). We simulate the Cretaceous climate with these increases in r_e and with P_e increased for liquid clouds by a factor of 2.2, reflecting the maximum likely effect of extreme global warmth on marine and terrestrial biological productivity and CCN production rate.

Our Cretaceous model results are shown in Fig. 1. In common with previous GCM studies, increasing CO_2 from 1× to 4× preindustrial atmospheric level (PAL) (Fig. 1, A and B) fails to produce the extreme high-latitude warmth implied by temperature proxy data (Fig. 1D). We then performed another 4× PAL simulation with the increases in r_e and P_e described above (Fig. 1C). Global cloud cover is reduced from 64 to 55%, and the less extensive and optically thinner clouds reduce planetary albedo from 0.30 to 0.24. The ensuing warming is dramatic, both in the tropics and in high latitudes, where it is augmented by surface albedo feedback of almost vanishing snow and sea-ice cover. (Other feedbacks due to changes in cloud types and levels are minor.) High-latitude continental temperatures remain above or very close to freezing year round, in better accord with proxy evidence (Fig. 1D).

Our results support the hypothesis that widespread increases in r_e can explain the drastic warming and equable high latitudes during supergreenhouse intervals of the Cretaceous and early Cenozoic. The increases in r_e could plausibly have been caused by an order of magnitude decrease in CCN concentrations, which we suggest was caused in turn by declines in biological productivity triggered by the climatic consequences of high CO_2 levels of ~4× PAL.

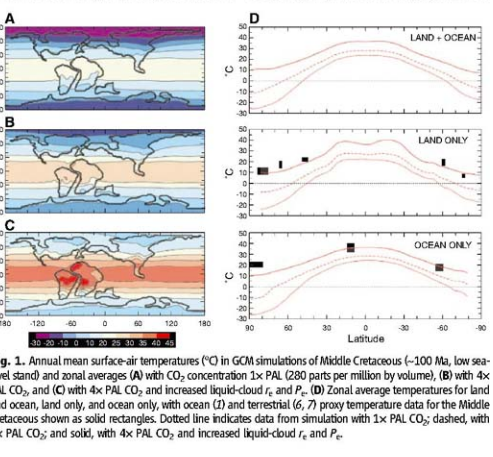

Fig. 1. Annual mean surface-air temperatures (°C) in GCM simulations of Middle Cretaceous (~100 Ma, low sea-level stand) and zonal averages (**A**) with CO_2 concentration 1× PAL (280 parts per million by volume), (**B**) with 4× PAL CO_2, and (**C**) with 4× PAL CO_2 and increased liquid-cloud r_e and P_e. (**D**) Zonal average temperatures for land and ocean, land only, and ocean only, with ocean (*1*) and terrestrial (*6*, *7*) proxy temperature data for the Middle Cretaceous shown as solid rectangles. Dotted line indicates data from simulation with 1× PAL CO_2; dashed, with 4× PAL CO_2; and solid, with 4× PAL CO_2 and increased liquid-cloud r_e and P_e.

References and Notes

1. K. L. Bice *et al.*, *Paleoceanography* **21**, PA2002 10.1029/2005PA001203 (2006).
2. L. C. Sloan, D. Pollard, *Geophys. Res. Lett.* **25**, 3517 (1998).
3. Materials and methods are available on *Science* Online.
4. M. O. Andreae, *Science* **315**, 50 (2007).
5. R. J. Charlson, J. E. Lovelock, M. O. Andreae, S. G. Warren, *Nature* **326**, 655 (1987).
6. J. E. Francis, I. Poole, *Palaeogeogr. Palaeoclim. Palaeoecol.* **182**, 47 (2002).
7. R. A. Spicer, R. M. Corfield, *Geol. Mag.* **129**, 169 (1992).
8. This work was supported in part by grants from NSF's Carbon and Water in the Earth System (to L.R.K.) and Paleoclimate History (to D.P.) programs.

Supporting Online Material

www.sciencemag.org/cgi/content/full/320/5873/195/DC1
Materials and Methods
Fig. S1
References

7 December 2007; accepted 19 February 2008
10.1126/science.1153883

[1]Department of Geosciences and Earth System Science Center, Pennsylvania State University, University Park, PA 16802, USA. [2]Earth and Environmental Systems Institute, Pennsylvania State University, University Park, PA 16802, USA.

*To whom correspondence should be addressed. E-mail: lkump@psu.edu

Electronic Origin of the Inhomogeneous Pairing Interaction in the High-T_c Superconductor $Bi_2Sr_2CaCu_2O_{8+\delta}$

Abhay N. Pasupathy,[1]* Aakash Pushp,[1,2]* Kenjiro K. Gomes,[1,2]* Colin V. Parker,[1] Jinsheng Wen,[3] Zhijun Xu,[3] Genda Gu,[3] Shimpei Ono,[4] Yoichi Ando,[5] Ali Yazdani[1]†

Identifying the mechanism of superconductivity in the high-temperature cuprate superconductors is one of the major outstanding problems in physics. We report local measurements of the onset of superconducting pairing in the high–transition temperature (T_c) superconductor $Bi_2Sr_2CaCu_2O_{8+\delta}$ using a lattice-tracking spectroscopy technique with a scanning tunneling microscope. We can determine the temperature dependence of the pairing energy gaps, the electronic excitations in the absence of pairing, and the effect of the local coupling of electrons to bosonic excitations. Our measurements reveal that the strength of pairing is determined by the unusual electronic excitations of the normal state, suggesting that strong electron-electron interactions rather than low-energy (<0.1 volts) electron-boson interactions are responsible for superconductivity in the cuprates.

Central to the current debate on the mechanism underlying high-temperature superconductivity is the question of whether electron pairing in cuprates is caused by the exchange of bosonic excitations and can therefore be described by an extension of the Bardeen-Cooper-Schrieffer (BCS) theory, which has successfully explained phonon-mediated superconductivity in metals and alloys for the past 50 years (*1*, *2*). Alternatively, it has been argued that the large Coulomb interaction in doped Mott insulators can result in a fundamentally different mechanism for pairing that cannot be approximated by a retarded boson-mediated interaction between electrons (*3*–*5*). In copper oxides, candidates for a BCS-like bosonic glue for pair binding include a magnetic resonance mode (near 40 meV for hole-doped cuprates) (*6*–*8*), the spectrum of high-energy spin excitations (above 40 meV) (*9*–*12*), fluctuations around a quantum critical point (up to several hundred millielectron volts) (*13*), and phonons (e.g., those near 40 meV) (*14*, *15*). Various spectroscopic measurements have probed these bosonic excitations and their coupling to electronic states in the cuprates (*14*–*20*); however, the connection between these excitations and the pairing mechanism has remained elusive (*5*, *21*).

Particularly challenging is the fact that the pairing strength and the temperatures over which pairs form in cuprate samples such as $Bi_2Sr_2CaCu_2O_{8+\delta}$ are spatially inhomogeneous (*22*–*24*), a behavior that complicates the interpretation of macroscopically averaged experiments. Our technique allows for quantitative characterization of the electron-boson coupling and its correlation with the inhomogeneous pairing on the nanometer scale in the high-T_c superconductor $Bi_2Sr_2CaCu_2O_{8+\delta}$. Our key finding is that although the coupling between electrons and bosons in the energy range of 20 to 120 meV influences the energy dependence of the pairing interaction, it does not control its local strength. We show instead that the local pairing strength is determined by asymmetric electron-hole excitations that are seen in the normal-state properties well above the temperature where pairs first form.

Lattice-tracking tunneling spectroscopy of inhomogeneous superconductors. Electron tunneling spectroscopy of superconductors is a powerful method for quantitative measurements of the onset of electron pairing and the boson exchange mechanism in superconductors (*25*). The pioneering measurements of McMillan and Rowell (*26*), and their analysis (*27*) based on the extension of the BCS theory by Eliashberg (*28*), provided unequivocal evidence for a phonon-mediated mechanism of superconductivity in metals and alloys. In their study, the dependence of the tunnel conductance on the voltage was used to extract the phonon density of states and the strength of the electron-phonon coupling. These two quantities determine the transition temperature as well as the energy dependence of the pairing gap.

The success of tunneling as a quantitative spectroscopic probe in conventional superconductors relied on performing measurements in both the superconducting and normal state (*29*) in order to exclude the complication due to tunneling matrix elements as well as inelastic tunneling processes. For an inhomogeneous superconductor such as $Bi_2Sr_2CaCu_2O_{8+\delta}$, in which electronic states and the superconducting energy gap vary on the nanometer scale, similar experiments pose a technical challenge. It is necessary to track specific atomic locations on the lattice of the sample from low temperatures to temperatures above T_c with a scanning tunneling microscope (STM) (*24*, *30*). To enable such measurements, we have developed a thermally compensated ultrahigh vacuum STM system that can maintain thermal stability to better than 10 mK during spectroscopy experiments up to temperatures of 110 K.

The lattice-tracking spectroscopy technique has been used to measure the evolution of tunneling conductance $dI/dV(r,V,T)$ with temperature in samples of $Bi_2Sr_2CaCu_2O_{8+\delta}$ that are overdoped (T_c = 68 K; Fig. 1, A and B) and optimally doped (T_c = 93 K; Fig. 1, D and E) at specific atomic sites. Spectra at different atomic sites show different energy gaps at low temperatures and evolve differently with increasing temperature (*24*). We find that all low-temperature spectra in highly overdoped samples (Fig. 1, A and B) evolve into spectra at high temperatures that are relatively featureless at low energies (<100 meV). In contrast, for optimally doped samples, we find that the spectra in most regions continue to have energy and temperature dependence at temperatures well above T_c (Fig. 1, D and E).

When the tunneling conductance at high temperatures is weakly dependent on temperature and energy, following previous work on conventional superconductors (*29*, *31*), we probe the effects of superconductivity by examining the ratio $R(r,V,T)$ between the tunneling conductance in the superconducting and normal states measured under the same STM setup conditions

$$R(r,V,T) = \frac{[dI/dV(r,V,T)]_S}{[dI/dV(r,V)]_N} = \frac{N_S(r,V,T)}{N_N(r,V)} \quad (1)$$

Here, $N_S(r,V,T)$ and $N_N(r,V)$ are the respective superconducting and normal density of electronic states at atomic site r as a function of energy (eV). This ratio, which is independent of the tunneling matrix element, will be used to extract the temperature dependence of the energy gap and features associated with strong coupling of electrons to bosonic modes. Although our experimental technique can be extended to study samples at any doping, we focus on the quantitative analysis of the local temperature dependence of electronic states on overdoped samples. Photoemission (*17*) and Raman spectroscopy (*32*) studies on $Bi_2Sr_2CaCu_2O_{8+\delta}$ samples have shown the absence of pseudogap phenomena at similar doping levels, simplifying the analysis of the normalized spectra.

[1]Joseph Henry Laboratories and Department of Physics, Princeton University, Princeton, NJ 08544, USA. [2]Department of Physics, University of Illinois at Urbana-Champaign, Urbana, IL 61801, USA. [3]Condensed Matter Physics and Materials Science, Brookhaven National Laboratory (BNL), Upton, NY 11973, USA. [4]Central Research Institute of Electric Power Industry, Komae, Tokyo 201-8511, Japan. [5]Institute of Scientific and Industrial Research, Osaka University, Ibaraki, Osaka 567-0047, Japan.

*These authors contributed equally to this work.
†To whom correspondence should be addressed. E-mail: yazdani@princeton.edu

Temperature dependence of the local pairing gap and quasiparticle lifetime. The temperature evolution of the conductance ratio $R(r,V,T)$, in overdoped $Bi_2Sr_2CaCu_2O_{8+\delta}$ samples at two representative locations of the sample with different low-temperature energy gaps, is shown in Fig. 2, A and B. Motivated by the fact that the low-temperature ratio resembles that expected from a single energy gap in the spectrum, we compare these ratios with that expected from the thermally broadened density of states of a d-wave superconductor

$$\frac{N_S(r,V,T)}{N_N(r,V)} = \frac{1}{\pi}\int dE \frac{df(E+V,T)}{dE} \int_0^{\pi} d\theta \,\mathrm{Real}\frac{E - i\Gamma(r,T)}{\sqrt{[E - i\Gamma(r,T)]^2 - \Delta(r,T)^2\cos^2 2\theta}} \quad (2)$$

Here, i is the square root of -1, $\Delta(r,T)$ is the local d-wave gap amplitude (considered energy-independent for low energies), $\Gamma(r,T)$ corresponds to the local inverse lifetime of the quasiparticle excitations (*33*), and $f(E,T)$ is the Fermi function. Such an analysis neglects the complication resulting from the momentum dependence of the band structure as well as higher-order angular terms in the superconducting gap.

Given that the experimental spectra in our sample display a gap above T_c, one can question the appropriateness of using a single gap parameter to describe the normalized spectrum (Eq. 2). In general, the value of the energy gap can be determined by two different methods: from the slope of the normalized spectra near zero energy and from the energy at which the conductance spectra show a peak. If there were two different gaps—for example, one dominating the nodal (near zero energy) and one dominating the antinodal (energy of the conductance peak) regions [as might be the case in underdoped $Bi_2Sr_2CaCu_2O_{8+\delta}$ samples (*17*, *24*, *32*)]—the two procedures would yield two different gap values. We find that the gap values obtained from the two methods agree at all locations on the sample, which further justifies the use of a single gap (Eq. 2) to describe the spectra in our overdoped samples.

In general, we find that the model in Eq. 2 provides an excellent fit to the experimental data at low energies for all points on the overdoped samples (Fig. 2, A and B). Using this model, we can extract the local values of $\Delta(r,T)$ and $\Gamma(r,T)$, showing that at each point the gaps decrease monotonically with increasing temperature and close at a local temperature $T_g(r) > T_c$ (Fig. 2C). We find that $\Gamma(r,T)$ is much smaller than the gaps at all locations at low temperatures (Fig. 2D).

With increasing temperature, we find that the smaller gaps close first, with the largest gaps surviving to temperatures well above T_c. Regions of the sample with smaller gaps also show $R(r,V,T)$, which exceeds that predicted from the local d-wave model in Eq. 2 for $eV \sim \Delta(r,T)$. This behavior is likely due to localization effects experienced by the quasiparticles in small gap regions that cannot penetrate the larger gap regions (*34*). The extracted values of $\Gamma(r,T)$ also agree with this scenario: The regions with the smallest gaps show no lifetime broadening, whereas the larger gap regions have a small lifetime broadening at low temperatures (Fig. 2D). The variation in $\Gamma(r,T)$ is a consequence of the fact that the excitations in the large gap regions can decay into nearby regions with smaller energy gaps, but not vice versa.

As the smaller gaps begin to close with increasing temperature, we find that the $\Gamma(r,T)$ in the large gap regions begins to increase rapidly. Overall, the analysis of the experimental data for all regions on the sample demonstrates that the spatially averaged $\Gamma(T)$ shows a dramatic increase at a temperature $T \sim T_c$, when the sample loses long-range phase coherence (Fig. 2D, inset). This observation is in accordance with previous

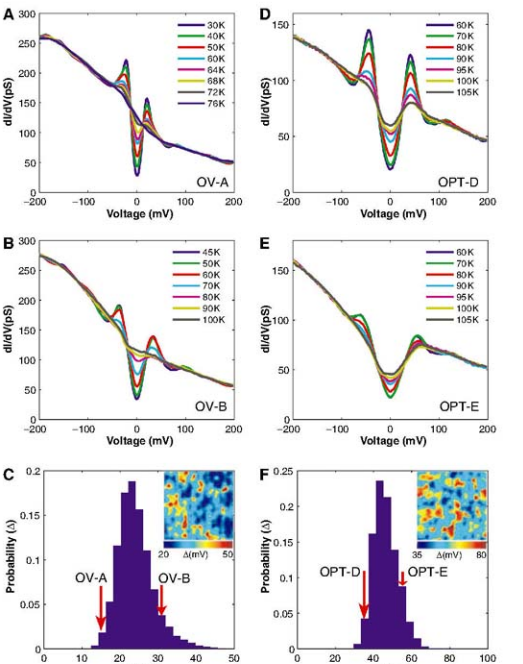

Fig. 1. (A and **B)** Spectra taken at two different atomic locations on an overdoped $Bi_2Sr_2CaCu_2O_{8+\delta}$ sample (T_c = 68 K, OV68) at various temperatures. The gaps in the spectra close at different temperatures, leading to a temperature-independent background conductance at high temperature. **(C)** Histogram of pairing gap values measured in the OV68 sample. (Inset) A typical pairing gap map (300 Å) obtained for an OV68 sample at 30 K. **(D** and **E)** Spectra taken at two different atomic locations on an optimally doped sample (T_c = 93 K, OPT) at various temperatures. The background continues to be temperature dependent well above T_c. **(F)** Histogram of gap values observed in the OPT sample. (Inset) A typical pairing gap map (300 Å) obtained for an OPT sample at 40 K.

macroscopically averaged measurements (*35*) on samples in the overdoped regime; however, previous measurements did not correlate inhomogeneous behavior of the gaps and quasiparticle lifetimes.

Coupling of electrons to bosonic modes. Having established that our measurements can be examined within the context of a local *d*-wave gap model, we turn to examining the deviation of the conductance ratio from this model for $E > \Delta$. Although other effects such as inelastic tunneling (*29*, *36*) can cause such deviations, only strong coupling of electrons to bosonic modes is known to cause the superconducting-state tunneling conductance to dip strongly below the normal state (*27*, *29*). As illustrated in Fig. 3A, all points on the samples show a voltage range (around 50 to 80 meV) in which the conductance ratio $R(r,V,T)$ is reduced below 1 and show systematic deviations from the local *d*-wave model. Analogous to previous work on conventional superconductors (*2*), these deviations provide a quantitative method to determine the strength of electron-boson coupling. The analysis of the spectra based on the features of $R(r,V,T)$ instead of the bare $dI(dV(r,V,T)$ or $d^2I/dV^2(r,V,T)$ avoids complications due to the spatial variation of normal-state features and tunneling matrix element variations (*21*). Although many previous studies, including those that used an STM (*15*, *37*), have examined electron-boson features in the 20- to 120-meV range, a quantitative comparison of the electron-boson coupling at different locations of the sample with different pairing gaps has not been accomplished. The comparison of $R(r,V,T)$ at different locations allows us to quantitatively evaluate the role of bosonic features in the development of the pairing gaps and their inhomogeneity.

To study the relative strength of electron-boson coupling at different locations on the sample, we consider that the strong coupling to a bosonic mode at energy Ω in a superconductor results in features in the conductance ratio at $eV = \Delta + \Omega$ (*15*, *29*, *38*). As the pairing gap is locally varying, we plot the $R(r,V,T)$ as a function of $eV-\Delta(r)$ for different atomic sites on the sample with low-temperature $\Delta(r)$ ranging between 15 and 32 meV in Fig. 3B. This figure demonstrates that different locations on the sample show similar $R(r,V,T)$ curves in magnitude and shape, once we take into account their varying pairing gaps. The only significant difference between the spectra occurs at low energies, where lifetime broadening effects, as well as the angle dependence of the electron-boson coupling, play a role. A measure of the energy Ω of the bosonic mode is the energy at which the dip occurs in the spectrum. We find that the average energy of this dip is 35 ± 3 meV. A quantitative measure of the strength of the local coupling constant is the root mean square deviation (RMSD) of $R(r,V,T)$ from the weak-coupling *d*-wave model (Eq. 2) in the energy range 20 to 120 meV beyond the gap. These deviations show no correlation [for both positive and negative biases (Fig. 3C)] with the size of the local gap within our experimental error.

For boson-mediated pairing, variation of the pairing gap can be caused by changes in either the local boson energy or the local coupling between the boson and electrons (*2*). Such changes are reflected directly in the size and energy range of the strong-coupling features in the conductance ratio. Indeed, in metallic alloy systems (*39*, *40*) where pairing is controlled by strong electron-phonon coupling, the magnitude of strong-coupling features in the conductance ratio scales with the gap size [see supporting online material (SOM) text S1]. Because both the energy scale of the boson modes and the local electron-boson coupling do not correlate strongly with the magnitude of the local pairing gap in our samples, we conclude that the coupling to bosons in the range of 20 to 120 meV cannot be responsible for these inhomogeneous pairing gaps.

Although bosons may not be critical to pairing in $Bi_2Sr_2CaCu_2O_{8+\delta}$, the $R(r,V,T)$ curves clearly show that these boson modes give a strong energy dependence to the gap function. Specifically, modification of Eq. 2 with a complex energy-dependent pairing gap $\Delta(r,\omega) = \Delta_R(r,\omega) + i\Delta_I(r,\omega)$, where Δ_R and Δ_I are the real and imaginary part of the gap function at energy ω, can be used to capture the bosonic features in the conductance ratio at higher energies. Within such a model, we estimate that the interaction with bosonic excitations (in the range of 20 to 120 meV) results in a substantial imaginary component of the pairing interaction (about 25 meV in magnitude at E = 40 meV).

Spatial structure of normal-state excitations and inhomogeneous pairing interaction. In search of the origin of the inhomogeneity in the pairing interaction in the cuprates, we focus on spectroscopic measurements of the electronic excitations in the normal state and their correlation with the inhomogeneity in the superconducting gaps. To reach the normal state, the temperature has to be high enough such that all the local pairing gaps have collapsed. For overdoped $Bi_2Sr_2CaCu_2O_{8+\delta}$ samples (hole-doping $x = 0.24$, $T_c = 62$ K), less than 1% of the sample shows a gap at 90 K. In the intermediate temperature between T_c and 90 K, these samples show a mixture of ungapped and partially gapped spectra, as previously reported (*24*). Above 90 K, the tunneling spectra (Fig. 4A) are gapless at all locations on the sample but show asymmetric behavior for electron and hole tunneling. Careful examination of these spectra, over a wide range of energies, shows that elec-

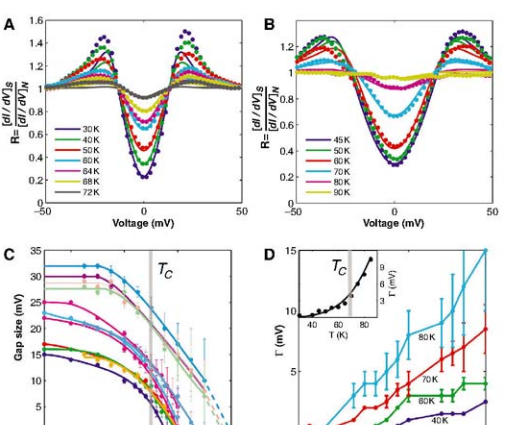

Fig. 2. (A and **B)** The conductance ratio $R = [dI/dV(V,T)]/[dI/dV(V,T>>T_c)]$ (circles) obtained by dividing the raw spectra in Fig. 1, A and B, by the high-temperature background spectrum. Fits to the conductance ratio with the use of a thermally broadened *d*-wave BCS model are depicted as lines. In general, the fits work well at low V where the slope of the conductance ratio is inversely proportional to the gap. **(C)** Extracted values of the pairing gap for several different locations plotted as a function of temperature. The resistive T_c is indicated by the gray line. **(D)** Extracted lifetime broadening at different temperatures plotted as a function of the corresponding low-temperature gap. (Inset) The average lifetime broadening as a function of temperature. Error bars in (C) and (D) indicate the SD of the fits.

tronic excitations in the sample are still spatially inhomogeneous at temperatures well above that when pairs first form in the sample. The spatial inhomogeneity of the normal state's electronic excitations can be measured by means of conductance (dI/dV) maps at various voltages, which show variations on the length scale of order 20 Å (Fig. 4, B and D to I). The magnitude of the variations is strongest for the conductance map obtained at the Fermi level (Fig. 4B), but such variations persist up to a few hundred millielectron volts.

The spatial variations of the normal-state conductance can be compared with the low-temperature variations of the gap by means of our lattice-tracking technique. Shown in Fig. 4C is a gap map measured at 50 K over the exact same area of the sample as in Fig. 4B (*41*). We can see a marked similarity between this gap map and the conductance map at the Fermi energy (Fig. 4B): Regions with a lower normal-state conductance at the Fermi level nucleate superconducting gaps at higher temperatures, resulting in larger low-temperature gaps. Quantifying these correlations in Fig. 5A, we show that the normal-state conductance map and the low-temperature gap map are strongly anticorrelated (–0.75). Further, both these maps have very similar autocorrelation lengths, indicating that the spatial variation of the normal state is intimately linked to that of the low-temperature gap. These measurements show that the variation of the superconducting state in $Bi_2Sr_2CaCu_2O_{8+\delta}$ samples, which for typical superconductors is characterized by a temperature-dependent superconducting coherence length, appears to be primarily determined by the spatial variation of the normal state.

Because our measurements show that the spatial variation of the normal-state conductance and the low-temperature pairing gap maps are intimately connected, we can associate an average normal-state spectrum with a low-temperature gap value. We thus average together normal-state spectra of regions of the sample that show identical low-temperature gaps and plot these average spectra in Fig. 5B. Systematic differences in the normal-state spectra foreshadow the eventual variation of the gap in the superconducting state. In particular, the systematic shift of a "hump" in the normal-state tunneling spectra at negative bias, in the range of –150 to –300 meV (Fig. 5C), as well as the value of tunneling conductance at the Fermi energy (Fig. 5B, inset), tracks the size of the superconducting gap observed at low temperatures. Whereas both the tunneling matrix element and the density of states of the tip influence the shape of the tunneling conductance in the normal state, the features of the normal state and the correlation (Fig. 5) have been observed in measurements with several different microtips (*42*).

It is important to compare our measurements of the normal state with those obtained from other spectroscopic techniques. In both angle-resolved photoemission and optical spectroscopy, strong renormalization of the single-particle excitations has been observed over an energy range of ~200 to 400 meV below the Fermi energy in $Bi_2Sr_2CaCu_2O_{8+\delta}$ samples (*17–20*, *38*, *43–45*). Such effects have been interpreted either as a result of the coupling of electrons with a spectrum of bosonic excitations (such as spin fluctuations) or as a consequence of the energy band structure (such as the bilayer splitting) of this compound (*19*, *46*). Although strong electron-boson coupling can be expected to modify the shape of the normal-state spectrum, it is difficult to associate the normal-state features that we measure with coupling to bosonic excitations because of their strong electron-hole asymmetry. Although we cannot rule out bosonic excitations as the origin of these features, candidate bosons would have to couple very asymmetrically to the tunneling of electrons and holes. Assigning these features to effects calculated from a simple non-interacting band structure can also be questioned, given both the strong spatial variation at the atomic scale of the normal-state spectra reported here and the strong renormalization of single-particle states at similar energies in other spectroscopic studies of the normal state. Instead, these features might be the excitations of a doped Mott insulator where the electron and hole excitations are naturally asymmetric as a consequence of the strong Coulomb interaction (*47–49*). Some recent calculations indeed produce a hump in hole-like excitations that correlate with the strength of pairing (*47*, *49*). Although there is no clear consensus on the right model for these excitations, our experiments show that the spectroscopic features of this state are indeed the origin of the nanoscale variation of the pairing strength in the superconducting state. Further experiments in samples at different hole-doping levels at higher temperatures will be required to provide the detailed evolution of these atomic-scale spectroscopic features of the normal state across the phase diagram.

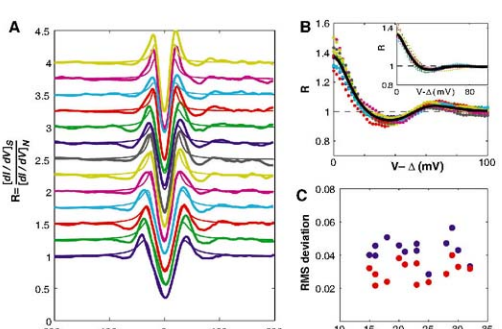

Fig. 3. **(A)** The low-temperature (T = 30 K) conductance ratio plotted for several different gaps. The conductance ratios deviate systematically from the d-wave model (Eq. 1, thin lines) and go below unity over a range of voltages (50 to 80 mV), indicating the strong coupling to bosonic modes. **(B)** The positive-bias conductance ratios are referenced to the local gap at different locations, showing that the magnitude of the dip-hump feature is similar at all locations. The line is the average of all the locations. (Inset) Gap-referenced conductance ratios for negative bias. **(C)** The RMSD of the conductance ratios from the d-wave model for positive (blue circles) and negative (red circles) bias over the energy range 20 to 120 mV. No correlation is seen between the magnitude of the deviations and the size of the gap.

Concluding remarks. From a broader perspective, we have used the spatial variation of the pairing gaps, which gives rise to a range of pairing temperatures in nanoscale regions of our samples, as a diagnostic tool to find clues to the underlying mechanism of superconductivity. Temperature-dependent lattice-tracking spectroscopy has allowed us to demonstrate that electron-boson coupling in the 20- to 120-meV range does not cause the variation of pairing gaps and onset temperatures in our samples. In contrast, we find that the high-energy (up to ~400 mV) hole-like excitations of the normal state are a direct predictor of the strength of pairing and its spatial variation. The anticorrelation between the normal-state conductance at the Fermi level and local strength of pairing also runs contrary to a BCS-like pairing mechanism, where the coupling to bosons is proportional to the density of states at the Fermi energy (*2*).

Finally, we address the underlying cause of variations of the normal-state excitations in $Bi_2Sr_2CaCu_2O_{8+\delta}$ samples. Our analysis finds that both structural and electronic features of the samples contribute to such variations. We find that there are small correlations (about 10%) of the normal-state conductance maps with the

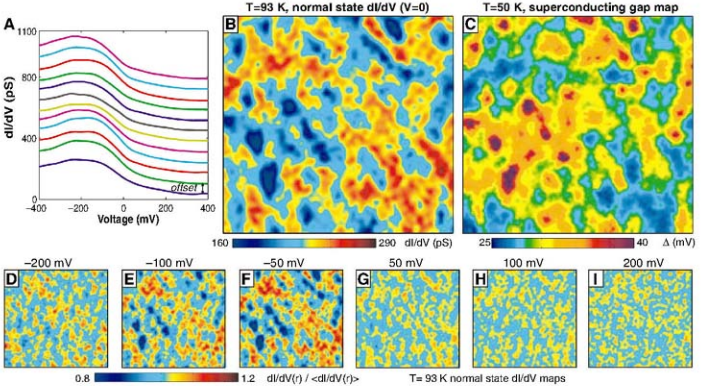

Fig. 4. **(A)** Spectra obtained at evenly spaced locations along a 250 Å line in the normal state (T = 93 K) of an OV62 sample. Less than 1% of the sample shows a remnant of a gap at this temperature. **(B)** Differential conductance map at the Fermi energy obtained at 93 K. **(C)** Low-temperature (50 K) gap map obtained on the same area as in (B). **(D** to **I)** Spatial maps of the conductance at different energies obtained in the normal state. The junction is stabilized at 1 V and 40 pA where there is minimum topographic disorder. Whereas conductance maps at high energies show mostly structural features (*b*-axis supermodulation), the low-energy spectra are inhomogeneous on the ~15 Å length scale.

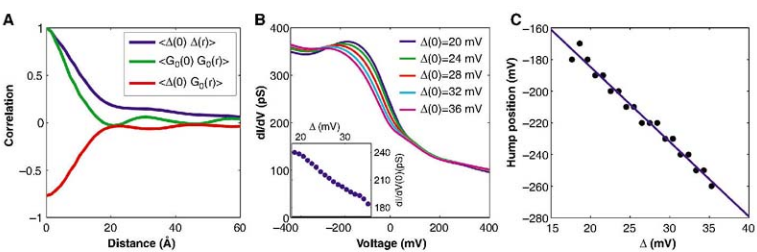

Fig. 5. **(A)** Angle-averaged autocorrelation of the low-temperature gap map in Fig. 4C (blue line), autocorrelation of the conductance map in Fig. 4B (green line), and cross correlation between the two images (red line). All the correlation lengths are similar (~15 Å), and there is a strong anticorrelation between the normal-state Fermi level conductance and the low-temperature gap map. **(B)** Average normal-state (T = 93 K) spectra measured in different regions that show distinct low-temperature superconducting gaps Δ_0. Systematic changes are seen in the shape and position of the hump feature seen for the hole-like excitations. (Inset) Differential conductance of the normal state at the Fermi energy as a function of Δ_0. **(C)** The energy corresponding to the hump feature in the spectra as a function of Δ_0.

structural supermodulation along the b axis in these samples. Similarly, we find that maps of electronic resonances around −900 meV, previously probed in similar samples with STM (*50*), are correlated with the normal-state conductance maps (about 30%) (SOM). Our measurements show that structural and chemical inhomogeneity affects both the excitations of the normal state and the superconducting gap. As is common to several correlated systems, many structural and electronic features can influence the onset and strength of collective phenomena (*51*). Our ability to correlate nanoscale excitation spectra between two distinct electronic states at the same atomic site provides the capacity to study correlated phenomena in compounds with heterogeneous chemical and structural properties.

References and Notes

1. J. R. Schrieffer, *Theory of Superconductivity* (W. A. Benjamin, New York, 1964).
2. J. Carbotte, *Rev. Mod. Phys.* **62**, 1027 (1990).
3. P. W. Anderson, *Science* **235**, 1196 (1987).
4. P. W. Anderson *et al.*, *J. Phys. Condens. Matter* **16**, R755 (2004).
5. P. W. Anderson, *Science* **316**, 1705 (2007).
6. Y. Sidis *et al.*, *Phys. Status Solidi B* **241**, 1204 (2004).
7. E. Dagotto, S.-C. Zhang, *Nature* **396**, 733 (1998).
8. J. P. Carbotte, E. Schachinger, D. N. Basov, *Nature* **401**, 354 (1999).
9. N. E. Bickers, D. J. Scalapino, S. R. White, *Phys. Rev. Lett.* **62**, 961 (1989).
10. A. J. Millis, H. Monien, D. Pines, *Phys. Rev. B* **42**, 167 (1990).
11. A. V. Chubukov, D. Pines, J. Schmalian, in *The Physics of Superconductors*, K. H. Bennemann, J. B. Ketterson, Eds. (Springer-Verlag, Berlin, 2003), pp. 495–590.

12. J. Hwang, T. Timusk, G. D. Gu, *Nature* **427**, 714 (2004).
13. C. M. Varma, *Phys. Rev. B* **55**, 14554 (1997).
14. A. Lanzara *et al.*, *Nature* **412**, 510 (2001).
15. J. Lee *et al.*, *Nature* **442**, 546 (2006).
16. J. P. Zasadzinski *et al.*, *Phys. Rev. Lett.* **87**, 067005 (2001).
17. J. C. Campuzano, M. R. Norman, M. Randeria, in *The Physics of Superconductors*, K. H. Bennemann, J. B. Ketterson, Eds. (Springer-Verlag, Berlin, 2003), pp. 167–265.
18. T. Cuk *et al.*, *Phys. Status Solidi B* **242**, 11 (2005).
19. J. Fink *et al.*, in *Very High Resolution Photoelectron Spectroscopy*, S. Hüfner, Ed. (Springer, Berlin, 2007), pp. 295–325.
20. J. Hwang, E. J. Nicol, T. Timusk, A. Knigavko, J. P. Carbotte, *Phys. Rev. Lett.* **98**, 207002 (2007).
21. D. J. Scalapino, *Nat. Phys.* **2**, 593 (2006).
22. C. Howald, P. Fournier, A. Kapitulnik, *Phys. Rev. B* **64**, 100504 (2001).
23. S. H. Pan *et al.*, *Nature* **413**, 282 (2001).
24. K. K. Gomes *et al.*, *Nature* **447**, 569 (2007).
25. J. Bardeen, *Science* **181**, 1209 (1973).
26. W. L. McMillan, J. M. Rowell, *Phys. Rev. Lett.* **14**, 108 (1965).
27. D. J. Scalapino, J. R. Schrieffer, J. W. Wilkins, *Phys. Rev.* **148**, 263 (1966).
28. G. M. Eliashberg, *Sov. Phys. JETP* **11**, 696 (1960).
29. W. L. McMillan, J. M. Rowell, in *Superconductivity*, R. D. Parks, Ed. (Dekker, New York, 1969), pp. 561–613.
30. M. C. Boyer *et al.*, *Nat. Phys.* **3**, 802 (2007).
31. J. M. Valles, S.-Y. Hsu, R. C. Dynes, J. P. Garno, *Physica B (Amsterdam)* **197**, 522 (1994).
32. M. Le Tacon *et al.*, *Nat. Phys.* **2**, 537 (2006).
33. R. C. Dynes, V. Narayanamurti, J. P. Garno, *Phys. Rev. Lett.* **41**, 1509 (1978).
34. A. C. Fang *et al.*, *Phys. Rev. Lett.* **96**, 017007 (2006).
35. M. R. Norman, M. Randeria, H. Ding, J. C. Campuzano, *Phys. Rev. B* **57**, R11093 (1998).
36. S. Pilgram, T. M. Rice, M. Sigrist, *Phys. Rev. Lett.* **97**, 117003 (2006).
37. F. C. Niestemski *et al.*, *Nature* **450**, 1058 (2007).
38. M. Eschrig, M. R. Norman, *Phys. Rev. B* **67**, 144503 (2003).
39. R. C. Dynes, J. M. Rowell, *Phys. Rev. B* **11**, 1884 (1975).
40. K. E. Kihlstrom, T. H. Geballe, *Phys. Rev. B* **24**, 4101 (1981).
41. On changing the temperature, the sample drifts laterally relative to the tip. We obtain large data sets at each temperature that include a common field of view. The topographic features are then used to crop the area common to all temperatures to within 2 Å.
42. The tunneling conductance depends on a matrix element that may have energy dependence over several hundred millielectron volts. The spectral shapes of the normal state shown in Figs. 4 and 5 have been reproduced with several tips made from both Pt/Ir as well as W. The position of the hump can vary by up to 100 mV between tips.
43. D. van der Marel *et al.*, *Nature* **425**, 271 (2003).
44. W. Meevasana *et al.*, *Phys. Rev. B* **75**, 174506 (2007).
45. J. Graf *et al.*, *Phys. Rev. Lett.* **98**, 067004 (2007).
46. A. Damascelli, Z. Hussain, Z.-X. Shen, *Rev. Mod. Phys.* **75**, 473 (2003).
47. A. Paramekanti, M. Randeria, N. Trivedi, *Phys. Rev. Lett.* **87**, 217002 (2001).
48. P. W. Anderson, *Nat. Phys.* **2**, 626 (2006).
49. K. Haule, G. Kotliar, *Phys. Rev. B* **76**, 104509 (2007).
50. K. McElroy *et al.*, *Science* **309**, 1048 (2005).
51. E. Dagotto, *Science* **309**, 257 (2005).
52. Our studies were inspired by discussions with D. J. Scalapino and P. W. Anderson. We also thank R. Melko and D. J. Scalapino for help with the analysis of the low-energy electron-boson coupling. The work at Princeton is supported by the U.S. Department of Energy (DOE) under contract DE-FG02-07ER46419 and NSF through the Princeton Center for Complex Materials. Y.A. was supported by KAKENHI 19674002. The work in BNL is supported by DOE under contract DE-AC02-98CH10886.

Supporting Online Material

www.sciencemag.org/cgi/content/full/320/5873/196/DC1
SOM Text S1 and S2
Figs. S1 and S2
References

28 December 2007; accepted 27 February 2008
10.1126/science.1154700

Surface Mobility of Postsynaptic AMPARs Tunes Synaptic Transmission

Martin Heine,[1]* Laurent Groc,[1] Renato Frischknecht,[1] Jean-Claude Béïque,[3] Brahim Lounis,[2] Gavin Rumbaugh,[3] Richard L. Huganir,[3] Laurent Cognet,[2] Daniel Choquet[1]†

AMPA glutamate receptors (AMPARs) mediate fast excitatory synaptic transmission. Upon fast consecutive synaptic stimulation, transmission can be depressed. Recuperation from fast synaptic depression has been attributed solely to recovery of transmitter release and/or AMPAR desensitization. We show that AMPAR lateral diffusion, observed in both intact hippocampi and cultured neurons, allows fast exchange of desensitized receptors with naïve functional ones within or near the postsynaptic density. Recovery from depression in the tens of millisecond time range can be explained in part by this fast receptor exchange. Preventing AMPAR surface movements through cross-linking, endogenous clustering, or calcium rise all slow recovery from depression. Physiological regulation of postsynaptic receptor mobility affects the fidelity of synaptic transmission by shaping the frequency dependence of synaptic responses.

The fidelity of synaptic transmission between coupled neurons depends on their ability to transmit activity over a wide range of frequencies. Because of the relative slowness of chemical transmission, synaptic transmission acts as a low-pass filter with a cutoff between 10 and 100 Hz (*1*). When a presynaptic cell is stimulated at repetitive short intervals, the postsynaptic response usually decreases over time, the rate of depression being faster as the stimulus frequency increases (*2*). Most studies explain paired-pulse depression (PPD) as a combination of depression of presynaptic glutamate release and intrinsic kinetic properties of postsynaptic AMPARs upon agonist binding (*2*). Return from depression is believed to arise from recovery of release, together with AMPAR exit from desensitization. This assumes that AMPARs are stable within the postsynaptic density (PSD). Dynamic imaging has shown that AMPARs are not static but diffuse rapidly at the surface of neurons, traveling micrometer distances per second by random movements both in the synaptic and extrasynaptic membranes (*3*–*8*). Traffic of AMPARs from and to synapses through endo/exocytosis takes place in tens of minutes (*9*, *10*). However, lateral diffusion allows AMPARs to explore the synapse in the second range (*6*, *8*, *11*), which suggests that surface AMPAR trafficking might be implicated in faster processes.

Cross-linking of surface AMPARs decreases the coefficient of variation and increases PPD. We measured the variations in the efficacy of synaptic transmission in response to changes in AMPAR mobility by specific cross-linking (X-link) of GluR2-AMPARs with antibodies against their extracellular N-terminal domains (*4*, *11*) (fig. S1, A and B). Pairs of monosynaptically connected cultured hippocampal neurons were recorded using dual whole-cell recordings (Fig. 1A, fig. S1, C and D, and table S1) (*12*). Evoked excitatory postsynaptic currents (eEPSCs) were not affected by X-link (fig. S1, E to G). The coefficient of variation (CV) of eEPSCs over time and paired eEPSCs are classically used to measure synaptic transmission variability (*13*). Interestingly, the CV after X-link was lower than in control (control, 0.33 ± 0.02; X-link, 0.25 ± 0.02; *t* test, $P < 0.05$) (Fig. 1, B and C). Furthermore, paired-pulse eEPSCs at 50-ms intervals displayed PPD for the majority of the recorded neuron pairs (24 out of 31) (Fig. 1D). The remaining neuron pairs displayed paired-pulse facilitation. After X-link of GluR2, pairs displayed a more pronounced PPD, measured as a decrease in paired pulse ratio (PPR) (PPR in control, 0.86 ± 0.02; after X-link, 0.71 ± 0.04; *t* test, $P < 0.05$) (Fig. 1, D and E).

Variations in CV and PPR are usual hallmarks of presynaptic changes (*2*, *13*). GluR2 X-link should in contrast lead to changes in postsynaptic properties. Rapid AMPAR movements inside synapses (*6*–*8*) or between synaptic and extrasynaptic sites (*4*, *6*, *8*, *11*), could theoretically lead to variations in AMPARs' density at the postsynaptic side causing variability in eEPSCs, including in the rate of recovery from PPD, by regulating the exchange of desensitized receptors for naïve receptors.

AMPAR mobility inside synapses. To measure the fraction of surface receptors that are mobile in the extrasynaptic membrane or within a spine head both in CA1 pyramidal neurons from hippocampal slices and in cultured hippocampal neurons, we used fluorescence recovery after photobleaching (FRAP) on AMPAR sub-

[1]CNRS, UMR 5091, Université Bordeaux, Bordeaux, France. [2]Centre de Physique Moleculaire Optique et Hertzienne, CNRS, UMR 5798, Université Bordeaux, Talence, France. [3]Department of Neuroscience, Johns Hopkins University, Baltimore, MD, USA. [4]Leibniz Institut für Neurobiologie, Magdeburg, Germany.

*Present address: Leibniz Institut für Neurobiologie, Magdeburg, Germany.

†To whom correspondence should be addressed: dchoquet@u-bordeaux2.fr

units tagged at their N termini with super-ecliptic pHluorin (*4*), a pH-sensitive form of green fluorescent protein (pHGFP) (Fig. 2, A to C, and fig. S2). GluR1::pHGFP was mostly homogenously distributed along the spines and dendrites, with occasional spines displaying strongly clustered GluR1::pHGFP. In contrast, GluR2::pHGFP was more systematically clustered within spine heads (fig. S2, A and B). A significant fluorescence recovery occurred in both shaft dendrite (~60% in 60 s) and spines (~30%) in hippocampal brain slices (Fig. 2, A to C), indicating that GluR2-AMPAR are mobile in intact hippocampi, as in cultured neurons (*5*, *7*–*9*). In cultures, GluR1::pHGFP and GluR2::pHGFP fluorescence also recovered after photobleaching, to a higher extent in extrasynaptic areas than in synaptic ones. About half of AMPARs exchanged from an extrasynaptic to a synaptic location for GluR2::pHGFP and nonclustered GluR1::pHGFP (Fig. 2C).

Individual GluR1- and GluR2-AMPARs were tracked using single quantum dots or organic dyes (*6*–*8*, *11*, *12*, *14*). Synapses were identified by Mitotracker (*7*, *8*) or the excitatory postsynaptic protein Homer1C::DsRed (*15*). In control, 70% of GluR1-AMPARs were mobile in the postsynaptic membrane, and half of this population exchanged continuously between synaptic and extrasynaptic domains, the other half being mobile but confined in the synapse (Fig. 2D and fig. S3) (*3*, *4*, *6*–*8*, *11*). The instantaneous diffusion coefficient, D, of mobile synaptic receptors ($D > 0.0075$ $\mu m^2/s$) was comparable for quantum dot (QD) or single dye (SD)–labeled receptors (Fig. 2E). These exchanging AMPARs only dwell for a few seconds in the synapse (Fig. 2G and fig. S3); the remaining AMPARs were transiently immobile. As expected, antibody-induced AMPARs X-link massively reduced receptor mobility and suppressed the exchange of receptors between synaptic and extrasynaptic sites (fig. S1, A and B).

AMPAR mobility contributes to recovery from PPD. Because PPD has been mainly envisioned as influenced by presynaptic processes (*2*, *13*), we investigated the effect of receptor immobilization on isolated postsynaptic AMPAR-mediated currents. For this, glutamate-evoked currents were recorded in whole-cell mode using rapid iontophoretic glutamate application onto synapses (identified by Homer1C::DsRed) (figs. S4 and S5). In control, application of glutamate for 1 ms with iontophoretic currents of ~100 to 200 nA evoked inward currents of 130.4 ± 11 pA ($n = 37$) with fast rise and decay times (Fig. 3A and fig. S5). When paired glutamate applications were applied, the second response was depressed (Fig. 3 and fig. S5). The extent of depression decreased as the time interval between paired glutamate applications increased, as expected from AMPARs' recovery from desensitization (*16*–*19*). Indeed, PPD was abolished by cyclothiazide (50 μM) (Fig. 3, A and B, and fig. S6A), an antagonist of AMPAR desensitization (*20*, *21*).

However, AMPAR immobilization through X-link reduced the response amplitude to the second contiguous glutamate application (Fig. 3, A and B). The X-link–induced reduction in paired-pulse ratio was dependent on the interstimulus interval, with a maximal effect (factor 2) for short intervals (10 to 20 ms) and no effect over 200 ms. Receptor X-link thus modified the characteristic time and the extent of recovery from depression.

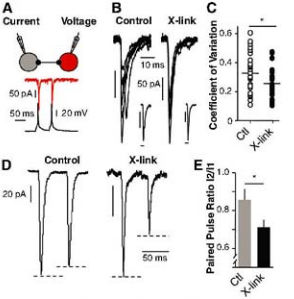

Fig. 1. AMPAR immobilization increases PPD and decreases variability. **(A)** Sample whole-cell recordings of a connected pair of cultured hippocampal neurons. The presynaptic neuron was recorded in current-clamp at 0 pA and the postsynaptic neuron voltage-clamped at −60 mV. A pair of depolarizing pulses in the presynaptic cell separated by 50 ms triggered action potentials that each elicited an AMPAR-mediated EPSC in the postsynaptic neuron. **(B)** Series of evoked EPSCs elicited at 10-s intervals in control conditions or at least 10 min after X-link surface GluR2-containing AMPARs with an antibody to GluR2 followed by a secondary antibody to immunoglobulin G (IgG). **(C)** Plot of the coefficient of variation of EPSCs recorded as in (B) in 24 cells. GluR2 X-link decreases variability. $P < 0.05$. **(D** and **E)** Paired-pulse traces of EPSCs recorded as in (A) in control conditions or at least 10 min after X-link surface GluR2. These are different cells from the same culture batch.

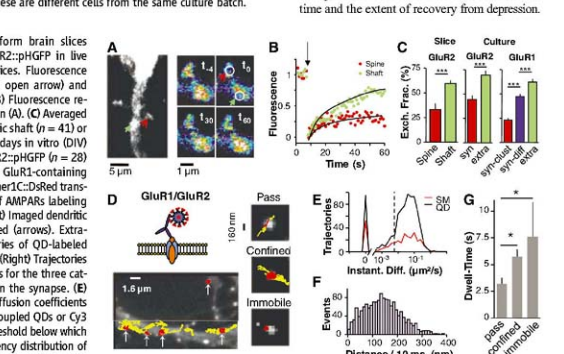

Fig. 2. Mobility of AMPARs in synapses form brain slices and cultured neurons. **(A)** Imaging of GluR2::pHGFP in live CA pyramidal neurons from hippocampal slices. Fluorescence was photobleached (t_0) in spine (circles, red open arrow) and dendritic shaft (circles, green filled arrow). **(B)** Fluorescence recovery versus time in the photobleached areas in (A). **(C)** Averaged recovered fraction of GluR2::pHGFP in dendritic shaft ($n = 41$) or spine ($n = 19$) in hippocampal slices and 21 days in vitro (DIV) cultured hippocampal neurons expressing GluR2::pHGFP ($n = 28$) or GluR1::pHGFP ($n = 40$). **(D)** Trajectories of GluR1-containing AMPARs on dendrites of a 21-DIV cultured Homer1C::DsRed transfected hippocampal neuron. (Top) Diagram of AMPARs labeling with a QD through GluR1 antibody. (Bottom left) Imaged dendritic segment. Postsynaptic sites accumulate DsRed (arrows). Extrasynaptic (yellow) and synaptic (red) trajectories of QD-labeled GluR1 receptors recorded for 66 s are plotted. (Right) Trajectories on Homer1C::DsRed labeled postsynaptic sites for the three categories of observed diffusion behaviors within the synapse. **(E)** Histogram distribution of the instantaneous diffusion coefficients of synaptic trajectories obtained from GluR1-coupled QDs or Cy3 single dye molecule (SM). Dotted line is the threshold below which receptors are counted as immobile. **(F)** Frequency distribution of the displacement ($\Delta t = 10$ ms) of mobile GluR1 receptors within the synapse (median = 0.14 nm ± interquartile range (IQR) 0.08/0.19 nm). **(G)** Histogram of the mean ± SEM dwell time of GluR1 receptors in synapses, sorted by their diffusion properties ($n = 10$). For immobile receptors, only those transiently stabilized in the synapse are counted. $P < 0.05$.

PPD was absent at extrasynaptic sites (PPR = 1.12 ± 0.15; n = 4), where AMPARs are more mobile and not confined (fig. S3) (*4*, *7*, *8*). Activation of successive AMPAR currents by two-photon 4-methoxy-7-nitroindolinyl-caged L-glutamate (MNI-glutamate) uncaging (2P-EPSCs) (*22*) provided comparable sensitivity to X-link, although a significant PPD was already present in control conditions at synaptic and extrasynaptic sites (Fig. 3, C and D, and fig. S7). In control, PPR was significantly higher after uncaging onto shaft regions compared with uncaging at the tip of closely located spines, where receptors are less mobile (Fig. 2). After GluR1 X-link, PPR onto shafts was decreased compared with controls and was no longer different than that onto spines (Fig. 3, C and D).

Several controls were performed to refute the possibility that antibody X-link modified the amount of recovery from depression through changes of receptor desensitization. First, primary antibody binding to the receptors did not modify the basic properties of mEPSCs (fig. S8, A and B). Second, X-link of the receptors did not modify individual glutamate-evoked iontophoretic responses (fig. S8, C to G). Third, the application of cyclothiazide totally abolished the decrease in recovery rate between glutamate applications induced by receptor X-link (Fig. 3, A and B, and fig. S7). Fourth, the kinetic properties of AMPARs were identical with and without antibodies, as measured in excised outside-out recordings (fig. S9).

The recovery from depression did not depend on receptor mobility during glutamate application to large membrane areas [iontophoretic current > 300 nA/1 ms (Fig. 3E); activated area ~2.5 μm (fig. S5C)]. At low iontophoretic currents (I < 100 nA/1 ms), receptors were activated over a small area (<0.5 μm) (Fig. 3E and fig. S5C), and PPD was only present after receptor immobilization. The parallel decrease in PPR and increase in iontophoretic current likely reflect prolonged presence of glutamate to desensitize receptors (*18*, *23*, *24*). That receptor immobilization only modifies PPR at low iontophoretic current amplitudes suggests that recovery from depression due to receptor movements in a large glutamate application zone is slower than the rate of recovery from desensitization of individual receptors.

To investigate this, we used the rapidly dissociating glutamate receptor antagonist kynurenic acid (Kyn) to modify the apparent spatiotemporal glutamate waveform. Kyn generates a block that is inversely related to glutamate concentration (*25*). Kyn (1 mM) reduced the current amplitude and accelerated the decay of iontophoretically elicited AMPAR currents (Fig. 3G) (*25*). The presence of Kyn reduced PPD in control but not in X-linked conditions (Fig. 3F). In the presence of Kyn, the area where AMPARs are activated and/or desensitized is smaller, allowing for their faster exchange with naïve AMPARs during the interpulse interval.

Interplay between AMPAR diffusion and recovery from PPD. To study the respective contributions of AMPAR recovery from desensitization and AMPAR mobility to the recovery from PPD, we took advantage of the fact that pHGFP::GluR1 can be either clustered or diffuse at synaptic sites, with slower mobility when clustered (Fig. 2C and fig. S2). Overexpression of the GluR1 subunit increases the formation of GluR1 homomeric receptors (*26*), which desensitize faster than heteromeric receptors but recover from desensitization one-third as fast (*27*). Thus, the rate of recovery from PPD should reflect the prolonged exit of receptors from a desensitized state mainly when lateral diffusion rate is low.

PPD was similar at synaptic sites of nontransfected neurons and at synapses expressing diffuse pHGFP::GluR1 in transfected neurons. In contrast, synapses with clustered pHGFP::GluR1 displayed a much stronger PPD (Fig. 4, A to C). Thus, recovery from PPD is dominated by receptor diffusion when pHGFP::GluR1 is highly mobile, whereas it is dominated by the intrinsic kinetic properties of GluR1 when pHGFP::GluR1 has a low mobility. We therefore specifically immobilized pHGFP::GluR1 containing receptors by X-link with an antibody to GFP (Fig. 4, A to C). PPD was strong in areas of clustered receptors, approaching the value obtained for not X-linked but clustered pHGFP::GluR1 receptors. PPD was more pronounced for immobilized GluR1

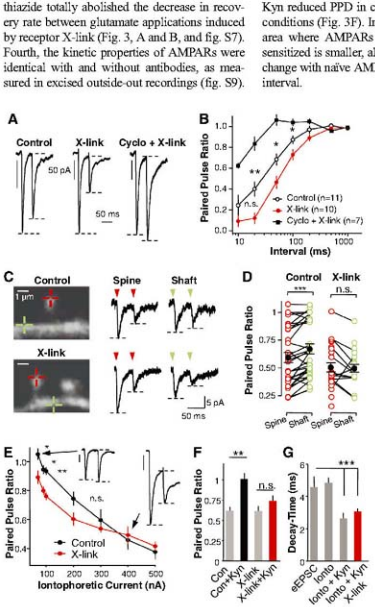

Fig. 3. AMPAR immobilization impedes recovery from depression during paired-pulse application of glutamate. **(A)** Whole-cell recordings of currents elicited by paired iontophoretic applications of glutamate to synaptic sites in control neurons (left), after X-link surface GluR2-containing AMPARs without (middle) or with (right) 50 μM cyclothiazide. Pulse interval is 50 ms; traces are averaged from 10 recordings. **(B)** Plot of the recovery rate as a function of interpulse interval; control (n = 11), X-link GluR2 (n = 15), with 50 μM cyclothiazide (n = 10). **(C)** (Left) Confocal images of individual spines and surrounding shaft area used to induce successive (50 ms apart) 2P-EPSCs in control (top) or after X-link of GluR1 (bottom). Uncaging spots were positioned (crosses) either at the spine tip (red) or on shaft (green). (Right) Current traces, uncaging at arrows. **(D)** Scattered plots of PPRs of 2P-EPSCs induced at spines or shaft regions in control conditions (n = 33 spines and shafts) and after X-link of GluR1 (n = 28 spines; shaft n = 22). Mean ± SEM is indicated by the black dots, and pairs of closely positioned spines and shafts are indicated by the connected lines (***P < 0.01). **(E)** Plot of the PPR versus applied iontophoretic current amplitude; control (n = 13), X-link (n = 8). (Insets) Sample traces for paired iontophoretic glutamate application (left, 90 nA/1 ms; right, 400 nA/1 ms). Scale bar, 50 pA (left), 100 pA (right). **(F)** Mean ± SEM of PPR for paired iontophoretic glutamate application (200 nA/1 ms) in control or after X-link of GluR2, without (Con) or with 1 mM kynurenic acid (Kyn) under the indicated conditions. n = 5 for each condition. **(G)** Mean ± SEM decay time constant of EPSCs, of currents evoked by iontophoretic glutamate application (200 nA/1 ms) in control (ionto), with 1 mM kynurenic acid (Kyn) before or after X-link of GluR2 (kyn + X-link).

containing clusters than immobilized wild-type AMPARs that recover faster from desensitization (*27*). The rectification index showed that the relative proportion of homomeric GluR1 receptors at synapses did not correlate with the clustered state of GluR1 and was unchanged by X-link (Fig. 4, D and E).

Calcium-induced AMPAR immobilization increases PPD. Because spontaneous clustering of AMPARs modified the extent of PPD, physiological processes that regulate AMPARs' mobility might also regulate PPD. AMPAR mobility is strongly decreased by local rises in intracellular calcium (*5*). We explored whether an increase in calcium triggered by physiological synaptic stimulations also modifies PPD. Stimulation of a large population of synapses at 50 Hz, but not 5 Hz, induced a profound decrease in AMPARs' mobility (Fig. 5A). This immobilization was stronger for GluR1 than GluR2 (explored surface, percentage of control, GluR2 83.1 ± 4%, GluR1 50 ± 5%, 5 min after stimulation). Stimulations of 50 Hz induced a stronger immobilization at synaptic than at extrasynaptic sites, accompanied by a reduction in the percentage of receptors that exchange between synaptic and extrasynaptic sites (Fig. 5, B to D). This immobilization was due to rises in intracellular calcium through activation of calcium-permeable *N*-methyl-D-aspartic acid receptors (NMDARs) (Fig. 5D and fig. S10) and did not alter the proportion of endocytosed GluR1-containing AMPARs (control 15 min, 12.5 ± 3%; 15 min after 50 Hz, 11.6 ± 4%). Diffusion of another membrane receptor N-Cam did not change after stimulation (Fig. 5, B and C). Immobilization of AMPARs was accompanied by an increase in PPD at a subpopulation of synapses after 50-Hz stimulation (Fig. 5, E and F), indicating that physiological immobilization of AMPARs also has an impact on recovery from synaptic depression.

Discussion. We report that AMPAR lateral diffusion influences synaptic transmission at different time scales. On the second to minutes time scale, the CV of synaptic currents depends in part on the surface trafficking of AMPARs that diffuse within the PSD and exchange between synaptic and extrasynaptic sites. In the tens of millisecond time scale, AMPAR lateral diffusion regulates the fast recovery from postsynaptic depression induced at high-frequency transmitter release. Consequently, we now propose that the rate of recuperation from synaptic depression results from the combination of the recovery of AMPAR from desensitization, the recuperation of transmitter release (*2*), and the fast lateral exchanges of desensitized receptors with naïve functional ones. In addition, the rate of AMPAR fluxes can be modulated in various physiological ways, such as clustering states or variations in intracellular calcium, and these regulations affect the synaptic signaling.

The role of AMPARs' desensitization during PPD at hippocampal synapses is debated (*18*, *28*–*31*), in part due to the absence of adequate tools (e.g., cyclothiazide having both pre- and postsynaptic effects) (*32*, *33*). The desensitization properties of AMPARs will depend on the glutamate clearance, particularly at synapses whose morphologies favor spillover from neighboring release sites (*19*, *34*–*39*). Measurements of AMPAR-mediated current amplitude and kinetics, as well as theoretical calculations, have suggested that the size of the field where receptors are occupied by glutamate only represents a subarea of the PSD that spans about 100 nm from the site of vesicle release and is only about 25% of the area of an average CA1 synapse for a single quantal release (*13*, *36*, *40*, *41*). At least 50% of the AMPARs are mobile at synaptic sites and can explore the whole PSD (*4*, *7*, *8*). Our single-molecule measurements, which likely underestimate receptor mobility (*42*), indicate that AMPARs can diffuse at rates above 0.25 $\mu m^2/s$ and can thus move >100 nm in 10 ms. This is sufficient to escape the area reached by glutamate within a short time (*13*). Within a region of 200-nm diameter, calculations indicate that ~30% of receptors are replaced within 10 ms by diffusion at 0.1 $\mu m^2/s$ (figs. S11 and S12C). Thus, the replacement of desensitized receptors occurs at a characteristic time (50% in 30 ms if all receptors are mobile at 0.1 $\mu m^2/s$ and escape from a 200-nm zone) similar to, or even faster than, that of the recovery of individual AMPAR from desensitization (50% in 40 to 60 ms). Along this line, PPR was more pronounced with uncaging than with iontophoresis, even at low amplitudes of AMPAR-mediated currents, likely due to the larger size of the uncaging spot versus the iontophoretic one.

The extent of frequency-induced synaptic depression depends on desensitization, glutamate release, and postsynaptic receptor redistribution rate. This notion is supported by a theoretical model that combines previously established parameters of glutamate release in the synaptic cleft, AMPAR activation, and desensitization kinetics schemes (*13*, *39*, *43*) with receptor mobility (fig. S11). The theoretical recovery of AMPAR currents from depression strongly depends on lateral diffusion, on the area over which receptors are activated, and on receptor confinement (fig. S12).

Postsynaptic receptors' mobility is acutely regulated by physiological processes such as temperature (*8*), depolarization (*7*), glutamate (*8*), and tetanic stimulations leading to calcium-induced immobilization of receptors (this study). These changes in the fraction of mobile receptors will affect frequency-dependent depression in parallel to presynaptic processes (*13*). This could be involved in providing a postsynaptic mechanism to modify the frequency dependence

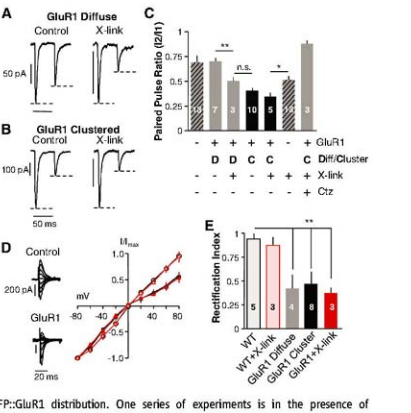

Fig. 4. Endogenous clustering of AMPARs increases PPD. (**A** and **B**) Sample whole-cell recordings of currents elicited by paired iontophoretic applications of glutamate to synaptic sites displaying diffuse (A) or clustered (B) GluR1 distribution in control neurons (left) or after X-link surface pHGFP::GluR1 by antibody to GFP (right). (**C**) Histograms of mean PPR ± SEM in the conditions exemplified in (A) and (B) and in controls. Measurements from recordings at Homer::DsRed synaptic sites in neurons expressing (GluR1+) or not (GluR1−) pHGFP::GluR1, with or without antibody to GFP–mediated X-link. Synaptic sites were sorted as bearing either a diffuse (D) or clustered (C) pHGFP::GluR1 distribution. One series of experiments is in the presence of cyclothiazide (Ctz). (**D**) (Left) Whole-cell currents elicited by iontophoretic applications of glutamate to synaptic sites recorded at various holding potentials in nontransfected (control) and pHGFP::GluR1 (GluR1)–expressing neurons. (Right) Plots of mean *I-V* curves for currents in the left. The curve is linear for control cells (empty circles), whereas it rectifies in pHGFP::GluR1-expressing neurons, at similar levels whether clustered (filled black circles) or diffuse (filled gray circles), indicating the higher proportion of GluR1 homomeric AMPARs. X-link either endogenous receptors with an antibody to GluR2 (empty triangles) or pHGFP::GluR1 with an antibody to GFP (filled triangles) does not modify the rectification index as compared to its matched control. (**E**) Mean + SEM of the rectification index in the indicated conditions.

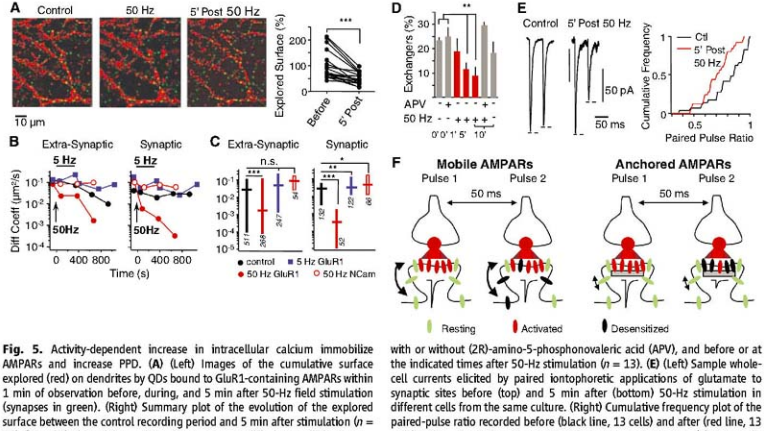

Fig. 5. Activity-dependent increase in intracellular calcium immobilize AMPARs and increase PPD. **(A)** (Left) Images of the cumulative surface explored (red) on dendrites by QDs bound to GluR1-containing AMPARs within 1 min of observation before, during, and 5 min after 50-Hz field stimulation (synapses in green). (Right) Summary plot of the evolution of the explored surface between the control recording period and 5 min after stimulation (n = 16). **(B** and **C)** Plots of the median of instantaneous diffusion coefficient versus time (B) or at 800 s (median ± IQR) of recording (C) for extrasynaptic (left) and synaptic (right) receptors. Both outside and inside synapses, stimulation at 5 Hz (blue squares) slightly increased receptor diffusion in comparison to the independent control (black circles), whereas 50-Hz stimulation (red circles) strongly decreased receptor mobility. Diffusion coefficient of N-cam (open red circles) was not changed after 50 Hz stimulation. **(D)** Plots of the mean fraction of GluR1 receptors that exchange between synaptic and extrasynaptic sites, with or without (2R)-amino-5-phosphonovaleric acid (APV), and before or at the indicated times after 50-Hz stimulation (n = 13). **(E)** (Left) Sample whole-cell currents elicited by paired iontophoretic applications of glutamate to synaptic sites before (top) and 5 min after (bottom) 50-Hz stimulation in different cells from the same culture. (Right) Cumulative frequency plot of the paired-pulse ratio recorded before (black line, 13 cells) and after (red line, 13 cells) 50-Hz stimulation. $P < 0.01$, Kolmogorov-Smirnov test. **(F)** Schematic diagram of the involvement of mobile AMPARs in regulating PPD. When AMPARs are largely mobile (left), AMPARs activated (red) and then desensitized (black) by a first glutamate release are rapidly exchanged by functional ones (green), which are then available for activation by a sequential glutamate release. In contrast, when AMPARs are immobilized (right), desensitized receptors remain in place, decreasing the amount of functional receptors available for activation by a sequential pulse.

of synaptic transmission after activity-dependent processes that trigger both short- and long-term synaptic plasticity.

References and Notes

1. E. S. Fortune, G. J. Rose, *Trends Neurosci.* **24**, 381 (2001).
2. R. S. Zucker, W. G. Regehr, *Annu. Rev. Physiol.* **64**, 355 (2002).
3. H. Adesnik, R. A. Nicoll, P. M. England, *Neuron* **48**, 977 (2005).
4. M. C. Ashby, S. R. Maier, A. Nishimune, J. M. Henley, *J. Neurosci.* **26**, 7046 (2006).
5. A. J. Borgdorff, D. Choquet, *Nature* **417**, 649 (2002).
6. M. D. Ehlers, M. Heine, L. Groc, M. C. Lee, D. Choquet, *Neuron* **54**, 447 (2007).
7. L. Groc *et al.*, *Nat. Neurosci.* **7**, 695 (2004).
8. C. Tardin, L. Cognet, C. Bats, B. Lounis, D. Choquet, *EMBO J.* **22**, 4656 (2003).
9. M. D. Ehlers, *Neuron* **28**, 511 (2000).
10. M. Passafaro, V. Piech, M. Sheng, *Nat. Neurosci.* **4**, 917 (2001).
11. C. Bats, L. Groc, D. Choquet, *Neuron* **53**, 719 (2007).
12. Materials and methods are available as supporting material on *Science* Online.
13. J. E. Lisman, S. Raghavachari, R. W. Tsien, *Nat. Rev. Neurosci.* **8**, 597 (2007).
14. M. Dahan *et al.*, *Science* **302**, 442 (2003).
15. Y. Sugiyama, I. Kawabata, K. Sobue, S. Okabe, *Nat. Methods* **2**, 677 (2005).
16. T. Otis, S. Zhang, L. O. Trussell, *J. Neurosci.* **16**, 7496 (1996).
17. K. M. Partin, M. W. Fleck, M. L. Mayer, *J. Neurosci.* **16**, 6634 (1996).
18. D. Colquhoun, P. Jonas, B. Sakmann, *J. Physiol.* **458**, 261 (1992).
19. I. M. Raman, L. O. Trussell, *Biophys. J.* **68**, 137 (1995).
20. L. O. Trussell, S. Zhang, I. M. Raman, *Neuron* **10**, 1185 (1993).
21. K. A. Yamada, C. M. Tang, *J. Neurosci.* **13**, 3904 (1993).
22. J. Bélque *et al.*, *Proc. Natl. Acad. Sci. U.S.A.* **103**, 19535 (2006).
23. B. K. Andrasfalvy, J. C. Magee, *J. Neurosci.* **21**, 9151 (2001).
24. M. A. Smith, G. C. Ellis-Davies, J. C. Magee, *J. Physiol.* **548**, 245 (2003).
25. J. S. Diamond, C. E. Jahr, *J. Neurosci.* **17**, 4672 (1997).
26. S. H. Shi *et al.*, *Science* **284**, 1811 (1999).
27. J. Grosskreutz *et al.*, *Eur. J. Neurosci.* **17**, 1173 (2003).
28. L. E. Dobrunz, C. F. Stevens, *Neuron* **18**, 995 (1997).
29. A. Arai, G. Lynch, *Brain Res.* **799**, 235 (1998).
30. G. O. Hjelmstad, J. T. Isaac, R. A. Nicoll, R. C. Malenka, *J. Neurophysiol.* **81**, 3096 (1999).
31. E. Hanse, B. Gustafsson, *J. Physiol.* **531**, 467 (2001).
32. T. Ishikawa, T. Takahashi, *J. Physiol.* **533**, 423 (2001).
33. J. S. Diamond, C. E. Jahr, *Neuron* **15**, 1097 (1995).
34. T. S. Otis, Y. C. Wu, L. O. Trussell, *J. Neurosci.* **16**, 1634 (1996).
35. M. A. Xu-Friedman, W. G. Regehr, *J. Neurosci.* **23**, 2182 (2003).
36. X. Xie, J. S. Liaw, M. Baudry, T. W. Berger, *Proc. Natl. Acad. Sci. U.S.A.* **94**, 6983 (1997).
37. M. V. Jones, G. L. Westbrook, *Trends Neurosci.* **19**, 96 (1996).
38. V. Scheuss, R. Schneggenburger, E. Neher, *J. Neurosci.* **22**, 728 (2002).
39. K. M. Franks, T. M. Bartol Jr., T. J. Sejnowski, *Biophys. J.* **83**, 2333 (2002).
40. K. M. Franks, C. F. Stevens, T. J. Sejnowski, *J. Neurosci.* **23**, 3186 (2003).
41. G. Liu, S. Choi, R. W. Tsien, *Neuron* **22**, 395 (1999).
42. L. Groc *et al.*, *J. Neurosci.* **27**, 12433 (2007).
43. P. Jonas, G. Major, B. Sakmann, *J. Physiol.* **472**, 615 (1993).

44. We thank E. Hanse, M. Ehlers, E. Gundelfinger, and A. Triller for helpful discussions; D. Perrais for outside-out experiments; C. Tigaret for producing the Sindbis pHGFP::GluR2 viral particles; C. Breillat, B. Tessier, and D. Bouchet for molecular biology and cell cultures; E. Normand for organotypic slice preparation; and E. Petrini for some control experiments. This work was supported by the Centre National de la Recherche Scientifique, the Conseil Régional d'Aquitaine, the Ministère de la Recherche, the Fondation pour la Recherche Médicale, the Human Frontier Science Program, the Association Française contre les Myopathies, European Community Grant CT-2005-005320, Howard Hughes Medical Institute (to R.L.H.), National Institute of Neurological Disorders and Stroke (to R.L.H.), the National Alliance for Research on Schizophrenia and Depression (to J.-C.B.), and postdoctoral fellowship HE-3604/1-1 for M.H. R.F. was supported by Deutsche Forschungsgemeinschaft project GU 230/5-2.

Supporting Online Material

www.sciencemag.org/cgi/content/full/320/5873/201/DC1
Materials and Methods
Figs. S1 to S12
Table S1
References

23 October 2007; accepted 15 February 2008
10.1126/science.1152089

Gate-Variable Optical Transitions in Graphene

Feng Wang,[1]* Yuanbo Zhang,[1] Chuanshan Tian,[1] Caglar Girit,[1,2] Alex Zetti,[1,2] Michael Crommie,[1,2] Y. Ron Shen[1,2]

Two-dimensional graphene monolayers and bilayers exhibit fascinating electrical transport behaviors. Using infrared spectroscopy, we find that they also have strong interband transitions and that their optical transitions can be substantially modified through electrical gating, much like electrical transport in field-effect transistors. This gate dependence of interband transitions adds a valuable dimension for optically probing graphene band structure. For a graphene monolayer, it yields directly the linear band dispersion of Dirac fermions, whereas in a bilayer, it reveals a dominating van Hove singularity arising from interlayer coupling. The strong and layer-dependent optical transitions of graphene and the tunability by simple electrical gating hold promise for new applications in infrared optics and optoelectronics.

Graphene, a single layer of honeycomb carbon lattice, exhibits many exotic behaviors, ranging from the anomalous quantum Hall effect (*1–3*) and Klein paradox (*4*) to coherent transport (*5*). In contrast to the extensive effort on electrical transport, optical study of graphene has been limited (*6–9*). Such optical investigation is important for understanding the electronic structures and excited-state properties of low-dimensional materials, as recently demonstrated in the case of carbon nanotubes, for example (*10*, *11*).

We have used infrared (IR) spectroscopy to probe interband optical transitions in monolayers and bilayers of graphene, which show distinctly different optical response. Unlike conventional materials, the optical transitions in graphene can be dramatically modified through electrical gating: The normalized gate-induced changes in transition strengths approach the order of unity. Although field-effect–modulated electrical conductivity has long been the basis of modern electronics, such large modification of optical transitions by electrical gating is unusual. (For comparison, relative refractive index change in typical electro-optical materials rarely reaches 10^{-3}.) The special behavior of graphene is due both to its two-dimensional (2D) structure that confines electrons in one atomic layer and to its low density of states (DOS) near the Dirac point, which causes the Fermi energy (E_F) to shift significantly with variation of carrier density.

The strong gate dependence of optical transitions allows detailed examination of graphene band structure. We observed the linear Dirac band in graphene monolayer and were able to determine through direct optical means the band dispersion. For a graphene bilayer, we observed a dominating van Hove singularity that results from interlayer band hybridization, and our results indicate that many-body effects may play a role in the excited-state properties of graphene. Aside from such fundamental interests, the very unusual optical properties of graphene make it a promising material for IR optoelectronics. This is particularly attractive considering that graphene possesses superior carrier mobility, current carrying capability, and thermal conductivity, and can readily incorporate electrical coupling as in field-effect devices (*12*) and pn junctions (*13*, *14*).

We prepared mechanically exfoliated graphene monolayer and bilayer samples on heavily doped Si/SiO_2 substrates by following the peeling procedure described in (*12*). Monolayers and bilayers of graphene were identified with an optical microscope and subsequently confirmed by Raman spectroscopy (*6*). On some of the samples, we attached a gold electrode (thickness ~30 nm) by deposition in a vacuum through a mask. The heavily doped Si underneath the 290-nm-thick SiO_2 served as a back gate, which allowed us to tune the charge carrier density in the graphene samples.

We investigated the graphene interband transitions using IR reflection spectroscopy in a microscopic setup at room temperature (*15*). Two types of measurements were performed. To probe optical transitions of graphene monolayers and bilayers, we measured the normalized change of IR reflectivity $\delta R/R$ from the sample with reference to the bare substrate, achieved by modulating the sample position such that the graphene film on the substrate was shifted in and out of the beam spot. To examine the gate dependence of the optical transitions, we fixed the sample position and applied a dc gate on the graphene sample. A small ac modulation was added to the dc gate voltage, and the modulated reflectivity change at the ac modulation frequency was detected by a lockin amplifier. The result yielded $\frac{\delta(\delta R/R)}{\delta V}$, the derivative of $\delta R/R$ with respect to the gate voltage V.

We plot in Fig. 1A the measured $-\delta R/R$ versus photon energy for a representative graphene monolayer (blue circle) and graphene bilayer (red square), whose optical microscopy images are displayed in Fig. 1, B and C, respectively. Note that $\delta R/R$ is related to the complex optical conductivity $\sigma(\omega)$ of graphene through the relation:

$$-\frac{\delta R}{R} = \frac{1}{c}\mathrm{Re}[\eta \cdot \sigma] \qquad (1)$$

where η is a dimensionless complex factor that includes an interfering contribution from substrate reflection and can be calculated exactly (*16*). The observed spectra of graphene monolayers and bilayers differ dramatically. The difference can be qualitatively understood from their different electronic band structures.

The graphene monolayer spectrum is basically featureless, which is consistent with the linear electronic bands (Fig. 1D). In fact, the absorption coefficient of an undoped graphene layer in the IR region is expected to be strictly a constant (*17*, *18*). The observed $-\delta R/R$, related but not proportional to graphene absorption, ac-

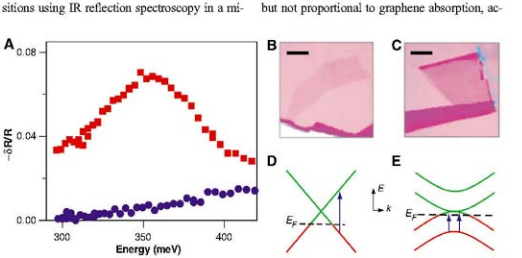

Fig. 1. **(A)** Normalized change of IR reflectivity $-\delta R/R$ referenced to the bare substrate for a graphene monolayer (blue circles) and bilayer (red squares). **(B** and **C)** Optical microscopy image of a graphene monolayer and bilayer, respectively, on a SiO_2/Si substrate. The scale bars are 20 μm. **(D** and **E)** Band structures of monolayer and AB stacking bilayer of graphene, respectively. The graphene samples are hole-doped. The linear bands of graphene monolayer produce a relatively flat $-\delta R/R$ spectrum, and the parallel bands of graphene bilayer lead to a peak in the $-\delta R/R$ spectrum.

[1]Department of Physics, University of California at Berkeley, Berkeley, CA 94720, USA. [2]Materials Science Division, Lawrence Berkeley National Laboratory, Berkeley, CA 94720, USA.

*To whom correspondence should be addressed. E-mail: fengwang76@berkeley.edu

quires slow wavelength dependence in the region we investigated, partly from dispersion in η of Eq. 1 and partly from free carrier response due to p-doping of the as-prepared exfoliated graphenes.

The bilayer electronic structure is affected by orbital hybridization between the adjacent layers. For a bilayer with AB stacking, tight-binding calculations predict two parallel conduction bands and two parallel valence bands. The band gap is zero, and the parallel band separation corresponds to the interlayer nearest-neighbor hopping rate γ_1 (Fig. 1E) (*19*–*22*). Both features are unique characteristics of the bilayer. The optical transitions between the parallel valence bands (indicated by the arrowed lines in Fig. 1E) lead to a strong van Hove singularity. They are allowed in bilayers that are p-doped. Indeed, our $-\delta R/R$ spectrum for the bilayer exhibits a clear peak around 350 meV, near the parallel band separation of 400 meV determined by photoemission (*21*, *23*).

The gate dependence of these optical transitions provides an extra dimension of information. A 2D plot (Fig. 2A) of the experimentally measured $\partial(\delta R/R)/\partial V$ as a function of probing photon energy and dc gate voltage for a graphene monolayer shows two main features. First, for a given photon energy, the absolute value of $\partial(\delta R/R)/\partial V$ has a maximum at a certain gate voltage, as can be seen from a vertical cut of the 2D plot (symbols in Fig. 2C). Second, the gate voltage for the maximum signal decreases with the photon energy (red line in Fig. 2A).

The 2D spectra of graphene monolayers allow us to determine directly the electronic band dispersion. We consider the interband transitions illustrated in the inset of Fig. 2C. The applied gate voltage changes the charge-carrier density in graphene, $n = \alpha(V + V_0)$, and accordingly shifts E_F, where $E_F = \mathrm{sgn}(n)\hbar v_F\sqrt{\pi|n|}$. Here, positive (negative) n means electron (hole) doping, v_F is the Fermi velocity, $\alpha \simeq 7 \times 10^{10}$ cm^{-2}V^{-1} (estimated from a simple capacitor model), and V_0 is the offset voltage caused by natural doping (which could vary from sample to sample) (*1*, *3*). The shift in E_F affects the IR spectrum through the Drude response of the altered electron density and through the change of band filling (for example, a down shift of E_F eliminates transitions originating from initially occupied states right above the down-shifted E_F).

The band-filling effect dominates at photon energy corresponding to transitions that originate from states near the Fermi surface, that is, $2|E_F| = \hbar\omega$. Thus, the trace for maximum $\partial(\delta R/R)/\partial V$ signal is defined by $\hbar\omega = 2\hbar v_F\sqrt{\alpha\pi|V + V_0|}$, and the slope of $(\hbar\omega)^2$ versus V yields directly the dispersion velocity of the Dirac band, $v_F = 0.8 \times 10^6$ m/s (Fig. 2D). Our value is comparable to that obtained by transport (*1*, *3*) and by photoemission (*23*–*25*), and the small difference could be due to the uncertainty in our determination of gate-coupling efficiency.

To describe the gate-dependent spectra quantitatively, we use the tight-binding model (*17*, *18*) to calculate the optical transitions and the frequency-dependent complex conductivity for different E_F. In this model, the Fermi velocity v_F is the only parameter needed to describe the band structure and optical transition matrix elements, and $V + V_0$ sets the Fermi energy level. We introduce an uncertainty ΔV_0 in V_0 to account for inhomogeneous doping of the sample. We can then calculate the spectrum of $\partial(\delta R/R)/\partial V$ for different V_0 using Eq. 1. The results with $v_F = 0.8 \times 10^6$ m/s, $V_0 = -70$ V, and $\Delta V_0 = \pm 16$ V are presented in Fig. 2B. They agree nicely with the experimental data in Fig. 2A (*26*).

The same model can be used to describe the ungated $-\delta R/R$ spectrum of the monolayer in Fig. 1A. The fitting is shown in the upper panel of Fig. 2E. We can compare it with the total gate-induced reflectivity change over the gate-voltage range of −50 to 60 V, $\Delta(\delta R/R) = (\delta R/R)_{V_R=60\,V} - (\delta R/R)_{V_R=-50\,V}$, displayed in the lower panel of Fig. 2E. The magnitude of $\Delta(\delta R/R)$ is obviously greater than reflection response, $-\delta R/R$, from the ungated monolayer. It follows from switch-off of IR transitions by electrical gating through a downshift of E_F.

The spectrum of gate-induced reflectance change, $\partial(\delta R/R)/\partial V$, for a graphene bilayer is shown in Fig. 3A. It exhibits features distinctly different from that of the monolayer (Fig. 2A). A clear peak exists in the modulation spectra,

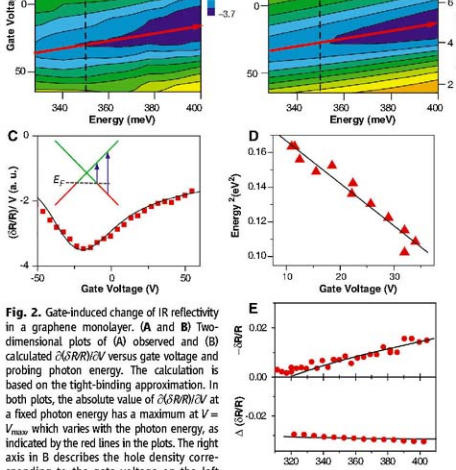

Fig. 2. Gate-induced change of IR reflectivity in a graphene monolayer. (**A** and **B**) Two-dimensional plots of (**A**) observed and (**B**) calculated $\partial(\delta R/R)/\partial V$ versus gate voltage and probing photon energy. The calculation is based on the tight-binding approximation. In both plots, the absolute value of $\partial(\delta R/R)/\partial V$ at a fixed photon energy has a maximum at $V = V_{max}$ which varies with the photon energy, as indicated by the red lines in the plots. The right axis in B describes the hole density corresponding to the gate voltage on the left axis. (**C**) A vertical line cut of the 2D plots at 350 meV, where the maximum modulation (in absolute value) is clearly observed. The inset illustrates interband transitions in graphene monolayers. E_F shifts upon gating, which affects the transitions. Gate-induced modification is strongest when the initial states for transitions are near the Fermi surface, i.e., $2|E_F| = \hbar\omega$. A small shift of E_F can block such transitions by changing the initial state from filled to empty, whereas transitions at significantly lower or higher energies are not affected. (**D**) The trace of maximum modulation plotted as squared photon energy versus gate voltage. Its slope yields directly the velocity dispersion of the Dirac band, $v_F = 8.1 \times 10^5$ m/s. (**E**) Experimental data (symbols) and model prediction (lines) of (upper panel) $-\delta R/R$ spectrum for an ungated graphene monolayer and (lower panel) the total gate-induced reflectivity spectrum change, $\Delta(\delta R/R)$, with gate voltage varied from −50 to 60 V. The magnitude of gate-induced reflectance change is larger than the initial monolayer reflectance.

which can be easily seen from a horizontal line cut in the 2D plot (symbols in Fig. 3C). Also, the signal at the peak has an opposite sign compared with that in the monolayer, indicating a fundamentally different mechanism.

Qualitatively, we can attribute this observation to the van Hove singularity associated with the optical transitions between parallel valence bands of a p-doped graphene bilayer, illustrated by the blue arrowed lines in the Fig. 3C inset. It leads to a peak in bilayer absorption at the band separation energy, and the peak becomes stronger with increasing hole concentration as E_F shifts down and more transitions become allowed. This situation is in contrast to the reduction of transition strength with down-shifting of the Fermi level in a graphene monolayer, which gives an opposite sign to $\partial(\delta R/R)/\partial V$. Transitions between other bands (black arrowed lines in the illustration in Fig. 3C) are also affected by gating, and a small band gap is expected to appear because of asymmetry of the gating effect on the upper and the lower layers of the bilayer (*21*, *27*). However, there is no strong van Hove singularity involved, and therefore these transitions contribute only to an overall slowly varying background.

To be more quantitative, we model the bilayer using the tight-binding approximation, following (*19*), to calculate the complex conductivity. We use the same set of parameter values as in the monolayer case but include the interlayer hopping rate γ_1 as an additional parameter to take into account the interlayer coupling. The best fit of the spectral variation with gate voltage from our calculation is shown in Fig. 3B; a horizontal line cut of the 2D plot is given in Fig. 3C to compare with the experimental data. The fit yields $\gamma_1 = 350$ meV and $V_0 = -50$ V from natural doping, assuming that all the dopants appear at the upper surface of the bilayer.

Comparisons between theory and experiment in Fig. 3, A and B, show that the main experimental features are reproduced by the model. However, significant deviations exist, such as the slight difference in peak energies and in gate dependences at spectral range from 370 to 400 meV. Also, our observed peak energy, ~350 meV, is close to, but smaller than, the energy separation of the parallel bands of 400 meV determined by photoemission measurements (*21*, *23*). These discrepancies could arise from strong many-body effects in the bilayer excited state. For instance, excitonic effects can modify the optical spectrum appreciably, whereas photoemission probes quasiparticle transitions in the absence of excitons. Such excitonic behavior in a graphene bilayer could be quite unusual, considering the existence of parallel bands and the associated van Hove singularity.

Next, we compare the ungated $-\delta R/R$ spectrum in a graphene bilayer (Fig. 3D) and the spectrum of the total gate-induced change, $\Delta(\delta R/R) = (\delta R/R)_{V_G=60V} - (\delta R/R)_{V_G=-50V}$ (Fig. 3E). Again, $\Delta(\delta R/R)$ is comparable in magnitude to $\delta R/R$.

Our study reveals rich IR optical behaviors in graphene monolayers and bilayers. The observed interband transitions are quite strong: Although only one or two atoms thick, the graphene monolayer and bilayer can absorb, respectively, more than 2% and 6% (peak value) of normally incident IR radiation. In comparison, a 10-nm-thick GaAs layer absorbs about 1% of the light near the band gap. Using multiply stacked graphene sheets or optical multipasses or waveguiding, the IR response of graphene can be considerable: for example, IR light propagating along a 100-μm-long waveguide on undoped graphene would be completely absorbed. With the tunability provided by electrical gating and charge injection, one might envision novel graphene-based optoelectronics devices such as tunable IR detectors, modulators, and emitters.

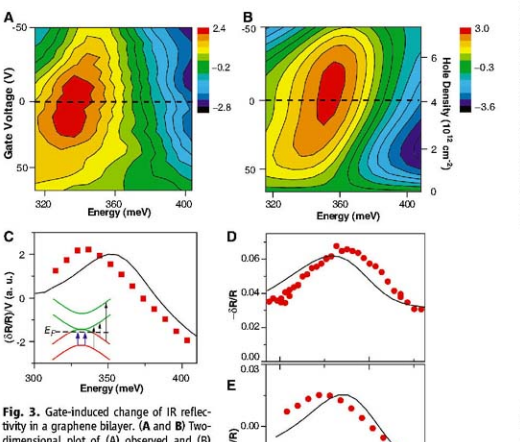

Fig. 3. Gate-induced change of IR reflectivity in a graphene bilayer. (**A** and **B**) Two-dimensional plot of (**A**) observed and (**B**) calculated $\partial(\delta R/R)/\partial V$ versus gate voltage and probing photon energy. The calculation is based on the tight-binding approximation. (**C**) A horizontal line cut of the 2D plot explicitly shows the peak in the modulation spectra. Symbols are experimental data, and the line is from the model prediction. The inset illustrates the interband transitions in bilayers. Transitions between the parallel valence bands of the hole-doped bilayer, denoted by the red arrowed lines, give rise to a van Hove singularity and the observed spectral peak. Other interband transitions (black arrowed lines) contribute to a relatively flat response over the spectral range. (**D** and **E**) Experimental data (symbols) and model prediction (lines) of (D) $-\delta R/R$ spectrum for an ungated graphene bilayer and (E) the total gate-induced reflectivity spectrum change, $\Delta(\delta R/R)$, with gate voltage varied from −50 to 60 V. The gate-induced change of reflectance is of the same order of magnitude as the initial graphene reflectance.

References and Notes

1. K. S. Novoselov *et al.*, *Nature* **438**, 197 (2005).
2. K. S. Novoselov *et al.*, *Nat. Phys.* **2**, 177 (2006).
3. Y. B. Zhang, Y. W. Tan, H. L. Stormer, P. Kim, *Nature* **438**, 201 (2005).
4. M. I. Katsnelson, K. S. Novoselov, A. K. Geim, *Nat. Phys.* **2**, 620 (2006).
5. F. Miao *et al.*, *Science* **317**, 1530 (2007).
6. A. C. Ferrari *et al.*, *Phys. Rev. Lett.* **97**, 187401 (2006).
7. J. Yan, Y. B. Zhang, P. Kim, A. Pinczuk, *Phys. Rev. Lett.* **98**, 166802 (2007).
8. Z. Jiang *et al.*, *Phys. Rev. Lett.* **98**, 197403 (2007).
9. C. Casiraghi *et al.*, *Nano Lett.* **7**, 2711 (2007).
10. S. M. Bachilo *et al.*, *Science* **298**, 2361 (2002).
11. F. Wang, G. Dukovic, L. E. Brus, T. F. Heinz, *Science* **308**, 838 (2005).
12. K. S. Novoselov *et al.*, *Science* **306**, 666 (2004).
13. B. Huard *et al.*, *Phys. Rev. Lett.* **98**, 236803 (2007).
14. J. R. Williams, L. DiCarlo, C. M. Marcus, *Science* **317**, 638 (2007).
15. Tunable IR radiation was generated by an optical parametric amplifier pumped by a femtosecond Ti:sapphire amplifier system. The IR pulses were attenuated to ~1 nJ and spectrally narrowed through a monochromator to ~10 cm^{-1} before they were focused onto the graphene samples. The back-reflected light was collected and detected by a mercury cadmium telluride detector. The samples had a typical lateral dimension around 20 μm. The microscope we used had a 36× reflective objective that confined the infrared beam to a diameter ≤10 μm on the sample.
16. See supporting material on *Science* Online.

17. V. P. Gusynin, S. G. Sharapov, J. P. Carbotte, *Phys. Rev. Lett.* **96**, 256802 (2006).
18. L. Falkovsky, A. Varlamov, http://arxiv.org/abs/cond-mat/0606800 (2006).
19. E. V. Castro *et al.*, http://arxiv.org/abs/cond-mat/0611342 (2006).
20. D. S. L. Abergel, V. I. Fal'ko, http://arxiv.org/abs/cond-mat/0610673 (2007).
21. T. Ohta, A. Bostwick, T. Seyller, K. Horn, E. Rotenberg, *Science* **313**, 951 (2006).
22. A small band gap can open in a doped graphene bilayer (*20*). At our doping level, the bandgap is relatively small and will not affect the qualitative behaviors. In the tight binding calculation described in the text, this gap-opening effect is included in a self-consistent way following (*26*).
23. S. Y. Zhou *et al.*, *Nat. Mater.* **6**, 770 (2007).
24. A. Bostwick, T. Ohta, T. Seyller, K. Horn, E. Rotenberg, *Nat. Phys.* **3**, 36 (2007).
25. S. Y. Zhou *et al.*, *Nat. Phys.* **2**, 595 (2006).
26. The electron density of the Si back gate will also be modulated by electrical gating. It will also contribute to the IR reflectivity change and is described by Drude free-carrier response. However, its contribution is more than an order of magnitude smaller than that of graphene and remains a constant at different dc gate voltages.
27. E. McCann, http://arxiv.org/abs/cond-mat/0608221 (2006).
28. We thank S. Louie and Y. Li for helpful discussions. This work was supported by the Office of Basic Energy Sciences, U.S. Department of Energy, under contract DE-AC03-76SF00098. F.W. and Y.Z. acknowledge the support from the Miller Institute for Miller research fellowships, and C.T. acknowledges support from an NSF grant through Water CAMPWS CTS-0120978.

Supporting Online Material

www.sciencemag.org/cgi/content/full/1152793/DC1
SOM Text

8 November 2007; accepted 3 March 2008
Published online 13 March 2008;
10.1126/science.1152793
Include this information when citing this paper.

Current-Controlled Magnetic Domain-Wall Nanowire Shift Register

Masamitsu Hayashi, Luc Thomas, Rai Moriya, Charles Rettner, Stuart S. P. Parkin*

The controlled motion of a series of domain walls along magnetic nanowires using spin-polarized current pulses is the essential ingredient of the proposed magnetic racetrack memory, a new class of potential non-volatile storage-class memories. Using permalloy nanowires, we achieved the successive creation, motion, and detection of domain walls by using sequences of properly timed, nanosecond-long, spin-polarized current pulses. The cycle time for the writing and shifting of the domain walls was a few tens of nanoseconds. Our results illustrate the basic concept of a magnetic shift register that relies on the phenomenon of spin-momentum transfer to move series of closely spaced domain walls.

More than three decades ago, the concept of storing information in movable domain walls (DWs) was introduced, and the following years saw intense interest in "magnetic bubble memories" (*1*). The magnetic bubbles were often arranged in the form of shift registers and manipulated with fixed and alternating magnetic fields (*2*). However, this required on-chip field generators at the same size scale as the individual magnetic bits, adding considerable complexity and cost to the device and making scaling to smaller dimensions very difficult (*3*). These obstacles can be overcome by taking advantage of the interaction of spin-polarized current with magnetization in the DWs, which results in a spin-transfer torque on the DW, causing it to move (*4*–*9*). This effect has been observed in a number of magnetic materials (*10*–*13*), but predominantly in permalloy ($Ni_{81}Fe_{19}$) nanowires (*14*–*17*). The use of spin-momentum transfer considerably simplifies the memory device because the current is passed directly across the DW without the need for any additional field generators.

In a permalloy nanowire in which the magnetization lies along the nanowire, adjacent DWs alternate between head-to-head (HH) and tail-to-tail (TT) configurations (Fig. 1, B and C). Under the application of a uniform magnetic field, these DWs will move in opposite directions, leading to their potential annihilation. In contrast, spin-polarized current can, in principle, move a series of neighboring DWs in the same direction. Moreover, spin-momentum transfer becomes more efficient the smaller the size of the magnetic element is (*18*). We describe here the basic working principle of a current-controlled magnetic DW shift register, the fundamental building block of magnetic racetrack memory (*19*).

In a scanning electron microscopy (SEM) image of a typical permalloy nanowire (Fig. 1A), three pulse generators (PG-1, PG-2, and PG-3) are connected to electrical contact lines A and B, spaced 6 μm apart (*20*) (SOM text A). The resistance of the nanowire was measured to determine whether a DW was present in the region between line A and B (section A-B). The nanowire resistance also provides information about the structure of the DW (*21*); that is, whether it is a transverse or a vortex DW (*22*). In these DWs, the magnetization largely lies in the plane of the nanowire. In the transverse case the magnetization rotates about an axis perpendicular to the length of the nanowire, whereas in the vortex case, the magnetization rotates about a tiny core in which a small net moment points into or out of the plane of the nanowire (Fig. 2 D).

A voltage pulse from one of the pulse generators (PG-1 or PG-2) was used to inject a current into line A as well as into the nanowire. The current that passes through line A generates a highly localized magnetic field that, when sufficiently large and when the magnetization of the nanowire is properly aligned, creates a DW in section A-B. The current that flows into the nanowire drives the DW along the nanowire between A and B in a direction determined by the current flow direction. The nanowire was first magnetized along the –(+) X direction with an external magnetic field $H = -(+)\ 300$ Oe, which was then set as close as possible to zero ($|H| < \sim 0.3$ Oe, unless otherwise noted). A HH (or TT) DW was subsequently created in section A-B when a negative voltage pulse was injected from PG-2 (PG-1). Throughout this study, the amplitude of the voltage pulse from PG-1 and PG-2 was fixed at –3.2 V.

Previous experiments showed that the DW created in section A-B moves along the nanowire and exits from line B only when the pulse length exceeds a threshold value τ_P. This pulse length is determined by the DW velocity, which depended on the current density flowing along the nanowire, and H (*17*). Only vortex and not transverse DWs could be moved with current under the experimental conditions used (*8*, *16*, *17*). For example, the probability of finding a vortex wall in section A-B is plotted as a function of the pulse length (Fig. 1, B and C) for TT and HH walls, respectively, for a current density of $\sim -2.0 \times 10^8$ A/cm^2. For both walls, $\tau_P = \sim 35$ ns.

When the injection pulse length is shorter than τ_P, we hypothesized that the DW would move along the nanowire a distance in proportion to the pulse length. This was verified by using an ejection voltage pulse to determine the time needed to move the DW either backward to A or forward to B as a function of the injection pulse length. The ejection pulse was applied from PG-3 to line B with an amplitude of $\sim \pm 1.6$ V, which corresponds to a current of $\sim \mp 2 \times 10^8$ A/cm^2 in the nanowire; that is, nearly equal to that of the injection pulse current density (fig. S1). Positive voltage applied to line B provides spin-transfer torque, which pushes the DW along the $+X$ direction, whereas negative voltage pushes it in the $-X$ direction.

The pulse length required to eject the DW from the nanowire is plotted as a function of the

IBM Research Division, Almaden Research Center, San Jose, CA 95120, USA.

*To whom correspondence should be addressed. E-mail: parkin@almaden.ibm.com

injection pulse length for TT and HH walls, respectively (Fig. 1, D and E). The length of the ejection pulse, for positive pulses, decreases as the injection pulse length is increased, which shows that when a longer injection pulse is used, the DW travels further from line A, therefore requiring a shorter ejection pulse to complete its motion toward line B. In contrast, when the ejection pulse is of negative polarity, its length increases in proportion to the injection pulse length, indicating that the time needed to move the DW back to line A scales with the injection pulse length. Therefore, the position of the DW along the nanowire can be controlled by varying the injection pulse length.

Up to this point, a large magnetic field (~±300 Oe) had been applied to reset the magnetic state of the nanowire before each injection of a DW. We developed a method by which we can reset the magnetic state of the nanowire by moving DWs with current, from one end of the nanowire to the other, without using any magnetic field. This requires the successive injection and motion of HH and TT walls. After setting the initial state of the nanowire by magnetizing it along $+X$ with an external field, a TT wall is created in section A-B, using a 10-ns-long pulse applied from PG-1, followed by a 70-ns-long pulse from the same pulse generator to move the TT wall out of this section (Fig. 2F). After this operation, the magnetic state of the nanowire has been reversed. The same operation using PG-2 (Fig. 2E) subsequently generates and moves an HH wall through section A-B, again reversing the magnetization, therefore returning it to its original configuration. Each of these DW operations results in stepwise changes in the nanowire resistance (Fig. 2C) (*23*). Figure 2B shows the evolution of the nanowire resistance as the pulse sequence was repeated many times. In succession, TT and then HH walls are repeatedly created and moved, which shows that the magnetic state of the nanowire can be reset using current pulses alone.

However, when a transverse wall, which can readily be identified from its resistance value (*21*), was created in section A-B, the reset operation was disrupted (Fig. 2B, 16th iteration, and Fig. 2, D, G, and H). The injected TT wall remains in section A-B, even after the long pulse is applied so that the injection of the following HH wall annihilates it. These results indicate that transverse walls do not move at the current densities used here.

We next show that two adjacent vortex DWs can be moved together using the same current pulse. Because our measurement technique is limited to probing only the number of DWs stored in the nanowire, the following procedure was used to show that a pair of TT and HH walls move together (see fig. S2 for the detailed pulse sequence). First, a voltage pulse was injected from PG-1 to create a TT wall in section A-B. A voltage pulse from PG-2 was then injected to create a HH wall. The pulse length was made short enough so that the existing TT wall was not ejected from section A-B. After the injection of the two DWs, a voltage pulse from PG-2 was applied to eject only the TT wall by using a proper length. A sufficiently long voltage pulse from PG-2 was then applied to ensure ejection of the HH wall. The expected motion and the corresponding number of DWs in section A-B (Fig. 3B) is consistent with the measured variation in the nanowire resistance (Fig. 3A). The number of DWs changed from the initial state, zero, to 1, 2, 1, and 0, successively, which indicates that the two DWs were indeed moved together (see fig. S3 for the case of the current-induced motion of three neighboring DWs). The same variation in the nanowire resistance is observed when the pulse sequence is repeated many times (Fig. 3C).

There are occasional errors due, for example, to the injection of a transverse rather than a vortex DW or to the annihilation of the first DW when the second DW was injected (see fig. S2 for details of these probabilities). The latter becomes more probable as the separation distance between the DWs is reduced. This distance can be estimated by measuring the dependence of the probability of annihilation on the first pulse length (SOM text E). However, this measurement turned out to be very sensitive to small deviations of the magnetic field from zero, because the DW velocity, estimated from (section A-B length = 6 μm)/τ_p, strongly depends on the field (Fig. 3D). The dependence of the minimum separation distance on the magnetic field is plotted in Fig. 3E. Near zero field, the distance is ~ 2.5 μm. We attribute this large distance to the localized magnetic field created around line A when the pulse is applied as well as to the magnetostatic fields from the magnetic charge on the DWs themselves. The solid line shows the estimated threshold distance when both of these fields are taken into account

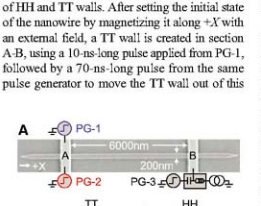

Fig. 1. (**A**) SEM image of the permalloy nanowire and the electrical contact lines A and B. PG, pulse generator. (**B** and **C**) Probability of TT (B) and HH (C) DWs remaining in section A-B of the nanowire as a function of the injection pulse length. Illustrations of the magnetization configurations of TT (white square) and HH (black square) walls are shown. Black arrows represent the magnetization direction within each domain. (**D** and **E**) The ejection time needed to move the injected DW [(D), TT; (E), HH] out of section A-B toward A or B using a second positive or negative voltage pulse, respectively, from PG-3, as a function of the injection pulse length.

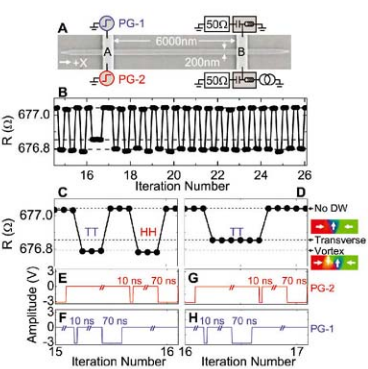

Fig. 2. (**A**) SEM image of the shift register device and electrical measurement setup used here and subsequently. (**B**) Variation of the nanowire dc resistance (R) when a pulse sequence from PG-1 and PG-2 is repeated to successively inject and move TT and HH DWs. (**C** and **D**) Resistance variations for the 15th and 16th iterations shown in (B). Dotted lines correspond to transverse, vortex, or no DW present in section A-B. Simulated images of the transverse and vortex DWs are shown to the right; arrows indicate the magnetization direction. The corresponding pulse sequences are shown in (**E** and **F**) and (**G** and **H**), respectively.

and it is assumed that a DW will move when subjected to a field that exceeds its propagation field along the nanowire. The dependence of the threshold distance on H can be explained using this model (fig. S4). If the localized magnetic field from the contact line could be eliminated, then the minimum separation distance at zero field was estimated to be ~0.8 μm in the nanowire used here. Local pinning centers can be used to provide stable positions for the DWs, thereby allowing them to be spaced more closely, as well as improving the reliability of their motion (*19*, *24*).

Using the concepts demonstrated above, we realized the construction of a DW shift register memory, namely a three-bit unidirectional serial-in, serial-out memory in which the data are coded as the magnetization direction of individual domains (Fig. 4A and fig. S7). A left-pointing domain represents a 0 and a right-pointing domain represents a 1. The data was written into the leftmost domain in section A-B, was shifted by 2 domains, and then read from the state of the rightmost domain. The magnetization configuration was inferred from the resistance. For example, when a data sequence of 010111 was written into the register, the resistance and the corresponding magnetization configuration evolved as shown in Fig. 4, B and C, respectively (see fig. S5 for the detailed pulse sequence). In Fig. 4B, the shaded regions correspond to a shift operation and the light regions to a write operation. The input sequence is accurately transferred to the output after two write/shift operations. In this example, the cycle time to write and shift one bit is ~30 ns, which was determined by the write time (here, ~3 to 4 ns) and the time required to shift the series of DWs by one domain length. The latter time was determined by the velocity of the DWs, which here was fast, ~150 m/s (Fig. 3D).

The motion of a series of DWs at high speed using nanosecond current pulses not only proves the viability of a shift-register memory but also presages the possibility of current-controlled DW–based logic devices.

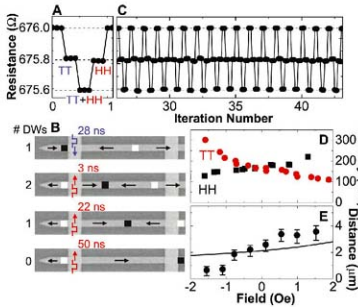

Fig. 3. **(A)** Variation of the nanowire dc resistance and **(B)** illustration of the corresponding injection and motion of TT and HH DWs (see fig. S2 for the pulse sequence used). Black squares and white squares in (B) represent HH and TT DWs, respectively. Black arrows represent the magnetization direction within each domain. Blue and red arrows represent the electron flow directions. **(C)** Variation of the nanowire resistance when the pulse sequence is repeated. **(D)** DW velocity and **(E)** the minimum separation distance between a first injected TT DW and a second injected HH DW required to avoid their annihilation as a function of the external magnetic field. The solid line shows the estimated separation distance (fig. S4).

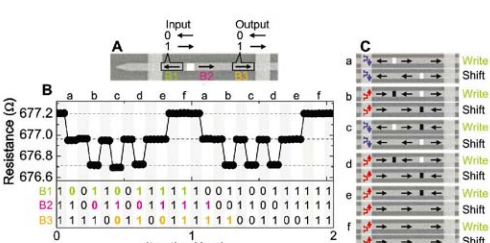

Fig. 4. Demonstration of a three-bit unidirectional magnetic DW shift register. **(A)** Data are encoded by the magnetization direction of three domains in the nanowire. **(B)** Nanowire resistance variation when a pulse sequence is used to write and shift along the register the sequence 010111 two times in succession. The light and dark regions indicate writing and shifting operations, respectively. The table shows the corresponding evolution of the states of the three bits during these operations. The highlighted digits show how the input bit sequence is transferred to the output after two write/shift operations. **(C)** Schematic illustration of the shift-register operation. Black squares and white squares represent HH and TT DWs, respectively. Black arrows represent the magnetization direction within each domain. Blue and red arrows represent the electron flow direction.

References and Notes

1. A. P. Malozemoff, J. C. Slonczewski, *Magnetic Domain Walls in Bubble Materiel* (Academic Press, New York, 1979).
2. A. H. Bobeck, P. I. Bonyhard, J. E. Geusic, *Proc. IEEE* **63**, 1176 (1975).
3. S. Middelhoek, P. K. George, P. Dekker, *Physics of Computer Memory Devices* (Academic Press, London, 1976).
4. L. Berger, *J. Appl. Phys.* **55**, 1954 (1984).
5. G. Tatara, H. Kohno, *Phys. Rev. Lett.* **92**, 086601 (2004).
6. S. Zhang, Z. Li, *Phys. Rev. Lett.* **93**, 127204 (2004).
7. S. E. Barnes, S. Maekawa, *Phys. Rev. Lett.* **95**, 107204 (2005).
8. A. Thiaville, Y. Nakatani, F. Piechon, J. Miltat, T. Ono, *Eur. Phys. J. B* **60**, 15 (2007).
9. M. D. Stiles, W. M. Saslow, M. J. Donahue, A. Zangwill, *Phys. Rev. B* **75**, 214423 (2007).
10. M. Yamanouchi, D. Chiba, F. Matsukura, H. Ohno, *Nature* **428**, 539 (2004).
11. D. Ravelosona, D. Lacour, J. A. Katine, B. D. Terris, C. Chappert, *Phys. Rev. Lett.* **95**, 117203 (2005).
12. M. Feigenson, J. W. Reiner, L. Klein, *Phys. Rev. Lett.* **98**, 247204 (2007).
13. S. Lepadatu *et al.*, *Appl. Phys. Lett.* **90**, 232505 (2007).
14. N. Vernier, D. A. Allwood, D. Atkinson, M. D. Cooke, R. P. Cowburn, *Europhys. Lett.* **65**, 526 (2004).
15. A. Yamaguchi *et al.*, *Phys. Rev. Lett.* **92**, 077205 (2004).
16. M. Kläui *et al.*, *Phys. Rev. Lett.* **95**, 026601 (2005).
17. M. Hayashi *et al.*, *Phys. Rev. Lett.* **98**, 037204 (2007).
18. J. Slonczewski, *J. Magn. Magn. Mat.* **159**, L1 (1996).
19. S. S. P. Parkin, U.S. Patent 6834005 (2004).
20. Materials and methods are available as supporting material on *Science* Online.
21. M. Hayashi, L. Thomas, C. Rettner, R. Moriya, S. S. P. Parkin, *Nat. Phys.* **3**, 21 (2007).
22. Y. Nakatani, A. Thiaville, J. Miltat, *J. Magn. Magn. Mater.* **290–291**, 750 (2005).
23. The nanowire dc resistance was measured three times after each pulse application to confirm that a stable state was obtained. Also, a slightly different electrical setup was used thereafter (Fig. 2A and fig. S1), as compared with that used in Fig. 1.
24. L. Thomas *et al.*, *Science* **315**, 1553 (2007).

Supporting Online Material

www.sciencemag.org/cgi/content/full/320/5873/209/DC1
Materials and Methods
SOM Text
Figs. S1 to S5

26 December 2007; accepted 3 March 2008
10.1126/science.1154587

Impact of Artificial Reservoir Water Impoundment on Global Sea Level

B. F. Chao,* Y. H. Wu, Y. S. Li

By reconstructing the history of water impoundment in the world's artificial reservoirs, we show that a total of ~10,800 cubic kilometers of water has been impounded on land to date, reducing the magnitude of global sea level (GSL) rise by −30.0 millimeters, at an average rate of −0.55 millimeters per year during the past half century. This demands a considerably larger contribution to GSL rise from other (natural and anthropogenic) causes than otherwise required. The reconstructed GSL history, accounting for the impact of reservoirs by adding back the impounded water volume, shows an essentially constant rate of rise at +2.46 millimeters per year over at least the past 80 years. This value is contrary to the conventional view of apparently variable GSL rise, which is based on face values of observation.

The various causes of the observed global sea level (GSL) rise have been under study, and debate, for years. The Intergovernmental Panel on Climate Change (*1*) concluded in 2007 that "the budget (of GSL rise) has not yet been closed satisfactorily," primarily because the anthropogenic contribution from land water alterations is too poorly known. Among them, the negative contribution due to water impoundment in artificial reservoirs behind dams has long been recognized to be a major term (*1–7*), although one poorly quantified in the absence of compiled information. Such incomplete data have led to a wide range of estimates of the total water impoundment: from ~15,000 km^3 (extrapolated to year 2000) (*2*) to ~10,000 km^3 (*3*) [which includes the volume of only the "top 100" (named) reservoirs, ~4000 km^3 (*4*)] to 5000 to 6000 km^3 (*5–7*) and even less (*8*).

To reconstruct the water impoundment history and study its impact on GSL rise, we assembled a comprehensive tally of the world's reservoirs constructed since ~1900. Our main source of data was the International Commission on Large Dams (ICOLD) World Register of Dams (*9*), augmented and corrected for apparently erroneous or inconsistent entries by consulting with various ancillary data sources (*10–16*) to yield a list of 29,484 named reservoirs with nominal capacity and year of completion (*17*).

Let $V(t)$ be the (cumulative) total volume of water impoundment in the world's reservoirs at any given calendar year t, and let V_i be the capacity of a given individual reservoir modeled as an addition to V in year t_i of its completion, causing an instantaneous GSL drop (recognizing the ocean as the ultimate source of the water). That is, $V(t) = \Sigma_i V_i H(t - t_i)$ and the corresponding GSL drop $d(t) = -V(t)/A$ (a negative value), where H is the Heaviside function and $A = 3.61 \times 10^8$ km^2 is the total ocean area. This "nominal" time history for $V(t)$ is shown in Fig. 1 (dashed blue curve); the total nominal V to date is 8300 km^3, corresponding to $d = -23$ mm. The inset shows the number of reservoirs completed per year, which has soared since ~1950 but distinctly decreased in the past three decades, especially in North America and Europe, because of environmental concerns. The slowdown during the Second World War is also noted (see below). In addition, the continental breakdown in Fig. 1 reflects the contrasting and changing societal behavior and economic activity of populations on different continents.

Next, the following potentially important modifications to the nominal history above should be considered.

First, although our tally of reservoirs is essentially complete for the major and relatively large ones, the tally inevitably becomes less complete with decreasing reservoir size as those reservoirs become more numerous. We assess the untallied amount of water as follows. We plot in Fig. 2 the histogram of the number of tallied reservoirs n (in logarithm) versus a convenient reservoir "magnitude" $M = \log(C)$, where C is the reservoir capacity in cubic meters. The drop-off of the tally of n is found to occur around $M \sim 6.5$ (corresponding to a moderate reservoir of, say, 1 km long, 150 m

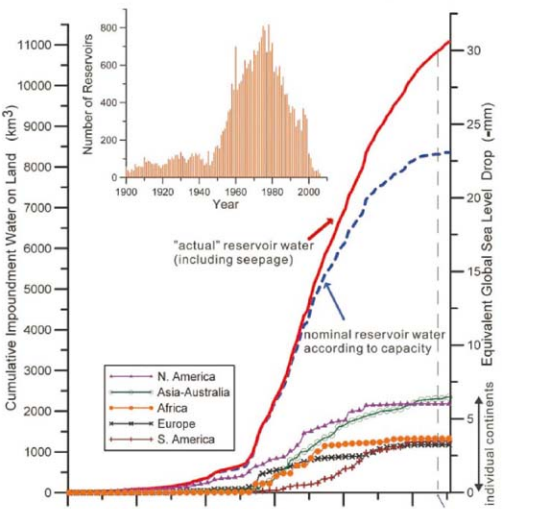

Fig. 1. Cumulative water impoundment [$V(t)$, red solid curve] as a function of calendar year, based on the nominal water impoundment (dashed blue curve) according to our compiled tally of 29,484 reservoirs' capacity (*17*) but also including realistic modifications to account for phenomena such as subsurface seepage. The lower thin lines are the breakdowns for individual continents, showing continental contrasts. The inset shows the number of reservoirs completed per year.

College of Earth Sciences, National Central University, Chung-Li, Taiwan, ROC.

*To whom correspondence should be addressed. E-mail: bfchao@ncu.edu.tw

wide, and 20 m deep). Over the main body of the histogram for $M > 6.5$ (numbering 16,600 reservoirs), up to $M = 10.5$ with bin width of 0.1, the (log-log) relation conforms to a straight line corresponding to an empirical power law: $n(C) = 10^{6.69} \times C^{-0.52}$ (*18*). Extrapolating to zero capacity, this relation yields the integrated water amount for all reservoirs smaller than $M = 6.5$, which amounts to only 0.73%, to be augmented to the total (*19*, *20*). This reassures us that our tally's incompleteness in small reservoirs is inconsequential with respect to total water volume.

Second, accounting only for the "visible" part of the impounded water, the nominal V_i ignores the water that inevitably seeps underground to manifest as water table elevation. Typically comparable to the capacity, the volume of this invisible subsurface water varies greatly from case to case, depending on the local geology and climate. Short of detailed information, here we make an average, conservative estimate: For all reservoirs we assume an annual subsurface seepage rate of 5% of the capacity volume for the first year of existence (*6*). For the out-years following (*21*), we use a dynamic fluid diffusion model that dictates the water seepage to decrease as $1/\sqrt{t}$, so that the total water seepage grows slowly as $\sqrt{t}$. We then integrate this seepage into the total volume accordingly.

Third, reservoirs are not always filled to 100% of V_r. Depending on the usage and the regional climatology and hydrology, actual reservoir storage can fluctuate considerably, especially seasonally and often interannually. Here, following (*6*), we adopt a long-term average percentage of 85% and thus an overall scale factor of 0.85. Incidentally, to first order, the inevitable silting of reservoirs need not be of concern here [contrary to (*5*–*7*)] because, just like water, the silt represents that much volume withheld on land that would otherwise flow to the ocean, raising GSL. Whether the volume withheld by the dam is water or silt has the same impact on GSL.

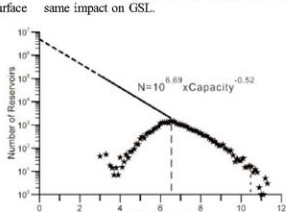

Fig. 2. Histogram of the number of tallied reservoirs (in logarithm) versus the reservoir magnitude $M = \log(C)$, where C is the reservoir capacity in units of m^3 of volume. Over the main body of the histogram for $M = 6.5$ to 10.5, the (log-log) relation conforms to a straight line with slope −0.52.

Fig. 3. History of annual GSL drop due to water impoundment in artificial reservoirs.

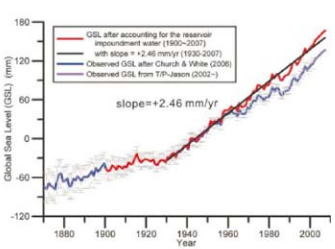

Fig. 4. The blue curve with error bar is the observed GSL history [(*1*, *25*); zero level is arbitrary], with a purple segment from altimetry data (*23*) spliced on for the past few years after adjusting a vertical offset. The red line is the GSL corrected for the impact of artificial reservoirs, reconstructed by adding back the reservoir impoundment contribution (in Fig. 1) to the blue curve. It exhibits an essentially constant slope of +2.46 mm/year for the past 80 years.

Combining the above, a modified water impoundment curve for $V(t)$ and $d(t)$ (solid red curve in Fig. 1) emerges from the nominal curve. The total actual water impoundment to date is $V = 10{,}800$ km^3, corresponding to $d = -30.0$ mm (*22*). Figure 3 shows the annual GSL drop [essentially the time derivative of $V(t)$]; in peak years, ~1960 to 1990, it reached as high as –0.4 to –0.9 mm/year. The average GSL drop rate during the past half century is about –0.55 mm/year.

Sea level varies on all temporal and spatial scales for a host of reasons. Tide gauge data indicate that GSL has risen at +1.7 to 1.8 mm/year during the 20th century [(*1*) and references therein], whereas satellite altimetry during 1993–2007 shows an accelerated rate of +3.36 ± 0.4 mm/year (*23*), although it is uncertain whether this is a long-term trend or decadal variability (*1*). One-quarter to one-half of the rise in the past half century is believed to have come from the thermal expansion of the top layers of global oceans (the steric effect). The rest, barring a relatively small but uncertain portion from the mantle glacial isostatic adjustment, is attributed to water mass addition occurring in two forms: (i) melting of mountain glaciers (estimated contribution to GSL rise: +0.50 ± 0.18 mm/year during 1961–2003 and +0.77 ± 0.22 mm/year during 1993–2003) plus that of the ice sheets on Antarctica (+0.14 ± 0.41 mm/year and +0.21 ± 0.35 mm/year, respectively) and Greenland (+0.05 ± 0.12 mm/year and +0.21 ± 0.07 mm/year, respectively), and (ii) climate-driven variations in soil water, inland seas, and large lakes (+0.12 mm/year during the past two decades, although with large interannual and decadal fluctuations), plus various anthropogenic contributions including the impoundment under study here.

Thus, our estimate of a difference of –0.55 mm/year due to artificial reservoirs represents a considerable (negative) impact to the GSL rise budget for the past several decades, which has more than compensated for nearly all of the individual natural or anthropogenic (positive) contributions described above (*24*). This creates an even larger gap in the GSL rise budget, demanding a larger contribution from the natural (and perhaps anthropogenic) causes than otherwise required.

Equally important, our study has intriguing implications for the history of GSL rise, a key indicator of global climatic change. In Fig. 4 we plot the observed GSL history (*1*, *25*) as the blue line, with a splice-on segment for the most recent decade derived from the altimetry result (*23*) (the purple segment) after adjusting a vertical offset to match the former. That curve implies that the observed GSL rise during the past century has been variable in a piecewise manner: A slower section before ~1930 is followed by a faster section until ~1960, with a slower section again extending until ~1990 before becoming faster again. We suggest that this seeming variability in rate is "artificial." If we add back the actual $V(t)$ in Fig. 1 to reconstruct

a GSL curve, giving the GSL variation that would have been free from the impact of artificial reservoirs, it becomes evident that, in contrast to the observations, the post-1930 GSL rose essentially at a constant rate all the way to the recent years (barring any interspersed interannual fluctuations such as El Niño–Southern Oscillation events or volcanic activities) at a rate of +2.46 mm/year, versus an average of +1.7 to 1.8 mm/year during the 20th century with recent acceleration. Whether this means that the global changes causing the GSL rise have been in operation in a rather steady fashion, or instead fortuitously compensated one another over at least the past 80 years, remains to be examined.

Our findings differ from the conventional wisdom, which holds an apparent variable GSL rise according to the face values of observation as stated above. This, of course, by no means precludes the most recent or possible future acceleration of GSL rise (*23*) due to natural causes, compounded by the further slowdown of reservoir-building in the near future (*26*).

References and Notes

1. N. L. Bindoff *et al.*, in *Climate Change 2007: The Physical Science Basis. Contribution of Working Group I to the Fourth Assessment Report of the Intergovernmental Panel on Climate Change*, S. Solomon *et al.*, Eds. (Cambridge Univ. Press, New York, 2007), chap. 5.
2. W. S. Newman, R. W. Fairbridge, *Nature* **320**, 319 (1986).
3. B. F. Chao, *Eos* **72**, 492 (1991).
4. B. F. Chao, *Geophys. Res. Lett.* **22**, 3533 (1995).
5. V. Gornitz, C. Rosenzweig, D. Hillel, *Global Planet. Change* **14**, 147 (1997).
6. V. Gornitz, in *Sea Level Rise*, B. Douglas, M. Kearney, S. Leatherman, Eds. (Academic Press, London, 2001).
7. D. L. Sahagian, *Global Planet. Change* **25**, 39 (2000).
8. D. L. Sahagian, F. W. Schwartz, D. K. Jacobs, *Nature* **367**, 54 (1994).
9. *World Register of Dams* (International Commission on Large Dams, Paris, 2007) (www.icold-cigb.net).
10. F. van der Leeden, *Water Resources of the World* (Water Information Center Inc., New York, 1975).
11. *World Water Balance and Water Resources of the Earth* (UNESCO, Paris, 1978).
12. U.S. Department of the Interior, *Major Dams, Reservoirs, and Hydroelectric Plants* (Bureau of Reclamation, Denver, 1983).
13. *International Water Power & Dam Construction Handbook*, R. M. Taylor, Ed. (Reed Business, Surrey, UK, 1993).
14. World Commission on Dams, *Dams and Development* (Earthscan, London, 2000).
15. UNESCO, *World Water Resources at the Beginning of the 21st Century* (Cambridge Univ. Press, New York, 2003).
16. W. W. Storage, *in Man-Made Reservoirs* (Foundation for Water Research, Marlow, UK, 2005).
17. See supporting material on *Science* Online.
18. Different (least-squares) fit ranges and bin widths were tried; the results vary little.
19. The rapid convergence of the extrapolated integration, consistent with (*20*), down to small reservoir size is assured as follows. For a self-similar fractal "map" distribution of self-similar reservoirs with respect to the linear dimension L, the reservoir number decreases as L^{-2} while the corresponding volume increases as L^3. Hence, the water impoundment for a given size increases as L, dominated by large reservoirs. The actual reservoir number increases with smaller size even more slowly than the above, only at $L^{-1.56}$ ($-1.56 = -0.52 \times 3$). The situation is analogous to the (Richter-Gutenberg) frequency-moment relationship for seismicity, where the "β value" (or the negative of the power-law slope) is ⅔, hence the total seismic energy release is dominated by large earthquakes even though the smaller earthquakes are much more numerous.
20. M. I. L'vovich, G. F. White, in *The Earth as Transformed by Human Action*, B. L. Turner II *et al.*, Eds. (Cambridge Univ. Press, Cambridge, 1990).
21. P. C. D. Milly *et al.*, position paper, World Climate Research Programme Workshop on Understanding Sea-Level Rise and Variability (UNESCO, Paris, 2006).
22. By comparison, in terms of GSL the total atmospheric water content is equivalent to ~35 mm and the total biological water is equivalent to ~3 mm.
23. B. D. Beckley, F. G. Lemoine, S. B. Luthcke, R. D. Ray, N. P. Zelensky, *Geophys. Res. Lett.* **34**, L14608 (2007).
24. Among other anthropogenic (positive) contributions to GSL, groundwater mining (mainly for irrigation) is potentially important (*2*, *5*–*7*), which partially offsets the impact of the reservoir impoundment. Its amount is considerably smaller (*6*), albeit far less certain, than the reservoirs', and presumably grew over the decades with a different time signature. A separate assessment is needed.
25. J. A. Church, N. J. White, *Geophys. Res. Lett.* **33**, L01602 (2006).
26. The slowdown is already evident in Fig. 1, which includes the projection into the next few years according to our tally (for example, $d = -30.6$ mm by 2010), although late reporting of reservoir-building may have also contributed to the apparent slowdown.
27. We thank J. Church, R. Ray, D. Sahagian, A. Cazenave, C. K. Shum, L. Y. Tsai, S. T. Li, and L. Lin for discussions and assistance. Supported by the Taiwan Semiconductor Manufacturing Company Ltd. Chair professorship and by National Science Council of Taiwan grant NSC96-2111-M-008-016-MY2.

Supporting Online Material

www.sciencemag.org/cgi/content/full/1154580/DC1
Materials and Methods
Table S1

26 December 2007; accepted 5 March 2008
Published online 13 March 2008;
10.1126/science.1154580
Include this information when citing this paper.

Determining Chondritic Impactor Size from the Marine Osmium Isotope Record

François S. Paquay,[1]* Gregory E. Ravizza,[1] Tarun K. Dalai,[1]† Bernhard Peucker-Ehrenbrink[2]

Decreases in the seawater $^{187}Os/^{188}Os$ ratio caused by the impact of a chondritic meteorite are indicative of projectile size, if the soluble fraction of osmium carried by the impacting body is known. Resulting diameter estimates of the Late Eocene and Cretaceous/Paleogene projectiles are within 50% of independent estimates derived from iridium data, assuming total vaporization and dissolution of osmium in seawater. The variations of $^{187}Os/^{188}Os$ and Os/Ir across the Late Eocene impact-event horizon support the main assumptions required to estimate the projectile diameter. Chondritic impacts as small as 2 kilometers in diameter should produce observable excursions in the marine osmium isotope record, suggesting that previously unrecognized impact events can be identified by this method.

Terrestrial and lunar impact craters, as well as impact debris in the sediment record, reveal that Earth has been struck by asteroids many times throughout its history. However, it is difficult to estimate the size of the impacting bodies, and it is likely that many impacts remain unrecognized because of the continuous reshaping of Earth's surface. Rough estimates of projectile size result from inventories of excess Ir (*1*), called Ir fluences (nanograms per square centimeter), and from models of impact-crater formation (*2*). The former approach involves averaging many individual fluence estimates to obtain a meaningful global signal (*3*–*5*), whereas the latter approach requires that an impact crater be preserved.

Since the first application of the Os isotopic system to the study of impact events (*6*), this system has been extensively applied to estimating the contribution of the projectile to impact breccias and impact melts (*7*). These studies report high Os concentrations and low $^{187}Os/^{188}Os$ ratios of the projectile compared with the target rock, demonstrating that Os isotopes are very sensitive tracers of the presence of residual projectile material. Most previous Os isotope studies of impact events have focused narrowly on the impact horizon (*6*–*11*). However, Os isotope studies of the marine sediment record that span longer time intervals show that the dissolution of impact-derived Os in seawater lowers the $^{187}Os/^{188}Os$ values of the global ocean (*12*, *13*).

We show here that impact-induced excursions in the marine Os isotope record can be used to estimate chondritic impactor size (*14*). These excursions can be understood as the result of mixing ambient seawater Os (characterized by relatively high $^{187}Os/^{188}Os$) with meteoritic Os [with low $^{187}Os/^{188}Os$ (*15*)] that is vaporized on impact and subsequently dissolved in seawater. This interpretive framework allows for the estimation of

[1]Department of Geology and Geophysics, University of Hawaii, Honolulu, HI 96822–2225, USA. [2]Department of Marine Chemistry and Geochemistry, Woods Hole Oceanographic Institution, Woods Hole, MA 02543, USA.
*To whom correspondence should be addressed. E-mail: paquay@hawaii.edu
†Present address: Department of Geology and Geophysics, Indian Institute of Technology, Kharagpur 721302, India.

projectile size by isotope dilution, provided that the fraction of impact-derived Os that dissolves in seawater is known. The Os isotope composition of seawater is nearly homogeneous, so data from only a single section that accurately records seawater $^{187}Os/^{188}Os$ can be used to make meaningful estimates of projectile size. No analogous variations in Ir isotope composition occur in nature, making the Os isotope system unique among the highly siderophile elements.

As an example, we applied this approach to the known Late Eocene impacts (LEIs) (*16*) and the Cretaceous-Tertiary (K-T) impact (*1*) events. The three key parameters that we used to estimate the fractional increase in the seawater Os reservoir that results from an impact are the $^{187}Os/^{188}Os$ of seawater immediately before and after the impact event (*17*) and the $^{187}Os/^{188}Os$ of the impacting body, which varies over a narrow range (0.123 to 0.129) (*15*). During the LEIs, seawater $^{187}Os/^{188}Os$ shifted from 0.5 to 0.28 (Fig. 1 and table S1), corresponding to a roughly 2.5-fold increase in the size of the seawater Os reservoir because of the impact-derived Os (*18*). Agreement between data from the equatorial Pacific [Ocean Drilling Program (ODP) 1219] and the Southern Ocean (ODP 1090) indicates that these data reflect the response of seawater $^{187}Os/^{188}Os$ to the impacts, rather than mixing of particulate Os from different sources. We suspect that the time required for the impact-induced Os isotope excursion to mix throughout the global ocean is brief, on the order of several thousand years. However, the decline in the sediment $^{187}Os/^{188}Os$ from preimpact levels to minimum values is ~30 to 40 thousand years (ky). The length scale of this decline is 110 to 130 cm, consistent with limited redistribution by diagenesis and/or bioturbation. The Os isotope shift derived from a low-resolution record of the K-T event ranges from 0.4 to 0.157 (Fig. 2), indicating a nearly 10-fold increase in seawater Os inventory.

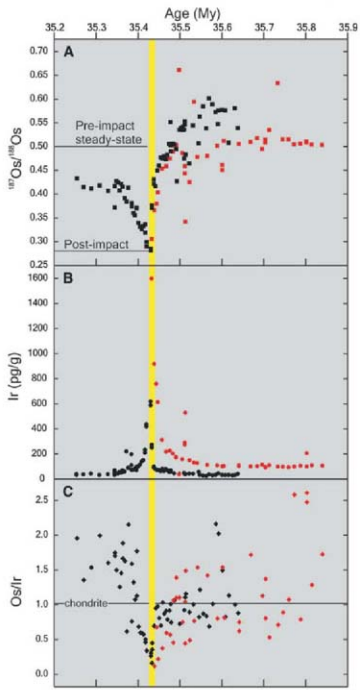

Fig. 1. Profiles of $^{187}Os/^{188}Os$ ratios, Ir concentrations, and Os/Ir ratios from ODP 1219 (7°48.01'N, 142°00.94'W) and ODP 1090 (42°54.8'S, 8°54.0'E). Age control is based on magnetic stratigraphy (*44*, *45*). Most samples are from within magnetochron C16n.1n. Sediments from Site 1219 deposited immediately after the LEIs were unavailable for analysis because of a gap between cores and limited drilling disturbance. Black symbols represent ODP Site 1090; red symbols represent ODP 1219. My, million years. **(A)** Minimum values in $^{187}Os/^{188}Os$ coincide with the Ir maximum, defining an asymmetric excursion with an abrupt onset and gradual recovery. The yellow line indicates the impact horizon. **(B)** Elevated Ir concentrations mark the impact horizon. In ODP Site 1090, clino-pyroxene spherules and microtektites were recognized and coincide with maximum Ir concentrations (*20*). **(C)** At both sites, local maxima in Os concentration are much less pronounced than those in Ir. Os/Ir ratios therefore display a clear minimum at the impact horizon.

A quantitative comparison of the Os isotope method to independent Ir fluence estimates can be made by assuming that the Os concentration of Late Eocene and Late Cretaceous seawater is the same as that of the modern ocean (*19*). This fixes the preimpact size of the seawater Os reservoir at 1.4×10^{19} ng Os (*18*) and allows the mass of impact-derived Os dissolved in the ocean after the LEI (2×10^{19} ng Os) and K-T events (8×10^{19} ng Os) to be calculated. These Os inventories are between 30 and 40% of the Ir inventories for the LEI (4.6×10^{19} ng Ir) and K-T events (28×10^{19} ng Ir), calculated as the product of the average global Ir fluence [LEI = 9 ng/cm^2 (*20*) and K-T = 55 ± 3 ng/cm^2 (*3*)] and the surface area of Earth. Os and Ir inventories can be compared directly because the Os/Ir ratio in chondrites (*15*, *21*) is close to 1. We suspect that the deficit of Os relative to Ir probably results from nonquantitative dissolution of Os in seawater, but the uncertainties in the estimated Os and Ir fluences are too large to argue this point strongly (*22*). Nevertheless, observations that some terrestrial K-T sections are enriched in Os (*7*) are consistent with the idea that Os dissolution is incomplete and Os isotope-based estimates of projectile size that assume quantitative vaporization are biased to low values.

The Os and Ir inventories estimated above can be recast as projectile-size estimates (*23*). The Popigai impactor associated with the LEIs is thought to be an L-type ordinary chondrite (*24*). Using appropriate average bulk density (*25*) and Os and Ir concentrations (*21*) yields an Os-based diameter estimate of 2.8 to 3.0 km for the Popigai impactor (*26*), compared with an Ir-based diameter estimate of 4 km (*27*). For the K-T event, a carbonaceous chondrite (*11*, *28*) is the likely culprit, and analogous calculations yield diameter

estimates of 4.1 to 4.4 and 6 km, based on Os isotopes (*23*) and Ir fluence (*27*), respectively. The smaller size of the Os-based estimates (as compared with Ir is a direct consequence of the relative magnitude of the Os and Ir inventories given above. The most recent simulations of impact-crater formation yielded projectile-size estimates of 15 to 19 km for the K-T Chixulub crater (*2*), 8 km for the Late Eocene Popigai crater (*2*), and 3 km for the Late Eocene Chesapeake Bay crater (*29*, *30*). If these larger projectile-size estimates are correct, this implies that only 2 to 7% of the Os carried by the K-T and LEI projectiles dissolved in seawater. The box-model results below suggest that substantially more than a few percent of the total amount of Os carried by the projectile becomes dissolved in seawater. An important implication of this interpretation is that impact simulations overestimate the projectile diameter. The relatively good agreement between diameter estimates based on Os isotopes and Ir fluence is consistent with this inference. Whereas the choice of projectile velocity and angle of incidence might contribute to the difference in estimated projectile sizes, we do not believe that this is the sole source of the discrepancy. A projectile with substantially lower siderophile-element concentration than any known chondrite—perhaps a comet (*20*)—could account for this difference. However, no independent data are available to support this claim for either the K-T impact events or the LEIs.

Our interpretation requires that dissolved Os and Ir concentrations in the open ocean greatly exceed steady-state values immediately after an impact event. A box model that simulates the postimpact removal of excess dissolved Os and Ir from seawater by first-order kinetics captures the major features preserved in Late Eocene sediments from ODP Site 1090 (Fig. 3). We used initial conditions that correspond to dissolved Os concentrations that are elevated 2.5 times above steady-state levels with an initial postimpact $^{187}Os/^{188}Os$ of 0.28 (Fig. 1). These conditions were chosen to match the estimates of seawater and projectile-derived Os inventories made above. To simulate Ir removal from seawater, we assumed equal masses of impact-derived Os and Ir (2×10^{19} ng). This assumption, together with the very low Ir concentration of modern seawater (*31*) as compared with that of Os (*19*), resulted in model initial conditions where dissolved Ir was elevated 50 times above steady-state levels. The postimpact steady state $^{187}Os/^{188}Os$ was set at 0.42 to match the postimpact sediment data (Fig. 3A). The Os/Ir ratio of modern seawater is ~100 (*20*), whereas the Os/Ir ratio of modern pelagic carbonates falls between 2 and 3 (*21*). This difference indicates more rapid scavenging of Ir relative to Os in the open ocean. Therefore, to compare measured sediment Os/Ir ratios to model seawater ratios, we used $(Os/Ir)_{sediment} = 0.02(Os/Ir)_{seawater}$ (see note S1 in the supporting online material for detailed information about the model). The change in the sediment $^{187}Os/^{188}Os$ and Os/Ir with time was visually fit by adjusting the marine residence times of Os and Ir to match the sediment data (Fig. 3).

The comparison of model calculations with measured data yields estimated Late Eocene marine residence times of 25,000 years for Os and 5000 years for Ir. These values are similar to the modern marine residence-time estimates for Os and Ir—40,000 and 2000 years, respectively (*31*, *32*). The Os/Ir ratio calculated for Eocene

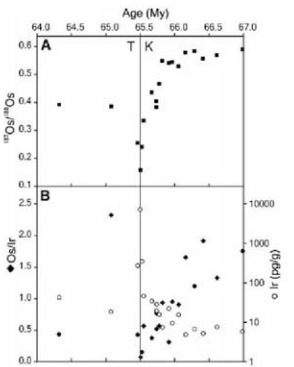

Fig. 2. (**A**) Low-resolution record of sediment $^{187}Os/^{188}Os$ across the K-T boundary in Deep Sea Drilling Project 577 (*13*). (**B**) Associated record of Ir and Os concentration variations from the same site. There is a distinct minimum in Os/Ir at the K-T boundary, similar to the pattern observed in the LEI event record (Fig. 1).

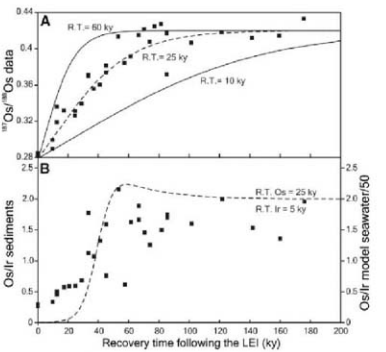

Fig. 3. Comparison of results from a one–box model simulation of recovery of seawater Os and Ir chemistry after the LEI impact event to data from ODP 1090 (Fig. 1). Initial conditions were chosen to mimic mixing the Os and Ir (2×10^{19} ng) with a seawater Os and Ir reservoir equivalent to that of the modern ocean. (**A**) We used a range of residence times (R.T.) for Os to fit the $^{187}Os/^{188}Os$ recovery with a visual best-fit at 25 ky (dashed line). The lower bound was set with an R.T. of 60 ky and the upper bound at 10 ky. (**B**) Os and Ir residence times were set at 25 and 5 ky, respectively [fractional increase in seawater reservoir (*18*) Os = 2.5 and Ir = 147]. The model Os/Ir curve (dashed line) was multiplied by 0.02 to allow a direct comparison of the range in Os/Ir measured in sediments to that of seawater.

seawater immediately after the impact (1.6) is initially close to the chondritic ratio of 1 and gradually recovers to higher values (Fig. 3B). The same trend is apparent in the ODP 1090 record, but the absolute Os/Ir ratios are shifted to distinctly subchondritic ratios as a result of preferential Ir scavenging as described above. The same pattern is also apparent in our low-resolution Os/Ir record spanning the K-T impact (Fig. 2). This simple model based on the behavior of Os and Ir in modern seawater yields reasonable residence-time estimates and can account for the observed sedimentary Os/Ir ratios. Thus, the major features of the ODP 1090 record can be understood as a result of the scavenging of dissolved elements from seawater without contributions from a large inventory of particulate Os or Ir from refractory phases that may have condensed in the atmosphere (*33*) and subsequently settled through the water column. Together with reported Os burial fluxes in pelagic sediments, Os residence-time estimates obtained from the model provide evidence that our assumption that the Os concentration of Late Eocene seawater is similar to that of the modern ocean is reasonable (*34*–*38*).

Paired Os/Ir and Os isotope records can also serve as an effective tool for distinguishing impact events, which vaporize Os and Ir and modify global seawater chemistry, from local enrichment of particulate extraterrestrial material. The latter could result from either a variable sediment-accumulation rate or fluctuation in the background flux of particulate extraterrestrial matter. Elevated Ir concentrations and lower $^{187}Os/^{188}Os$ could result from either an impact or particulate extraterrestrial matter. However, particle enrichment would not shift sediment Os/Ir to the distinctly subchondritic values observed in both Late Eocene records, because small unvaporized particles with chondritic Os/Ir ratios would accumulate intact. For example, some particulate extraterrestrial enrichment seems to characterize the Late Eocene sections of the ODP 1090 record before the impact events (Fig. 1). This may be causally linked to the episodes of increased flux of interplanetary dust particles inferred from ^{3}He data (*39*).

There are two distinctly different sources of uncertainty associated with the projectile-size estimates made here. The first is associated with the Os isotope-dilution calculation and the related assumptions about the dissolution of Os in seawater. The effects of these parameters on the projectile-diameter estimates are illustrated by sigmoidal curves (Fig. 4) showing that as the $^{187}Os/^{188}Os$ of postimpact seawater approaches that of the projectile (~0.13), error amplification becomes extremely large. This is important for K-T projectile-size estimates because small variations in boundary horizon $^{187}Os/^{188}Os$ can give rise to large changes in the projectile-size estimate (*40*). At the opposite end of the size spectrum, there is also substantial error amplification, corresponding to decreases in the seawater $^{187}Os/^{188}Os$ that are difficult to resolve from other sources of natural variability. The offset between the LEI and K-T fields in Fig. 4 illustrates the second source of uncertainty, which results from the need to constrain projectile Os concentration and bulk density by choosing a particular type of projectile. This offset provides a reasonable representation of the range of uncertainty introduced when the type of chondrite is unknown, because the Os concentration difference between the K-T and LEI projectile type spans nearly the maximum range in average Os concentrations among the major chondrite classes (*21*). Estimates of projectile size based on Ir fluence require equivalent assumptions about projectile type. An iron meteorite impact would produce an Os isotope excursion larger than that produced by a chondritic projectile of the same size (Fig. 4) because of higher densities (*25*) and larger Os concentrations (*41*). However, Cr isotopes (*11*) and $^{186}Os/^{188}Os$ (*9*) differentiate chondrites from irons and could be used to eliminate this potential source of uncertainty in projectile-size estimates.

The marine Os isotope record should also be sensitive to impact events smaller than the LEIs. For 30% dissolution of impact-derived Os in seawater, a 2-km chondritic body would produce a decrease of ~0.05 in seawater $^{187}Os/^{188}Os$ (Fig. 4). If only 5% of the total Os supplied by the projectile dissolves in seawater, as implied by impact-crater simulations (*2*, *41*), then a 4-km body would be reuired to produce the same magnitude of excursion (~0.05). The model results presented above suggest that it is probable that the fraction of the impact-derived Os dissolved in seawater is much larger than 5%, because the major features of the bulk sediment $^{187}Os/^{188}Os$ and Os/Ir records can be reproduced with a model in which the entire sedimentary Os and Ir inventories are scavenged from seawater. Based on observations of near-Earth asteroids, the estimated recurrence interval for bodies 4 km and larger is ~12 million years; for bodies 2 km and larger, it is ~2.5 million years (*42*). If correct, these recurrence intervals suggest that there should be between 5 and 27 impact-related excursions in the Cenozoic marine Os isotope record. Whereas we are confident that sediments recovered from the modern sea floor (like those studied here) will preserve the record of such events, we are not certain that older marine sequences now preserved on land will have the same fidelity.

Testing the lower limit of projectile detection warrants further investigation. The efficiency of Os and Ir vaporization may decrease with decreasing projectile size and may vary with target material. In addition, small regional heterogeneities in seawater $^{187}Os/^{188}Os$ [like those implied by the small offset between the ODP 1090 and 1219 records before LEIs (Fig. 1)] make it difficult to precisely estimate the $^{187}Os/^{188}Os$ of preimpact seawater. Both factors could make detection and size estimation of smaller impacts more difficult than is implied by Os isotope results from the larger K-T and LEI events. Other known Cenozoic impact craters provide an opportunity to investigate these issues. For example, the Ir-rich Eltanin asteroid [estimated at 1 to 4 km in size (*43*)] that hit the Pacific Ocean west of the southern end of South America in the Bellinghausen Sea is of particular interest because, in contrast to the LEI and K-T events, it is a deep-ocean impact.

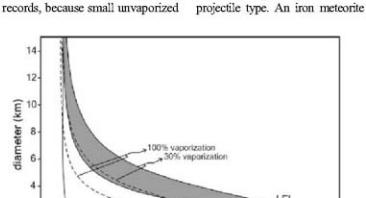

Fig. 4. Variation of estimated projectile diameter as a function of postimpact seawater $^{187}Os/^{188}Os$, projectile type, and fraction of Os vaporized. Projectile-diameter estimates are sensitive to the $^{187}Os/^{188}Os$ ratio of seawater before the impact and projectile Os concentration, requiring that the K-T boundary (white field bounded by dashed lines) and the LEI (gray field) be represented by different curves. The curve labeled "Irons," calculated with an average Os concentration of 30,000 ng/g (*40*) and a density of 8 g/cm^3 (*25*), predicts the strong influence of a relatively small iron meteorite on the $^{187}Os/^{188}Os$ of seawater. Projectiles as small as 2 km are expected to produce a detectable shift in $^{187}Os/^{188}Os$ (~0.05), assuming that 100% dissolution of impact-derived Os is soluble in seawater.

References and Notes

1. L. W. Alvarez, W. Alvarez, F. Asaro, H. V. Michel, *Science* **208**, 1095 (1980).
2. B. A. Ivanov, *Sol. Syst. Res.* **39**, 381 (2005).
3. S. Donaldson, A. R. Hildebrand, *Meteorit. Planet. Sci.* **36** (suppl.), A50 (2001).
4. P. Claeys, W. Kiessling, W. Alvarez, *Geol. Soc. Am. Spec. Pap. 356* (2002), pp. 55–68.
5. A synthesis of existing Ir fluence data reveals a nearly 100-fold range in Ir fluence among the 55 sections studied to date (*3*). A review of data from the K-T

boundary shows maximum Ir concentrations ranging from 0.1 to 87 ng/g in 85 sections from deep marine to continental depositional environments (4).
6. J. M. Luck, K. K. Turekian, *Science* **222**, 613 (1983).
7. C. Koeberl, S. B. Shirey, *Palaeogeogr. Palaeoclimatol. Palaeoecol.* **132**, 25 (1997).
8. T. Meisel, U. Krähenbühl, M. A. Nazarov, *Geology* **23**, 313 (1995).
9. R. Frei, K. M. Frei, *Earth Planet. Sci. Lett.* **203**, 691 (2002).
10. D. G. Pearson *et al.*, *Geol. Soc. Am.* **31**, 123 (1999).
11. G. Quitté *et al.*, *Meteorit. Planet. Sci.* **42**, 1567 (2007).
12. B. Peucker-Ehrenbrink, G. E. Ravizza, A. W. Hofmann, *Earth Planet. Sci. Lett.* **130**, 155 (1995).
13. G. Ravizza, B. Peucker-Ehrenbrink, *Science* **302**, 1392 (2003).
14. The marine Os isotope record, like the Ir fluence approach, is not well suited to detecting the impact of differentiated projectiles, such as achondrites with siderophile-element concentrations that are two to three orders of magnitude lower than chondrites (*7*).
15. M. F. Horan, R. J. Walker, J. W. Morgan, J. N. Grossman, A. E. Rubin, *Chem. Geol.* **196**, 5 (2003).
16. J. Whitehead, D. A. Papanastassiou, J. G. Spray, R. A. F. Grieve, G. J. Wasserburg, *Earth Planet. Sci. Lett.* **181**, 473 (2000).
17. Methods and data table are available as supporting material on *Science* Online.
18. The increase in the seawater Os reservoir after an impact event is determined by knowing (i) the Os concentration in modern seawater (~10 pg/kg) (*19*) and (ii) the estimated mass of the seawater (~1.4×10^{21} kg). The product of these gives the mass of Os in the ocean before an impact [mass Os_{sw} (ng)]. The mass of Os derived from the impactor [mass $Os_{impactor}$ (ng)] is $(f1 - f) \times$ mass Os_{sw} where $f = ({}^{187}Os/{}^{188}Os_{postimpact} - {}^{187}Os/{}^{188}Os_{preimpact})/({}^{187}Os/{}^{188}Os_{impactor} - {}^{187}Os/{}^{188}Os_{preimpact})$. The fractional increase in the seawater Os reservoir is (mass Os_{sw} + mass $Os_{impactor}$)/mass Os_{sw}).
19. S. Levasseur, J.-L. Birck, C. J. Allègre, *Science* **282**, 272 (1998).
20. F. T. Kyte, S. Liu, *Lunar Planet. Sci.* XXXIII, 1981 (abstr.) (2002).
21. J. T. Wasson, G. W. Kallemeyn, *Philos. Trans. R. Soc. London Ser. A* **325**, 535 (1988).
22. A doubling of seawater Os concentration to 20 pg/kg would erase the Os deficit.
23. The diameter *D* is estimated assuming a spherical projectile *D* (km) = [2 × [mass $Os_{impactor}$ × 3/($Os_{impactor}$ (ng/g) × $\rho_{impactor}$ (kg/m^3) × 4π]$^{1/3}$]/1E4 with mass $Os_{impactor}$ derived from (*18*). [$Os_{impactor}$ is the Os concentration in the impactor (*21*), and $\rho_{impactor}$ is the density of the impactor (*25*).
24. R. Tagle, P. Claeys, *Geochim. Cosmochim. Acta* **69**, 2877 (2005).
25. R. L. Kootev, Washington Univ. (St. Louis); available at http://meteorites.wustl.edu/id/density.htm.
26. In the calculations (*23*), an Os concentration ([$Os_{impactor}$] of 490 ng/g (*21*) and an average density ($\rho_{impactor}$) of 3.35 g/cm^3 (*25*) were representative of an L chondrite meteorite (Popigai LEI event), whereas an Os concentration of 807.5 ng/g (*21*) and an averaged density of 3 g/cm^3 (*25*) were used as representative of a carbonaceous chondrite (*28*) for the K-T event.
27. The Ir-based estimate is calculated by knowing the Ir fluence (*3*, *20*), chondritic Ir concentration (Os/Ir = 1.08) (*25*), average density of a chondrite (*25*), and Earth global Ir inventory.
28. F. T. Kyte, *Nature* **396**, 237 (1998).
29. G. S. Collins, K. Wunnemann, *Geology* **33**, 925 (2005).
30. The Ir and Os isotope-based projectile-size estimates probably represent the integrated signal from both the Popigai and the Chesapeake Bay impacts, because spherules believed to derive from both events are found within the single Ir peak at ODP 1090 (*20*). The smaller estimated size for the Chesapeake Bay projectile (*29*) suggests that >90% of the Os and Ir released to the environment was derived from the Popigai event.
31. A. D. Anbar, G. J. Wasserburg, D. A. Papanastassiou, P. S. Andersson, *Science* **273**, 1524 (1996).
32. C.-T. A. Lee, G. J. Wasserburg, F. T. Kyte, *Geochim. Cosmochim. Acta* **67**, 655 (2003).
33. D. S. Ebel, L. Grossman, *Geology* **33**, 293 (2005).
34. In the steady-state, the relation between reservoir size *N*, removal flux *F*, and residence time *t* is $t = N/F$. This relation implies that the Eocene seawater Os concentration was similar to the modern value, because Eocene estimates of Os burial flux (*35*) and Os residence time made in this work are very similar to recent values (*36*–*38*).
35. T. K. Dalai, G. E. Ravizza, B. Peucker-Ehrenbrink, *Earth Planet. Sci. Lett.* **241**, 477 (2006).
36. T. K. Dalai, G. E. Ravizza, *Geochim. Cosmochim. Acta* **70**, 3928 (2006).
37. S. Levasseur, J.-L. Birck, C. J. Allègre, *Earth Planet. Sci. Lett.* **174**, 7 (1999).
38. R. Oxburgh, *Earth Planet. Sci. Lett.* **159**, 183 (1998).
39. K. A. Farley, A. Montanari, E. M. Shoemaker, C. S. Shoemaker, *Science* **280**, 1250 (1998).
40. For example, the lowest K-T boundary $^{187}Os/^{188}Os$ ever reported (0.137) (*8*) corresponds to a projectile size of greater than 6 km in diameter. On the basis of the unusually large Os concentration at this section, we believe that this section does not accurately reflect the true $^{187}Os/^{188}Os$ concentration of seawater immediately after the K-T event. Instead, we suspect a substantial inventory of particulate impact-derived Os.
41. J. W. Morgan, M. F. Horan, R. J. Walker, J. N. Grossman, *Geochim. Cosmochim. Acta* **59**, 2331 (1995).
42. G. S. Collins, H. J. Melosh, R. A. Marcus, *Meteorit. Planet. Sci.* **40**, 817 (2005).
43. F. T. Kyte, *Deep-Sea Res. II* **49**, 1049 (2002).
44. J. E. T. Channell *et al.*, *Geol. Soc. Am. Bull.* **115**, 607 (2003).
45. H. Pälike *et al.*, *Sci. Res., Proc. Ocean Drill. Prog.* (Ocean Drilling Program, College Station, TX, 2005), vol. 199.
46. We thank the ODP for providing the samples, D. Vonderhaar for technical assistance, E. Scott for his advice and expertise on meteorites, and R. Smith for support. Comments by three anonymous reviewers greatly improved the paper. This work was supported by NSF grants OCE and EAR to G.E.R. and B.P.-E.

Supporting Online Material

www.sciencemag.org/cgi/content/full/320/5873/214/DC1
Materials and Methods
SOM Text
Table S1

12 November 2007; accepted 29 February 2008
10.1126/science.1152860

Linked Reactivity at Mineral-Water Interfaces Through Bulk Crystal Conduction

Svetlana V. Yanina and Kevin M. Rosso*

The semiconducting properties of a wide range of minerals are often ignored in the study of their interfacial geochemical behavior. We show that surface-specific charge density accumulation reactions combined with bulk charge carrier diffusivity create conditions under which interfacial electron transfer reactions at one surface couple with those at another via current flow through the crystal bulk. Specifically, we observed that a chemically induced surface potential gradient across hematite (α-Fe_2O_3) crystals is sufficiently high and the bulk electrical resistivity sufficiently low that dissolution of edge surfaces is linked to simultaneous growth of the crystallographically distinct (001) basal plane. The apparent importance of bulk crystal conduction is likely to be generalizable to a host of naturally abundant semiconducting minerals playing varied key roles in soils, sediments, and the atmosphere.

The chemical behavior of mineral-water interfaces is central to aqueous reactivity in natural waters, soil evolution, and atmospheric chemistry and is of direct relevance for maintaining the integrity of waste repositories and remediating environmental pollutants. Traditionally, explorations of fundamental reactions at these interfaces have probed the interaction of water and relevant dissolved ions with crystallographically well-defined mineral surfaces. The pursuit so far has been dominated by the assumption that distinct surfaces of any given crystal behave independently of each other. Except by diffusion through the solution phase or across surface planes, exchange of mass or electron equivalents between sites of differing potential energy at different locations on any given crystal is typically assumed to be negligible. This assumption is nonetheless questionable for the widespread group of minerals that are electrical semiconductors. For example, iron oxides often have moderate to low electrical resistivity (*1*) and have been studied as electrode materials for decades (*2*–*4*). Iron oxide crystal surfaces are chemically reactive with water and ions, leading to solution-dependent charging behavior that differs from one surface type to the next; differing points of zero charge for proton adsorption is but one example (*5*, *6*). This difference should give rise to a surface electric potential gradient ($\Delta\psi_0$) across any crystal that has two or more structurally distinct faces exposed to solution. In principle, this gradient can bias the diffusion of charge carriers (*7*, *8*). Hence, conditions could exist when the gradient across a single crystal is sufficiently large and the electrical resistivity of the material sufficiently

Chemical and Materials Sciences Division, Pacific Northwest National Laboratory, Post Office Box 999, MSIN K8-96, Richland, WA 99352, USA.

*To whom correspondence should be addressed. E-mail: kevin.rosso@pnl.gov

low that interfacial electron transfer reactions at one surface couple with those at another by a current flowing spontaneously through the crystal bulk. The situation is analogous to galvanic metal corrosion, but instead of spatially disordered anodic and cathodic electron transfer sites, the anode and cathode are spatially confined to crystallographically distinct surface planes and are therefore physically separable for measurement. We demonstrate operability of these conditions for iron oxide, uncover their effects on the surface chemical behavior, and make the case that, in nature, different surfaces of certain abundant crystals are inextricably linked.

We examined hematite (α-Fe_2O_3) because it is a wide band gap semiconductor (band gap 1.9 to 2.3 eV) (*1*, *3*) and the most stable form of iron oxide under dry oxidizing conditions; it is extremely common in nature (*9*). It has the corundum structure type based on hexagonal close packed oxygen planes in which 2/3 of the available octahedral cavities are occupied by Fe^{3+}. This structure gives rise to anisotropic electrical resistivity that is higher in the basal plane than along the trigonal axis by up to four orders of magnitude (*10*, *11*); reported bulk resistivities range from 10^2 to 10^6 ohm·m (*1*). When hematite is subjected to oxygen-limited aquatic environments, particularly in acidic conditions, it can be reductively dissolved according to Eq. 1:

$$Fe_2O_3 + 6H^+ + 2e^- \rightarrow 2Fe^{2+}_{(aq)} + 3H_2O \quad (1)$$

which has a standard reduction potential $E^o \sim 0.7$ V (*8*, *12*). The fundamental reaction central to the overall process is

$$Fe^{3+}_{(s)} + e^- \rightarrow Fe^{2+}_{(aq)} \quad (2)$$

Sorbed Fe^{2+} from the aqueous phase is capable of reducing hematite Fe^{3+} in this system (*13*–*15*), yielding an iron redox cycle in which no net reduction occurs. Introduction of dicarboxylic acids such as oxalate causes net dissolution by chelating surface Fe^{3+} (ligand assisted dissolution); it also enhances reduction, possibly through the formation of ternary surface complexes with $Fe^{2+}_{(aq)}$, for example (*16*). This collective chemistry is a good test case for our main hypothesis because it involves a source of electron equivalents from Fe^{2+} in solution, a range of potential-determining ions, electron transfer across hematite-solution interfaces, and the possibility of moving electron equivalents through the crystal bulk.

Development of a potential gradient $\Delta\psi_0$ of significant magnitude across the crystal requires selective interaction between potential-determining ions and specific hematite surfaces. We focus here on roles of protons (low pH) and oxalate as a representative dicarboxylic acid. The hematite (001) basal surface is structurally distinct from any edge surfaces. In water, the (001) surface is terminated predominantly by doubly coordinated hydroxyls (*17*–*19*) that are relatively inert to the protonation and deprotonation reactions needed for charge accumulation. Smaller populations of more reactive singly coordinated and triply coordinated hydroxyls, capable of positive charge accumulation, are associated with terminal Fe groups (*19*). Terminal Fe groups with low coordination to the underlying surface can be easily chelated by oxalate anions to form negatively charged mononuclear bidentate inner-sphere surface complexes (*20*, *21*). In contrast, many remaining low-index surfaces of hematite crystals such as (012) are dominated by higher-coordinated Fe (*17*, *22*). This higher-coordinated Fe is more difficult to chelate yet bears singly and/or triply coordinated hydroxyls for charge accumulation. In general therefore, we expect that, relative to other hematite surfaces, the (001) surface should show weaker pH-dependent charge accumulation, an observation increasingly confirmed by recent data and theory (*23*, *24*), and stronger interaction with oxalate anions that increases with decreasing pH.

We performed several experiments to potentiometrically measure $\Delta\psi_0$ for specific hematite surfaces and to determine its effect on their behavior in Fe^{2+} and oxalate solutions. We chose a large natural specular hematite crystal with well-defined surfaces that could be isolated for study. The crystal was low in impurity content (*25*), a natural *n*-type semiconductor (*1*), and had a room temperature electrical resistivity of 10^5 ohm·m as measured by the four-point probe method. Generating replicate samples required cutting specific crystallographic surfaces from the crystal as rectangular prism-shaped specimens, which also yielded a vicinal surface type along cut edges. For example, we prepared millimeter-sized oriented prisms exposing two (001) surfaces on the top and bottom of the prism and four orthogonal (*hk*0) vicinal sides (*25*). Annealing in air under conditions where hematite is the only stable iron oxide effectively cleans and organizes the surfaces without modifying the bulk electrical conductivity. This procedure yields highly organized (001) surfaces, with accompanying (*hk*0) vicinal surfaces that are microfaceted with stable edge terminations (Fig. 1, A and B). Similarly, prism specimens bearing (012) and (113) surfaces (Fig. 1, C and D) with accompanying vicinal surfaces were prepared.

To determine the magnitude of $\Delta\psi_0$ and the roles of Fe^{2+} and oxalate solution components,

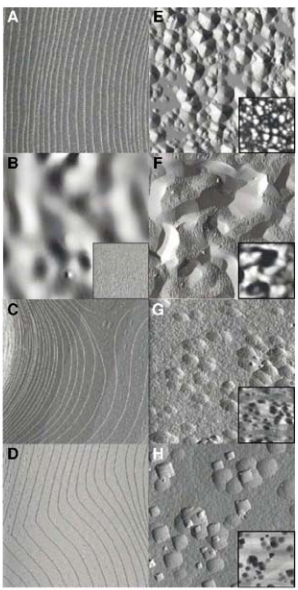

Fig. 1. AFM images of representative hematite surfaces of the natural samples before (**A** to **D**) and after (**E** to **H**) reaction at 75°C for 12 hours in the pH range of 2 to 3 in 1 mM Fe^{2+} and 10 mM oxalate solution free of oxygen. Initial surface morphologies [(A) to (D) 10 μm by 10 μm deflection images] for (A) a (001) surface, (B) a (*hk*0) surface, (C) a (012) surface, and (D) a (113) surface are extremely flat and in all cases except (*hk*0) crystallographically well ordered into terrace-and-step structures at the micrometer scale. At higher resolution [(B) inset, 2 μm by 2 μm deflection image], the (*hk*0) surface is microfaceted with edge terminations. Reacted surfaces [(E) to (H), 20 μm by 20 μm deflection images with corresponding topographic height images in the insets] show a sharp distinction between (E) the (001) surface behavior and (F) the (*hk*0) surface, (G) the (012) surface, and (H) the (113) surface. Large hematite pyramids of uniform orientation nucleate as islands on the initially flat (001) surface (E), achieving average heights of 200 nm and average lateral diameters on the order of a micrometer. In contrast, all other surfaces dissolve. Dissolution of the (*hk*0) surface yields large irregular pits and coarsens the faceted appearance of the surface (F). Dissolution of (012) and (113) surfaces yields large crystallographically controlled etch pits combined with smaller scale roughening [(G) and (H), respectively].

we measured the open-circuit potential (E_{OCP}) in four solution types. The E_{OCP} is the electrode rest potential relative to a standard reference electrode. Changes in the E_{OCP} are directly related to changes in ψ_0 (*26*, *27*), which in turn is sensitive to surface complexation reactions with our potential-determining ions H^+, Cl^-, Fe^{2+}, and oxalate species (*28*). The measurements were performed at room temperature at effectively constant ionic strength under anaerobic conditions (*25*). We focused these measurements on the (001) and the accompanying (*hk*0) vicinal surface type. The observed approximately linear pH dependence, with predominantly negative slopes, is consistent with the accumulation of positive surface charge with decreasing pH (Fig. 2). As expected, in pure electrolyte solution the (001) surface showed a less-negative slope relative to that of the (*hk*0) surface, consistent with a lower density of charge accumulation sites on the (001) surface (Fig. 2A). In contrast, oxalate anions bind preferentially to the (001) surface with decreasing pH, even to the point of sign reversal in the slope (Fig. 2B). Addition of Fe^{2+} to either solution shows that its primary effect is to lower the overall potential for both the (001) and (*hk*0) surfaces without substantially modifying the pH dependence (Fig. 2, A and B). Taking $E_{(hk0)} - E_{(001)}$ as an estimate of $\Delta\psi_0$, in the presence of oxalate and irrespective of the presence of $Fe^{2+}_{(aq)}$ we found that the potential gradient is large and positive, on the order of tenths of volts below pH = 3 (Fig. 2C). Under these conditions, we expect that mobile electrons acting as majority carriers in hematite would be directed by $\Delta\psi_0$ from the (001) surface to the (*hk*0) surface. E_{OCP} measurements directly between identical surface types [e.g., $E_{(001)} - E_{(001)}$] (*25*) showed no significant voltage.

To examine the effects of $\Delta\psi_0$ of this sign and magnitude on the surface chemical behavior, we examined surfaces of the oriented prisms from the same sample by using atomic force microscopy (AFM) before and after anaerobic reaction with Fe^{2+}-oxalate solutions. Thermostated batch vessels were used with temperatures ranging from room temperature to 75°C and pH ranging from 2 to 3 (*25*). Fe^{2+}-oxalate concentrations consistent with previously published experiments that establish net dissolution in terms of $Fe^{3+}_{(aq)}$ release on fine-grained powders were used (*16*, *29*, *30*). Collectively, these conditions were selected in keeping with Eq. 1 while also accelerating surface transformations into a more easily observable time frame. Light was excluded in all cases to avoid oxalate acting as a reductant. Equilibrium thermodynamic calculations along with Eh measurements at run conditions confirm that all our reaction conditions lie within the $Fe^{2+}_{(aq)}$ stability field (*25*). Hematite was the limiting reactant; total dissolution would retain undersaturation with respect to any possible iron oxide phases.

AFM examination of (001) surfaces after reaction runs showed remarkable features. In every case, for both natural and synthetic samples, (001) surfaces were overgrown with a hexagonal pseudo-pyramidal morphology of uniform orientation. Images at early stages show the island growth of these features on the initially flat (001) surface (Fig. 1E). After 12 hours, the reaction yielded merged pyramid-covered (001) surfaces with peak-to-valley heights averaging 200 nm and pyramid bases approaching a micrometer in width, imparting a distinct matte appearance to the reacted (001) surface visible to the naked eye. Transmission electron microscopy (TEM) and selected area diffraction measurements along [001] transects of this sample type (fig. S1), along with x-ray photoelectron spectroscopy, x-ray diffraction, and energy dispersive x-ray spectroscopy, confirmed that the grown material is structurally and compositionally α-Fe_2O_3 of identical orientation as the underlying material without detectable impurities. The line of intersection of apparent pyramid "facets" with the (001) plane is consistent with lines of {012}/{001} intersec-

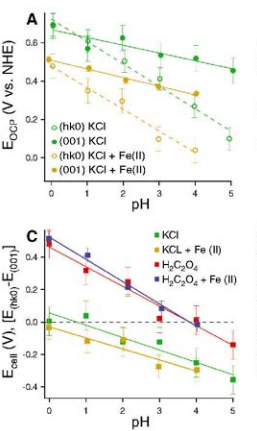

Fig. 2. The pH dependence of open-circuit potentials with respect to the normal hydrogen electrode (NHE) for (001) and (*hk*0) surfaces in **(A)** pure electrolyte solution (10 mM KCl) with and without $Fe^{2+}_{(aq)}$ (1 mM $FeCl_2$) and in **(B)** electrolyte solution (10 mM KCl) with oxalate (10 mM) with and without $Fe^{2+}_{(aq)}$ (1 mM $FeCl_2$). The pH dependence of the potential difference between (001) and (*hk*0) surfaces in the four solution types is shown in **(C)**. Error bars indicate ± two standard deviations from a linear trend.

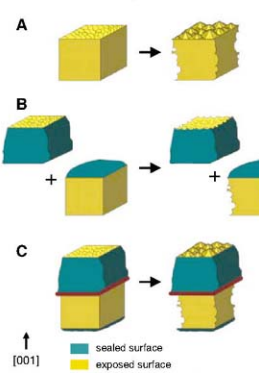

Fig. 3. Schematic diagram summarizing the observed reaction behavior for hematite crystals showing **(A)** (001) pyramidal growth coupled to (*hk*0) dissolution, **(B)** (001) and (*hk*0) dissolution for selectively sealed two-crystal cases where the same surface area and type as in (A) are exposed to solution, and **(C)** (001) pyramidal growth coupled to (*hk*0) dissolution facilitated by a conducting paste connection between two crystals.

tion, but the interplanar angle varies with run duration and does not correspond to low-index planes in hematite. The large size, morphologic symmetry, and mutual orientation of these pyramids require homoepitaxy, that is, growth of additional hematite on hematite.

In contrast, all other surfaces examined show features characteristic of dissolution. For example, the four (*hk*0) vicinal sides of prism samples bearing (001) surfaces on top and bottom exhibited fine-scale pitting and roughening (Fig. 1F). The (012) and (113) surfaces of prism samples show development of etch pits at various length scales and with symmetry corresponding to crystallographic orientation (Fig. 1, G and H). We observed identical behavior under the same conditions with use of synthetic tabular hematite crystals bearing primarily (001) and (012) surfaces, in which case no surface preparation by annealing was required (fig. S2). The conclusion is that the hematite (001) surface grows under our conditions whereas all other surfaces sampled dissolve, as represented schematically in Fig. 3A.

We designed experiments using the prism samples to test whether or not pyramid islands are deposited on the (001) surface by precipitation of trace Fe^{3+} from solution (*16*). In these experiments, two prism samples were used in the reaction vessel instead of one. Four (*hk*0) vicinal sides of one crystal were sealed with an inert epoxy (*25*), leaving two (001) surfaces exposed, whereas on the other crystal the two (001) surfaces were sealed, leaving four vicinal surfaces exposed. Collectively, the two crystals expose the same six kinds of surfaces to solution as in the runs above with one crystal, in the same relative proportion and surface area, but they involve (001) surfaces that are physically separated from the (*hk*0) surfaces (Fig. 3B). In this case, the results of reaction runs show only dissolution features on all exposed surfaces, including (001) (fig. S3A). The (001) pyramidal morphology does not develop in this separated two-crystal configuration. The same experiment performed on samples in which the pyramidal morphology had already been grown on (001) before sealing its (*hk*0) sides showed dissolution of the pyramidal overgrowths on the (001) surface (fig. S3B). Therefore, the (001) pyramidal overgrowths do not form by precipitation of ferric iron. Furthermore, we deduce that chemical processes at the (001)-solution interface causing pyramidal growth during reaction are facilitated by solid contact between the (001) and (*hk*0) surfaces; that is, these surfaces must be on the same crystal.

The behavior strongly suggests that bulk charge transport provides the link between the two types of surfaces. As a further test, we again prepared two crystals with partial exposure of (001) on one and (*hk*0) surfaces on the other, except this time with an electrical connection between them (Fig. 3C). A crystal exposing only (001) surfaces was connected to a crystal beneath exposing only (*hk*0) surfaces by electrically conductive colloidal Ag paste, which was subsequently cured, sealed off from contact with solution using additional epoxy, and tested for ohmic behavior by resistivity measurements. In this design, the crystals are effectively wired together by the (001)-Ag-(001) junction between them. Reaction in this wired two-crystal configuration proceeds as if the crystals were one; pyramidal hematite grows on the exposed (001) surface of the upper crystal (fig. S3C), whereas the four (*hk*0) sides of the lower crystal dissolve (Fig. 3C). Therefore, the nature of the interaction between the (001) and vicinal surfaces that gives rise to the pyramidal growth of hematite (001) during reaction derives from bulk charge transport. Surface diffusion along the hematite-solution interface was ruled out by painting a ring of sealant on a (001) surface so that only bulk transport could access the circumscribed region, and within that region hematite island growth also occurred (fig. S4).

The collective behavior of the system is therefore suggestive of two distinct but coupled interfacial processes: growth at (001) by

$$Fe^{2+}_{(aq)} \rightarrow Fe^{2+}_{(001)} \rightarrow Fe^{3+}_{(001)} + e^- \quad (3)$$

and dissolution of edge surfaces, for example, (*hk*0) surfaces, by

$$Fe^{3+}_{(hk0)} + e^- \rightarrow Fe^{2+}_{(hk0)} \rightarrow Fe^{2+}_{(aq)} \quad (4)$$

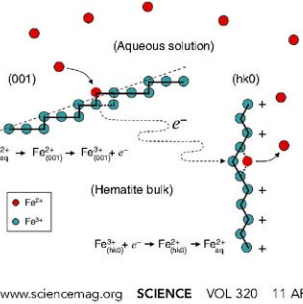

Fig. 4. Schematic diagram depicting the inferred coupled interfacial electron transfer process operative under our conditions for the hematite single crystals. The chemically self-induced surface potential gradient across the crystal directs current flow through the bulk. The current is facilitated by sufficiently low electrical resistivity in a process that is fed by net injection of electron equivalents at (001) surfaces and net release of electron equivalents at (*hk*0) surfaces.

with coupling mediated by charge transport from (001) to (*hk*0) surfaces through the crystal bulk. The process involves preferential net oxidative adsorption of $Fe^{2+}_{(aq)}$ at the (001)-solution interface and valence interchange with structural Fe^{3+} at that surface (Fig. 4). At temperatures of interest (room temperature and higher), bulk charge transport is sufficiently facile to support a small current through the bulk. Net electron equivalents injected into the (001) surface follow an electrically biased random walk through the crystal to (*hk*0) surfaces. At (*hk*0) exit points, internal reduction of Fe^{3+} to Fe^{2+} solubilizes and releases iron into solution. This circuit is driven by the $\Delta\psi_0$ gradient generated across the crystal from divergent charge accumulation at structurally distinct surface types. The sign and magnitude of $\Delta\psi_0$, the conductivity of the natural crystal, and the growth rates of the pyramidal islands are all mutually consistent. For example, taking $\Delta\psi_0 = 0.2$ V at pH = 2, a temperature-adjusted electrical resistivity = 10^4 ohm·m for 75°C (*31*, *32*), and an electron transport path length of 1 mm, the maximum amount of additional hematite expected on the (001) surface in 12 hours is a layer ~100 nm thick, the same order of magnitude as that observed. Surface potential–driven charge carrier diffusivity has been invoked qualitatively to explain microscopic oxide transformation processes before (*13*, *33*, *34*) but not on the length scale examined here nor with surface specificity. Given the observation that the (001) surface continues to grow beyond the coalescence of the pyramidal islands, at the atomic scale the pyramidal (001) morphology must retain the essential structural and therefore chemical characteristics that give rise to the potential of the initial (001) surface. Furthermore, the observed process does not preclude traditionally held spatially localized dissolution in the hematite system. Rather, the evidence suggests that the processes operate in parallel and that the behavior based on the electrical circuit through the crystal dominates when chemical requirements that establish a large enough surface electric potential gradient are met.

The finding provides insight into the reductive transformation of iron oxides, which is important in the biogeochemical cycling of iron in nature and the removal of iron oxide films in industry. Because this finding can be easily generalized to a host of naturally abundant semiconducting transition metal oxide and sulfide minerals capable of dominating the interfacial surface area in soils, sediments, and among atmospheric particles, its implications are fairly widespread. Of immediate impact is the concept that the reactivity of any given surface on such materials can be coupled to that of another surface, with a dependence on crystal morphology as a whole. This phenomenon should apply to natural crystals in the environment as well as those selectively cut, broken, or otherwise prepared for laboratory study.

References and Notes

1. R. T. Shuey, *Semiconducting Ore Minerals*, vol. 4 of *Developments in Economic Geology* (Elsevier, Amsterdam, 1975).
2. J. H. Kennedy, K. W. Frese, *J. Electrochem. Soc.* **125**, 723 (1978).
3. C. Gleitzer, J. Nowotny, M. Rekas, *Appl. Phys. A Mat. Sci. Proc.* **53**, 310 (1991).
4. B. A. Balko, K. M. Clarkson, *J. Electrochem. Soc.* **148**, E85 (2001).
5. P. Venema, T. Hiemstra, P. G. Weidler, W. H. van Riemsdijk, *J. Colloid Interface Sci.* **198**, 282 (1998).
6. F. Gaboriaud, J. Ehrhardt, *Geochim. Cosmochim. Acta* **67**, 967 (2003).
7. C. G. B. Garrett, W. H. Brattain, *Phys. Rev.* **99**, 376 (1955).
8. P. Multaney, V. Swayambunathan, F. Grieser, D. Meisel, *J. Phys. Chem.* **92**, 6732 (1988).
9. R. M. Cornell, U. Schwertmann, *The Iron Oxides: Structure, Properties, Reactions, Occurrence and Uses* (VCH, Weinheim, Germany, 2003).
10. T. Makau, *J. Phys. Soc. Jpn.* **15**, 727 (1960).
11. N. Iordanova, M. Dupuis, K. M. Rosso, *J. Chem. Phys.* **122**, 144305 (2005).
12. J. S. LaKind, A. T. Stone, *Geochim. Cosmochim. Acta* **53**, 961 (1989).
13. P. Multaney, R. Cooper, F. Grieser, D. Meisel, *Langmuir* **4**, 1206 (1988).
14. A. G. B. Williams, M. M. Scherer, *Environ. Sci. Tech.* **38**, 4782 (2004).
15. P. Larese-Casanova, M. M. Scherer, *Environ. Sci. Tech.* **41**, 471 (2007).
16. D. Suter, C. Siffert, B. Sulzberger, W. Stumm, *Naturwissenschaften* **75**, 571 (1988).
17. V. Barron, J. Torrent, *J. Colloid Interface Sci.* **177**, 407 (1996).
18. C. M. Eggleston *et al.*, *Geochim. Cosmochim. Acta* **67**, 985 (2003).
19. T. P. Trainor *et al.*, *Surf. Sci.* **573**, 204 (2004).
20. O. W. Duckworth, S. T. Martin, *Geochim. Cosmochim. Acta* **65**, 4289 (2001).
21. T. H. Yoon, S. B. Johnson, C. B. Musgrave, G. E. Brown, *Geochim. Cosmochim. Acta* **68**, 4505 (2004).
22. J. R. Rustad, E. Wasserman, A. R. Felmy, *Surf. Sci.* **424**, 28 (1999).
23. T. Hiemstra, W. H. Van Riemsdijk, *Langmuir* **15**, 8045 (1999).
24. P. Zarzycki, *Appl. Surf. Sci.* **253**, 7604 (2007).
25. Materials and methods are available on *Science* Online.
26. M. J. Avena, O. R. Camara, C. P. Depauli, *Colloid Surf.* **69**, 217 (1993).
27. N. Kallay, T. Preocanin, *J. Colloid Interface Sci.* **318**, 290 (2008).
28. J. A. Davis, R. O. James, J. O. Leckie, *J. Colloid Interface Sci.* **63**, 480 (1978).
29. B. Zinder, G. Furrer, W. Stumm, *Geochim. Cosmochim. Acta* **50**, 1861 (1986).
30. S. Banwart, S. Davies, W. Stumm, *Colloid Surf.* **39**, 303 (1989).
31. S. Kerisit, K. M. Rosso, *Geochim. Cosmochim. Acta* **70**, 1888 (2006).
32. S. Kerisit, K. M. Rosso, *J. Chem. Phys.* **127**, 124706 (2007).
33. N. M. Dimitrijevic, D. Savic, O. I. Micic, A. J. Nozik, *J. Phys. Chem.* **88**, 4278 (1984).
34. J. P. Jolivet, E. Tronc, *J. Colloid Interface Sci.* **125**, 688 (1988).

35. This research was supported by the U.S. Department of Energy (DOE), Office of Basic Energy Sciences, Geosciences Program. It was performed at the William R. Wiley Environmental Molecular Sciences Laboratory (EMSL) at the Pacific Northwest National Laboratory (PNNL). The EMSL is funded by the DOE Office of Biological and Environmental Research. PNNL is operated by Battelle for the DOE under contract DE-AC06-76RLO 1830. We gratefully acknowledge the assistance of C. Wang for TEM; B. Arey for scanning electron microscopy; D. McCready for pole reflection x-ray diffraction; Y. Lin for access to electrochemistry apparatus; and A. Felmy, E. Ilton, and J. Amonette for comments on an early version of this manuscript.

Supporting Online Material

www.sciencemag.org/cgi/content/full/1154833/DC1
Materials and Methods
Figs. S1 to S4
References

4 January 2008; accepted 25 February 2008
Published online 6 March 2008;
10.1126/science.1154833
Include this information when citing this paper.

Aligning Conservation Priorities Across Taxa in Madagascar with High-Resolution Planning Tools

C. Kremen,[1,2]*† A. Cameron,[1,2]† A. Moilanen,[3] S. J. Phillips,[4] C. D. Thomas,[5] H. Beentje,[6] J. Dransfield,[6] B. L. Fisher,[7] F. Glaw,[8] T. C. Good,[9] G. J. Harper,[10] R. J. Hijmans,[11] D. C. Lees,[12] E. Louis Jr.,[13] R. A. Nussbaum,[14] C. J. Raxworthy,[15] A. Razafimpahanana,[2] G. E. Schatz,[16] M. Vences,[17] D. R. Vieites,[18] P. C. Wright,[19] M. L. Zjhra[9]

Globally, priority areas for biodiversity are relatively well known, yet few detailed plans exist to direct conservation action within them, despite urgent need. Madagascar, like other globally recognized biodiversity hot spots, has complex spatial patterns of endemism that differ among taxonomic groups, creating challenges for the selection of within-country priorities. We show, in an analysis of wide taxonomic and geographic breadth and high spatial resolution, that multitaxonomic rather than single-taxon approaches are critical for identifying areas likely to promote the persistence of most species. Our conservation prioritization, facilitated by newly available techniques, identifies optimal expansion sites for the Madagascar government's current goal of tripling the land area under protection. Our findings further suggest that high-resolution multitaxonomic approaches to prioritization may be necessary to ensure protection for biodiversity in other global hot spots.

Approximately 50% of plant and 71 to 82% of vertebrate species are concentrated in biodiversity hot spots covering only 2.3% of Earth's land surface (*1*). These irreplaceable regions are thus among the highest global priorities for terrestrial conservation; reasonable consensus exists on their importance among various global prioritization schemes that identify areas of both high threat and unique biodiversity (*2*). The spatial patterns of species richness, endemism, and rarity of different taxonomic groups within priority areas, however, rarely align and are less well understood (*3*–*6*). Detailed analysis of these patterns is required to allocate conservation resources most effectively (*7*, *8*).

To date, only a few quantitative, high-resolution, systematic assessments of conservation priorities have been developed within these highly threatened and biodiverse regions (*9*, *10*). This deficiency results from multiple obstacles, including limited data or access to data on species distributions and computational constraints on achieving high-resolution analyses over large geographic areas. We have been able to overcome each of these obstacles for Madagascar, a global conservation priority (*1*, *2*, *11*). Like many other regions (*3*–*6*), Madagascar has complex, often nonconcordant patterns of microendemism among taxa (*12*–*17*), rendering the design of efficient protected-area networks particularly difficult (*4*, *6*). We collated data for endemic species in six major taxonomic groups [ants, butterflies, frogs, geckos, lemurs, and plants (table S1)], using recent robust techniques in species distribution modeling (*18*, *19*) and conservation planning (*20*, *21*) to produce the first quantitative conservation prioritization for a biodiversity hot spot with this combination of taxonomic breadth (2315 species), geographic extent (587,040 km^2), and spatial resolution (30-arc sec grid = ~0.86 km^2).

Currently, an important opportunity exists to influence reserve network design in Madagascar, given the government's commitment, announced at the World Parks Congress in 2003, to triple its existing protected-area network to 10% coverage (*22*). Toward this goal, our high-resolution analysis prioritizes areas by their estimated contribution to the persistence of these 2315 species and identifies regions that optimally complement the existing reserve network in Madagascar.

We input expert-validated distribution models for 829 species and point occurrence data for the remaining species [those with too few occurrences to model, called rare target species (RTS)] into a prioritization algorithm, Zonation (*20*, *21*), which generates a nested ranking of conservation priorities (*23*). Species that experienced a large proportional loss of suitable habitat (range reduction) between the years 1950 and 2000 were given higher weightings [equation 2 of (*23*), (*24*)]. We evaluated all solutions [defined here as the highest-ranked 10% of the landscape to match the target that Madagascar has set for conservation (*22*)] in two ways: (i) percent of species entirely

absent from the solution ["complete gaps" (*11*)] and (ii) proportional representation of species.

Avoiding complete gaps for all species considered, or "minimal representation," is a basic goal of conservation prioritization (*8*) and can be accomplished in only 1020 grid squares (0.1% of the area of Madagascar) in a multitaxon analysis. The single-taxon solutions (fig. S1), however, did a poor job of minimally representing other species (Table 1) because of their low overlap (fig. S2). In single-taxon solutions, 25 to 50% of RTS species from other taxa were entirely omitted (Table 1A). Zero to 18% of modeled species were omitted, depending on whether evaluation was based on actual occurrence points (Table 1B) or distribution models (Table 1D). Overall, the use of any single-taxon solution would result in 16 to 39% of all species ending up as complete gaps (Table 1C, based on actual occurrence records).

In addition to ensuring minimal representation, our goal is to maximize proportional representation (the proportion of distribution or occurrence points) of species, especially those most vulnerable to extinction, in order to increase the probability of their persistence (*11*). In single-taxon solutions, we found that species from other taxa would often be represented at lower levels than the target taxon. Mean proportional representation for modeled species outside of the taxon was lower by a factor of 1.2 to 1.5 relative to the target taxon for all groups except plants (Fig. 1A), which include the most species and the smallest-ranged species within this data set, making it comparatively difficult to protect large proportions of each species even in the plant-specific solution. Similarly, single-taxon solutions contained only 69 to 83%, on average, of the occurrence points for included (species that are represented by at least one record) RTS outside the target taxon, as compared to 100% of RTS records for species within the target taxon (Table 1E). Thus, any conservation prioritization based on a single surrogate taxon would be of limited utility for identifying conservation priorities across taxa in Madagascar.

The ideal solution to the surrogacy problem is to include all species in a single analysis (Fig. 2A), thus avoiding complete gaps (Table 1, last column) while optimizing proportional representation across all taxa. Until now, because of computational constraints, such analyses have not been feasible for this spatial resolution, geographic extent, and number of taxa. Figure S3A shows what can be achieved with the core-area Zonation method when used with weightings that account for historical range reductions. Without this weighting scheme, two species with the same current range size could be included at identical proportional representation, even though one had experienced a precipitous decline in range whereas the other had not. This approach thus prioritizes two classes of vulnerability. Narrow-ranged species, which are vulnerable to habitat loss coincident with their small ranges, are inherently prioritized by the Zonation algorithm [equation S1 of (*23*)]. Species that have suffered extensive recent range reductions (red dots in fig. S3) are additionally prioritized by their weightings, and the proportion of their historical (baseline) range included is thus increased.

Covering all six taxonomic groups simultaneously necessarily invokes tradeoffs, decreasing, for example, the proportions of species distributions represented in each taxon significantly relative to its own single-taxon solution (Fig. 1B, –0.04 ± 0.002 SE, paired Wilcoxon signed-ranks test, $P < 0.0001$). To assess this tradeoff, we calculated a potential extinction risk for modeled species based on future distributional loss under the single- and multitaxon solutions, assuming loss of all habitat outside of prioritized areas and an aggregate species-area response (*24*). The increase in potential extinction risk for each taxonomic group incurred under the multitaxon solution relative to its own (fig. S4) constitutes the cost of including hundreds of species in the protected-area network that would otherwise be omitted (Table 1C).

We compared our multitaxon solution (Fig. 2A) against the actual parks selected during the recent protected-area expansion phase of 2002–2006 that has increased the total reserve coverage from 2.9 to 6.3% of Madagascar (Fig. 2B). The mean proportion of modeled species distributions included in the multitaxon solution (using the top 6.3% prioritized to compare with the area protected by 2006) was not significantly higher than in the actual selections (+0.004 ± 0.002 SE, paired test, NS), as is expected because of tradeoffs among species (that is, given the fixed area of 6.3%, some species increased in representation when the optimized solution was compared to the actual solution, whereas others necessarily decreased, resulting in no mean change). The multitaxon solution, however, included all species, whereas the actual selections entirely omitted 28% of species (based on actual occurrence points, fig. S5). In addition, proportions included for the species with narrowest ranges or largest scores for the proportional range-reduction index were significantly larger in the multitaxon solution (at 6.3% of area) as compared to the actual selection [Kolmogorov-Smirnov two-sample test, first (smallest) quartile of range size, $D = 0.28$, $n = 207$ species, $P < 0.001$; fourth (largest) quartile of proportional range-reduction index, $D = 0.149$, $n = 207$ species, $P = 0.001$].

Finally, because we are operating in a real-world conservation context and many protected areas have already been established in Madagascar, we developed a realistic Zonation solution,

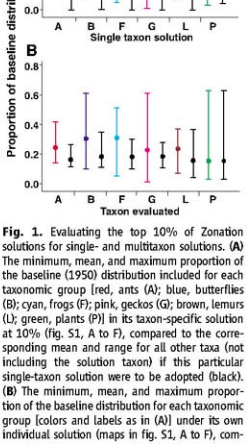

Fig. 1. Evaluating the top 10% of Zonation solutions for single- and multitaxon solutions. **(A)** The minimum, mean, and maximum proportion of the baseline (1950) distribution included for each taxonomic group [red, ants (A); blue, butterflies (B); cyan, frogs (F); pink, geckos (G); brown, lemurs (L); green, plants (P)] in its taxon-specific solution at 10% (fig. S1, A to F), compared to the corresponding mean and range for all other taxa (not including the solution taxon) if this particular single-taxon solution were to be adopted (black). **(B)** The minimum, mean, and maximum proportion of the baseline distribution for each taxonomic group [colors and labels as in (A)] under its own individual solution (maps in fig. S1, A to F), compared to the values obtained for its taxonomic group only under the multitaxon solution (black, map in Fig. 2A).

[1]Department of Environmental Sciences, Policy and Management, 137 Mulford Hall, University of California, Berkeley, CA 94720-3114, USA. [2]Réseau de la Biodiversité de Madagascar, Wildlife Conservation Society, Villa Ifanomezantsoa, Soavimbahoaka, Boîte Postale 8500, Antananarivo 101, Madagascar. [3]Metapopulation Research Group, Department of Biological and Environmental Sciences, Post Office Box 65, Viikinkaari 1, FI-00014, University of Helsinki, Finland. [4]AT&T Labs-Research, 180 Park Avenue, Florham Park, NJ 07932, USA. [5]Department of Biology (Area 18), University of York, Post Office Box 373, York YO10 5YW, UK. [6]Royal Botanic Gardens, Kew, Richmond TW9 3AB, Surrey, UK. [7]Department of Entomology, California Academy of Sciences, San Francisco, CA 94103, USA. [8]Zoologische Staatssammlung München, Münchhausenstrasse 21, 81247 München, Germany. [9]Department of Biology, Georgia Southern University, Statesboro, GA 30460, USA. [10]Conservation International, Center for Applied Biodiversity Science, 2011 Crystal Drive, Suite 500, Arlington, VA 22202, USA. [11]International Rice Research Institute, Los Baños, Philippines. [12]Department of Entomology, Natural History Museum, London SW7 5BD, UK. [13]Center for Conservation and Research, Henry Doorly Zoo, Omaha, NE 68107, USA. [14]Museum of Zoology, University of Michigan, Ann Arbor, MI 48109-1079, USA. [15]American Museum of Natural History, Central Park West at 79th Street, New York, NY 10024-5192, USA. [16]Missouri Botanical Garden, Post Office Box 299, St. Louis, MO 63166-0299, USA. [17]Zoological Institute, Technical University of Braunschweig, 38106 Braunschweig, Germany. [18]Museum of Vertebrate Zoology and Department of Integrative Biology, University of California, 3101 Valley Life Sciences Building, Berkeley, CA 94720-3160, USA. [19]Department of Anthropology, State University of New York, Stony Brook, NY 11794, USA.

*To whom correspondence should be addressed. E-mail: ckremen@nature.berkeley.edu

†These authors contributed equally to this work.

optimized to expand on existing protected areas (6.3%) by adding an additional 3.7% of area (Fig. 2B, constrained solution). Like the unconstrained solution (Fig. 2A and Table 1), this solution (Fig. 2B) omits no species. The proposed expansion achieves relatively large increases in mean proportional representation (+0.05 ± 0.001 SE of modeled species' distributions and +58.8 ± 1.1% SE of RTS' occurrences). Most important, it realizes gains among the most vulnerable species, because of both the algorithm (*20*, *21*) and the weighting system used. Among modeled species, those that have already lost much of their range (Fig. 3, A to C; red indicates the highest quartile of proportional range-reduction index) or are currently narrow-ranged (Fig. 3, D to F; red indicates the smallest quartile of range) increase most in proportional representation when moving from current parks (Fig. 3, B and E) to the constrained optimized solution (Fig. 3, C and F). For RTS species, expansion from current parks to the optimized solution would increase mean proportional representation to 99.9 ± 0.1% SE of occurrences from 0% for gap species (39% of all RTS, fig. S5) or 67.8 ± 1.9% SE for included species (fig. S6). Thus, although the protected areas selected to date have captured a relatively high proportion of Madagascar's species (~70% of species considered here, fig. S5), careful selection of the remaining 3.7% of area (as in the plan proposed in Fig. 2B) can produce further substantial conservation gains, both by including many more species and by increasing the proportional representation of the most vulnerable ones.

Our analysis provides fresh insights into conservation needs for Madagascar, identifying, for example, several regions within the central plateau massifs and littoral forests as priorities (Fig. 2): areas with relatively low forest cover but considerable endemism that have been historically neglected in favor of protecting large forest blocks. Although our national-scale analysis identifies important biodiversity priorities at high resolution, precise delineation of protected areas requires taking socioeconomic factors into account (*25*). Within these priority areas, those that are most vulnerable to habitat destruction or are most highly ranked (fig. S7) should receive immediate attention (*26*). Although conservation areas must be identified by the end of 2008, final refinement and legal designation will not be completed until 2012. Thus, time is available for implementation of an iterative process (*8*): rerunning this analysis to select optimal replacement sites each time areas within the solution are definitively rejected or destroyed, or alternate areas are definitively selected. Such updates could

Table 1. Surrogacy of higher taxa, comparing single- and multitaxon solutions. Section A, percentage of complete gap species for RTS species (n = 1486). B, percentage of complete gap species for modeled species (n = 829). C, percentage of complete gap species for all species (modeled and RTS, n = 2315). Sections A, B, and C are based on occurrence data, and complete gaps are species with no points included in the solution. The diagonals and the multitaxon columns have no unrepresented species, demonstrating as expected that Zonation includes all species considered within its solution. For D, the gap analysis was performed with models rather than occurrence points. E, mean percent of occurrence points included for nongap RTS species (species represented by at least one point in the solution). n.a., not applicable because all species are included in the solution by definition.

		Taxon targeted by zonation solution						
	Taxon assessed	Ants	Butterflies	Frogs	Geckos	Lemurs	Plants	All taxa
A. Percent of unmodeled (RTS) species unrepresented, based on point occurrence records	Ants	0	21.3	28.9	33.6	32.4	26.9	0
	Butterflies	14.5	0	22.1	25.2	38.9	24.4	0
	Frogs	34.1	25.7	0	30.7	25.7	21.2	0
	Geckos	26.9	23.1	23.1	0	26.9	19.2	0
	Lemurs	42.9	50.0	50.0	71.4	0	35.7	0
	Plants	45.2	52.3	42.8	62.2	54.8	0	0
	All species except target taxon	40.0	42.4	37.7	50.2	45.5	24.5	n.a.
B. Percent of modeled species unrepresented, based on point occurrence records	Ants	0	0	5.5	2.7	0	0	0
	Butterflies	0	0	4.7	0.6	0	0.6	0
	Frogs	5.0	5.0	0	5.0	0	0	0
	Geckos	0	0	0	0	0	0	0
	Lemurs	3.2	6.5	3.2	9.7	0	0	0
	Plants	13.3	14.1	23.4	26.2	16.4	0	0
	All species except target taxon	9.3	11.4	16.4	17.5	10.5	0.3	n.a.
C. Percent of modeled and RTS unrepresented, based on point occurrence records	All species except target taxon	28.3	32.3	29.6	38.5	33.2	16.2	0
D. Percent of modeled species with no part of their model protected by the Zonation solution	Ants	0	0	0	0	0	0	0
	Butterflies	0	0	1.2	0	0	0	0
	Frogs	0	0	0	0	0	0	0
	Geckos	0	0	0	0	0	0	0
	Lemurs	0	0	3.2	0	0	0	0
	Plants	1.6	0.4	8.0	2.0	1.6	0	0
	All species except target taxon	1.1	0.3	5.4	1.2	1.0	0.0	n.a.
E. Mean percent point occurrence records included for (nongap) RTS species only	Ants	100.0	84.9	87.6	80.5	75.7	77.1	100.0
	Butterflies	77.4	100.0	84.3	81.0	68.9	70.1	100.0
	Frogs	71.8	75.7	100.0	75.4	76.2	75.5	100.0
	Geckos	75.7	73.7	74.8	100.0	64.3	69.9	100.0
	Lemurs	68.1	49.9	45.6	39.0	100.0	56.3	100.0
	Plants	65.7	66.5	71.6	65.9	61.1	99.9	99.86
	All species except target taxon	68.7	72.8	76.6	72.7	67.5	74.4	n.a.

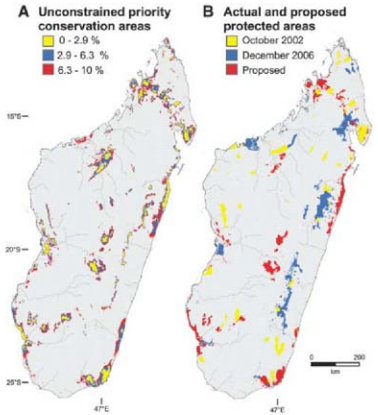

Fig. 2. Conservation priority zones in Madagascar. **(A)** Unconstrained multitaxon solution, showing what would have been selected based on these 2315 species if no areas were already protected. Colors indicate priority level: The top-ranked 2.9% priority areas are shaded yellow (equivalent to the area actually protected by 2002), the next-ranked priorities to 6.3% are blue (equivalent to the area actually protected by 2006), and the next-ranked priorities to 10% (equivalent to the conservation target) are red. **(B)** Constrained multitaxon solution, expanding (red) from existing parks in 2006 (yellow + blue = 6.3% of area) to 10% protection. The red areas are thus those that our analysis selects as the most important areas to consider for expansion of the current reserve network.

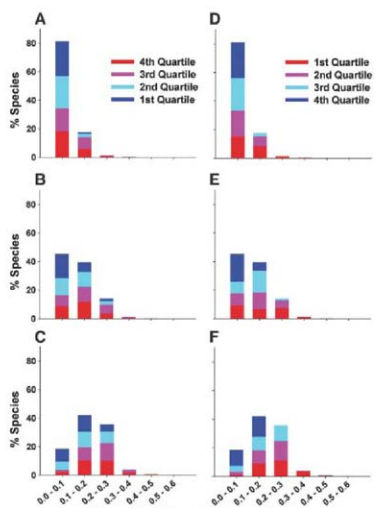

Fig. 3. Proportions of baseline (1950) species ranges (modeled) included at different phases of park expansion, as frequency histograms. **(A** to **C)** Within each histogram, species are coded by their proportional range-reduction index (weights used in Zonation), binned by quartiles, with the fourth quartile (red) representing the largest reductions. **(D** to **F)** Within each histogram, species are coded by their current range size, binned by quartiles, with the first quartile (red) representing the smallest-ranged species. [(A) and (D)] Protected areas designated by the year 2002, equaling 2.3% of the landscape (shaded yellow in Fig. 2B). [(B) and (E)] Protected areas designated by the year 2006, 6.3% of the landscape (shaded yellow and blue in Fig. 2B). [(C) and (F)] Constrained optimized expansion to 10% of the landscape (shaded yellow, blue, and red in Fig. 2B).

incorporate other taxonomic groups, new species records, and changing species designations (*27*). Our results suggest that conducting comparable analyses for other globally biodiverse areas is not only feasible but necessary, because of the inadequacy of single-taxon analyses to identify cross-taxon priorities and the need to develop high-resolution priorities within hot spots. As conservation targets are approached, optimization techniques become particularly critical to guide the final, toughest choices, so as to increase both the future representation of species in reserves and the probability that populations of these species will persist.

References and Notes

1. R. A. Mittermeier *et al.*, *Hotspots Revisited: Earth's Biologically Richest and Most Endangered Terrestrial Ecoregions* (Conservation International, Univ. of Chicago Press, Chicago, 2005).
2. T. M. Brooks *et al.*, *Science* **313**, 58 (2006).
3. R. Grenyer *et al.*, *Nature* **444**, 93 (2006).
4. A. S. van Jaarsveld *et al.*, *Science* **279**, 2106 (1998).
5. C. Moritz *et al.*, *Proc. R. Soc. London Ser. B* **268**, 1875 (2001).
6. J. R. Prendergast, R. M. Quinn, J. H. Lawton, B. C. Eversham, *Nature* **365**, 335 (1993).
7. R. M. Cowling, R. L. Pressey, A. T. Lombard, P. G. Desmet, A. G. Ellis, *Divers. Distrib.* **5**, 51 (1999).
8. C. R. Margules, R. L. Pressey, *Nature* **405**, 243 (2000).
9. R. M. Cowling, R. L. Pressey, M. Rouget, A. T. Lombard, *Biol. Conserv.* **112**, 191 (2003).
10. A. T. Knight *et al.*, *Conserv. Biol.* **20**, 739 (2006).
11. A. S. L. Rodrigues *et al.*, *Bioscience* **54**, 1092 (2004).
12. M. J. Raherilalao, S. M. Goodman, *Rev. Ecol. Terre Vie* **60**, 355 (2005).
13. C. J. Raxworthy, R. A. Nussbaum, in *Biogeography of Madagascar*, W. R. Lourenco, Ed. (Orstom, Paris, 1996), pp. 369–383.
14. C. Kremen, D. C. Lees, J. Fay, in *Butterflies: Ecology and Evolution Taking Flight* (Univ. of Chicago Press, Chicago, 2003), pp. 517–540.
15. G. E. Schatz, C. Birkinshaw, P. P. Lowry II, F. Randriantafika, F. Ratovoson, in *Diversité et Endémisme à Madagascar*, W. C. Lourenco, S. M. Goodman, Eds. (Mémoires de la Société de Biogéographie, Paris, 2000), pp. 11–24.
16. G. E. Schatz, *Mem. Soc. Biogeogr. (Paris)* **2000**, 1 (2000).
17. S. Goodman, J. Benstead, *Oryx* **39**, 73 (2005).
18. J. Elith *et al.*, *Ecography* **29**, 129 (2006).
19. S. J. Phillips, R. P. Anderson, R. E. Schapire, *Ecol. Model.* **190**, 231 (2006).
20. A. Moilanen *et al.*, *Proc. R. Soc. London Ser. B* **272**, 1885 (2005).
21. A. Moilanen, *Biol. Conserv.* **134**, 571 (2007).
22. Gouvernement Malgache, *J. Off. Repub. Madagascar* **2004**, 2936 (2004).
23. Supporting material is available on *Science* Online.
24. C. D. Thomas *et al.*, *Nature* **427**, 145 (2004).
25. C. Kremen *et al.*, *Conserv. Biol.* **13**, 1055 (1999).
26. W. R. Turner, D. S. Wilcove, *Conserv. Biol.* **20**, 527 (2006).
27. J. Köhler *et al.*, *Bioscience* **55**, 693 (2005).

28. We thank C. Golden, C. Moritz, and W. Turner for valuable feedback on an earlier version. We are grateful to members of the Système d'Aires Protégées de Madagascar (SAPM) for facilitating the comparative work and for support from the MacArthur Foundation (grant no. 06-86793 to C.K.). The study was devised by C.K. and A.C. A.C. and C.K. conducted the analyses. A.M., S.J.P., and C.D.T. provided expert input on analytical methods and interpretation. R.J.H. and G.J.H. prepared environmental layers. A.C., H.B., J.D., B.L.F., F.G., T.C.G., C.K., D.C.L., E.L., R.A.N., C.J.R., G.E.S., M.V., D.R.V., P.C.W., and M.L.Z. contributed biodiversity data and

evaluated species distribution models and Zonation solutions for their taxa. A.R. conducted the geographic information system (GIS) analyses to produce the SAPM priority map (Fig. 2B, black outlines). C.K. and A.C. wrote the initial draft of the manuscript; all authors commented on subsequent drafts.

Supporting Online Material
www.sciencemag.org/cgi/content/full/320/5873/222/DC1
Methods
SOM Text
Figs. S1 to S11
Table S1

References
Extended Acknowledgments
Appendix S1
GIS data of Fig. 2

14 January 2008; accepted 7 March 2008
10.1126/science.1155193

An Agonist of Toll-Like Receptor 5 Has Radioprotective Activity in Mouse and Primate Models

Lyudmila G. Burdelya,[1]* Vadim I. Krivokrysenko,[2]* Thomas C. Tallant,[3] Evguenia Strom,[2] Anatoly S. Gleiberman,[2] Damodar Gupta,[1] Oleg V. Kurnasov,[4] Farrel L. Fort,[2] Andrei L. Osterman,[4] Joseph A. DiDonato,[3] Elena Feinstein,[2]† Andrei V. Gudkov[1,2]†

The toxicity of ionizing radiation is associated with massive apoptosis in radiosensitive organs. Here, we investigate whether a drug that activates a signaling mechanism used by tumor cells to suppress apoptosis can protect healthy cells from the harmful effects of radiation. We studied CBLB502, a polypeptide drug derived from *Salmonella* flagellin that binds to Toll-like receptor 5 (TLR5) and activates nuclear factor–κB signaling. A single injection of CBLB502 before lethal total-body irradiation protected mice from both gastrointestinal and hematopoietic acute radiation syndromes and resulted in improved survival. CBLB502 injected after irradiation also enhanced survival, but at lower radiation doses. It is noteworthy that the drug did not decrease tumor radiosensitivity in mouse models. CBLB502 also showed radioprotective activity in lethally irradiated rhesus monkeys. Thus, TLR5 agonists could potentially improve the therapeutic index of cancer radiotherapy and serve as biological protectants in radiation emergencies.

The toxicity of high-dose ionizing radiation (IR) is associated with induction of acute radiation syndromes (*1*) involving the hematopoietic system (HP) and gastrointestinal tract (GI). The extreme sensitivity of HP and GI cells to genotoxic stress largely determines the adverse side effects of anticancer radiation therapy and chemotherapy (*2*). Development of radioprotectants for medical and biodefense applications has primarily focused on antioxidants that protect tissues (*3*) and cytokines that stimulate tissue regeneration (*4*).

Here, we have explored whether radioprotection can be achieved through suppression of apoptosis, the major mechanism underlying massive cell loss in radiosensitive tissues (*5*–*7*). Specifically, we have attempted to pharmacologically mimic an antiapoptotic mechanism frequently acquired by tumor cells, i.e., constitutive activation of the nuclear factor–κB (NF-κB) pathway (*8*). NF-κB is a transcription factor that plays a key role in cellular and organismal response to infectious agents as a mediator of innate and adaptive immune reactions. The link between NF-κB and the mammalian response to IR has been established by previous work showing that GI radiosensitivity is enhanced in mice with a genetic defect in NF-κB signaling (*9*). Activation of NF-κB induces multiple factors that contribute to cell protection and promote tissue regeneration, including apoptosis inhibitors, reactive oxygen species scavengers, and cytokines. Finally, NF-κB activation is among the mechanisms by which tumors inhibit function of the p53 tumor suppressor pathway (*10*), one of the major determinants of radiosensitivity (*11*).

In order to activate NF-κB in GI cells without inducing acute inflammatory responses, we studied factors produced by benign microorganisms in the human gut that activate NF-κB by binding to Toll-like receptors (TLRs) expressed by host cells (*12*). Stimulation of TLR signaling by commensal microflora plays a protective role in the GI tract (*13*). In particular, we focused on TLR5, which is expressed on enterocytes, dendritic cells (*14*), and endothelial cells of the small intestine lamina propria (*15*). Endothelial cell apoptosis has been identified as an important contributor to the pathogenesis of GI acute radiation syndrome (*16*). The only known ligand and agonist of TLR5 is the bacterial protein flagellin (*17*).

To investigate whether flagellin has in vivo radioprotective activity, we injected flagellin purified from *Salmonella enterica* serovar Dublin (*18*) into NIH-Swiss mice 30 min before total-body γ irradiation (TBI). Treatment with 0.2 mg/kg of body weight of flagellin protected mice from lethal doses of 10 and 13 Gy that induce mortality from HP and GI acute radiation syndromes, respectively (Fig. 1A). Flagellin did not rescue mice from 17 Gy TBI but prolonged their median survival from 7 to 12 days. The dose-modifying factor (DMF, the fold change in irradiation dose lethal for 50% of animals) of CBLB502 in NIH-Swiss mice was 1.6, exceeding that of other radioprotective compounds, such as cytokines or amifostine, used at nontoxic doses (*3*).

To reduce the immunogenicity and toxicity of flagellin, we took advantage of studies that mapped the TLR5-activating domains of flagellin to its evolutionarily conserved N and C termini (Fig. 1B) (*19*). We tested a series of engineered flagellin derivatives for NF-κB activation in vitro (Fig. 1B and fig. S1). The most potent NF-κB activator, designated CBLB502, included the complete N- and C-terminal domains of flagellin separated by a flexible linker (fig. S1). CBLB502 produced in *Escherichia coli* as a recombinant protein retains entirely the NF-κB–inducing activity and exceptional stability of flagellin (*18*), yet is substantially less immunogenic (fig. S2). It is also less toxic than flagellin, with a maximum tolerated dose (MTD) in mice of 25 mg/kg as compared with the 12 mg/kg MTD of flagellin (*20*). Flagellin derivatives that failed to activate NF-κB in vitro did not provide radioprotection in vivo (one example is shown in Fig. 1C), which suggested that activation of TLR5 signaling is necessary for radioprotection.

To test whether CBLB502 retained the radioprotective efficacy of flagellin, we administered a single injection of the compound (0.2 mg/kg) to NIH-Swiss mice 30 min before 13 Gy TBI. The treatment (*18*) rescued more than 87% of mice from radiation-induced death (Fig. 1C). At this radiation dose, the most powerful previously described radioprotectants provided about 54% protection [amifostine (*21*)] or had no protective effect at all [5-androstenediol (5-AED) or Neumune (*22*)] (Fig. 1C). Notably, the moderate protective effect observed with amifostine against 13 Gy TBI required injection of a dose (150 mg/kg) close to its MTD (200 mg/kg in NIH-Swiss mice). CBLB502 showed a significantly stronger protective effect ($P < 0.05$) when it was injected at less than 1% of its MTD.

To address the practicality of CBLB502 as an antiradiation drug, we investigated the time frame for effective administration of the compound at different radiation doses. CBLB502 protected mice against the very high doses of radiation that induce lethal HP or combined HP and GI syndromes (10 Gy and 13 Gy, respectively) only when injected 15 to 60 min before TBI (Fig. 1D). The compound provided no survival benefit if injected before this time interval or after irradiation.

[1]Department of Cell Stress Biology, Roswell Park Cancer Institute, Buffalo, NY 14263, USA. [2]Cleveland BioLabs, Inc. (CBLI), Buffalo, NY 14203, USA. [3]Department of Cell Biology, Lerner Research Institute, Cleveland Clinic, Cleveland, OH 44195, USA. [4]Burnham Institute for Medical Research, La Jolla, CA 92037, USA.

*These authors contributed equally to this work.
†To whom correspondence should be addressed. E-mail: andrei.gudkov@roswellpark.org; efeinstein@cbiolabs.com

However, at a radiation dose of 9 Gy, which killed >90% of control [phosphate-buffered saline (PBS)–injected] mice, CBLB502 provided radioprotective benefits when administered as early as 24 hours before, or up to 1 hour after, irradiation. With injection of CBLB502 1 hour postirradiation, 40% of the CBLB502-treated mice survived as compared with 7% of the control mice (Fig. 1D). Thus, CBLB502 is effective as both protects against and mitigates radiation-induced injury.

We next evaluated the effect of CBLB502 on radiation damage to the GI tract and HP system at the tissue and cellular levels. Treatment of NIH-Swiss mice with 0.2 mg/kg CBLB502 30 min before 15 Gy TBI dramatically reduced the proportion of apoptotic cells in the lamina propria of the small intestine of irradiated mice, including vascular endothelial cells (Fig. 2A and fig. S3A) (*18*). This observation is consistent with the postulated role of endothelial apoptosis in the GI toxicity of radiation (*16*). In addition, we found that the radiation-induced reduction in small intestine crypt size and cell density that was observed in control NIH-Swiss mice was ameliorated by CBLB502 pretreatment (0.2 mg/kg given 1 hour before 15 Gy TBI) (Fig. 2B and fig. S3B). CBLB502 treatment did not preserve the morphology of the small intestine in irradiated MOLF/Ei mice (Fig. 2B), a strain with defective TLR5 response because of a germline mutation (*23*), which suggests that radioprotection by CBLB502 is indeed TLR5-dependent. CBLB502-mediated protection of the GI tract was also illustrated by preservation of crypt stem cells in the small intestine. 5-Bromo-2′-deoxyuridine (BrdU) was used to label proliferating crypt cells in irradiated (13 Gy) NIH-Swiss mice pretreated with PBS or CBLB502 (*18*). PBS-injected mice showed a near-complete loss of crypt stem cells, whereas CBLB502-treated mice

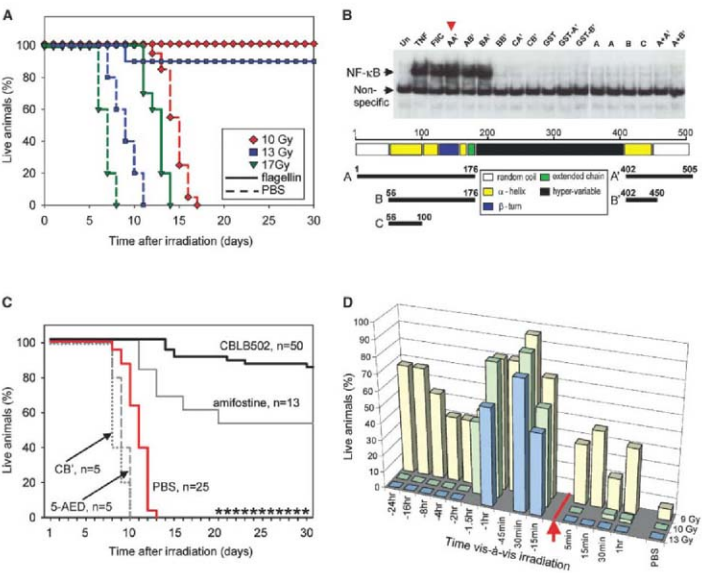

Fig. 1. Flagellin-mediated radioprotection of mice (*18*). (**A**) Groups of 20 NIH-Swiss mice were injected with flagellin or PBS 30 min before TBI. Representative results from one of three independent experiments are shown. The difference in survival between control and experimental groups was statistically significant ($P < 0.05$ by two-tailed Fisher's test) on days 15 to 30, 9 to 30, and 8 to 13 after 10, 13 and 17 Gy TBI, respectively. (**B**) Generation of an optimized flagellin derivative. (Bottom) Schematic of the domain composition of flagellin. Flagellin derivatives were composed from sequences in the conserved N- and C-terminal domains required for TLR5 activation (A, B, and C and A′ and B′, respectively). Amino acid numbering is from flagellin of *Salmonella enterica* serovar Dublin (GenBank accession no. AAA27081). (Top) Assessment of NF-κB activation by flagellin (FliC) derivatives using electrophoretic mobility shift assay. Flagellin itself and variants AA′, AB′, and BA′ induced NF-κB, whereas other combinations of N and C termini (BB′, CA′, and CB′); isolated N termini (A, B, and C); glutathione-*S*-transferase (GST)-fusions of C termini (GST-A′, GST-B′); and mixtures of isolated N and C termini (A+A′, A+B′) were not active. Positive control: TNFα; negative controls: untreated cells (Un) and cells incubated with GST alone (GST). Flagellin variant AA′ (red arrow) was renamed CBLB502. (**C**) NIH-Swiss mice were treated with CBLB502 (0.2 mg/kg), flagellin derivative CB′ (0.2 mg/kg), amifostine (150 mg/kg), 5-AED (30 mg/kg), or PBS before receiving 13 Gy TBI. *$P < 0.03$ by two-tailed Fisher's test for comparison of survival in CBLB502- and amifostine-treated groups. (**D**) ICR mice (15 per group) were injected with CBLB502 at the indicated times relative to 9, 10, or 13 Gy TBI (red arrow). Control mice received PBS 30 min before TBI. The percentage of mice surviving at day 30 post-irradiation is plotted.

retained normal levels of proliferative cells (Fig. 2C and fig. S4).

The antiapoptotic effect of CBLB502 was also evident in the HP system. CBLB502 injection 1 hour before lethal TBI (10 or 13 Gy) of NIH-Swiss mice did not alleviate radiation-induced decreases in bone marrow and peripheral blood cellularity (table S1); however, it did protect HP stem cells and early progenitors as judged by preservation of granulocyte/macrophage colony-forming cells (Fig. 2D) and flow cytometric analysis of stem cell populations in the bone marrow (table S1) (*18*).

To explore potential molecular mechanism(s) that might underlie CBLB502-mediated radioprotection, we assessed the drug's effect on the levels of several known NF-κB–responsive factors. Superoxide dismutase 2 (SOD2) is an NF-κB–induced antioxidant known to have radioprotective properties (*24*). We found that pretreatment of NIH-Swiss mice with CBLB502 (0.2 mg/kg given 30 min before 15 Gy TBI) resulted in enhanced expression of SOD2 in the lamina propria of the small intestine of irradiated mice (Fig. 2E). We also investigated the possible involvement of prostaglandins and cytokines that are regulated by NF-κB and known to act as radioprotectants (*4*, *25*). Inhibition of cyclooxygenase-2 (COX2), a key enzyme in prostaglandin biosynthesis, by a small-molecule inhibitor (NS-398) did not affect CBLB502-mediated radioprotection (fig. S5). However, CBLB502 injection (in the absence of irradiation) led to induction of multiple cytokines in mouse plasma (Fig. 2F), including radioprotective cytokines such as granulocyte colony–stimulating factor (G-CSF) (*26*), interleukin 6 (IL-6) (*27*) and tumor necrosis factor–α (TNFα) (*28*). Consistent with its low toxicity, CBLB502 activated only sub-inflammatory levels of TNFα. These results suggest that CBLB502-mediated radioprotection is likely to involve multiple mechanisms.

CBLB502 was also effective as a radioprotectant in a pilot study of nonhuman primates (*18*). Nineteen rhesus monkeys (*Macaca mulatta*) were subjected to 6.5 Gy (a dose lethal for 70% of

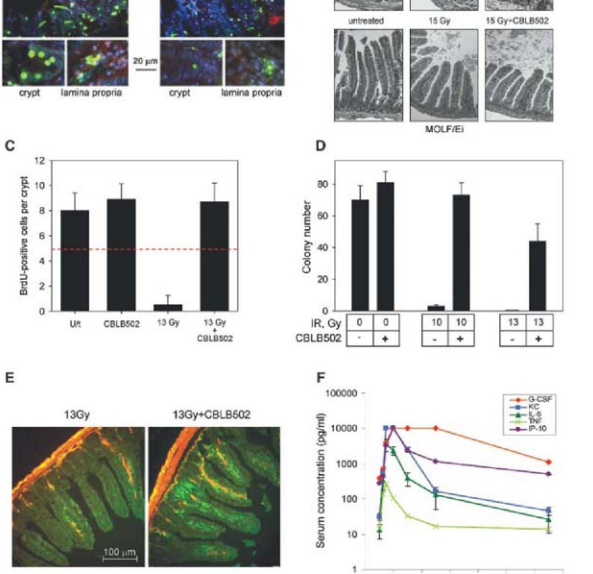

Fig. 2. CBLB502-mediated protection of radiosensitive tissues (*18*). **(A)** Representative terminal deoxynucleotidyl transferase–mediated deoxyuridine triphosphate nick end labeling (TUNEL) staining of apoptotic cells (5 hours postirradiation) in the small intestine of NIH-Swiss mice injected with CBLB502 or PBS 30 min before 15 Gy TBI. Apoptotic endothelial cells displayed yellow fluorescence resulting from overlap of green TUNEL staining and red CD31-specific antibody (endothelial marker) staining. Nuclei were stained with 4′,6′-diamidino-2-phenylindole (DAPI, blue). **(B)** Morphology of the small intestine in NIH-Swiss and MOLF/Ei mice either untreated or 5 days after 15 Gy TBI with or without prior injection of CBLB502. Representative hematoxylin and eosin (H&E) stained sections are shown. **(C)** Immunohistochemical detection of in vivo BrdU incorporation in the crypts of the small intestine. Mice (three per group) were left untreated (Ut), given CBLB502 without TBI (CBLB502), or exposed to 13 Gy TBI 30 min after injection of PBS (13 Gy) or CBLB502 (13Gy + CBLB502). BrdU-positive cells were counted in 12 complete, well-oriented cross sections for each animal. Dashed line: number of BrdU-positive cells considered critical for crypt survival (*36*). $P < 0.05$ for the differences between "13 Gy" and other groups. **(D)** Granulocyte-macrophage colony-forming units were quantified in bone marrow cells obtained from NIH-Swiss mice ($n = 3$) 3 hours after 0, 10, or 13 Gy TBI (with or without CBLB502 injection 30 min before TBI). $P < 0.05$ for the differences between irradiated CBLB502- and vehicle-treated groups. **(E)** Immunohistochemical detection of SOD2 expression (green staining) in sections of small intestine collected 5 hours post-irradiation from NIH-Swiss mice injected with either PBS (13 Gy) or CBLB502 (13Gy + CBLB502) 30 min before 13 Gy TBI. Red staining, smooth muscle actin. **(F)** Cytokine induction by CBLB502 treatment in the absence of irradiation. Plasma was prepared at the indicated times (0.5 to 24 hours) after intramuscular injection of CBLB502 into ICR mice ($n = 3$). KC, keratinocyte-derived chemokine; IP-10, interferon-inducible protein 10.

monkeys, LD_{70}) TBI. Monkeys received a single intramuscular injection of CBLB502 (0.04 mg/kg, $n = 11$) or PBS ($n = 8$) 45 min before TBI. This dose provided a blood concentration of CBLB502 equivalent to 0.2 mg/kg in mice and did not cause any overt signs of toxicity. Injection of CBLB502 before TBI delayed the onset of radiation-induced mortality by 10 days and increased the 40-day survival rate from 25 to 64% (Fig. 3A). Notably, no supportive therapy was provided in this study. Gross and histopathological evaluation of CBLB502-treated monkeys surviving 40 days postirradiation ($n = 7$) revealed only minor damage to major HP and lymphoid organs (bone marrow, spleen, and thymus) (fig. S6). In contrast, the two surviving PBS-treated monkeys displayed moderate-to-high levels of damage in these tissues. Radiation-induced thrombocytopenia, a key predictor of primate death after lethal irradiation (*29*), was less protracted and less severe in CBLB502-treated monkeys than in controls (Fig. 3B).

To assess the potential of CBLB502 as an adjuvant for anticancer radiotherapy, we used two models of experimental radiotherapy in which tumor-bearing mice were subjected to three daily treatments of 4 Gy TBI (a cumulative TBI dose of 12 Gy) (*18*). To evaluate whether CBLB502 affected the radiosensitivity of the tumors, groups of the mice were injected with either PBS or CBLB502 (0.2 mg/kg) 1 hour before each radiation treatment. The two models used were TLR5-positive mouse sarcoma of NIH-Swiss fibroblast origin implanted in NIH-Swiss mice and growing subcutaneously (Fig. 4A) and TLR5-negative B16 melanoma of C57BL/6 origin implanted in C57BL/6 mice (fig. S7). In both models, the antitumor effect of irradiation was accompanied by death of all PBS-treated animals from radiation toxicity by day 18. In contrast, CBLB502 treatment completely prevented radiation-induced mortality [NIH-Swiss mice (Fig. 4A)] or significantly protected against radiation-induced mortality [C57BL6 mice (fig. S7)], but had no radioprotective effect on the tumors. These data illustrate the potential for use of CBLB502 to protect healthy tissues from the adverse side effects of radiotherapy, which are frequently dose-limiting, while not interfering with killing the tumor. These experiments also showed that CBLB502 can protect mice from lethal cumulative damage of fractioned irradiation (three doses of 4 Gy). This is important because radiotherapy of cancer patients is commonly applied as fractioned irradiation. Furthermore, there was no evidence of desensitization with multiple injections of CBLB502. The radioprotective efficacy of CBLB502 injected into ICR mice 30 min before 11 Gy TBI was not affected by previous exposure to the drug with as many as five sequential daily injections (fig. S8). In both mouse tumor models, a slight reduction in tumor growth was observed in CBLB502-treated animals (nonirradiated and irradiated) as compared with corresponding controls. Although these results did not reach statistical significance, they might reflect the known immunostimulatory activity of flagellin (*30*) and other TLR agonists (*31*). The differential radioprotective effect of CBLB502 in tumor versus normal tissues is likely due to the constitutive activation of NF-κB observed in most tumor cells (*32*) and/or inhibition of downstream TLR5 signaling by the activated phosphatidylinositol-3 kinase present in many tumors (*33*).

A theoretical risk of using CBLB502 in cancer treatment is that suppression of apoptosis in-

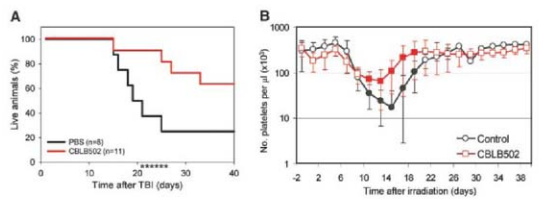

Fig. 3. A single injection of CBLB502 improves survival of lethally irradiated rhesus macaques. **(A)** In a single pilot experiment, rhesus macaques were injected with 0.04 mg/kg CBLB502 ($n = 11$) or PBS ($n = 8$) 45 min before 6.5 Gy TBI ($LD_{70/40}$), a dose lethal for 70% of monkeys within 40 days after irradiation. *$P < 0.03$ by two-tailed Fisher's test. **(B)** Platelet counts in the peripheral blood of irradiated monkeys. Days with statistically significant ($P < 0.05$ by two-tailed t test) differences between control and CBLB502 groups are indicated by filled symbols.

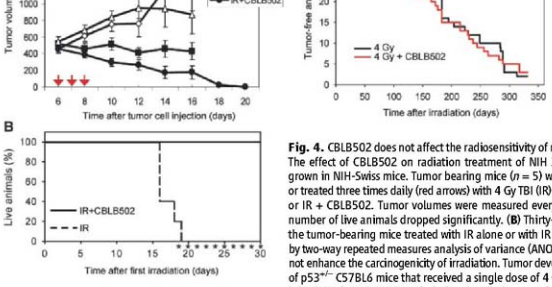

Fig. 4. CBLB502 does not affect the radiosensitivity of mouse tumors (*18*). **(A)** The effect of CBLB502 on radiation treatment of NIH 3T3–derived sarcomas grown in NIH-Swiss mice. Tumor bearing mice ($n = 5$) were left untreated (U/t) or treated three times daily (red arrows) with 4 Gy TBI (IR) alone, CBLB502 alone, or IR + CBLB502. Tumor volumes were measured every second day until the number of live animals dropped significantly. **(B)** Thirty-day survival curves for the tumor-bearing mice treated with IR alone or with IR + CBLB502. *$P < 0.03$ by two-way repeated measures analysis of variance (ANOVA). **(C)** CBLB502 does not enhance the carcinogenicity of irradiation. Tumor development in two groups of $p53^{+/-}$ C57BL6 mice that received a single dose of 4 Gy TBI, with or without injection of CBLB502 30 min before irradiation, was followed for 49 weeks.

duced by systemic genotoxic stress might promote cancer. To address this concern, we tested the effect of CBLB502 on radiation-induced carcinogenicity in cancer-prone $p53^{+/-}$ mice, 100% of which develop tumors (lymphomas and sarcomas) within 1 year after sublethal (4 Gy) TBI (*34*). We found that the timing and frequency of tumor appearance in this model were not affected by a single CBLB502 injection given 30 min before 4 Gy TBI (Fig. 4C). Furthermore, there was no difference in median survival times for TBI-only and CBLB502 + TBI groups: 195 [95% confidence interval (CI): 170 to 220] days versus 195 (95% CI: 144 to 246) days, respectively (log-rank test for equality of distributions: $P = 0.96$). We also evaluated wild-type NIH-Swiss mice that were rescued from lethal irradiation (13 Gy) by CBLB502 treatment 6 months postirradiation. Although the analyzed animals showed signs of radiation-induced tissue damage (cataracts, reduced body weight, and involution of reproductive organs) as compared with age-matched controls that were neither irradiated nor treated, there was no evidence of cancer or massive fibrosis (table S2).

In summary, CBLB502 reduces radiation toxicity without diminishing the therapeutic anti-tumor effect of radiation and without promoting radiation-induced carcinogenicity. These properties of a TLR5 agonist acting as an NF-κB–inducing agent provide further support for our concept of pharmacological imitation of tumor-specific antiapoptotic mechanisms as an approach to radioprotection. This approach was first validated by our demonstration that a chemical inhibitor of the proapoptotic p53 pathway safeguarded mice from lethal acute radiation syndrome (*11*). However, we subsequently found that wild-type p53 plays an unexpected role as a survival factor in GI cells exposed to high doses of γ-irradiation (*35*), limiting the usefulness of p53 inhibitors to protection against HP, but not GI, acute radiation syndrome. This problem has been resolved by our identification of CBLB502 as a TLR5 agonist that can protect against both major acute radiation syndromes. Our results suggest that TLR5 agonists may be valuable as both adjuvants for cancer radiotherapy and protectants or mitigators for radiation emergencies.

References and Notes

1. J. K. Waselenko *et al.*, *Ann. Intern. Med.* **140**, 1037 (2004).
2. M. J. Dodd, *Managing the Side Effects of Chemotherapy and Radiation* (UCSF Nursing Press, San Francisco, 2001).
3. J. F. Weiss, M. R. Landauer, *Toxicology* **189**, 1 (2003).
4. R. Neta *et al.*, *J. Exp. Med.* **173**, 1177 (1991).
5. A. V. Gudkov, E. A. Komarova, *Nat. Rev. Cancer* **3**, 117 (2003).
6. C. S. Potten, *Cancer Metastasis Rev.* **11**, 179 (1992).
7. R. Kolesnick, Z. Fuks, *Oncogene* **22**, 5897 (2003).
8. M. Karin, *Nature* **441**, 431 (2006).
9. Y. Wang *et al.*, *Cancer Res.* **64**, 6240 (2004).
10. K. V. Gurova *et al.*, *Proc. Natl. Acad. Sci. U.S.A.* **102**, 17448 (2005).
11. P. G. Komarov *et al.*, *Science* **285**, 1733 (1999).
12. C. Pasare, R. Medzhitov, *Adv. Exp. Med. Biol.* **560**, 11 (2005).
13. S. Rakoff-Nahoum, J. Paglino, F. Eslami-Varzaneh, S. Edberg, R. Medzhitov, *Cell* **118**, 229 (2004).
14. S. Uematsu *et al.*, *Nat. Immunol.* **7**, 868 (2006).
15. C. Maaser *et al.*, *J. Immunol.* **172**, 5056 (2004).
16. F. Paris *et al.*, *Science* **293**, 293 (2001).
17. T. Tallant *et al.*, *BMC Microbiol.* **4**, 33 (2004).
18. Materials and methods are available as supporting material on *Science* Online.
19. K. G. Murthy, A. Deb, S. Goonesekera, C. Szabo, A. L. Salzman, *J. Biol. Chem.* **279**, 5667 (2004).
20. T. Eaves-Pyles *et al.*, *J. Immunol.* **166**, 1248 (2001).
21. J. F. Weiss, *Environ. Health Perspect.* **105**, 1473 (1997).
22. M. H. Whitnall *et al.*, *Int. J. Immunopharmacol.* **22**, 1 (2000).
23. G. Sebastiani *et al.*, *Genomics* **64**, 230 (2000).
24. M. W. Epperly *et al.*, *Radiat. Res.* **157**, 568 (2002).
25. K. S. Chun, Y. J. Surh, *Biochem. Pharmacol.* **68**, 1089 (2004).
26. D. C. Dale, *Drugs* **62** (suppl. 1), 1 (2002).
27. K. Atkinson *et al.*, *Cytokines Mol. Ther.* **1**, 47 (1995).
28. L. V. Karkanitsa, M. E. Komarovskaya, S. I. Krivenko, *Stem Cells* **15** (suppl. 2), 95 (1997).
29. D. R. Stickney *et al.*, *Int. Immunopharmacol.* **7**, 500 (2007).
30. A. N. Honko, S. B. Mizel, *Immunol. Res.* **33**, 83 (2005).
31. L. Apetoh *et al.*, *Cancer Genomics Proteomics* **4**, 65 (2007).
32. T. Lu, G. R. Stark, *Cell Cycle* **3**, 1114 (2004).
33. Y. Yu *et al.*, *J. Immunol.* **176**, 6194 (2006).
34. C. J. Kemp, T. Wheldon, A. Balmain, *Nat. Genet.* **8**, 66 (1994).
35. E. A. Komarova *et al.*, *Oncogene* **23**, 3265 (2004).
36. A. Vidrich *et al.*, *Am. J. Pathol.* **166**, 1055 (2005).

37. We thank P. Baker for help with manuscript preparation and editing. Supported by grants CA75179 and AI066497 from NIH and grants from NASA (U.S. National Aeronautics and Space Administration), the Defense Advanced Research Projects Agency (DARPA) and Cleveland BioLabs, Inc., to A.V.G. and grant CA84406 from NIH to J.A.D. A.V.G., E.F., L.G.S., and J.A.D. have a paid consulting relationship with Cleveland BioLabs, Inc. We dedicate this paper to the memory of our friend and colleague Alexander (Shurik) Neyfakh.

Supporting Online Material

www.sciencemag.org/cgi/content/full/320/5873/226/DC1
Materials and Methods
Figs. S1 to S8
Tables S1 and S2
References

8 January 2008; accepted 12 March 2008
10.1126/science.1154986

Evidence for Editing of Human Papillomavirus DNA by APOBEC3 in Benign and Precancerous Lesions

Jean-Pierre Vartanian, Denise Guétard, Michel Henry, Simon Wain-Hobson*

Cytidine deaminases of the APOBEC3 family all have specificity for single-stranded DNA, which may become exposed during replication or transcription of double-stranded DNA. Three human *APOBEC3A* (*hA3A*), *hA3B*, and *hA3H* genes are expressed in keratinocytes and skin, leading us to determine whether genetic editing of human papillomavirus (HPV) DNA occurred. In a study of HPV1a plantar warts and HPV16 precancerous cervical biopsies, hyperedited HPV1a and HPV16 genomes were found. Strictly analogous results were obtained from transfection experiments with HPV plasmid DNA and the three nuclear localized enzymes: hA3A, hA3C, and hA3H. Thus, stochastic or transient overexpression of *APOBEC3* genes may expose the genome to a broad spectrum of mutations that could influence the development of tumors.

Human APOBEC3 molecules deaminate cytidine residues in single-stranded DNA (ssDNA) and have been demonstrated to have antiviral effects (*1*–*5*). Human immunodeficiency virus–1 (HIV-1) cDNA in particular is vulnerable to the action of the cytoplasmic APOBEC3F and APOBEC3G cytidine deaminases (hA3F and hA3G) (*6*, *7*). Of the seven-gene cluster on chromosome 22, hA3A, hA3C, and hA3H are mainly nuclear, whereas hA3B is both nuclear and cytoplasmic (*8*, *9*). Human *A3A* and *hA3B* are expressed in psoriatic keratinocytes, and *hA3A* is up-regulated in acne lesions and can be induced by phorbol 12-myristate 13-acetate (*10*, *11*). Incidentally, *hA3H* is also expressed in normal skin (*12*, *13*). We hypothesized that the DNA of human papillomaviruses, which replicate in cutaneous and mucosal keratinocytes, might be vulnerable to editing by some of the nuclear A3 deaminases.

In light of the predominant APOBEC3 expression data in cutaneous keratinocytes, total DNA was extracted from six HPV1a-positive plantar warts. For mutational analysis, a region corresponding to the origin of replication/promoter region was selected, because it seemed likely that this region might exist in a single-stranded state more frequently than any other region of the HPV genome. Differential DNA denaturation polymerase chain reaction (3D-PCR) was used to selectively amplify AT-rich edited genomes (*14*, *15*). This technique relies on the fact that AT-rich DNA denatures at a lower temperature than GC-rich

Molecular Retrovirology Unit, Institut Pasteur, 28 Rue de Docteur Roux, 75724 Paris cedex 15, France.
*To whom correspondence should be addressed. E-mail: simon@pasteur.fr

DNA and has proven successful at selectively amplifying APOBEC3-edited retroviral cDNA (*16*). For one out of the six plantar warts, monotonously G→A or C→T substituted HPV1a sequences were identified (Fig. 1, A and B), meaning that both strands had undergone editing.

Averaging across both strands, we determined that the mean cytidine editing frequency was ~11% (range: 4 to 61% per clone). Within the nucleus, G:U mismatch repair, which predominantly yields the original G:C, will mitigate against the effects of APOBEC3 editing. Hence, it is possible that a vestigial C→T transition reflects the opposing forces of APOBEC3 editing and G:U mismatch repair. Analysis of the dinucleotide context of edited sites showed that there was no pronounced 3′ nucleotide context (Fig. 1C), such as CpG, thus ruling out a cytidine hypermethylation/deamination-related phenomenon. By contrast, there was a strong 5′ effect favoring TpC and CpC, typical of some APOBEC3 deaminases (*17*) (Fig. 1D).

Based on this evidence for in vivo editing of HPV sequences, we next tested the potential for APOBEC3 editing of HPV DNA in vitro. Human embryonic kidney–293T cells were cotransfected by HPV1a plasmid DNA along with each of six *APOBEC3* genes: *hA3A, hA3B, hA3C, hA3F, hA3G*, and *hA3H*. At 72 hours, total DNA was recovered and 3D-PCR was performed. When compared with the HPV1a plasmid plus vector alone transfection [denaturation temperature (T_d) = 84.6°C], 3D-PCR products were recovered at a lower T_d (82.0°C) from the *hA3A, hA3C*, and *hA3H* cotransfections. Sequencing of cloned 3D-PCR products showed extensive and monotonous cytidine deamination of both DNA strands (Fig. 1, A and B). The mean cytidine editing frequencies in vitro, 25 to 29% (range: 13 to 60% per clone), were about twofold higher than those in vivo, which may reflect stronger *APOBEC3* gene expression driven by the powerful cytomegalovirus immediate-early promoter. The ssDNA cytidine editing activity reported here for human A3H appears to be just as strong as that seen for hA3A and hA3C. Furthermore, the dinucleotide context of edited sites for all three hA3 deaminases showed a clear 5′ preference for TpC and CpC and a strong aversion for ApC that correlates well with the observed editing contexts in vivo (Fig. 1D). Because the preferred dinucleotide context for human activation-induced deaminase (AID) is ApC and GpC (*18, 19*), it seems probable that this enzyme can be excluded from the list of potential mutators.

Analysis of site-specific editing frequencies, which factors in cold spots, revealed significant correlations ($P < 10^{-4}$) between the in vivo data set and all three in vitro data sets. Indeed, as *hA3A* and *hA3H* are expressed in keratinocytes, whereas *hA3C* is probably the most widely expressed of all the human A3 deaminases (*20*), there is no reason to exclude one from the others. Cotransfection experiments with plasmids encoding human *APOBEC1* and *APOBEC2* (*hA1* and *hA2*), or the orthologous murine genes *mA1*, *mA2*, and *mA3*, failed to yield hyperedited HPV1a genomes. Given the negative result for *hA3B* and the fact that hA1 and mA1 traffic between the cytoplasm and nucleus, a nuclear localization per

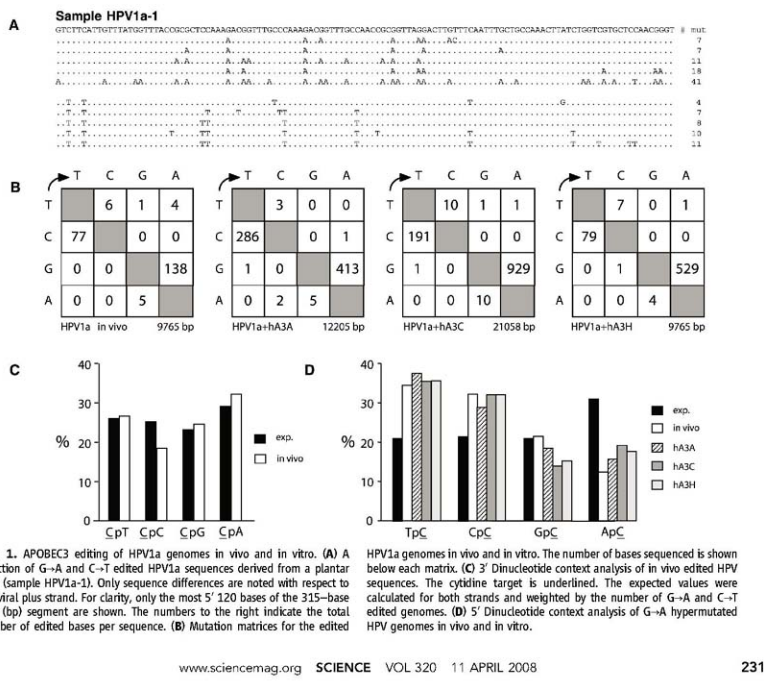

Fig. 1. APOBEC3 editing of HPV1a genomes in vivo and in vitro. **(A)** A selection of G→A and C→T edited HPV1a sequences derived from a plantar wart (sample HPV1a-1). Only sequence differences are noted with respect to the viral plus strand. For clarity, only the most 5′ 120 bases of the 315–base pair (bp) segment are shown. The numbers to the right indicate the total number of edited bases per sequence. **(B)** Mutation matrices for the edited HPV1a genomes in vivo and in vitro. The number of bases sequenced is shown below each matrix. **(C)** 3′ Dinucleotide context analysis of in vivo edited HPV sequences. The cytidine target is underlined. The expected values were calculated for both strands and weighted by the number of G→A and C→T edited genomes. **(D)** 5′ Dinucleotide context analysis of G→A hypermutated HPV genomes in vivo and in vitro.

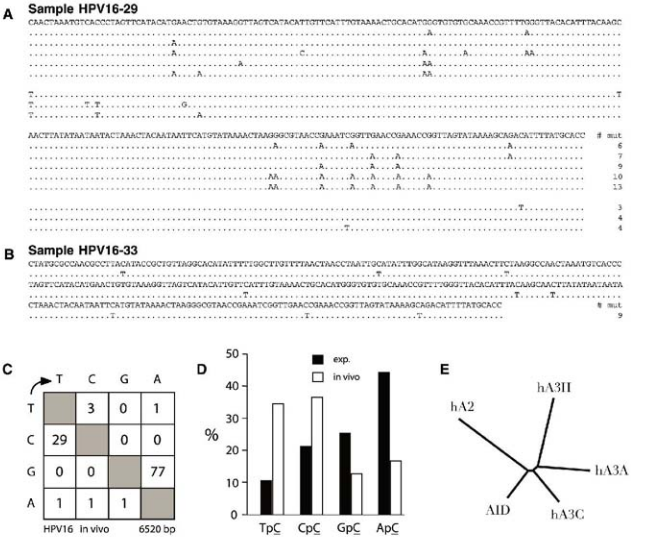

Fig. 2. APOBEC3 editing of HPV16 genomes in vivo. **(A)** A selection of G→A and C→T edited HPV16 sequences derived from precancerous cervical biopsies from sample HPV16-29. Only sequence differences are noted with respect to the viral plus strand. For clarity, only the most 5′ 225 bases of the 325-bp segment are shown. The numbers to the right indicate the total number of edited bases per sequence. **(B)** C→T hypermutated sequence derived from precancerous cervical biopsy HPV16-33, the complete region being shown. The unedited reference sequence for samples 29 and 33 is identical to that of AF067024. **(C)** Mutation matrices for the edited HPV16 genomes in vivo. The number of bases sequenced is shown below the matrix. **(D)** 5′ Dinucleotide context analysis of hyper-edited HPV16 genomes in vivo. **(E)** Neighbor-joining tree based on the protein sequences of five human single-domain cytidine deaminases including hA2.

se is apparently insufficient for deamination of HPV1a DNA. These findings extend the range of viral targets for APOBEC3 enzymes to include double-stranded DNA viruses.

Human papillomaviruses can be generally divided into those that infect cutaneous or mucosal keratinocytes, a feature strongly reflected in their phylogenic clustering (*21*). Among the latter group are found the HPVs that are strongly associated with cervical cancer. In an extensive European study, ~65 and ~6% of cervical cancers were associated with HPV16 and HPV18, respectively (*22*), with at least 11 other strains also showing a strong association (*23*).

Although it is unclear whether *APOBEC3* genes are expressed in mucosal keratinocytes, the evidence for APOBEC3 editing of HPV1a genomes led us to examine total DNA from nine HPV16-positive precancerous cervical biopsies. 3D-PCR was again used to amplify a comparable region spanning the origin of replication/promoter region. Cloning and sequencing of the last positive points of sample HPV16-29 yielded 19 sequences with monotonously G→A or C→T transitions, which is indicative of editing of both DNA strands (Fig. 2A). A single C→T edited sequence was also recovered from a second HPV16 sample (HPV16-33, Fig. 2B). A cutoff of three or more C→T transitions was imposed to reduce the impact of natural variation and PCR error in designating APOBEC3 editing. Nonetheless, an analysis of all the remaining HPV16 genomes recovered by 3D-PCR showed a net excess of G→A and C→T transitions (Fig. 2, A to C). The mean editing frequency was ~9% (range: 5 to 24% per clone). Just as for HPV1a in vivo, the preferred dinucleotide context for editing was TpC and CpC, suggesting that hA3A, hA3C, and hA3H were involved (Fig. 2D).

Transcriptionally active HPV genomes are in the form of minichromosomes, complete with nucleosomes (*24*). If they are as the data suggest (i.e., vulnerable to cytidine deamination, say in a subset of cells with overexpressed *hA3A*, *hA3C*, and *hA3H*), then it raises the question as to how chromosomal DNA is normally protected from these three powerful deaminases (Figs. 1 and 2). AID is a cytidine deaminase that mediates class switch recombination and somatic hypermutation of rearranged immunoglobulin genes (*25*, *26*). Not only does this gene have an exon-intron structure similar to that of *hA3A*, *hA3C*, and *hA3H*, but human AID also falls into a cluster with hA3A and hA3C, showing ~43 to 46% amino acid identity (Fig. 2E). By contrast, hA3H shows only 34 to 37% amino acid identity with members of this AID/hA3A/hA3C cluster. Ectopic expression of *AID* may be found in a variety of cell types including nonlymphoid tumors, again suggesting a link between cytidine deamination and tumorigenesis (*27*). As the predominant mutation in cancer genomes is the C→T transition (*28*, *29*), irrespective of CpG, the present findings are consistent with the possibility that stochastic or transient overexpression of either of four human cytidine deaminase genes—*AID*, *hA3A*, *hA3C*, and *hA3H*—might be sufficient to create an initial broad mutant spectrum from which the cancer genome eventually emerges.

References and Notes

1. D. Lecossier, F. Bouchonnet, F. Clavel, A. J. Hance, *Science* **300**, 1112 (2003).
2. B. Mangeat *et al.*, *Nature* **424**, 99 (2003).
3. R. Mariani *et al.*, *Cell* **114**, 21 (2003).
4. R. Suspène *et al.*, *Nucleic Acids Res.* **32**, 2421 (2004).
5. H. Zhang *et al.*, *Nature* **424**, 94 (2003).
6. R. S. Harris *et al.*, *Cell* **113**, 803 (2003).
7. H. L. Wiegand, B. P. Doehle, H. P. Bogerd, B. R. Cullen, *EMBO J.* **23**, 2451 (2004).
8. H. P. Bogerd *et al.*, *Proc. Natl. Acad. Sci. U.S.A.* **103**, 8780 (2006).

9. M. Kinomoto *et al.*, *Nucleic Acids Res.* **35**, 2955 (2007).
10. P. Madsen *et al.*, *J. Invest. Dermatol.* **113**, 162 (1999).
11. N. R. Trivedi, K. L. Gilliland, W. Zhao, W. Liu, D. M. Thibodeaux, *J. Invest. Dermatol.* **126**, 1071 (2006).
12. Y. Dang, X. Wang, W. J. Esselman, Y. H. Zheng, *J. Virol.* **80**, 10522 (2006).
13. M. Ohainle, J. A. Kems, H. S. Malik, M. Emerman, *J. Virol.* **80**, 3853 (2006).
14. R. Suspène, M. Henry, S. Guillot, S. Wain-Hobson, J.-P. Vartanian, *J. Gen. Virol.* **86**, 125 (2005).
15. Materials and methods are available as supporting material on *Science* Online.
16. R. Suspène *et al.*, *Proc. Natl. Acad. Sci. U.S.A.* **102**, 8321 (2005).
17. K. N. Bishop *et al.*, *Curr. Biol.* **14**, 1392 (2004).
18. S. G. Conticello, C. J. Thomas, S. K. Petersen-Mahrt, M. S. Neuberger, *Mol. Biol. Evol.* **22**, 367 (2005).
19. P. Pham, R. Bransteitter, J. Petruska, M. F. Goodman, *Nature* **424**, 103 (2003).
20. A. Jarmuz *et al.*, *Genomics* **79**, 285 (2002).
21. E. M. de Villiers, C. Fauquet, T. R. Broker, H. U. Bernard, H. zur Hausen, *Virology* **324**, 17 (2004).
22. M. Arbyn, J. Dillner, *J. Clin. Virol.* **38**, 189 (2007).
23. V. Cogliano *et al.*, *Lancet Oncol.* **6**, 204 (2005).
24. W. Stunkel, H. U. Bernard, *J. Virol.* **73**, 1918 (1999).
25. J. M. Di Noia, M. S. Neuberger, *Annu. Rev. Biochem.* **76**, 1 (2007).
26. M. F. Goodman, M. D. Scharff, F. E. Romesberg, *Adv. Immunol.* **94**, 127 (2007).
27. I. M. Okazaki, A. Kotani, T. Honjo, *Adv. Immunol.* **94**, 245 (2007).
28. C. Greenman *et al.*, *Nature* **446**, 153 (2007).
29. T. Sjoblom *et al.*, *Science* **314**, 268 (2006).
30. We thank AL Fawe for the *HPV* samples and plasmid; B. Cullen for the hA3A expression plasmid, and N. Zidane of the Institut Pasteur sequencing platform for the high-throughput sequencing.

Supporting Online Material

www.sciencemag.org/cgi/content/full/320/5873/230/DC1
Materials and Methods

20 November 2007; accepted 5 March 2008
10.1126/science.1153201

Segregation of Axial Motor and Sensory Pathways via Heterotypic Trans-Axonal Signaling

Benjamin W. Gallarda,[1]* Dario Bonanomi,[1]* Daniel Müller,[2,3]* Arthur Brown,[4] William A. Alaynick,[1] Shane E. Andrews,[1] Greg Lemke,[5] Samuel L. Pfaff,[1]† Till Marquardt[2,3]†

Execution of motor behaviors relies on circuitries effectively integrating immediate sensory feedback to efferent pathways controlling muscle activity. It remains unclear how, during neuromuscular circuit assembly, sensory and motor projections become incorporated into tightly coordinated, yet functionally separate pathways. We report that, within axial nerves, establishment of discrete afferent and efferent pathways depends on coordinate signaling between coextending sensory and motor projections. These heterotypic axon-axon interactions require motor axonal EphA3/EphA4 receptor tyrosine kinases activated by cognate sensory axonal ephrin-A ligands. Genetic elimination of trans-axonal ephrin-A → EphA signaling in mice triggers drastic motor-sensory miswiring, culminating in functional efferents within proximal afferent pathways. Effective assembly of a key circuit underlying motor behaviors thus critically depends on trans-axonal signaling interactions resolving motor and sensory projections into discrete pathways.

During neuromuscular circuit assembly, spinal motor neurons and dorsal root ganglion (DRG) sensory neurons coextend axons en route to peripheral targets, such as muscle and dermis (*1*, *2*). Their close proximity and eventual pooling into common nerves prompts the question of how sensory and motor projections become organized into tightly coordinated, yet functionally separate afferent and efferent pathways. In chick embryos, peripheral sensory-motor trajectories become rapidly organized into defined mutually exclusive intranerve fascicles (*3*). This early appearance of discrete intranerve trajectories suggests that trans-axonal interactions might drive the segregation (*3*, *4*). Axon-axon interactions have been implicated in olfactory and retinal axon targeting in *Drosophila* and mouse (*5*–*7*) and also in chick lateral motor column (LMC) and sensory axon sorting, respectively (*8*, *9*). Moreover, embryological studies suggest that trans-axonal interactions impart vital cues for proper navigation of proprioceptive sensory axons (*4*, *10*). The nature of such interactions and their contribution to neuromuscular circuit assembly, however, remain unclear (*11*).

To study the mechanisms underlying the establishment of discrete peripheral nerve pathways, we first analyzed the relative behavior of identified motor and sensory projections during neuromuscular development (*12*). We generated mice carrying ventral motor neuron–specific *Hb9::eGFP* (*13*) and previously generated sensory neuron-targeted *Brn3a::tau:lacZ* transgenes (*14*). In proximal peripheral nerves of *Hb9::eGFP;Brn3a::tau:lacZ* embryos, sensory and motor projections segregate into discrete eGFP$^+$ (where eGFP is enhanced green fluorescent protein) and tau:βGal$^+$ (where βGal is β-galactosidase) fascicles (Fig. 1, A to C and F). This pattern emerges after sensory axons join motor projections at the dorsal root–ventral root (DR-VR) junction (Fig. 1, A to C, and fig. S1) and precedes the stages of Schwann cell precursor invasion (Fig. 1, A to C; Fig. 2, A to C; and fig. S1) (*15*). In most cases, sensory projections trail earlier-extending motor axons (Fig. 1D and fig. S1, A to C and J to K) (*1*). However, median medial motor column (MMCm) axons extend toward axial targets with a delay that results in a much closer association with pioneering sensory axons in the dorsal ramus pathway (Fig. 1E and fig. S1, D to I and L to M) (*16*). The initial interactions between MMCm and DRG neurites eventually resolve into sharply segregated proximal motor-sensory pathways (Fig. 1, A to C and F, and fig. S1K). These observations suggest that, particularly within axial nerves, axon type-segregated patterns may emerge through interactions among coextending motor and sensory projections.

To address this possibility, we established an assay to study the interactions between axial motor and sensory projections in vitro (Fig. 1G and fig. S2) [see supporting online material (SOM)]. After extended co-culture periods, axial motor and sensory axons became organized into almost completely exclusive but parallel sensory and motor trajectories (Fig. 1, H to J, and fig. S3, A and M to N)—a pattern remarkably reminiscent of the aligned but discrete efferent and afferent pathways observed in situ (Fig. 1, A to C and F). Using nerve growth factor (NGF) and neurotrophin-3 to select for nociceptive and proprioceptive classes of sensory neurons, respectively, we found that effective segregation of sensory and motor projections occurred irrespective of sensory subtype. Nevertheless, MMCm axons more frequently crossed into proprioceptive explants compared with nociceptive cultures (fig. S2, F to K). Homotypic (e.g., motor-motor) co-cultures failed to display axon segregation, stressing the heterotypic nature of the underlying interactions (Fig. 1, K to L).

To address the cellular basis for these interactions, we monitored live co-cultured axial motor and sensory axons (fig. S3, C to L, and movies S1 and S2). Acute encounters of motor axons with sensory processes triggered repulsive growth-cone behaviors, including wholesale

[1]Gene Expression Laboratory, Salk Institute for Biological Studies, 10010 North Torrey Pines Road, La Jolla, CA 92037, USA. [2]Developmental Neurobiology Laboratory, European Neuroscience Institute Göttingen, Max Planck Society/University Medical School Göttingen, Grisebachstrasse 5, 37077 Göttingen, Germany. [3]Deutsche Forschungsgemeinschaft Emmy Noether Group, European Neuroscience Institute Göttingen, Grisebachstrasse 5, 37077 Göttingen, Germany. [4]Biotherapeutics Research Group, Roberts Research Institute, Department of Anatomy and Cell Biology, University of Western Ontario, 100 Perth Drive, London, Ontario N6A 5K8, Canada. [5]Molecular Neurobiology Laboratory, Salk Institute for Biological Studies, 10010 North Torrey Pines Road, La Jolla, CA 92037, USA.

*These authors contributed equally to this work.
†To whom correspondence should be addressed. E-mail: till.marquardt@mpi-mail.mpg.de (T.M.); pfaff@salk.edu (S.L.P.)

collapse followed by partial axon retraction (11.7%, $n = 51$ growth-cone encounters) (fig. S3, B and C to G, and movie S2). Heterotypic encounters, however, more frequently elicited intermittent retraction of filopodial and lamellipodial processes, followed by motor growth-cone reorientation parallel to sensory axon trajectories (70.5%, $n = 51$) (fig. S3, H to L; movie S1; and table S1). Homotypic encounters between either intersecting motor or sensory axons, in contrast, failed to evoke repulsive behaviors, allowing largely unhindered crossings of axons (2.3% total motor growth-cone repulsion, $n = 43$, versus 82.3% heterotypic repulsion, $n = 51$) (Fig. 1, K to L; movie S3; and table S1). These observations raise the possibility that the sorting of axial motor and sensory projections into separate intranerve pathways is achieved through heterotypic contact-dependent repulsive interactions.

What are the mechanisms underlying heterotypic motor-sensory segregation? Among several candidate molecules, we focused on the EphA family of receptor tyrosine kinases and their cognate cell surface–linked glycosylphosphatidylinositol-anchored ephrin-A ligands, whose distribution is consistent with a role in trans-signaling between motor and sensory axons (*17*, *18*). When engaged by ephrin-As, EphAs typically trigger contact-dependent repulsion, which has been shown to drive diverse aspects of central nervous system development and plasticity (*5*, *19*). DRG sensory neurons and their peripheral processes express high levels of ephrin-A protein (Fig. 2, D to F, and fig. S4, B, F to G, K, and N), consistent with the reported *ephrin-A2* and *ephrin-A5* mRNA expression in DRGs (*17*, *20*). Conversely, high levels of both EphA3 and EphA4 are detected on MMCm axons (Fig. 2, G to I; fig. S4, C, H to I, L, and O; and fig. S6, A to D). Likewise, EphA4 (but not EphA3) is also expressed on LMC axons (*17*, *18*, *20*, *21*). The complementary distribution of EphAs and ephrin-As on MMCm and sensory axons thus mirrors the segregation of axonal processes within proximal nerves.

To address the potential role of signaling between sensory ephrin-As and motor axonal

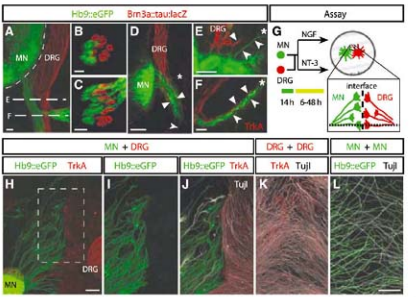

Fig. 1. Spontaneous delineation of axial motor and sensory projections during neuromuscular circuit assembly. **(A)** 120-μm lumbar (L5 to L6) transversal E12.5 section at the DR-VR junction. eGFP, motor axons; anti-βGal, sensory axons (red); MN, motor neurons. **(B** and **C)** 120-μm nerve cross sections. Levels, dashed lines in (A). (C) MMCm projections through sensory fascicles. **(D** and **E)** 120-μm lumbar E10.0. Sequential advance: nonaxial motor axons, bottom arrowheads; sensory axons, top arrowheads. Asterisks denote emerging MMCm axons. (E) E10.0 dorsal ramus, emerging sensory; MMCm growth cone, top and bottom arrowheads. **(F)** E12.5 dorsal ramus, segregated sensory-motor pattern; TrkA, tropomyosin-related kinase A. (A to F) Scale bars, 20 μm. **(G)** Sensory-motor interaction assay (see SOM). MN and DRG explants. **(H** to **J)** Motor (green) and sensory (red) axons segregate in vitro. The dashed-line box indicates the enlarged area in (I) and (J); TuJI, βIII-tubulin. (I and J) Axon interface of (H). **(K** and **L)** Absence of homotypic axon segregation. (H) Scale bar, 100 μm. (I to L) Scale bar, 100 μm.

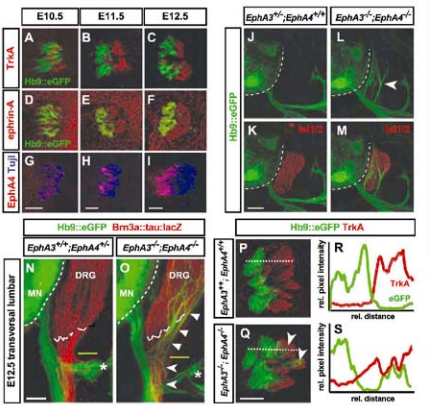

Fig. 2. Loss of proximal motor-sensory segregation upon eliminating MMCm-expressed EphA receptors. **(A** to **I)** 60-to-120–μm L3 to L5 nerve cross sections: complementary distribution of EphA4 (anti-EphA4), ephrin-As (EphA3-Fc) in motor (eGFP), and sensory axons (TrkA). Scale bar, 25 μm. **(J** to **M)** 60-μm thoracic transversal. Scale bars, 100 μm. (K and L) No motor projections in DRG (Isl1/2: sensory nuclei). (L and M) MMCm axons misproject into DRG [arrowhead in (L)]. Dashed line indicates the spinal cord. **(N** and **O)** 180-μm transversal. (N) Control motor-sensory trajectories. (O) MMCm axons invade proximal sensory pathways and DRG (arrowheads). Solid lines indicate the DR-VR junction; asterisks denote the dorsal ramus; and dashed lines indicate motor and sensory somas. Scale bar, 50 μm. **(P** and **Q)** 120-μm T10 nerve cross. Dotted lines indicate line measurements in (R) and (S). (P) Control motor-sensory trajectories. (Q) Ectopic MMCm axons associate with sensory fascicles (arrowheads). Scale bar, 20 μm. **(R** and **S)** Intensity profiles of line measurements indicated in (P) and (Q).

EphAs, we first examined the impact of eliminating EphA receptors from motor neurons on interaxonal segregation in vivo. To tackle potential redundant functions shared by different EphAs, we generated mice carrying targeted null mutations for both *EphA3* (*18*) and *EphA4* (*21*) to obtain *EphA3/EphA4*-deficient (*EphA3*$^{-/-}$;*EphA4*$^{-/-}$) animals. Subsequent intercrossing with *Hb9::eGFP* facilitated selective analysis of motor axon behavior upon EphA removal in *EphA3*$^{-/-}$;*EphA4*$^{-/-}$;*Hb9::eGFP* embryos. The loss of either *EphA3* or *EphA4* alone did not trigger overt defects in motor-sensory organization, although *EphA4*$^{-/-}$ mutants displayed marked peroneal-nerve thinning, consistent with the well-established role of EphA4 in dorsal-ventral LMC axon routing in the limb (*21*, *22*). However, the successive loss of wild-type (WT) *EphA3* and *EphA4* alleles in either *EphA4* or *EphA3* null backgrounds, respectively, resulted in the cumulative misrouting of motor axons into DRGs (Fig. 2, L to M; Fig. 3, D to E; and fig. S5, A to F). *EphA3/EphA4* double-null mutants displayed marked ectopic invasion of motor axons into DRGs at all rostro-caudal levels (Fig. 2, L to M, and fig. S4, A to F). Retrograde neuronal tracing experiments revealed that the motor axons entering the DRG originated from axial motor neurons normally coexpressing EphA3 and EphA4, but not from other motor neuron subtypes (fig. S6, A to D). Despite drastic changes in axial motor projections, sensory axons retain normal segregation from motor trajectories in *EphA3/EphA4* mutants (fig. S6, I to T)—indicating the cell-autonomous action of motor axonal EphAs in establishing discrete proximal motor and sensory trajectories.

We next generated *EphA3*$^{-/-}$;*EphA4*$^{-/-}$;*Hb9::eGFP;Brn3a::tau:lacZ* mice, allowing the simultaneous visualization of motor and sensory axons at high resolution in EphA-deficient backgrounds. The examination of the intranerve segregation pattern *EphA3*$^{-/-}$;*EphA4*$^{-/-}$;*Hb9::eGFP*; *Brn3a::tau:lacZ* embryos revealed that misrouted axial motor axons entered proximal sensory pathways after initially following proper VR trajecto-

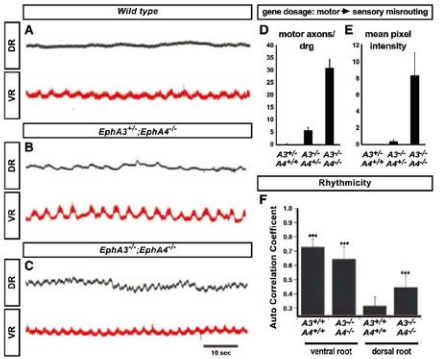

Fig. 3. Axial motor axons within sensory pathways retain functional coupling with spinal locomotor circuits. (**A** to **C**) E18.5 DR recordings (top). Genotype-matched VR traces (bottom). Locomotor activity evoked by 10 μM *N*-methyl D,L-aspartate (NMA) and 20 μM serotonin [5-hydroxytryptamine (5-HT)]. (**A**) No rhythmic activity in WT DR, rhythmic activity in VR. (**B**) Some DR activity. (**C**) Strong rhythmic DR activity. (**D** and **E**) Quantitative summary: motor-sensory misrouting (see SOM and fig. S5, A to C). *EphA3*$^{+/-}$;*EphA4*$^{-/-}$ (n = 6 spinal cords), *EphA3*$^{-/-}$;*EphA4*$^{+/-}$ (n = 8), *EphA3*$^{-/-}$;*EphA4*$^{-/-}$ (n = 6). Error bars indicate SD. (**F**) Autocorrelation analysis. Significance: WT, *EphA3/EphA4*-deficient VRs ($P < 0.001$, each); WT DR ($P > 0.05$), *EphA3/EphA4*-deficient DR ($P < 0.001$). WT (n = 6), *EphA3/EphA4*-deficient (n = 6). Asterisks denote significance; error bars indicate SD.

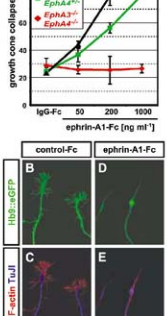

Fig. 4. Motor axonal EphAs impose sensitivity toward sensory-expressed ephrin-As. (**A**) *EphA3/EphA4* deficiency abolishes ephrin-A–induced MMCm growth-cone collapse in vitro. IgG, immunoglobulin G. (**B** to **E**) Example of control-Fc (B and C) and ephrin-A1–Fc (D and E) stimulation. Typical Hb9::eGFP$^+$ MMCm growth cones (B and C); ephrin-A1–Fc triggers collapse to filopodialike thread, F-actin$^+$TuJI$^+$ swelling. Scale bar, 10 μm. (**F** to **K**) Autonomous *EphA3/EphA4* requirement in MMCm axons for repulsion by sensory axons. Scale bars, 100 μm. (F and G) *EphA3/EphA4*-deficient MMCm axons extensively cross WT sensory axons and (H) invade WT DRGs (dashed outline). (I and J) *EphA3/EphA4* null sensory axons repel WT MMCm axons. (K) No WT motor axon invasion of *EphA3/EphA4* null DRG. (**L**) Quantitative summary. Mean number of invasion events per DRG (left); stacked column diagram represents percent invaded DRGs per genotype (right). Explant combinations are indicated. Relative distance is between motor-sensory explants.

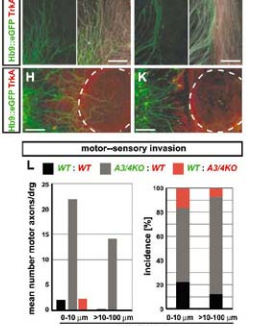

ries (Fig. 2, O to P, and fig. S5, G to I). Upon reaching the DR-VR junction, however, these motor axons fanned out into proximal sensory pathways before entering the DRG proper (Fig. 2, O to P, and fig. S5, G to N). The elimination of *EphA3* and *EphA4* from axial motor neurons thus resulted in the extensive intermingling of motor and sensory projections within proximal peripheral nerves (Fig. 2, Q to T), yet this did not lead to defasciculation outside peripheral nerve pathways (Fig. 2P and fig. S5, E to I). In contrast, distal nerve segments supplied by nonaxial motor columns innervating thorax and limb muscles maintained largely normal motor-sensory intranerve patterns (fig. S6, I to Z). Thus, with decreasing EphA receptor activity, axial motor axons become progressively capable of invading proximal sensory pathways.

Spinal motor neurons are embedded within local neural circuitries that determine stereotypic patterns of activity (*23*, *24*), raising the question of whether ectopic motor projections sustained within sensory pathways would display normal activity patterns (fig. S7, D and E). To address this, we performed electrophysiological recordings from DRs and VRs in perinatal *EphA3/EphA4*-deficient and control animals. In these preparations, central pattern generator (CPG)–driven rhythmic motor activity was pharmacologically evoked and recorded with extracellular suction electrodes from lumbar VRs (Fig. 3, A to C, and fig. S7, A and B) (*25*). We reasoned that ectopic activity coupled to CPG-driven locomotor patterns, such as derived from MMCm neurons (*26*), would be detectable through recordings from DR central afferents (fig. S6, A and B).

EphA3/EphA4-deficient lumbar (L2) VRs displayed typical periodic activity bursts, reflecting CPG-coupled locomotor activity (Fig. 3, A to C) (*23*–*25*). In contrast, the activity recorded from DRs of WT and *EphA3/EphA4* single or double heterozygous animals was irregular, small in amplitude, and did not display significant rhythmicity (Fig. 3, A and F). This suggests that the normal segregation of proximal motor-sensory pathways effectively isolates the DR from exhibiting detectable locomotor activity. Even so, DRs of *EphA3/EphA4* double-null mutants showed strong amplitude activity bursts mirroring the rhythmicity of VR-derived motor activity (Fig. 3, C and F, and fig. S6C). Recordings performed on $EphA3^{+/-}$;$EphA4^{-/-}$ DRs frequently revealed similar, albeit weaker and less regular, locomotor-like activity bursts (Fig. 4, B and F), consistent with the *EphA3/EphA4*-dose dependency of motor-sensory miswiring (Fig. 3, D to E, and fig. S5, A to F). Loss of *EphA3/EphA4* thus erodes the normal segregation pattern between axial motor neurons and DRG sensory neurons and results in MMCm projections within afferent pathways that maintain their functional coupling with spinal locomotor circuits.

The drastic proximal motor-sensory miswiring in *EphA3/EphA4* mutants suggests that these effects were due to a loss of trans-axonal ephrin-A → EphA signaling. To test this, we analyzed the impact of *EphA3/EphA4* elimination on the sensitivity of axial motor neurons toward increasing doses of exogenous recombinant ephrin-A protein in vitro (Fig. 4, A to E; fig. S2, A to E; and movie S4) (*20*). In this assay, *EphA3/EphA4*-deficient MMCm axons displayed a complete loss of sensitivity toward ephrin-A–induced growth-cone collapse (Fig. 4A). We next tested whether elimination of sensitivity toward ephrin-As would translate into a loss of motor growth-cone responsiveness toward repulsion by sensory axons. To this end, MMCm explants derived from $EphA3^{-/-}$;$EphA4^{-/-}$;*Hb9::eGFP* or control embryos were co-cultured with stage-matched WT DRGs (Fig. 4, F to K). In this assay, *EphA3/EphA4*-deficient axial motor axons crossed over and intermingled with sensory trajectories that, in the control, were marked by two discrete sheets of parallel motor and sensory projections (Fig. 4, F to G, I, and J). Moreover, *EphA3/EphA4*-deficient motor axons frequently invaded co-cultured DRGs, mirroring motor-sensory misrouting defects in $EphA3^{-/-}$;$EphA4^{-/-}$ mutants in situ (Fig. 4, H and L). We further addressed whether cell-autonomous EphA-mediated activity is required in motor axons, or if some of the observed effects were due to non-cell–autonomous and/or pleiotrophic requirements, such as proper sensory neuron maturation. To investigate this, we co-cultured MMCm explants derived from WT embryos with DRGs derived from stage-matched *EphA3/EphA4*-deficient embryos. In these experiments, co-cultured motor and sensory projections organized into mutually exclusive parallel trajectories, demonstrating that *EphA3/EphA4* elimination does not affect the ability of DRG sensory axons to repel WT motor axons (Fig. 4, I to K and L). The loss of motor axonal EphA receptors thus leads to severely reduced sensitivity toward repulsion by sensory axons (Fig. 4L), consistent with an ephrin-A → EphA–mediated repulsive signaling event that normally operates between adjacent axial motor axons and sensory projections.

Assembly of complex circuitries generating meaningful homeostatic, behavioral, or cognitive outputs necessarily entails the formation of concisely delineated neural pathways (*27*). This is highlighted by conditions abolishing segregation of normally discrete axonal pathways, including nerve injury–induced neuropathic pain (*28*). The present study provides evidence that, during neuromuscular circuit assembly, repulsive trans-axonal ephrin-A → EphA signaling contributes to the establishment of discrete peripheral afferent and efferent pathways. These interactions act at the level of newly extending axial motor growth cones and sensory neurites, effectively blocking efferent access to proximal afferent pathways. Our findings suggest that the heterotypic motor-sensory segregation diverges between axial and nonaxial motor neuron classes at two levels: (i) first, by means of relative outgrowth order favoring direct motor-sensory growth-cone encounter for late-extending axial over earlier nonaxial projections and (ii) second, through differential reliance on ephrin-A/EphA-dependent and -independent mechanisms. The mechanistic basis for the orderly segregation of nonaxial motor-sensory components remains to be identified. Apart from mechanisms driving axon targeting and synaptogensis, the finely tuned coordination between coextending, yet functionally distinct projection types may thus emerge as a key feature in the assembly of neural circuits in general.

References and Notes

1. L. T. Landmesser, *Int. J. Dev. Neurosci.* **19**, 175 (2001).
2. H. H. Chen, S. Hippenmeyer, S. Arber, E. Frank, *Curr. Opin. Neurobiol.* **13**, 96 (2003).
3. M. G. Honig, P. A. Frase, S. J. Camilli, *Development* **125**, 995 (1998).
4. L. Landmesser, M. G. Honig, *Dev. Biol.* **118**, 511 (1986).
5. L. Luo, J. G. Flanagan, *Neuron* **56**, 284 (2007).
6. P. Feinstein, P. Mombaerts, *Cell* **117**, 817 (2004).
7. A. Brown *et al.*, *Cell* **102**, 77 (2000).
8. J. Tang, U. Rutishauser, L. Landmesser, *Neuron* **13**, 405 (1994).
9. M. G. Honig, U. S. Rutishauser, *Dev. Biol.* **175**, 325 (1996).
10. K. W. Tosney, M. S. Hageman, *J. Exp. Zool.* **251**, 232 (1989).
11. G. Wang, S. A. Scott, *Dev. Biol.* **208**, 324 (1999).
12. Materials and methods are available as supporting material on *Science* Online.
13. S. K. Lee, L. W. Jurata, J. Funahashi, E. C. Ruiz, S. L. Pfaff, *Development* **131**, 3295 (2004).
14. L. A. Quina *et al.*, *J. Neurosci.* **25**, 11595 (2005).
15. Z. Dong *et al.*, *J. Neurosci. Res.* **56**, 334 (1999).
16. R. Shirasaki, J. W. Lewcock, K. Lettieri, S. L. Pfaff, *Neuron* **50**, 841 (2006).
17. H. Iwamasa *et al.*, *Dev. Growth Differ.* **41**, 685 (1999).
18. A. Valdya, A. Pnlak, G. Lemke, A. Brown, *Mol. Cell. Biol.* **23**, 8092 (2003).
19. R. Klein, *Curr. Opin. Cell Biol.* **16**, 580 (2004).
20. T. Marquardt *et al.*, *Cell* **121**, 127 (2005).
21. F. Helmbacher, S. Schneider-Maunoury, P. Topilko, L. Tiret, P. Charnay, *Development* **127**, 3313 (2000).
22. E. R. Kramer *et al.*, *Neuron* **50**, 35 (2006).
23. M. Goulding, S. L. Pfaff, *Curr. Opin. Neurobiol.* **15**, 14 (2005).
24. O. Kiehn, *Annu. Rev. Neurosci.* **29**, 279 (2006).
25. C. P. Myers *et al.*, *Neuron* **46**, 37 (2005).
26. A. Groenbergen, H. C. Geisler, H. Tashkenta, L. A. van Eykern, *Brain Res. Dev. Brain Res.* **112**, 217 (1999).
27. J. C. Eccles, *Appl. Neurophysiol.* **44**, 5 (1981).
28. E. M. McLachlan, W. Janig, M. Devor, M. Michaelis, *Nature* **363**, 543 (1993).

29. We thank K. Lettieri and A. Klusowski for outstanding technical assistance. E. Turner for sharing *Brn3a::tauLacZ* mice, and M. Goulding and A. Boyd for *EphA4* mice. T.M. was supported by the Deutsche Forschungsgemeinschaft Emmy Noether Program and Pioneer Foundation Awards. G.L. and S.L.P. were supported by National Institute of Neurological Disorders and Stroke grants NS031249-14A1 and NS054172-01A2.

Supporting Online Material

www.sciencemag.org/cgi/content/full/320/5873/233/DC1
Materials and Methods
Figs. S1 to S7
Table S1
References
Movies S1 to S4

4 December 2007; accepted 25 February 2008
10.1126/science.1153758

Convergence of *Campylobacter* Species: Implications for Bacterial Evolution

Samuel K. Sheppard, Noel D. McCarthy, Daniel Falush,*† Martin C. J. Maiden†

The nature of species boundaries in bacteria remains controversial. In particular, the mechanisms of bacterial speciation and maintenance in the face of frequent genetic exchange are poorly understood. Here, we report patterns of genetic exchange that show two closely related zoonotic pathogenic species, *Campylobacter jejuni* and *Campylobacter coli*, are converging as a consequence of recent changes in gene flow. Population expansion into a novel ecological niche generated by human activity is the most probable explanation for the increase in genetic exchange between these species. Bacterial speciation can therefore occur by mechanisms analogous to those seen in metazoans, where genetic diversification and incipient speciation caused by ecological factors have been reported in several genera.

The dynamic nature of bacterial gene pools, especially the mobility of bacterial genes among unrelated groups (*1*), has complicated the development of a coherent species concept for these organisms (*2*). Biological speciation requires barriers to gene flow (*3*), and in the bacteria, this can occur as a consequence of a single clone expanding into a niche and becoming isolated from its parent population, for example, in the evolution of pathogens, such as *Yersinia pestis* (*4*) and *Salmonella typhi* (*5*), from ancestral hosts into human beings. In the absence of ecological isolation, we might expect that observed levels of genetic exchange should prevent the divergence of bacterial subpopulations (*6*–*9*). Although there are several ways in which gene flow can be limited (*10*), there is little evidence as to which of these have resulted in the evolution of particular bacterial species. Here, we demonstrate convergence of the zoonotic pathogens *Campylobacter jejuni* and *C. coli*, driven by changes in their ecology.

Campylobacter jejuni and *C. coli*, the most common bacterial causes of human gastroenteritis worldwide (*11*, *12*), are recognized as distinct microbiological species. Their housekeeping genes share 86.5% nucleotide sequence identity (*13*), a level similar to that observed between the well-studied enteric bacteria *Salmonella enterica* and *Escherichia coli*, which are thought to have diverged 120 million years ago (*14*). *Campylobacter* species have a broad host range and are present in the gastrointestinal tracts and feces of many birds (*15*) and mammals (*16*). Both *C. jejuni* and *C. coli* can also be isolated from a wide variety of environmental sources, presumably as a consequence of fecal contamination (*17*), and there is evidence of genetic exchange within and between these two species (*18*, *19*). As part of ongoing efforts to elucidate the epidemiology of human campylobacteriosis, isolates from diverse sources and multiple geographic locations have been characterized by the same seven-locus multilocus sequence typing (MLST) scheme (*19*, *20*). There is an extensive archive of these data available from the *C. jejuni* and *C. coli* PubMLST database (http://pubmlst.org/campylobacter), which contains allelic profiles based on the nucleotide sequences of seven housekeeping gene fragments (MLST alleles) (*20*). These profiles are assigned to sequence types (STs). Here, we analyze 2953 distinct STs either directly or as haplotypes of 3309 base pairs in length, generated by combining the seven allele sequences corresponding to each ST (*21*).

The distinct nature of *C. jejuni* and *C. coli* was demonstrated by the clustering of the haplotypes into two main groups corresponding to the microbiological species designations. Although some haplotypes did occupy intermediate positions in a neighbor-joining tree (Fig. 1A), these had alleles at the seven loci that could each be clearly assigned to one species or other, which indicated that the haplotypes were hybrids generated by interspecies gene exchange (*19*). A more formal species assignment was performed with the linkage model of the Bayesian clustering algorithm STRUCTURE (*22*, *23*), with a threshold probability of 0.75 used as the cut-off for membership of a particular ST in each species. According to this criterion, 2221 (75.2%) of the STs were assigned to *C. jejuni* and 715 (24.2%) to *C. coli*; only 17 STs (0.6%, triangles in Fig. 1A) could not be assigned to a species in this way. A total of 79 (11%) of the *C. coli* STs exhibited *C. jejuni* ancestry, >1%, whereas only 15 (0.6%) of the *C. jejuni* STs exhibited any *C. coli* ancestry; these findings provide evidence for asymmetric gene flow between these populations.

Structuring within the *C. coli* population, not apparent from the cluster analysis (Fig. 1A), was evident from a genealogical analysis of the derived *C. coli* haplotypes with CLONALFRAME (*24*) (Fig. 1B), a model-based approach that estimates clonal relations while accounting for the fact that a single import can change multiple nucleotides at once. This indicated the division of *C. coli* into three subclades, which was supported by cluster analysis of the seven housekeeping genes individually (Fig. 1C). All but 26 (3.6%) of the 715 *C. coli* haplotypes could be assigned to one of the three clades (clades 1 to 3) in the genealogy, of which clade 1 was the largest and most diverse in this data set (Fig. 1B). Combining these data enabled the assignment of each ST to a given clade and the assignment of individual alleles to a clade of origin, independent of the clade assignment of the corresponding ST (Fig. 1, B and C).

Asymmetric gene flow was apparent among *C. jejuni* and *C. coli* clades 1, 2, and 3 (Table 1 and table S1); most gene flow involved *C. coli* clade 1, which had imported *C. jejuni* alleles at every locus on multiple occasions. A high proportion (18.6%, 54 out of 290) of the alleles in hybrids assigned to *C. coli* clade 1 originated in *C. jejuni*. Clade 1 also had the highest frequency of alleles originating in the other two *C. coli* clades, although the numbers were small. There was also evidence that clade 1 was a more frequent donor, at least to *C. jejuni*, with 25 of the 27 imported *C. coli* alleles arising from clade 1, which indicated a substantially elevated, although still low, rate of import compared with that observed from the other *C. coli* clades (Table 1 and table S1).

The rate of import of *C. jejuni* alleles by *C. coli* must have changed, subsequent to the divergence of the three clades from their shared common ancestor, with several lines of evidence indicating that the low rates seen for *C. coli* clades 2 and 3 were closer to historical levels than the high rates estimated for clade 1. First, because clade 1 and clade 2 are sister taxa (Fig. 1B), a change in rates of import for clade 1 is a more parsimonious explanation than changes for both clades 2 and 3. Second, there were short but similar branch lengths observed for each of the seven MLST loci between the predominant sequence clusters of the three clades (Fig. 1C). This pattern was consistent, with divergence occurring progressively by point mutation rather than abruptly by genetic import from a foreign source. Third, most (49 out of 50) of the alleles assigned a *C. jejuni* origin, but found in *C. coli*, were identical to alleles present in *C. jejuni*, which showed that they have not mutated since being acquired by *C. coli*. Finally, an ongoing process of recombination would be expected to fragment imported DNA progressively and to lead to the creation of hybrid alleles. Hybrid alleles were much less common than *C. jejuni* alleles in *C. coli* clade 1; they were observed at only three of the seven loci, namely, *tkt*, *aspA*, and *glyA* (Fig. 1C). In conclusion, the high rates of import into *C. coli* clade 1 represent a recent change from historical patterns of gene flow.

Quantitative analysis of these recent events showed that the genetic changes leading to the convergence of *C. coli* clade 1 with *C. jejuni* occurred at least four times more frequently than those leading to their divergence (*21*). If maintained over time, these relative rates would lead to progressive genetic convergence unless countered by strong genome-wide natural selection against *C. jejuni* nucleotide sequence in *C. coli*.

Departments of Zoology and Statistics, University of Oxford, Peter Medawar Building, South Parks Road, Oxford OX1 3SY, UK.

*Present address: Environmental Research Institute, University College Cork, Lee Road, Cork, Ireland.

†To whom correspondence should be addressed. E-mail: d.falush@ucc.ie (D.F.); martin.maiden@zoo.ox.ac.uk (M.C.J.M.)

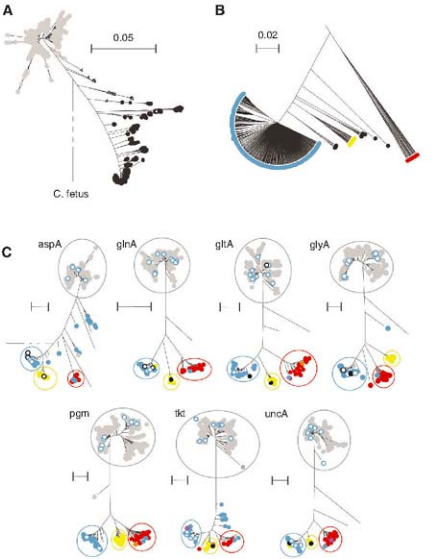

Fig. 1. Relations among haplotypes and alleles derived from STs from the *C. jejuni* and *C. coli* pubMLST database. **(A)** Neighbor-joining tree of the 2953 *C. jejuni* and *C. coli* haplotypes (concatenated MLST alleles) rooted with a *C. fetus* sequence. Isolates belonging to *C. jejuni* are shown in gray and those belonging to *C. coli* in black. Haplotypes that could not be assigned to a species are shown as open triangles. **(B)** CLONALFRAME genealogy generated from the *C. coli* haplotypes. Clade 1 haplotypes are indicated in blue, clade 2 in yellow, and clade 3 in red. **(C)** Neighbor-joining trees of individual gene sequences. The species and clade to which the haplotype containing each allele is assigned are indicated by color: gray, *C. jejuni*; blue, *C. coli* clade 1; yellow, *C. coli* clade 2; and red, *C. coli* clade 3. Open circles represent alleles that are found in *C. coli* and *C. jejuni*. Alleles found in more than one *C. coli* clade are indicated by the following colors: clades 1 and 2, black; clades 2 and 3, orange; and clades 1 and 3, purple. The colored circles show the boundaries used to assign alleles to a likely origin. For each tree, the scale bar represents a genetic distance of 0.02.

Table 1. The predicted origin of alleles is given for haplotypes assigned to *C. jejuni* and *C. coli* clades 1 to 3. Assignment of haplotypes to *C. jejuni* or *C. coli* was on the basis of the STRUCTURE analysis, and the three clades of *C. coli* were defined by the CLONALFRAME genealogy. Individual alleles were assigned to a predicted source on the basis of the neighbor-joining trees for each allele (Fig. 1).

Likely origin	Percentage of distinct alleles (total number of alleles)			
	C. jejuni (1218)	*C. coli* clade 1 (290)	*C. coli* clade 2 (82)	*C. coli* clade 3 (131)
C. jejuni	97.7	18.6	1.2	0.8
C. coli clade 1	2.1	75.9	12.2	0.8
C. coli clade 2	0.1	1.7	84.4	0.8
C. coli clade 3	0.1	3.8	2.4	97.7

There are several ways in which barriers to genetic exchange among bacterial populations, sufficient to cause speciation, could arise. These can be divided into three categories: mechanistic, ecological, and adaptive. Mechanistic barriers could be imposed by dependence on homologous recombination (*10*) or by other factors promoting DNA specificity (*25*), such as restriction and/or modification systems. Ecological barriers are a consequence of physical separation of bacterial populations, resulting from the occupation of distinct niches, whereas adaptive mechanisms imply selection against hybrid genotypes (*26*). We have shown that there has been a recent, bidirectional increase in the rate of recombination between *C. jejuni* and *C. coli* and a concomitant reversal of the speciation process. One of the three clades of *C. coli* is more affected by this increase in recombination than the others. This asymmetry cannot be easily explained by a mechanistic barrier but could be the result of the proliferation of this clade in an environment where *C. jejuni* dominates numerically. *C. jejuni* and *C. coli* display some host specificity and dominate in, for example, wild birds (*15*) and pigs (*16*), respectively; however, there is appreciable niche overlap. Both species are frequently isolated from chickens and cattle, in which they are provided opportunities for genetic exchange (*17*). Taken together, these observations suggest that ecological, and possibly adaptive, factors historically prevented gene flow between the two species and that an ecological change has disrupted this barrier and has led to a process whereby the two species are merging or "despeciating" (Fig. 2).

C. jejuni isolated from the intestinal tracts of different animal species have differentiated gene pools of MLST alleles that allow probabilistic assignment of alleles to host (*27*). We found that alleles imported from *C. jejuni* by *C. coli* were indistinguishable from *C. jejuni* alleles taken from agricultural sources (ruminants and poultry), but distinct from those found either in the environment or wild birds (*21*). Agriculture represents a highly plausible novel environment within which the two species could have been brought together. However, wider sampling, particularly of *C. coli* from natural environments, will be needed to confirm this hypothesis.

The interaction of two distinct bacterial species, *C. coli* and *C. jejuni*, has provided an opportunity to observe evolution by hybridization as it is occurring. The despeciation process that we have identified appears to be a consequence of ecological factors. This mechanism is analogous to that observed in sexual eukaryotic populations, such as Darwin's Finches, where incipient species are associated with distinct niches (*28*), and this process can be reversed through hybridization when selection pressures change (*29*). Humans continue to cause rapid and extensive environmental change. Preexisting environments have been degraded, and novel ones, such as intensive farms or acid mine drainage areas, have been created that provide a new adaptive landscape and opportunities for hybrid forms to

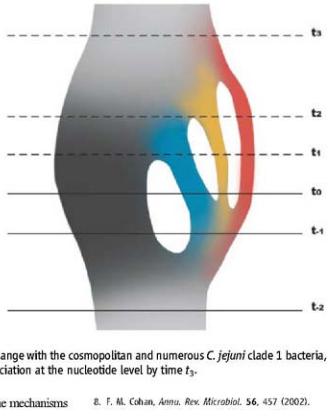

Fig. 2. An illustration of the genetic divergence and a scenario for despeciation of *C. jejuni* (gray) and *C. coli* clades 1 (blue), 2 (yellow), and 3 (red). Between time t_{-2} and t_{-1}, campylobacter split into two separate species, *C. jejuni* and *C. coli*. Between t_{-1} and the present (t_0), *C. coli* further separated into three distinct lineages representing incipient species. At t_0 *C. coli* clade 1 starts to accumulate genetic material imported from *C. jejuni*, owing to expansion into a novel agricultural niche. By t_1, recombination has been sufficient to make strains with a clade 1 clonal origin indistinguishable from *C. jejuni*. A more speculative projection would be that the change in environmental conditions could also have a substantial effect on clade 2 and clade 3 strains, with an elevated rate of exchange with the cosmopolitan and numerous *C. jejuni* clade 1 bacteria, which could lead to complete despeciation at the nucleotide level by time t_3.

evolve (*29*–*31*). By understanding the mechanisms of microbial evolution, we can hope to mitigate some of the harmful consequences of both environmental change and the biotic response to it.

References and Notes

1. H. P. Narra, H. Ochman, *Curr. Biol.* **16**, R705 (2006).
2. D. Gevers *et al.*, *Nat. Rev. Microbiol.* **3**, 733 (2005).
3. J. G. Lawrence, *Theor. Popul. Biol.* **61**, 449 (2002).
4. M. Achtman *et al.*, *Proc. Natl. Acad. Sci. U.S.A.* **101**, 17837 (2004).
5. P. Roumagnac *et al.*, *Science* **314**, 1301 (2006).
6. S. Gupta, M. C. J. Maiden, *Trends Microbiol.* **9**, 181 (2001).
7. D. Falush *et al.*, *Philos. Trans. R. Soc. London B Biol. Sci.* **361**, 2045 (2006).
8. F. M. Cohan, *Annu. Rev. Microbiol.* **56**, 457 (2002).
9. W. P. Hanage, B. G. Spratt, K. M. Turner, C. Fraser, *Philos. Trans. R. Soc. London B Biol. Sci.* **361**, 2039 (2006).
10. C. Fraser, W. P. Hanage, B. G. Spratt, *Science* **315**, 476 (2007).
11. A. O. Coker, R. D. Isokpehi, B. N. Thomas, K. O. Amisu, C. L. Obi, *Emerg. Infect. Dis.* **8**, 237 (2002).
12. M. C. Samuel *et al.*, *Clin. Infect. Dis.* **38** (suppl. 3), S165 (2004).
13. K. E. Dingle, M. C. Maiden, in *Campylobacter Molecular and Cellular Biology*, J. M. Ketley, M. E. Konkel, Eds. (Horizon Bioscience, Wymondham, Norfolk, UK, 2005), pp. 43–58.
14. H. Ochman, E. A. Groisman, *EXS* **69**, 479 (1994).
15. J. Waldenstrom *et al.*, *Appl. Environ. Microbiol.* **68**, 5911 (2002).
16. O. Rosef, B. Gondrosen, G. Kapperud, B. Underdal, *Appl. Environ. Microbiol.* **46**, 855 (1983).
17. S. A. Bull *et al.*, *Appl. Environ. Microbiol.* **72**, 645 (2006).
18. R. J. Meinersmann, K. E. Dingle, M. C. J. Maiden, *Genome Lett.* **2**, 48 (2003).
19. K. E. Dingle, F. M. Colles, D. Falush, M. C. Maiden, *J. Clin. Microbiol.* **43**, 340 (2005).
20. K. E. Dingle *et al.*, *J. Clin. Microbiol.* **39**, 14 (2001).
21. Materials and methods are available as supporting material on *Science* Online.
22. J. K. Pritchard, M. Stephens, P. Donnelly, *Genetics* **155**, 945 (2000).
23. D. Falush, M. Stephens, J. K. Pritchard, *Genetics* **164**, 1567 (2003).
24. X. Didelot, D. Falush, *Genetics* **175**, 1251 (2007).
25. A. K. Eggleston, S. C. West, *Curr. Biol.* **7**, R745 (1997).
26. P. Zhu *et al.*, *Proc. Natl. Acad. Sci. U.S.A.* **98**, 5234 (2001).
27. N. D. McCarthy *et al.*, *Emerg. Infect. Dis.* **13**, 267 (2007).
28. J. Mallet, *Nature* **446**, 279 (2007).
29. P. R. Grant, B. R. Grant, *Science* **256**, 193 (1992).
30. I. Lo *et al.*, *Nature* **446**, 537 (2007).
31. L. H. Rieseberg *et al.*, *Science* **301**, 1211 (2003).

32. K. A. Jolley, M.-S. Chan, M. C. J. Maiden, *BMC Bioinformatics* **5**, 86 (2004).
33. This work was funded by the U.K. Department of Environment, Food, and Rural Affairs (DEFRA, contract numbers OZ0604 and OZ0611) and the Food Standards Agency (contract number B15011). M.C.J.M. is a Wellcome Trust Senior Research Fellow in Basic Biological Sciences. N.D.McC. was funded by a Wellcome Trust Clinical Training Fellowship, and D.F. was funded by a Wellcome Trust Research Career Development Fellowship and is currently funded by the Science Foundation of Ireland. This publication made use of the *Campylobacter jejuni* Multi Locus Sequence Typing Web site (http://pubmlst.org/campylobacter/) developed by K. Jolley and M.-S. Chan and sited at the University of Oxford (*32*). The development of this site has been funded by the Wellcome Trust and DEFRA.

Supporting Online Material

www.sciencemag.org/cgi/content/full/320/5873/237/DC1
Materials and Methods
Fig. S1
Table S1
References

22 January 2008; accepted 11 March 2008
10.1126/science.1155532

Leiomodin Is an Actin Filament Nucleator in Muscle Cells

David Chereau,[1]*† Malgorzata Boczkowska,[2]† Aneta Skwarek-Maruszewska,[3] Ikuko Fujiwara,[4] David B. Hayes,[1] Grzegorz Rebowski,[2] Pekka Lappalainen,[3] Thomas D. Pollard,[4] Roberto Dominguez[2]‡

Initiation of actin polymerization in cells requires nucleation factors. Here we describe an actin-binding protein, leiomodin, that acted as a strong filament nucleator in muscle cells. Leiomodin shared two actin-binding sites with the filament pointed end–capping protein tropomodulin: a flexible N-terminal region and a leucine-rich repeat domain. Leiomodin also contained a C-terminal extension of 150 residues. The smallest fragment with strong nucleation activity included the leucine-rich repeat and C-terminal extension. The N-terminal region enhanced the nucleation activity threefold and recruited tropomyosin, which weakly stimulated nucleation and mediated localization of leiomodin to the middle of muscle sarcomeres. Knocking down leiomodin severely compromised sarcomere assembly in cultured muscle cells, which suggests a role for leiomodin in the nucleation of tropomyosin-decorated filaments in muscles.

Actin-binding proteins suppress the spontaneous nucleation of actin monomers into filaments, so cells use nucleation factors to initiate actin polymerization. In non-muscle cells, the best-characterized filament nucleators are actin-related protein 2 and 3 (Arp2/3) complex and formins (*1*). Less is known about the initiation of actin filaments in striated and smooth muscle cells, where specialized proteins may be used to assemble and remodel the tropomyosin-decorated filaments.

We identified the protein leiomodin (Lmod) as a potential filament nucleator in muscle cells because sequence analysis suggested that it contained at least three actin-binding sites and could possibly recruit three actin monomers to form a polymerization nucleus. Thus, the first ~340 residues of Lmod are ~40% identical to tropomodulin (Tmod) (fig. S1), a protein that caps actin filament pointed ends (*2*, *3*). The N-terminal portion of Tmod is unstructured, except for three helical segments involved in binding tropomyosin (residues 24 to 35 and 126 to 135) and actin (residues 65 to 75) (*4*). This region of Tmod caps the pointed end of actin filaments in a tropomyosin-dependent manner (*5*). Tmod has a second, tropomyosin-independent, actin-binding and -capping site within the C-terminal region (residues 160 to 359) (*5*), consisting almost entirely of a Leu-rich repeat (LRR) domain (*6*). Lmod shares this domain organization but has only one of the two tropomyosin-binding sites (Fig. 1A and fig. S1). More importantly, Lmod extends ~150–amino acids beyond the C terminus of Tmod. This

extension contains a short poly-proline (polyP) region, two segments with a predicted helical structure, and an actin-binding Wiskott–Aldrich syndrome protein (WASP)–homology 2 (WH2) domain.

To localize Lmod in cultured neonatal rat cardiomyocytes, we used fluorescent antibody staining and expression of enhanced green fluorescent protein (EGFP)–Lmod fusion proteins (*7*). Our rabbit polyclonal antibody against wild-type Lmod ($Lmod_{wt}$) reacted specifically with Lmod in extracts of skeletal muscle and did not cross-react with Tmod (fig. S2). In cardiomyocytes, this antibody concentrated close to the M-line protein myomesin, near the center of the sarcomere (Fig. 1B). EGFP-$Lmod_{wt}$ and EGFP-$Lmod_{1-342}$, comprising the Tmod-like portion of Lmod, also concentrated in the middle of sarcomeres, well separated from α-actinin in Z-discs (Fig. 1C). Thus, Lmod is located near the pointed ends of the actin filaments, which were not resolved from M lines. On the other hand, EGFP-$Lmod_{162-495}$, a fragment with strong nucleation activity (see below) that included the LRR and C-terminal extension, concentrated in the nucleus. Thus, the N-terminal domain is required for Lmod localization in the center of sarcomeres.

Strong overexpression of all three EGFP-Lmod constructs disrupted sarcomeric organization and induced the formation of aberrant actin structures (fig. S3). $Lmod_{162-495}$ had the most dramatic phenotype. Even moderate expression of $Lmod_{162-495}$ induced the formation of abnormal actin bundles in the nucleus, similar to those observed in intranuclear rod myopathy (*8*).

We investigated the role of Lmod in sarcomere assembly using RNA interference (RNAi) to knockdown Lmod expression in cardiomyocytes. Cells transfected with Lmod–small interfering RNA (Lmod-siRNA) had drastically lower levels of Lmod protein than control cells (fig. S4). Fluorescent antibody staining for Lmod was strongly reduced in Lmod-siRNA cells (Fig. 2), which also lacked the striated pattern of Lmod observed in control cells transfected with a scrambled oligonucleotide. Lmod knockdown cells lacked organized sarcomeres (Figs. 2 and S5). In Lmod-siRNA cells, the Z-disc protein α-actinin concentrated in small spots, in contrast with the typical striated pattern observed in control cells (fig. S5). Lmod knockdown cells were also less adherent and spread than wild-type cells. Thus, Lmod plays a role in sarcomere assembly and organization.

We studied the effect of Lmod on actin assembly by monitoring the fluorescence increase of 6% pyrene-labeled actin upon polymerization. Nanomolar concentrations of $Lmod_{wt}$ dramatically stimulated polymerization compared with spontaneous actin assembly (Fig. 3A). $Lmod_{1-342}$ was significantly less effective, although more active than Tmod, which has weak nucleation activity (*5*). $Lmod_{162-342}$, comprising the LRR and an additional 14 residues necessary for pointed-end capping in Tmod (*5*), and $Lmod_{343-495}$, corresponding to the C-terminal extension, both had low polymerization-inducing activity. However, the combination of these two constructs in $Lmod_{162-495}$ retained one-third of the activity of $Lmod_{wt}$ (Fig. 3D). Deletions and substitutions in $Lmod_{162-495}$ suggested that each of the modules of the C-terminal extension contributed to this activity; some seemed to bind actin directly, whereas others seemed to help properly position the actin-binding sites for assembly (fig. S6).

To determine whether Lmod promoted assembly by stimulating nucleation or elongation, we observed Lmod-induced actin polymerization directly by total internal reflection fluorescence (TIRF) microscopy. The number of filaments increased exponentially with $Lmod_{wt}$ concentration (Fig. 3, B and C, and movies S1 to S4), whereas $Lmod_{wt}$ had no effect on the elongation rate of either filament end (fig. S7). We obtained similar results with $Lmod_{162-495}$. In agreement with the bulk polymerization assay (fig. S6), constructs with deletions or substitutions of the modules of the C-terminal extension formed fewer filaments than $Lmod_{162-495}$ (Fig. 3B). Thus, Lmod stimulates polymerization by nucleat-

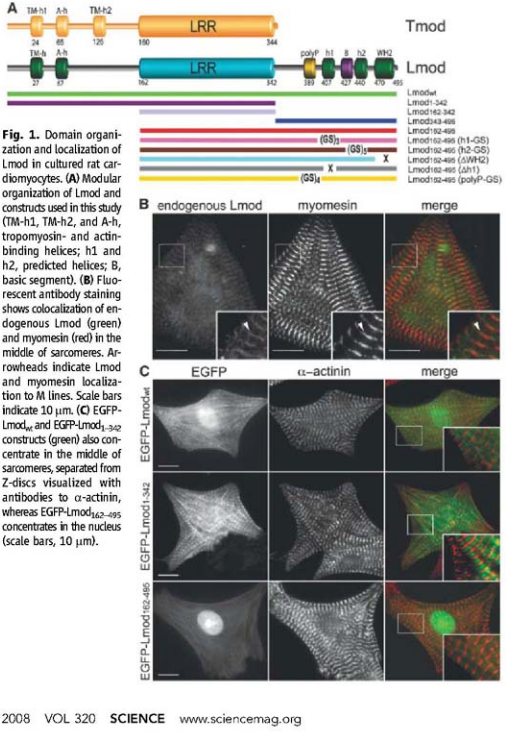

Fig. 1. Domain organization and localization of Lmod in cultured rat cardiomyocytes. **(A)** Modular organization of Lmod and constructs used in this study (TM-h1, TM-h2, and A-h, tropomyosin- and actin-binding helices; h1 and h2, predicted helices; B, basic segment). **(B)** Fluorescent antibody staining shows colocalization of endogenous Lmod (green) and myomesin (red) in the middle of sarcomeres. Arrowheads indicate Lmod and myomesin localization to M lines. Scale bars indicate 10 μm. **(C)** EGFP-$Lmod_{wt}$ and EGFP-$Lmod_{1-342}$ constructs (green) also concentrate in the middle of sarcomeres, separated from Z-discs visualized with antibodies to α-actinin, whereas EGFP-$Lmod_{162-495}$ concentrates in the nucleus (scale bars, 10 μm).

[1]Boston Biomedical Research Institute, Watertown, MA 02472, USA. [2]Department of Physiology, University of Pennsylvania School of Medicine, Philadelphia, PA 19104, USA. [3]Institute of Biotechnology, University of Helsinki, 00014 Helsinki, Finland. [4]Department of Molecular, Cellular, and Developmental Biology, Yale University, New Haven, CT 06520, USA.

*Present address: Elan Pharmaceuticals, San Francisco, CA 94080, USA.

†These authors contributed equally to this work.

‡To whom correspondence should be addressed. E-mail: droberts@mail.med.upenn.edu

ing filaments rather than increasing their elongation rates.

From the time course of polymerization (Fig. 3A and fig. S6) and the elongation rates established by TIRF (fig. S7), we determined that 2 μM actin formed 3.4 nM barbed ends per minute in the presence of 25 nM $Lmod_{wt}$ (Fig. 3D). This high nucleation rate is comparable to that of Arp2/3 complex (*9*). $Lmod_{162\ 495}$ retained one-third of this activity (Fig. 3D).

We tested the effect of tropomyosin on polymerization induced by $Lmod_{wt}$ and $Lmod_{162\ 495}$, which lacks the tropomyosin-binding site (fig. S1). All concentrations of tropomyosin inhibited polymerization by $Lmod_{162\ 495}$ (Fig. 4A). In contrast, polymerization by $Lmod_{wt}$ was stimulated at low tropomyosin concentrations but inhibited at tropomyosin concentrations higher than 1 μM. This biphasic effect of tropomyosin can be explained by two opposite mechanisms: Tropomyosin weakly promotes nucleation by $Lmod_{wt}$ but reduces the formation of ends via spontaneous fragmentation (*10*). At 1 μM concentration, tropomyosin promoted polymerization of 2 μM actin with a range of concentrations of $Lmod_{wt}$ and $Lmod_{1\ 342}$, but not Tmod, all of which were expected to bind tropomyosin (Fig. 4B). This stimulatory effect of tropomyosin on Lmod-induced nucleation occurred within a physiologically relevant range, because the ratio of tropomyosin to actin in muscle thin filaments is 1:7.

The C-terminal extension of Lmod contains a short polyP sequence, a potential binding site for profilin (fig. S1). However, profilin inhibited to the same extent polymerization induced by $Lmod_{162\ 495}$ and a construct in which the polyP sequence was replaced by a glycine-serine repeat, $Lmod_{162\ 495}$ (polyP-GS) (fig. S8). Thus, profilin does not seem to play a role in filament nucleation by Lmod.

We used sedimentation velocity to determine the stoichiometry of the Lmod-actin polymerization nucleus (fig. S9). We included latrunculin B (LatB) in the buffer to prevent polymerization. Separately, actin-LatB and Lmod constructs $Lmod_{wt}$, $Lmod_{162\ 495}$, and $Lmod_{1\ 342}$ were each monomeric and soluble (fig. S9). Complexes of $Lmod_{wt}$ with actin formed a reaction boundary (multiple species) around 12*S*, whose stoichiometry could not be determined by fitting. Mixtures of $Lmod_{1\ 342}$ with actin formed reaction boundaries around 3.5*S* (corresponding to actin-LatB) and 6.5*S* (Fig. 4C). The predominant

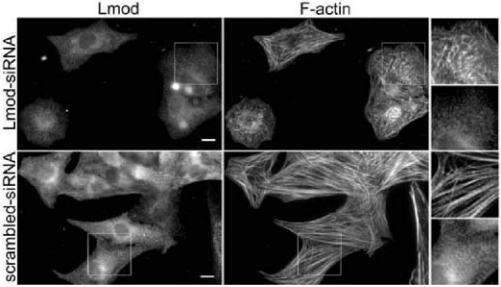

Fig. 2. Lmod knockdown disrupts sarcomere assembly in rat cardiomyocytes. Lmod antibody staining is reduced and the striated Lmod pattern is lost in cardiomyocytes transfected with Lmod-specific siRNA as compared with control cells (transfected with scrambled-siRNA). The micrographs of Alexa 568-phalloidin show that sarcomeric actin structures are severely disorganized in knockdown cells (scale bars, 10 μm).

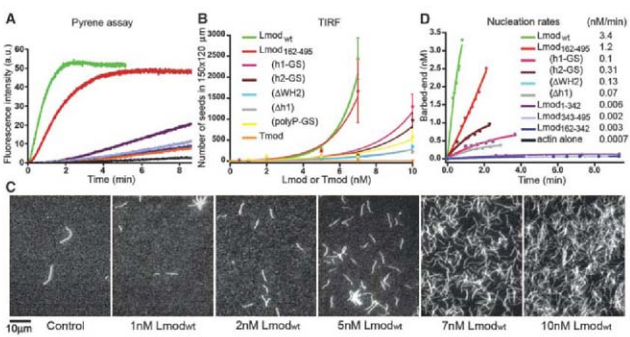

Fig. 3. Lmod nucleates actin filaments. (**A**) Time course of fluorescence increase upon polymerization of 2-μM Mg–adenosine 5′-triphosphate (ATP)–actin (6% pyrene-labeled) alone (black) or with 25-nM Lmod constructs (colored according to Fig. 1A) in polymerization buffer [10 mM Tris pH 7.5, 1 mM $MgCl_2$, 50 mM KCl, 1 mM EGTA, 0.1 mM NaN_3, 0.02 mg/ml bovine serum albumin, 0.2 mM ATP]. (**B**) Number of barbed ends formed after 4 min of polymerization with varying Lmod concentration measured by TIRF. For each construct, the average number of actin seeds was measured from 20 images (150 μm by 120 μm). Data reported are mean ± SD. (**C**) TIRF micrographs of fields of actin filaments prepared 4 min after initiating of polymerization of 1 μM Mg-ATP-actin with a range of $Lmod_{wt}$ concentrations. (**D**) Time course of barbed-end formation in the presence of Lmod constructs calculated from the polymerization rate, concentration of actin monomers remaining, and rate constant for barbed-end elongation (10 $\mu M^{-1}\ s^{-1}$) (fig. S7A). The table gives the nucleation rates.

species in the second peak was a 2:1 complex of actin:$Lmod_{1\text{–}342}$. Mixtures of $Lmod_{162\text{–}495}$ with actin-LatB precipitated. However, by quantitating the proteins in the supernatant using the interference optics of the ultracentrifuge, we determined the composition of the complexes in the pellets (Fig. 4D). When actin was present in twofold molar excess over $Lmod_{162\text{–}495}$, all of both proteins precipitated, indicating that $Lmod_{162\text{–}495}$ binds two actins. Actin may bind cooperatively to the two sites, because actin:$Lmod_{162\text{–}495}$ pelleted as a 2:1 complex even when $Lmod_{162\text{–}495}$ was present in excess.

$Lmod_{162\text{–}495}$ and $Lmod_{1\text{–}342}$ share one actin-binding site (LRR domain) and each binds two actin subunits, which suggests that full-length Lmod stabilizes a nucleus of three actin subunits, bound to the flexible N-terminal, LRR, and WH2 domains. Information about the affinities of actin for the three binding sites and potential cooperative binding effects will be required to trace the actual nucleation pathway [supporting online material (SOM) text]. Because $Lmod_{162\text{–}495}$ is a strong nucleator, we propose that assembly of the nucleus begins with actin monomers binding to the LRR and WH2 domains, followed by actin binding to the flexible N terminus. The N terminus is also necessary for Lmod localization near the center of sarcomeres, which suggests that Lmod (like Tmod) binds to filament pointed ends, because actin and tropomyosin are the only known binding partners of this region of Lmod. Because of steric hindrance, the WH2 domain may dissociate as the nucleus grows from the barbed end. After nucleation, the outcome of the other interactions of Lmod with actin and tropomyosin are unknown, but these interactions may serve to localize Lmod to actin filament pointed ends near the center of sarcomeres. It is unknown whether Lmod can coexist with Tmod at these sites.

The nucleation mechanism that we propose for Lmod has features in common with nucleation by Arp2/3 complex together with WH2-containing proteins, such as WASP (Fig. 4E). In both cases, a WH2 domain delivers an actin monomer to complete a trimeric seed consisting of three actin subunits (Lmod) or one actin subunit and the Arp2 and Arp3 subunits of Arp2/3 complex. However, Arp2/3 complex depends on an extrinsic WH2 domain, whereas Lmod has an intrinsic WH2 and is active on its own. Arp2/3 complex anchors the pointed end of the

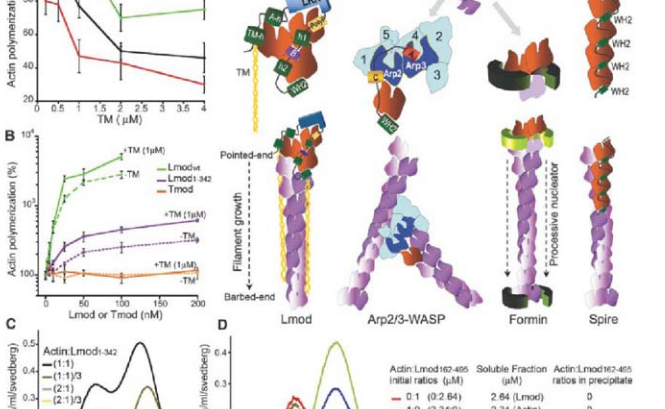

Actin:Lmod$_{162-495}$ initial ratios (μM)	Soluble Fraction (μM)	Actin:Lmod$_{162-495}$ ratios in precipitate
0:1 (0:2.64)	2.64 (Lmod)	0
1:0 (2.34:0)	2.34 (Actin)	0
5:1 (13.2:2.64)	5.02 (Actin)	3.1:1
2:1 (5.28:2.64)	0.00	2.0:1
1:1 (2.64:2.64)	0.90 (Lmod)	1.6:1
1:5 (0.53:2.64)	2.39 (Lmod)	2.1:1

Fig. 4. Mechanism of actin nucleation by Lmod. **(A)** Effect of tropomyosin on the polymerization of 2 μM actin induced by 0.5 μM F-actin seeds, 25 nM $Lmod_{wt}$, or 25 nM $Lmod_{162\text{–}495}$. Rates were determined from the slope of the curves at 50% polymerization and expressed as percentage of the rates without tropomyosin. Data reported are mean ±SD of three or more experiments. **(B)** Polymerization rates of 2 μM actin with increasing concentrations of $Lmod_{wt}$, $Lmod_{1\text{–}342}$, or Tmod in the absence (dashed lines) or the presence (solid lines) of 1 μM tropomyosin. Rates are expressed as percentages of the polymerization rate of actin alone. Data reported are mean ± SD of three or more experiments. **(C)** Sedimentation velocity dilution series of complexes of actin:$Lmod_{1\text{–}342}$ at two different molar ratios. The samples contained 50 μM LatB to prevent polymerization. The first peak corresponds to actin-LatB. The main species in the second peak is a 2:1 actin:$Lmod_{1\text{–}342}$ complex. **(D)** Sedimentation velocity analysis of actin:$Lmod_{162\text{–}495}$ mixed at different ratios (right). In the presence of LatB, actin:$Lmod_{162\text{–}495}$ complexes precipitated. The stoichiometries of the complexes in the precipitate were determined by difference from the amount of actin or $Lmod_{162\text{–}495}$ remaining in solution, using the interference optics of the ultracentrifuge. **(E)** Comparison of models for actin filament nucleation. We propose that Lmod stabilizes a trimeric actin nucleus and that tropomyosin enhances nucleation and mediates the localization of Lmod to filament pointed ends. Arp2 and Arp3 of Arp2/3 complex form a trimeric seed with an actin monomer bound to the WH2 of a nucleation-promoting factor. Formin dimers form nuclei and remain associated with the barbed end of the growing filament. Spire stabilizes a nucleus consisting of four actin subunits along a long-pitch filament strand.

new filament to the side of another filament, whereas Lmod does not form branches. Lmod is also distinct from formins and spire. Formins remain bound to elongating barbed ends after initiating a filament (*1*). Spire is thought to stabilize nuclei by bridging actin subunits along a filament strand (*11*). A unique feature of Lmod is its ability to work in conjunction with tropomyosin, which potentiates its nucleation activity and mediates its localization to the middle of sarcomeres. The strong nucleation activity and severe knockdown phenotype make Lmod a strong candidate to nucleate tropomyosin-decorated actin filaments in muscle sarcomeres.

Reference and Notes

1. T. D. Pollard, *Annu. Rev. Biophys. Biomol. Struct.* **36**, 451 (2007).
2. R. S. Fischer, V. M. Fowler, *Trends Cell Biol.* **13**, 593 (2003).
3. C. A. Conley, K. L. Fritz-Six, A. Almenar-Queralt, V. M. Fowler, *Genomics* **73**, 127 (2001).
4. A. S. Kostyukova, S. E. Hitchcock-Degregori, N. J. Greenfield, *J. Mol. Biol.* **372**, 608 (2007).
5. V. M. Fowler, N. J. Greenfield, J. Moyer, *J. Biol. Chem.* **278**, 40000 (2003).
6. I. Krieger, A. Kostyukova, A. Yamashita, Y. Nitanai, Y. Maeda, *Biophys. J.* **83**, 2716 (2002).
7. Materials and methods are detailed in the supporting material available on *Science* Online.
8. E. Clarkson, C. F. Costa, L. M. Machesky, *J. Pathol.* **204**, 407 (2004).
9. R. E. Mahaffy, T. D. Pollard, *Biophys. J.* **91**, 3519 (2006).
10. S. E. Hitchcock-DeGregori, P. Sampath, T. D. Pollard, *Biochemistry* **27**, 9182 (1988).
11. M. E. Quinlan, J. E. Heuser, E. Kerkhoff, R. D. Mullins, *Nature* **433**, 382 (2005).

12. Supported by NIH grants HL086655, GM073791 and GM026338.

Supporting Online Material

www.sciencemag.org/cgi/content/full/320/5873/239/DC1
Materials and Methods
SOM Text
Figs. S1 to S9
References
Movies S1 to S4

16 January 2008; accepted 19 February 2008
10.1126/science.1155313

Deconstruction of Iterative Multidomain Polyketide Synthase Function

Jason M. Crawford,[1]* Paul M. Thomas,[2] Jonathan R. Scheerer,[1] Anna L. Vagstad,[1] Neil L. Kelleher,[2]† Craig A. Townsend[1]†

PksA, which initiates biosynthesis of the environmental carcinogen aflatoxin B1, is one of the multidomain iterative polyketide synthases (IPKSs), a large, poorly understood family of biosynthetic enzymes. We found that dissection of PksA and its reconstitution from selected sets of domains allows the accumulation and characterization of advanced octaketide intermediates bound to the enzyme, permitting the reactions controlled by individual catalytic domains to be identified. A product template (PT) domain unites with the ketosynthase and thioesterase in this IPKS system to assemble precisely seven malonyl-derived building blocks to a hexanoyl starter unit and mediate a specific cyclization cascade. Because the PT domain is common among nonreducing IPKSs, these mechanistic features should prove to be general for IPKS-catalyzed production of aromatic polyketides.

Tens of thousands of natural products are known from microorganisms, plants, and animals that provide hormones, toxins, flavors and fragrances, pigments, drugs, and other materials of commercial value. A handful of biosynthetic pathways give rise to this rich diversity of useful structures. Among these, polyketides are synthesized from simple acyl–coenzyme A (acyl-CoA) substrates by polyketide synthases (PKSs) (*1*). We understand a great deal about the function of giant modular PKSs that synthesize complex products, for example, the antibiotic erythromycin and the immunosuppressant rapamycin (*2*). Each catalytic domain in these multidomain (type I) megaproteins is used once in an overall "assembly-line" process as a growing intermediate is advanced along the enzyme to yield a product. In contrast to these bacterial systems, in eukaryotes iterative PKSs (IPKSs) are generally the rule where a markedly smaller number of catalytic domains are similarly fused but individually reused in multiple catalytic cycles (iteration) that are "programmed" to yield specific products. How programming is achieved is a central unanswered question of iterative catalysis.

We undertook a "deconstruction" approach by domain dissection and reassembly of PksA, the nonreducing IPKS of aflatoxin biosynthesis, to reveal the global division of labor among the domains in these macromolecular machines to control polyketide chain length, cyclization of an extended poly–β-keto intermediate, and product release. A domain hypothesized to be a "product template" (PT) has been discovered to play a central role in product formation. These studies are combined with high-resolution mass spectrometry (MS) to monitor the highly processive construction of a natural product scaffold from multiple acyl-CoA units directly on a polyketide synthase.

We previously used the UMA bioinformatics algorithm, which identifies linkers in a family of homologous proteins, to characterize the domain architecture of PksA (*3*). Two unrecognized domains were identified in addition to four from

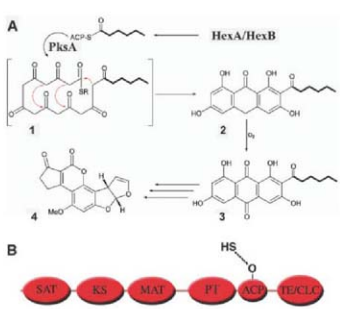

Fig. 1. Aflatoxin B_1 biosynthesis. **(A)** Biosynthetic pathway. PksA accepts a C_6 fatty acid from the associated fatty acid synthase subunits (HexA/HexB) and homologates acetyl units while attached to either the acyl carrier protein (ACP) or ketosynthase (KS) to a fixed chain length (octaketide), as shown in the hypothetical intermediate **1** (shown as the keto form), R = ACP or KS. PksA controls specific cyclization chemistry to release the norsolorinic acid anthrone (**2**), which is autooxidized in vitro to norsolorinic acid (**3**). **3** is processed through a series of oxidative rearrangements to aflatoxin B_1 (**4**). **(B)** Fungal nonreducing PKS domain architecture (PksA). Domains include SAT, KS, malonyl-CoA:ACP transacylase (MAT), PT, ACP, and thioesterase/Claisen cyclase (TE/CLC). Many known and apparently homologous enzymes that share similar domain organization synthesize an assortment of products with alternative chain lengths and cyclization scaffolds (*5*).

[1]Department of Chemistry, Johns Hopkins University, Baltimore, MD 21218, USA. [2]Department of Chemistry, University of Illinois, Urbana, IL 61801, USA.

*Present address: Department of Biological Chemistry and Molecular Pharmacology, Harvard Medical School, 240 Longwood Avenue, Boston, MA 02115, USA.

†To whom correspondence should be addressed. E-mail: ctownsend@jhu.edu (C.A.T.); kelleher@scs.uiuc.edu (N.L.K.)

sequence homology. The first was an unusually long N-terminal domain that was found to be a starter unit–acyl carrier protein (ACP) transacylase (SAT), which selectively transfers a hexanoyl unit onto PksA to initiate polyketide synthesis (*4*, *5*). The second domain is internal, comprising about 350 amino acids, and lies just N-terminal to the acyl carrier protein (ACP, Fig. 1B). Like the SAT, this domain bore minimal primary sequence similarity to any known protein except similarly placed domains in other known and presumed nonreducing IPKSs. The proximity of this domain to the ACP and our hypothesized need for a stabilizing/cyclizing PT domain to control the reactivity of poly–β-keto intermediates such as **1** led us to investigate its possible role in the synthesis of norsolorinic acid (**3**), the first isolable intermediate in the biosynthesis of the environmental carcinogen aflatoxin B_1 (**4**) (Fig. 1A).

To begin dissection of nonreducing IPKS function, we used the cDNA for *pksA* to clone various mono-, di-, and tridomains for combinatorial reconstitution experiments. The protein fragments were expressed in *Escherichia coli* and purified by affinity chromatography as either N- or C-terminal His_6-tag fusions. UMA was used to guide the choice of termini between domains and to accommodate His_6-tag fusions in formerly flexible linker regions to minimize domain-domain interference. To deconstruct the assembly steps of product formation, we independently expressed and purified the ACP, PT, and TE/CLC monodomains; the PT-ACP and ACP-TE/CLC didomains; and the SAT-KS-MAT and PT-ACP-TE/CLC tridomains. The cloned fragments containing the ACP (ACP, PT-ACP, ACP-TE/CLC, or PT-ACP-TE/CLC) were post-translationally modified with a CoA-derived arm in vitro to their active *holo*-forms by means of the promiscuous 4′-phosphopantetheinyltransferase (PPT) Svp (*6*) (fig. S1).

The individual catalytic roles of the domains in PksA were probed by mixing the acyl-CoA substrates (hexanoyl- and malonyl-CoA) with the loading and condensation tridomain (SAT-KS-MAT) and all possible combinations, fused or independent, of the activated *holo*-carrier (ACP) and tailoring domains (PT and TE/CLC). The small-molecule products of the reactions were analyzed by high-performance liquid chromatography (HPLC). Controls lacking the *holo*-ACP (SAT-KS-MAT and SAT-KS-MAT + PT + TE/CLC), which carries the growing polyketide through the catalytic process, exhibited no detectable product output (Fig. 2, experiments 1 and 2). Incubation in the presence of the *holo*-ACP (SAT-KS-MAT + ACP), but lacking the tailoring domains, yielded a minute quantity of the octaketides, norsolorinic acid (**3**) and the shunt product, naphthopyrone **5**. The identity of **5**, oxidized to its corresponding naphthoquinone, was assumed on the basis of its mass identity to its isomer norsolorinic acid (**3**, electrospray ionization MS) and the precedent that inactivation of analogous fungal TE/CLC domains led to the accumulation of pyrone products (*7*). The structure of **5** was proved by comparison to an authentic standard (fig. S2).

The machinery encoding the correct chain length was present in the SAT-KS-MAT + ACP combination alone, although product output was very inefficient. Addition of the TE/CLC domain to this combination of domains reduced the quantity of the naphthopyrone (**5**) and enhanced the ratio of the correctly cyclized norsolorinic acid (**3**), identifying its catalytic role directly in product release through an intramolecular Claisen reaction. Again, product output was low (Fig. 2, experiments 3 to 5). In contrast, addition of the PT domain strongly drove cyclization and dehydration chemistry to form the first two rings, leaving the third and final ring cyclization step unaffected. In the absence of the TE/CLC domain, product release was spontaneous; that is, both the oxygen-carbon (**5**) and carbon-carbon (**2** and **3**) cyclization products were formed (Fig. 2, experiments 6 and 7). Finally, the addition of both tailoring domains, PT and TE/CLC, resulted primarily in the correct cyclization chemistry and release of the norsolorinic acid anthrone (**2**) (Fig. 2, experiments 8 to 11). The anthrone is readily oxidized to the anthraquinone **3** during workup, although this oxidation might be driven enzymatically in vivo, as is known in other fungal pathways (*8*). Although the free-standing domains are able to interact properly and process faithfully wild-type polyketide formation, it is evident that domain fusion enhances catalytic efficiency (Fig. 2, experiments 4 to 11), which likely contributed to the evolutionary pressure to form iterative type I systems in fungi.

The fungal aromatic products resemble bacterial aromatic PKS (type II) products, such as tetracyclines and actinorhodins, which require biosynthetic tailoring steps. Combinations of the type II PKS components revealed that a chain-length factor (CLF) assists the KS in chain-length control (*9*–*11*), but fungal aromatic PKSs lack such domains. Whereas the PksA SAT and MAT (*12*) domains load the ACP with their respective starter and extender units, we demonstrate here that the fungal nonreducing KS domain carries out catalytic responsibilities similar to that of the KS/CLF complex. The initial aldol cyclization product(s), if set by the KS, are intrinsically reversible, but the PT acts to drive the dehydration/aromatization chemistry to irreversibly form rings A and B and to markedly increase the flux to product(s). Alternatively, the

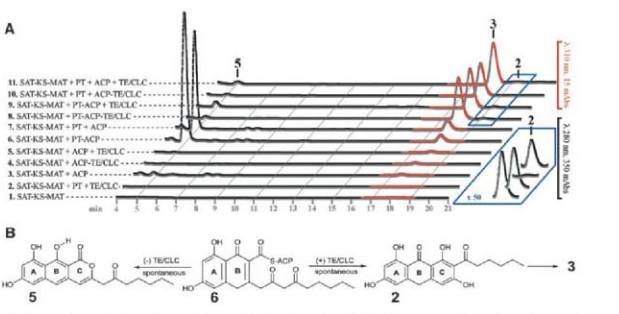

Fig. 2. Metabolite production from two-, three-, and four-part multidomain combinations. (**A**) HPLC analysis. The enzymatic products were extracted into ethyl acetate, dried, and redissolved in dimethyl sulfoxide. The solution was diluted with mobile phase (80/20 acetonitrile, 0.1% aqueous trifluoroacetic acid), and products were separated over a Prodigy octadecyl sulfate 3 column (100 Å, 5 μm, 4.6 × 250 mm; Phenomenex, Torrance, CA). The naphthopyrone **5** and norsolorinic acid anthrone (**2**) were observed at 280 nm, and norsolorinic acid (**3**) was observed at 310 nm. The boxed area at lower right shows the absorption at 280 nm of anthrone **2** amplified (50×). (**B**) Spontaneous versus enzymatic formation of ring C. The putative enzyme-bound intermediate **6** undergoes spontaneous chemistry in the absence of the TE/CLC domain to form the O-C cyclization product **5** or the C-C cyclization products **2** and **3**. Addition of the TE/CLC, however, leads to the correct C-C cyclization products, confirming its role in catalyzing final cyclization and product release. The enzymatic anthrone product **2** auto-oxidizes to the anthraquinone **3**.

KS simply elongates the polyketide chain to a fixed length and the PT disciplines the possible chemical fates of this reactive species to template cyclization and aromatization chemistry to a specific product. Recent results from a related fungal IPKS support this picture and show that heterologous bacterial type II (dissociated) enzymes can intercept these fungal polyketide intermediates and carry out regioselective reactions (*13*).

To examine more closely the polyketide assembly process, we repeated all experiments as time-course studies monitoring the change in ultraviolet (UV)–visible absorption behavior (Fig. 3 and fig. S3). The fully reconstituted PksA (SAT-KS-MAT + PT-ACP-TE/CLC) gave little change in visible absorption over 4 hours. In marked contrast, the same two-part combination, but lacking the TE/CLC domain, rapidly became yellow and displayed a long λ_{max} at 388 nm. By varying the PT-ACP concentration with respect to the SAT-KS-MAT tridomain, the intensity of the chromophore absorption was found to correlate linearly with the PT-ACP concentration (fig. S4). After dialysis to remove small molecules, the absorbing species remained either covalently bound to or tightly associated with the polydomain complex. The accumulation of strongly absorbing species suggested that the TE/CLC operates efficiently to sweep a common intermediate generated by the PT domain through Claisen cyclization to norsolorinic acid (**3**), overriding the accumulation of the 388-nm absorbing species. The synthetic naphthopyrone **5** showed a virtually identical spectral signature under the assay conditions. However, addition of the TE/CLC domain to the SAT-KS-MAT + PT-ACP mixture, after the long-wavelength absorption had reached steady state, only partially reduced this intensity; this finding suggests that the bicyclic acyl intermediate **6** destined for the TE/CLC is contributing to the overall absorbance.

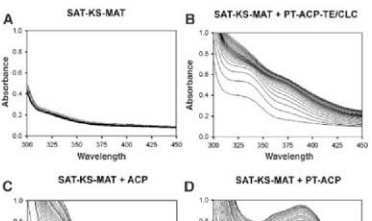

Fig. 3. Chromophore formation. Enzymatic reactions were monitored over 15-min intervals for 240 min by UV-visible spectrophotometry. **(A)** SAT-KS-MAT control. All constructs by themselves similarly showed no change in absorbance. **(B)** Reconstitution of PksA. A 330-nm shoulder appears before reaching steady state in the presence of both tailoring domains (PT and TE/CLC). **(C)** PksA lacking the tailoring domains. Buildup of less highly conjugated chromophore(s) (~330 nm shoulder) occurs. **(D)** Chromophore formation in the presence of the PT domain. A 388-nm long-wavelength maximum from the formation of more highly conjugated chromophore(s) appears. Figure S3 shows spectra for all of the domain combinations, and the chromophore formation is highly similar for the same domain combinations whether they are tethered or not.

Combining the SAT-KS-MAT tridomain with only the *holo*-ACP again gave an intense absorption, but at a considerably shorter wavelength (Fig. 3C), suggesting the formation of less highly conjugated chromophore(s). The intensity of UV-visible absorption was again dependent on ACP concentration. In sum, these experiments support the view that accumulation of ACP-bound intermediate(s) of PksA is modulated by the presence or absence of the PT domain.

To determine the function of the PT domain in the context of a reconstituted system, we combined the SAT-KS-MAT tridomain with the ACP monodomain alone or with the PT-ACP didomain to measure intermediates attached to the ACP by MS. The TE/CLC domain shows broad hydrolytic substrate tolerance for *N*-acetyl cysteamine thioesters, and (in the absence of the correct Claisen substrate) likely serves an editing function. For this reason the TE/CLC domain was not included. Reaction mixtures flash-frozen at 30, 120, and 840 min were thawed and trypsin-digested before analysis by HPLC-MS to determine the nature of the covalent intermediates with part-per-million (ppm) mass accuracy. Figure 4 shows the relative intensities of all observed forms of the acylated tryptic peptides containing the pantetheinylated active-site serine of the ACP domain (all <1.5 ppm and eluting as discrete HPLC peaks) for the incubation of 20 μM PT-ACP or ACP with 5 μM SAT-KS-MAT in the presence of hexanoyl- and malonyl-CoA. For both reactions, the only iteratively extended products detected as phosphopantetheine-tethered intermediates were from the condensation of one hexanoyl starter unit with seven malonyl units (**1**). This product was also seen either singly or

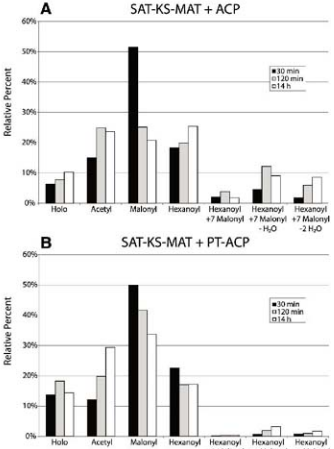

Fig. 4. Iterative intermediates. Relative intensities of acylated peptides from the ACP domain for reactions with the SAT-KS-MAT and either the ACP **(A)** or the PT-ACP **(B)**. Mass spectrometric confirmation for the structure of each species is provided in figs. S5 to S9. Note that these 4-kD peptides bear different acyl intermediates, creating possible intensity biases stemming from differential ionization efficiencies during electrospray.

doubly dehydrated (**6**) while still tethered to the protein. The complex intermediates were confirmed by the observation of each specific phosphopantetheinyl ejection ion within 1.5 ppm (*14*). These phosphopantetheinyl ejection ions were further subjected to ion trap fragmentation to provide data corroborating their proposed structures (figs. S5 to S9).

Apart from the relative populations of the fully extended polyketide intermediates, both two-part combination reactions gave remarkably similar outcomes (Fig. 4). Elaboration of only the hexanoyl-primed ACP, and not the acetyl-primed (from KS-mediated loss of CO_2 from malonyl) or malonyl-primed ACP, supports the notion that the KS domain exerts control over the selection and extension of only specific starter units tethered to the ACP domain (in this case hexanoyl-*S*-ACP). These data support the assertion that the PT domain maintains the correct intramolecular aldol addition intermediate and promotes its dehydration, facilitating nonenzymatic release of either the naphthopyrone **5** or the anthrone **2**. Note that the ACP active-site tryptic peptide with the doubly dehydrated hexanoate + 7 acetate species (**6**, PT product) showed an absorbance under single-wavelength analysis (310 nm), in further support that this species is indeed the TE/CLC substrate. Combined with the drastic reduction in the flux to product(s) in the absence of the tailoring domains (Fig. 2), the mass spectrometric data support assignment of the PT domain as an aromatase/cyclase domain.

The deconstruction approach taken here has demonstrated the synthetic roles of all recognized domains in an IPKS catalytic cycle, notably the product template (PT) domain, which should prove to be general for the broad class of multidomain IPKSs. The insights afforded by the catalytic autonomy of these dissected, free-standing domains enable a rational strategy for engineering these enzymes to synthesize alternative products.

References and Notes

1. J. Staunton, K. J. Weissman, *Nat. Prod. Rep.* **18**, 380 (2001).
2. M. A. Fischbach, C. T. Walsh, *Chem. Rev.* **106**, 3468 (2006).
3. J. M. Crawford, A. L. Vagstad, K. C. Ehrlich, C. A. Townsend, *Bioorg. Chem.* **36**, 16 (2008).
4. D. Udwary, M. Merski, C. A. Townsend, *J. Mol. Biol.* **323**, 585 (2002).
5. J. M. Crawford, B. C. R. Dancy, E. A. Hill, D. W. Udwary, C. A. Townsend, *Proc. Natl. Acad. Sci. U.S.A.* **103**, 16728 (2006).
6. C. Sanchez, L. Du, D. J. Edwards, M. D. Toney, B. Shen, *Chem. Biol.* **8**, 725 (2001).
7. I. Fujii, A. Watanabe, U. Sankawa, Y. Ebizuka, *Chem. Biol.* **8**, 189 (2001).
8. Z.-G. Chen, I. Fujii, Y. Ebizuka, U. Sankawa, *Phytochem* **38**, 299 (1995).
9. R. McDaniel, S. Ebert-Khosla, D. A. Hopwood, C. Khosla, *Science* **262**, 1546 (1993).
10. Y. Tang, S. C. Tsai, C. Khosla, *J. Am. Chem. Soc.* **125**, 12708 (2003).
11. A. T. Keatinge-Clay, D. A. Maltby, K. F. Medzihradszky, C. Khosla, R. M. Stroud, *Nat. Struct. Mol. Biol.* **11**, 888 (2004).
12. Y. Ma *et al.*, *ChemBioChem* **7**, 1951 (2006).
13. S. M. Ma *et al.*, *J. Am. Chem. Soc.* **130**, 38 (2008).
14. P. C. Dorrestein *et al.*, *Biochemistry* **45**, 12756 (2006).
15. Supported by NIH research grants ES001670 (C.A.T.) and GM067725 (N.L.K.), NIH Chemical Biology Interface training grant GM070421 (P.M.T.), and NIH postdoctoral fellowship GM079408 (J.R.S.).

Supporting Online Material

www.sciencemag.org/cgi/content/full/320/5873/243/DC1
Materials and Methods
Figs. S1 to S9
Tables S1 and S2
References

31 December 2007; accepted 29 February 2008
10.1126/science.1154711

Video-Rate Far-Field Optical Nanoscopy Dissects Synaptic Vesicle Movement

Volker Westphal,[1*] Silvio O. Rizzoli,[2,3*] Marcel A. Lauterbach,[1] Dirk Kamin,[3] Reinhard Jahn,[2] Stefan W. Hell[1†]

We present video-rate (28 frames per second) far-field optical imaging with a focal spot size of 62 nanometers in living cells. Fluorescently labeled synaptic vesicles inside the axons of cultured neurons were recorded with stimulated emission depletion (STED) microscopy in a 2.5-micrometer by 1.8-micrometer field of view. By reducing the cross-sectional area of the focal spot by about a factor of 18 below the diffraction limit (260 nanometers), STED allowed us to map and describe the vesicle mobility within the highly confined space of synaptic boutons. Although restricted within boutons, the vesicle movement was substantially faster in nonbouton areas, consistent with the observation that a sizable vesicle pool continuously transits through the axons. Our study demonstrates the emerging ability of optical microscopy to investigate intracellular physiological processes on the nanoscale in real time.

Many questions in the life sciences could be answered if lens-based optical microscopy featured the resolution of electron microscopy, or if the electron microscope operated under physiological conditions. However, for reasons deeply rooted in the working principles of these systems, nanoscale resolution and noninvasive cellular imaging seemed mutually incompatible. Although widely accepted for decades, this notion is rapidly changing. Particularly in fluorescence imaging, far-field optical concepts have emerged that are no longer limited by diffraction (*1*–*9*). For example, stimulated emission depletion (STED) microscopy (*1*, *2*) overcomes the diffraction barrier by producing fluorescent focal spots smaller than $D \approx 200$ to 300 nm in diameter. In a typical STED microscope, the focal spot of excitation light is overlapped with a doughnut-shaped spot of light of lower photon energy, quenching excited molecules in the excitation spot periphery by stimulated emission. The net result is a subdiffraction-sized fluorescent spot of diameter $d \approx D/\sqrt{1 + I/I_s} < D$, which, if scanned through the specimen, renders images of subdiffraction resolution d. I and I_s denote the intensity of the STED beam and the characteristic intensity for the quenching of the fluorescent dye used, respectively. Adjusting $I >> I_s$ allows one to tune the resolution d, in principle to the molecular scale.

Until now, the 20- to 70-nm resolution realized with STED has been used to map the nanoscale distribution of proteins inside cells (*3*) and on the plasma membrane (*2*). However, in all of these applications, the cells were fixed or basically static, leaving open the question of whether nanoscale imaging of fast physiological phenomena would be possible. Besides, the fast recording of high-resolution image frames is questionable given the limited number of photons emitted during the frame time. To meet these challenges, we balanced the resolution d, tuning the spot down to a size at which we were able to collect just enough photons from the features of interest to safely discern them from background. This strategy, a special feature of STED microscopy and related techniques (*7*), allowed reliable repeated imaging of rapidly moving small organelles inside living cells with nanoscale resolution. Specifically, we investigated the movement of synaptic vesicles in cultured neurons.

Although several steps in synaptic vesicle recycling are well understood (*10*), vesicle movement has been difficult to study, because the ~40-nm-diameter vesicles are housed in presynaptic nerve terminals of ~1 μm in diameter, referred to as synaptic boutons. Most current insights have therefore been gained by sparse vesicle labeling (*11*–*13*), or by indirect methods, such as fluorescence recovery after photobleaching (*14*–*16*) and correlation spectroscopy (*17*–*19*).

[1]Department of NanoBiophotonics, Max-Planck-Institute for Biophysical Chemistry, Göttingen 37077, Germany. [2]Department of Neurobiology, Max-Planck-Institute for Biophysical Chemistry, Göttingen 37077, Germany. [3]STED Microscopy of Synaptic Function, European Neuroscience Institute, Göttingen 37077, Germany.

*These authors contributed equally to this work.
†To whom correspondence should be addressed. E-mail: shell@gwdg.de

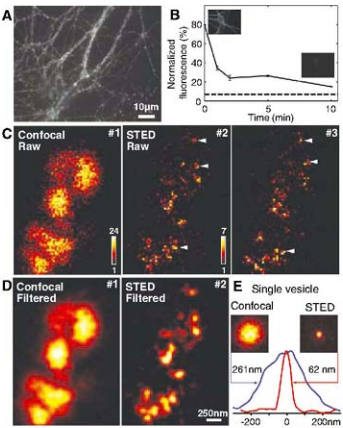

Fig. 1. Real-time STED microscopy resolves single synaptic vesicles in living neurons. **(A)** Typical wide-field overview of cultured hippocampal neurons whose surface vesicle pool was labeled with mouse anti-synaptotagmin and Atto647N-labeled anti-mouse Fab fragments. **(B)** The labeled pool of vesicles is rapidly endocytosed, as observed by the reduced number of surface-exposed synaptotagmin molecules with increasing time between primary and secondary antibody labeling (*20*). Data are shown as the mean ± SEM, with each data point representing three to seven independent neuronal cultures. The dashed line indicates the background fluorescence determined from unstained preparations. **(C)** Images of a short fragment of a stained axon, in confocal mode (frame #1) and in STED mode (frames #2 and #3). The increased resolution in the STED image and the reappearance of vesicles in subsequent frames can be seen (three arrowheads indicate relatively stable vesicles; also, many other spots can be recognized in both frames). The insers in #1 and #2 indicate the color maps used. **(D)** Smoothing in confocal mode does not improve the differentiation of single objects, although this filtering method helps to identify superresolved vesicles in the STED images. **(E)** Images of a single stationary vesicle in confocal and STED mode (summed over 10 and 50 frames, respectively) reveal the cross-section of the focal spot in each mode. The line profiles through their center demonstrate the reduction in focal spot area by a factor of 18.

Higher spatial resolution enables the imaging of a sizable fraction of the vesicles simultaneously. We labeled cultured hippocampal neurons with monoclonal mouse antibodies directed against the intravesicular (lumenal) domain of the synaptic vesicle protein synaptotagmin (*2*). The antibodies were briefly applied to the neurons (on ice), followed by an exposure to Fab fragments from antibodies to mouse (anti-mouse) labeled with the organic fluorophore Atto 647N featuring $I_s \approx 10$ to 20 MW/cm^2 at a de-excitation wavelength of 750 nm. This procedure ensured that only vesicles fused to the plasma membrane were labeled (*2*), because only these vesicles were exposed to the outside space [Fig. 1A and (*20*)]. The labeled vesicle pool encompassed as much as 10 to 20% of all vesicles (*21*); moreover, this pool fully participated in active vesicle recycling, as confirmed by the rapid endocytosis of the label (Fig. 1B). Two minutes after labeling, only ~18% of the label still resided on the surface; after 10 min, the value had dropped to ~8%.

Figure 1C shows that, unlike standard confocal imaging, STED microscopy enables the detection of single synaptic vesicles. Video-rate imaging was accomplished by scanning the excitation and depletion beam pair in the focal plane by means of a 16-kHz resonant mirror in one direction; the perpendicular axis was scanned by moving the sample with a piezo actuator (*22*). This configuration allowed us to image an 1.8 μm by 2.5 μm area within 35 ms, i.e., at 28 frames per second [movie S1 and (*20*)]. By imaging the fluorescence onto a pinhole and acquiring images rapidly, noise levels were only ~0.1 and 0.02 counts per pixel inside and outside the axons, respectively (Fig. 1C). Although a single detected pho-

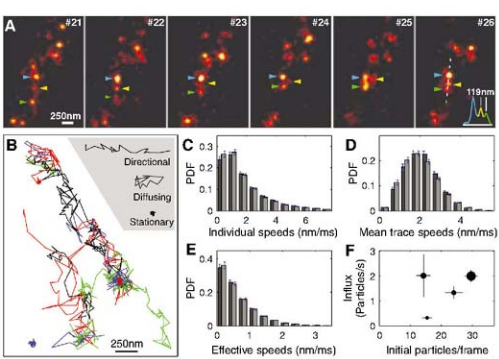

Fig. 2. Characteristics of synaptic vesicle movement. **(A)** Successive STED frames, filtered (movie S1). The arrowheads indicate three vesicles, which were tracked in all frames, localized in a sub-diffraction space. The inset in frame #26 shows an intensity profile along the dotted white line. **(B)** Example vesicle traces in one movie. Occasionally, vesicles may seem trapped in a small area, whereas other traces are reminiscent of active transport (examples in inset). **(C** to **E)** Histograms of vesicle speeds: (C) based on displacement between two consecutive frames, (D) mean speed per trace, and (E) effective speed determined by dividing the distance between the end and the origin of the trace by the trace duration. See (*20*) for details of the analysis. The results are shown as the mean ± SEM, with movies analyzed from four independent experiments. Black bars show results with normal buffer (53 movies); depolarized preparations (Tyrode solution containing 70 mM KCl) are shown in gray (75 movies). **(F)** Number of vesicles (traces) entering the imaged area per second, as a function of the number of vesicles detected in the first frames of the movie. Results from four independent experiments, each consisting of a number of movies, are shown. The circle area is proportional to the number of movies analyzed. PDF: probability density function (probability normalized to unity).

ton in a pixel could still be due to noise, the probability of simultaneously detecting three or more photons is several standard deviations above the noise level, allowing us to conclude that the detected signal originates from labeled features. This reasoning was confirmed by comparing consecutive frames, where the labeled objects moved only slightly (Fig. 1C, middle and right panels); random noise, by contrast, would manifest itself as flickering. We also measured the frequency of false-positive identifications in preparations where no specific signal was expected (*20*); we found it to be on average around 0.1 events per frame. Applying $I = 400$ MW/cm^2 renders a full width at half maximum (FWHM) of our vesicle images of 62 nm (Fig. 1E), which means that the effective focal detection area is reduced by a factor of 18 compared to confocal imaging.

To further improve the confidence of vesicle recognition in our data, we applied a mathematical filter (Fig. 1D), which was essentially a smoothing algorithm. The resolution enhancement, coupled with the filter, allowed us both to observe individual vesicle movements (Fig. 2A) and to track individual vesicles automatically [Fig. 2B and (*20*)]. Although bleaching did occur during data acquisition (fig. S1), we were able to trace large numbers of vesicles, in ~130 movies of 1000 frames each, from four independent experiments. Although the vesicles resided mainly in a low-mobility state (Fig. 2C) (*14*, *15*), most traces also included rapid movements, with the average speed for each individual vesicle peaking around ~2 nm/ms (Fig. 2D).

Because the movement was largely nondirectional, overall vesicle displacement appeared to be restricted (Fig. 2E). In agreement with previous observations, in which mobility was low also during synaptic activity (*13*), none of the mobility parameters increased substantially during stimulation with increased concentrations of KCl. To determine whether vesicle movement was diffusive or motor-driven, we perturbed cytoskeletal elements by using the actin-disrupting agent latrunculin A, or via the microtubule-disrupting nocodazole. The results (fig. S2) show that both drugs reduce vesicle mobility, indicating that active transport plays a role in vesicle traffic in axons. Nevertheless, vesicle motion persisted, suggesting that a substantial fraction of the vesicle movement is diffusive.

Even after bleaching the vesicles that were initially present (fig. S1), fluorescence persisted as new vesicles continuously entered the imaged area, at a rate of 0.5 to 3 vesicles per second in different experiments (Fig. 2F). This result, even taken at its lowest value, indicates that a fairly large number of vesicles passes constantly through the boutons [see also (*23*)].

As a control, we also imaged and analyzed the vesicles in chemically fixed neurons, in which case the vesicle movement was substantially reduced (fig. S3). We occasionally observed vesi-

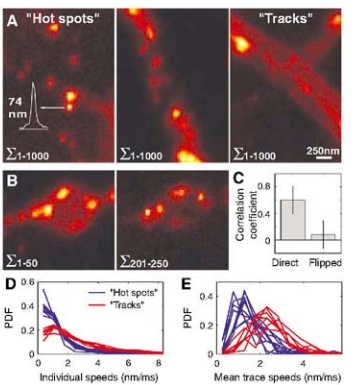

Fig. 3. Synaptic vesicle movement in different axonal areas. **(A)** Summing all frames of the individual movies indicates vesicle traces. In many movies, the vesicles seemed to concentrate in "hot spots" (left), which typically assemble in what resembles confocal images of presynaptic boutons. However, other movies showed few spots and were instead dominated by the presence of linear "tracks" of vesicle movement (right). The center panel shows an example of intermediate behavior. The inserted graph displays the intensity profile (with its FWHM) through the hot spot indicated by the thin white arrow. **(B)** The areas preferred by the vesicles are relatively constant. The sums of the first 50 frames (left), and of the frames 201 to 250 (right), are surprisingly similar for the same movie. **(C)** A correlation coefficient analysis between these images performed for all of our movies shows that the areas of vesicle movement tend to correlate (bars show mean ± SD, $n > 100$ images, from four independent experiments). Controls with horizontally flipped images exhibited a substantially reduced correlation. **(D** and **E)** Histograms of individual speeds (D) and mean trace speeds (E) for 8 to 10 different movies dominated by hot spots or tracks.

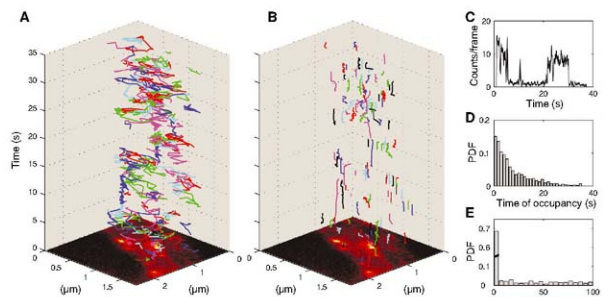

Fig. 4. Hot spots of vesicle localization. Comparison between synaptic vesicle traces **(A)** and hot spot traces **(B)**. Hot spots were defined as pointlike objects appearing in a 50-frame moving average; they indicate small areas where fluorescence occurs over longer times (*20*). The average image of the complete movie is placed at the bottom. **(C)** Vesicles can move in and remain trapped in hot spots, as shown here by the strong signal fluctuation in a single hot spot. **(D)** Probability histogram of the occupancy time of the hot spots (the fraction of time they were filled by vesicles). **(E)** Histogram of the percentage of time each vesicle spent in a hot spot.

cles instantly losing their fluorescence and then reappearing after up to a few seconds ("blinking"), a phenomenon known from single-molecule recordings but also from few-molecule ensembles (*24*) (fig. S4).

To better understand the patterns of overall vesicle movements, we investigated the sum of all frames for each of the individual movies. Areas where vesicles moved randomly appeared blurred, whereas stationary vesicles induced "hot spots" (Fig. 3A, left panel). A number of movies also showed linear patterns, indicative of vesicle routes or "tracks" (Fig. 3A, right panel). Typically, the hot spots assembled in areas reminiscent of confocal images of the synaptic boutons (Fig. 3B); the tracks, however, seemed to form between such boutons. The pattern of summed staining was not due to random vesicle accumulations, because it was relatively stable throughout each movie (Fig. 3, B and C). We analyzed 8 to 10 movies clearly dominated by hot spots or tracks, respectively, and we observed, as expected, that the vesicles within spot-dominated areas (boutons) tended to be much less mobile (Fig. 3, D and E), exhibiting a behavior much closer to that in fixed neurons (fig. S3).

To investigate the nature of the hot spots, we performed a running average analysis of the movies. Unlike the vesicles, the hot spots appeared to be immobile and persistent (Fig. 4, A and B). We frequently observed vesicles moving into hot spots and remaining temporarily trapped (Fig. 4C). However, we also observed vesicles disappearing instantly from hot spots, a behavior that we attribute to either blinking or to moving out of the focal plane. The hot spots were occupied for about 22% of the time (Fig. 4D); 31% of the vesicles passed through a hot spot and individual vesicles remained for 16% of the time in hot spots on average (Fig. 4E). The large number and wide distribution of hot spots argues against their being release sites where the vesicles would dock, because in this preparation typically only one, and rarely two, small active zones (~200 nm diameter) are found per bouton (*25*). The hot spots are likely to be "pockets" in the synaptic vesicle clusters where the labeled vesicles are occasionally constrained, although the molecules involved in the synaptic vesicle cross-linking have yet to be clearly defined (*26*).

In general, synaptic vesicles are quite mobile, although their tendency to move nondirectedly generally impedes their effective translation. Our data support the recently proposed stick-and-diffuse model (*18*, *19*), in which the vesicles repeatedly bind and diffuse away from the cellular elements. Nevertheless, a strong flux of synaptic vesicles is present through the axons (Fig. 2F). To place vesicle movement in perspective, if only one vesicle passes through a bouton each second, in about 3 min the number of vesicles passed through equals the total number of vesicles in the bouton (*25*). This suggests that the boutons from the same axon may be strongly interlinked, with their (recently endocytosed) vesicles participating in a common "superpool."

We conclude that STED microscopy can be used to investigate fast biological processes in vivo. The relatively low count rates in our images were less problematic than one might have thought, because the small spot size (62 nm), similar to the size of the vesicles (40 nm), allowed vesicles to be treated as distinct bright objects, which were easily distinguished from the low background. We used low-pass filtering to increase the confidence of detecting photon clusters representing vesicles. However, with a better knowledge of the background statistics and more sophisticated mathematical methods such as maximum-likelihood estimation, it should be possible to identify vesicles without such filtering. Moreover, brighter samples, or more sensitive imaging, would allow for higher resolution, a larger field of view, and/or faster recordings. Besides using higher densities of fluorescent markers, two relatively obvious improvements would allow us to reach this goal: STED with continuous-wave beams (*27*) would increase the instant photon flux and detection with two opposing high-aperture lenses would double the detection efficiency (*28*). This would permit further improvement of the data, because faster recordings would facilitate automatic tracking at even higher densities, eventually allowing the rapid imaging of a multitude of intracellular processes in living cells.

References and Notes

1. S. W. Hell, J. Wichmann, *Opt. Lett.* **19**, 780 (1994).
2. K. I. Willig, S. O. Rizzoli, V. Westphal, R. Jahn, S. W. Hell, *Nature* **440**, 935 (2006).
3. G. Donnert *et al.*, *Proc. Natl. Acad. Sci. U.S.A.* **103**, 11440 (2006).
4. E. Betzig *et al.*, *Science* **313**, 1642 (2006).
5. M. J. Rust, M. Bates, X. Zhuang, *Nat. Methods* **3**, 793 (2006).
6. S. T. Hess, T. P. K. Girirajan, M. D. Mason, *Biophys. J.* **91**, 4258 (2006).
7. S. W. Hell, *Science* **316**, 1153 (2007).
8. G. Donnert *et al.*, *Biophys. J.* **92**, L67 (2007).
9. M. Bates, B. Huang, G. P. Dempsey, X. Zhuang, *Science* **317**, 1749 (2007).
10. T. C. Südhof, *Annu. Rev. Neurosci.* **27**, 509 (2004).
11. A. M. Aravanis, J. L. Pyle, R. W. Tsien, *Nature* **423**, 643 (2003).
12. S. P. Gandhi, C. F. Stevens, *Nature* **423**, 607 (2003).
13. E. A. Lemke, J. Klingauf, *J. Neurosci.* **25**, 11034 (2005).
14. A. W. Henkel, L. L. Simpson, R. M. A. P. Ridge, W. J. Betz, *J. Neurosci.* **16**, 3960 (1996).
15. K. Kraszewski, L. Daniell, O. Mundigl, P. De Camilli, *J. Neurosci.* **16**, 5905 (1996).
16. M. A. Gaffield, S. O. Rizzoli, W. J. Betz, *Neuron* **51**, 317 (2006).
17. R. Jordan, E. A. Lemke, J. Klingauf, *Biophys. J.* **89**, 2091 (2005).
18. M. Shtrahman, C. Yeung, D. W. Nauen, G. Q. Bi, X. L. Wu, *Biophys. J.* **89**, 3615 (2005).
19. C. Yeung, M. Shtrahman, X. L. Wu, *Biophys. J.* **92**, 2271 (2007).
20. Material and methods are available as supporting material on *Science* Online.
21. S. O. Rizzoli, R. Jahn, *Traffic* **8**, 1137 (2007).
22. V. Westphal, M. A. Lauterbach, A. Di Nicola, S. W. Hell, *N. J. Phys.* **9**, 435 (2007).
23. K. J. Darcy, K. Staras, L. M. Collinson, Y. Goda, *Nat. Neurosci.* **9**, 315 (2006).
24. P. Tinnefeld, V. Buschmann, K. D. Weston, M. Sauer, *J. Phys. Chem. A* **107**, 323 (2003).
25. T. Schikorski, C. F. Stevens, *J. Neurosci.* **17**, 5858 (1997).
26. S. O. Rizzoli, W. J. Betz, *Nat. Rev. Neurosci.* **6**, 57 (2005).
27. K. I. Willig, B. Harke, R. Medda, S. W. Hell, *Nat. Methods* **4**, 915 (2007).
28. S. Hell, E. H. K. Stelzer, *J. Opt. Soc. Am. A* **9**, 2159 (1992).

29. S.O.R is the recipient of a long-term fellowship from the Human Frontier Science Program. This work was supported in part by funds from the Gottfried Wilhelm Leibniz Program of the Deutsche Forschungsgemeinschaft to R.J., by a grant from the German Ministry of Research and Education (BMBF, Nanolive) to S.W.H., and by a grant from the German Ministry of Research and Education (BMBF, Nanolive, "Vesikelbewegungen durch Nanoauflösung") to S.O.R. We thank I. Herfort for assistance with cell culturing and A. Di Nicola for his custom data-acquisition-card. We also thank L. Kastrup, J. Keller, and A. Schönle for helpful discussions and for help with the software ImSpector. Finally, we thank B. Rankin for critical reading of the manuscript.

Supporting Online Material

www.sciencemag.org/cgi/content/full/1154228/DC1
Materials and Methods
Figs. S1 to S4
References
Movie S1

17 December 2007; accepted 8 February 2008
Published online 21 February 2008;
10.1126/science.1154228
Include this information when citing this paper.

New Products

High Throughput DNA/RNA Purification

The Clarity QSP system for synthetic RNA and DNA purification delivers nearly impurity-free, concentrated, full-length oligonucleotide sequences. Clarity QSP is offered in three cartridge formats and in 96-well plates. The cartridge formats are suitable for applications that require increased loading capacities, and can purify oligonucleotide samples in less than eight minutes using vacuum or positive pressure systems. The 96-well plate format can be easily automated for high throughput parallel purification and eliminates the tube-in-plate combination of other approaches. Clarity QSP overcomes the pitfalls of first generation trityl-on purification. The system's unique buffer works synergistically with ammonia-based deprotecting solutions to selectively retain the full-length trityl-on DNA or RNA sequence. The method eliminates subsequent wash steps and does not require toxic ion-pairing reagents. It delivers DNA at 90 percent to 95 percent purity, with recovery rates of more than 80 percent and RNA at 89 percent to 93 percent purity, with recovery rates of more than 75 percent.

Phenomenex
For information 310-212-0555
www.phenomenex.com

cDNA Synthesis Kit

The SuperScript VILO cDNA Synthesis Kit, the latest in a family of reverse transcription kits, provides reliable and sensitive first-strand complementary DNA (cDNA). The kit features RNase-H–reduced SuperScript III Reverse Transcriptase, which generates increased yields of cDNA and improves quantitative polymerase chain reaction (qPCR) sensitivity up to fourfold over similar systems, according to the manufacturer. In addition, the new kit allows linear detection in a downstream qPCR reaction from as little as 1 picogram of starting RNA up to 2.5 micrograms in a 20-microliter reaction. The kit makes use of an enhanced reaction mix that includes a helper protein designed for minimizing qPCR inhibition, leading to improved detection.

Invitrogen
For information 800-955-6288
www.invitrogen.com/vilo

Single Nucleotide Polymorphism Chips

The new Infinium HD BeadChip product line for DNA analysis features up to 2.3 million single nucleotide polymorphisms (SNPs) per BeadChip. The Human 1M-Duo BeadChip offers two samples per chip, and the Human610-Quad BeadChip offers four samples per chip. Both feature enhanced signal discrimination and a new SNP calling algorithm. The new BeadChips offer significant advances over previous products, including increased sample throughput, lower input sample volume, and improvements to the Infinium assay that enhance system performance. Both arrays on the Human 1M-Duo BeadChip contain markers for more than 1 million diverse genetic variants, all of which can be used for both whole-genome genotyping and copy number variation analysis. It includes recently identified disease-associated SNPs and intelligently selected high-density SNPs in coding regions of the genome. Built on the content of Illumina's broadly adopted HumanHap550 BeadChip, the Human610-Quad BeadChip has 550,000 SNPs plus an additional 60,000 genetic markers per sample.

Illumina
For information 800-809-4566
www.illumina.com

Proteasome Inhibitors

The proteasome is a large barrel-like protein in the cytoplasm and nucleus of eukaryotic cells. The main function of the proteasome is to degrade unneeded and damaged proteins by proteolysis. The proteasomal degradation pathway is involved in many cellular processes including the cell cycle, gene expression, and responses to oxidative stress. A variety of proteasome inhibitors are available for research in these areas.

Tocris Bioscience
For information 800-421-3701
www.tocris.com

Monoclonal Antibody

Human glypican 3 (GPC3) is an oncofetal tumor antigen involved in growth regulation, cell division, and migration. The GPC3 Monoclonal Antibody (clone 1G12) can detect GPC3 in tissue by immunohistochemistry. Suitable for use on formalin-fixed, paraffin-embedded tissue sections, it is available in prediluted and concentrated form for manual use or in automated instruments.

BioMosaics
For information 802-656-5443
www.biomosaics.com

Spill Detector

The OS*250 system detects spills and leaks before they can cause a problem in an expensive microscope or other piece of equipment. As little as three drops of liquid cause the OS*250 to react. The system consists of a control unit and moisture sensing mat made from a material specially developed for detecting spills. It is connected to the control unit by a simple connection cable. When liquid is detected on the sensing mat, the controller sounds an audible alarm, flashes an LED, and turns off the power of any device plugged into the single outlet, solid-state power controller. The spill sensor is supplied with the controller and four reusable 30 cm by 30 cm mats that can be cut to any size.

KD Scientific
For information 508-429-6809
www.kdscientific.com

Electronically submit your new product description or product literature information! Go to **www.sciencemag.org/products/newproducts.dtl** for more information.

Newly offered instrumentation, apparatus, and laboratory materials of interest to researchers in all disciplines in academic, industrial, and governmental organizations are featured in this space. Emphasis is given to purpose, chief characteristics, and availability of products and materials. Endorsement by *Science* or AAAS of any products or materials mentioned is not implied. Additional information may be obtained from the manufacturer or supplier.